DESIGN AND CONTROL OF CUSTOM POWER DEVICES FOR MITIGATION OF POWER QUALITY PROBLEMS

A Thesis Submitted
In Partial Fulfillment of the Requirement
for the Degree of

DOCTOR OF PHILOSOPHY

by

KANCHAN BALA RAI

(2K19/PHDEE/503)

Under the Supervision of

Dr. Narendra Kumar and Dr. Alka Singh

Professor, Electrical Engineering Department,
Delhi Technological University

To the
Department of Electrical Engineering

DELHI TECHNOLOGICAL UNIVERSITY

(Formerly Delhi College of Engineering)

Shahbad Daulatpur, Main Bawana Road, Delhi-110042. India

April, 2024

DELHI TECHNOLOGICAL UNIVERSITY

(Formerly Delhi College of Engineering)
Shahbad Daulatpur, Main Bawana Road, Delhi-42

ACKNOWLEDGEMENT

I would like to express my deep and sincere gratitude to my supervisors **Prof. Narendra Kumar** and **Prof. Alka Singh** for their valuable guidance and continuous monitoring of my research work. It was great honour for me to pursue my research work under their supervisions. **Prof. Narendra Kumar** has been the motivating and inspiring factor behind my research work. It's his Vigor and hunger to perform in adverse situation, which has inspired me to thrive for excellence. Continuous monitoring by **Prof. Alka Singh**, valuable guidance and input has always been a driving force to complete my research work. It is a life time experience to work under both of my supervisors and humbly acknowledge lifetime gratitude to them.

I would like to express my thanks to **Prof. Rachna Garg, HOD (EE)** for her kind support. I would like to thank the SRC members mainly **Prof. T.S Bhatti**, who has given me valuable guidance and advice to improve quality of my research work. I am extremely thankful to staff member of Power System Lab **Komal Singh** for providing me immense facility and assistance to carry out my research work. I would like to thank other office staffs, Central library and Computer Centre staff members, for their valuable co-operation and support. I would like my sincere thanks to **Dr. Prakash Chittora,** who have guided me to develop hardware at initial level of my research work.

I am extremely grateful to my research group and friends **Sudhansu Mittal, Amarendra Pandey, Vineet Kumar, Oinam Lotika Devi, and Md. Modassir Masoom, Dr. Saket Gupta, Dr. Hemant Saxena and Dr. Ankita Arora** for their valuable assistance, co-operation and great source of learning. If I get any success today for my research work, the entire credit should go to my mother **Smt. Kiran Bala Rai**, Brother **Abhishek Narayan Rai**, and father **Shri. Krishna Kumar Rai**. I deeply convey my gratitude to my husband **Mr. Punit Rai** who has endured me and my long hours spent in the laboratory with patience and encouraged me to carry out my research work. I would like to thank other family members supporting me directly or indirectly to carry out my research work. Last, but not the least, I thank Mother Nature and Almighty God for providing me the opportunity for pursuing doctoral studies.

Kanchan Bala Rai

Roll No. 2K19/PHDEE/503

DELHI TECHNOLOGICAL UNIVERSITY

(Formerly Delhi College of Engineering)
Shahbad Daulatpur, Main Bawana Road, Delhi-42

CANDIDATE'S DECLARATION

I Kanchan Bala Rai hereby certify that the work which is being presented in the thesis entitled "Design and Control of Custom Power Devices for Mitigation of Power Quality Problems" in partial fulfillment of the requirements for the award of the Degree of Doctor of Philosophy, submitted in the Department of Electrical Engineering, Delhi Technological University is an authentic record of my own work carried out during the period from January 2020 to April 2024 under the supervision of Prof. Narendra Kumar and Prof. Alka Singh.

The matter presented in the thesis has not been submitted by me for the award of any other degree of this or any other Institute.

Candidate's Signature

DELHI TECHNOLOGICAL UNIVERSITY

(Formerly Delhi College of Engineering)
Shahbad Daulatpur, Main Bawana Road, Delhi-42

CERTIFICATE BY THE SUPERVISOR(s)

Certified that **Kanchan Bala Rai** (2K19/PHDEE/503) has carried out their search work presented in this thesis entitled **"Design and Control of Custom Power Devices for Mitigation of Power Quality Problems"** for the award of **Doctor of Philosophy** from Department of Electrical Engineering, Delhi Technological University, Delhi, under our supervision. The thesis embodies results of original work, and studies are carried out by the student herself and the contents of the thesis do not form the basis for the award of any other degree to the candidate or to anybody else from this or any other University/Institution.

Signature
Prof. Narendra Kumar
Department of Electrical Engineering
Delhi Technological University
Delhi-110042, India

Signature
Prof. Alka Singh
Department of Electrical Engineering
Delhi Technological University
Delhi-110042, India

Date: 25.04.2024

DELHI TECHNOLOGICAL UNIVERSITY

(Formerly Delhi College of Engineering)

Shahbad Daulatpur, Main Bawana Road, Delhi-42

PLAGIARISM VERIFICATION

Title of the Thesis Design and Control of Custom Power Devices for Mitigation of Power Quality Problems Total Pages 235 Name of the Scholar Kanchan Bala Rai Supervisor (s)

(1) Prof. Narendra Kumar

(2) Prof. Alka Singh

Department Electrical Engineering

This is to report that the above thesis was scanned for similarity detection. Process and outcome is given below:

Software used: Turnitin Similarity Index: 8%, Total Word Count: 57573.

Date: 25.04.2024

Candidate's Signature **Signature of Supervisor(s)**

ABSTRACT

The combination of various power electronic loads and linear loads in the modern distributed grid offers a dynamic and complex electrical environment. These loads may have a major impact on power quality, resulting in problems like low power factor and harmonic production that compromise the grid's stability and effectiveness. This thesis work includes both current and voltage related PQ issues such as voltage sag, voltage swell, voltage harmonics, load unbalancing, reactive power compensation and poor power factor.

In this work, design and control of single and three-phase grid connected PV system has been presented. It permits power quality enhancement, load balancing, and active and reactive distribution compensation in single-phase and three-phase grid connected system. A single-phase, single-stage topology of a grid-integrated PV system is utilized to feed nonlinear loads at the point of common coupling (PCC). A simple Perturb and observe (P&O) MPPT technique is used to extract the maximum available power from PV in single stage single phase and three-phase grid connected PV system.

The Parameters of grid connected PV system are estimated and hence the prototype of single-phase and three-phase grid connected PV system are designed for Shunt Active Power Filter (SAPF), Series Active Power Filter and Unified Power Quality Compensator (UPQC). The shunt and series active power filter are also named as DSTATCOM and DVR respectively in the thesis work. Ideally, a control algorithm requires a synchronizing technique, fundamental component, a DC link voltage controller and the feed-forward term. The generation of reference source current for providing switching signals to voltage source converter (VSC) requires synchronizing signals or sine template. Most of the proposed control scheme for DSTATCOM and DVR are using unit template based synchronizing signals. But the unit template method will not generate balanced and sinusoidal synchronizing signals under weak grid conditions. For that weak grid condition, a conventional Synchronous Reference Frame Theory (SRFT), Second order generalized integrator and modified PLL is utilized in the single and three-phase grid connected system.

The fundamental component extraction techniques are used to estimate the fundamental component of load current and source voltage. SRFT, Instantaneous Reactive Power Theory (IRPT), Hermite Polynomial, and Bernoulli Polynomial based load compensation control schemes are used in single-phase grid connected PV system.

The fundamental load component is extracted from distorted load current using a single layer neural network. The objective of the designed controller is to fulfill the load's active power demand from the generated solar PV power and feed the excess power back to the grid when surplus. When solar PV is not integrated with the grid, the voltage source converter (VSC) acts as a distribution static compensator (DSTATCOM), improving the system's utilization factor.

In order to mitigate power quality issues in electrical systems, specialised power device design and control are essential. The development and implementation of novel solutions to problems including voltage sags, swells, harmonics, transients, and other power quality issues is the main goal of this research. The research highlights the incorporation of customised power components designed for particular uses, providing improved efficiency and dependability. The results are validated as per IEEE-519 standards.

Developing advanced power electronics solutions, such as shunt active power filter, series active power filter, and unified power quality compensator, is included in the design part. These devices are designed to deliver a modified response to the system's particular features under consideration, enabling focused mitigation of power quality issues. A significant aspect of this research is control techniques, which highlight the innovative and flexible management of customized power devices.

The study investigates advanced control methods, including as adaptive ε-NSRLMMN, and q-LMF to maximise device performance in various kinds of operating conditions. The objective is to assure efficient power quality improvement by real-time monitoring, efficient responses, and effective compensation. In conclusion, this research advances custom power devices as useful equipment for reducing issues with power quality. The integration of detailed design techniques with smart control methods presents an auspicious path towards enhancing the

dependability and efficiency of electrical systems, consequently strengthening the reliable and sustainable functioning of modern power grids.

Table of Contents

LIST OF FIGURES

LIST OF TABLES

LIST OF SYMBOLS

Z_S	Source Impedance
R_S	Source Resistance
L_S	Source Inductance
L_f	Interfacing inductor
R_C	Ripple Filter
V_{rms}	RMS Grid Voltage
V_{dc}	DC link Voltage
C_{dc}	DC Link Capacitance
K_1	Constant
$V_{dc(min)}$	Calculated minimum level of DC link Voltage
I_{ph}	Phase Current
a	Overloading Factor
f_{sw}	Switching Frequency
ΔI_{cr}	Ripple in Current
m	Modulation Index
I_m	Current Maximum Level
R_{in}	Input Side Resistance
P_{mp}	PV Maximum Power
V_{OC}	Open Circuit Voltage
I_{Sc}	Short Circuit Current
V_m	Peak Amplitude source voltage
I_{mp}	Maximum Current
D	Duty Cycle
P_{PV}	PV Power
V_{MPP}	Voltage at Maximum Power
$V_{dc(ref)}$	Reference DC link Voltage
V_{dce}	Error Difference in DC Link voltage and Reference DC Link Voltage
L_f	Interfacing inductor
K_P	Proportional Gain of PI controller
K_i	Integral Gain of PI controller
I_0	Output current of PV cell
I_{ph}	Photon Current
I_d	Diode Current
I_{sh}	Leakage current in parallel resistor
$i_{L\alpha}, i_{L\beta}$	Alpha and beta components of load current
V_t	Terminal voltage
u	In-phase unit template
i_s^*	Reference source current
i_s	Sensed source current
i_L	Load current
p_L, q_L	Instantaneous active and reactive power component

S	Summation of the product of weights and function of input vector.
$e(n)$	Calculated error at every instant of time
H_0, H_1, H_2	Hermite Polynomials
$w(n)$	Updated Weight
μ	Step-Size
P_{PV}	PV power
B_0, B_1, B_2	Bernoulli's Polynomial
I_{LFavg}	Average fundamental current
I_{PVff}	PV feedforward current
$D(s)$	Transfer function of the in-phase component
$Q(s)$	Transfer function of the Quadrature component
P_s	Source Power
Q_c	VSC reactive Power
V_{dc}	DC link voltage
i_{cc}	Compensating Current
$i_{La}, i_{Lb} i_{Lc}$	Three-phase load current
$u_{pa}, u_{pb} u_{pc}$	Unit template for each phase a, b, c
$W_{pa}, W_{pb} W_{pc}$	Fundamental weight for each phase a, b, c
W_{pm}	Average fundamental current
W_{eq}	Total current
i^*_{sabc}	Three phase Reference source current
i_{Sabc}	Actual three-phase reference source current
G	Diagonal matrix
i_{Cabc}	Three-phase compensating current
i_{Labc}	Three-phase load current
$v_{Cabc(inj)}$	compensating voltage of DVR
T_r	Series Transformer
S	Transformer KVA rating
V_{sd}	Supplied source voltages
V_{Ld}	Direct component actual load voltages

LIST OF ABBREVIATIONS

ANN	Artificial Neural Network
APF	Active Power Filter
ASD	Adjustable Speed Drive
BESS	Battery Energy Storage System
CCF	Complex Coefficient Filter
CDSC	Cascaded Delay Signal Cancellation
CGI	Cascaded Generalised Integrator
CPD	Custom Power Device
DAC	Digital to Analog
DC	Direct Current
DER	Distributed Energy Resources
DG	Distributed Generation
DOD	Depth of Discharge
DSC	Delay Signal Cancellation
DSO	Digital Signal Oscilloscope
DSP	Digital Signal Processor
DSTATCOM	Distributed Static Compensator
DVR	Dynamic Voltage Restorer
EPLL	Enhanced Phase Locked Loop
FAMAF	Frequency Adaptive Moving Average Filter
FFA	Firefly Algorithm
FFT	Fast Frequency Transform
FLL	Frequency Locked Loop
FMAF	Frequency Moving Average Filter
FPGA	Field Programmable Gate Array
GA	Genetic Algorithm
GI	Generalized Integrator
GSC	Grid-Side Converter
HCC	Hysteresis Current Controller
HIL	Hardware in loop
IEC	International Electrotechnical Commission
IEEE	Institute of Electrical and Electronics Engineers
IGBT	Insulated Gate Bipolar Transistor
IRPT	Instantaneous Reactive Power Theory
LANN	Legendre Functional Neural Network
LF	Loop Filter
LMF	Least Mean Fourth
LMMN	Least Mean Mixed Norm
LMS	Least Mean Square

LPF	Low Pass Filter
MA	Moving Average
MAF	Moving Average Filter
MATLAB	MATrix LABoratory
MCCF	Multiple Complex Coefficient Filter
MPPT	Maximum Power Point Tracking
MSE	Mean Square Error
MSTOGI	Multiple second and third-order generalized integrator
NN	Neural Network
NSRLMF	Normalized Sign Regressor Least Mean Fourth
NSRLMMN	Normalized Sign Regressor Least Mean Mixed Norm
NSRLMS	Normalized Sign Regressor Least Mean Square
OSG	Orthogonal Signal Generator
PCC	Point of Common Coupling
PI	Proportional Integrator
PLL	Phase Locked Loop
PQ	Power Quality
PV	Photo Voltaic
PWM	Pulse Width Modulation
RNN	Recurrent Neural Network
ROGI	Reduced Order Generalized Integrator
SAPF	Shunt Active Power Filter
SMC	Sliding Mode Controller
SOGI	Second Order Generalized Integrator
SRFT	Synchronous Reference Frame Theory
STATCOM	Static Compensator
THD	Total Harmonic Distortion
TOGI	Third Order Generalized Integrator
UPQC	Unified Power Quality Compensator
UVT	Unit Vector Template
VSC	Voltage Source Converter

CHAPTER 1

INTRODUCTION

1.1 General

The process of integrating renewable energy sources into our existing electrical grids is revolutionary and marks a fundamental change in how we produce and use electricity. The need to switch to sustainable and clean energy sources, fight climate change, and cut greenhouse gas emissions is driving this transformation. Renewable energy sources must be seamlessly assimilated into conventional power grids, which have traditionally relied heavily on fossil fuels and centralized generation. Examples of such sources are solar, wind, and hydropower. Integrating renewable energy sources with existing electrical networks has become crucial on a global scale in response to rising environmental concerns and the need for a more sustainable energy future. In order to fulfill the world's rising energy needs and reduce carbon emissions and climate change, it is essential and environmentally appropriate to produce electrical energy from renewable energy sources. Because they are endless, renewable energy sources that employ natural processes to produce electricity are seen as sustainable. Photovoltaic solar panels turn sunlight directly into electricity. These cells produce DC electricity, which is transformed into AC power for usage in buildings, commercial establishments, and the grid. Rooftop solar PV systems, solar farms, and smaller off-grid applications are all examples of their utilization.

The presence of a large number of nonlinear loads in the existing power system causes undesirable effect. The nonlinear loads draw non-sinusoidal current from the power source, which makes the source current non-sinusoidal. These are some examples of nonlinear loads personal computers (PC), adjustable speed drives (ASDs), and power electronics-related equipment. Harmonics, which are integer multiples of the fundamental frequency (often 50 Hz) in AC power networks, can be produced by nonlinear loads. These harmonics can cause problems with power quality by altering the voltage and current waveforms. Harmonic distortion can make equipment overheat, decrease the effectiveness of power distribution, and impair the functionality of other delicate electrical devices.

A single-stage photovoltaic (PV) connected grid system is a reasonably straightforward solar power design that links a solar array to the electrical grid directly without the need for complicated power electronics or energy storage. The solar electricity produced in such a system is delivered directly into the grid, where it can be utilized to power electrical loads or credited to the owner's utility account.

1.2 Power Quality standards

The regulatory authorities and standards organization establishes the technical guidelines and specifications related to power quality (PQ) standards in electrical distribution systems. In order to ensure that electrical systems and equipment operate properly and effectively, these standards aid in defining permissible values of certain power quality criteria. Issues including voltage and current waveforms, frequency, harmonics, voltage sags, voltage swells, and other disturbances are often covered by power quality standards. Classification of PQ comes under the standards IEC 61000-2-5:1995, IEC61000-2-1:1990, and IEEE 1159:1995. Transients' phenomenon comes under the standards IEC 61000-2-1:1990, IEC-1159:1995, and IEC 816:1984. Voltage sag and swells come under IEC 61009-2-1:1990 and harmonics come under IEEE 519:1992, IEC 61000-2-1:1990.

1.3 Classification of Power Quality Problems

Problems with an electrical power supply's voltage and current waveforms are referred to as power quality concerns, and they can have an impact on the functionality and performance of connected electrical and electronic equipment. Based on their nature and behaviors, these issues can be divided into several categories. The power quality problems are classified into different categories such as voltage variations, frequency variation, harmonics, transients voltage disturbance, voltage flicker, and voltage imbalance. In this research work, two main PQ problems are considered voltage-related and current-related. The voltage-related PQ issues are subcategorized into voltage sag, voltage swell, voltage unbalance, and voltage flicker and these PQ problems occur at grid/source voltage. Other related PQ problems are current harmonics, poor power factor, and reactive power demand due to nonlinear loads present in the distribution system.

1.3.1 Voltage-based PQ issues

Voltage-based PQ issues that occur at the source side or grid side are as follows:

- **Voltage Sag:** When the supply voltage drops between 0.1 pu and 0.9 pu of the standard rated rms voltage at a power frequency between 0.5 cycles and 1 minute, this is referred to as voltage sag. These are temporary decreases in voltage below a specific level, which are often brought on by power grid problems or the startup of major machinery. Equipment failures or shutdowns can result from voltage sags. Voltage sag lasts for a short duration from a few milliseconds to a few seconds.
- **Voltage Swell:** Voltage swells are momentary raises of voltage above a predetermined threshold. They may cause sensitive equipment to be damaged and can be brought on by the switching of capacitor banks or the disconnecting of heavy loads. Voltage swell lasts for a short duration from a few milliseconds to a few seconds.
- **Voltage imbalance:** An imbalance in the voltage levels of the three phases in a three-phase power system. This can cause equipment overheating and inefficiency in three-phase motors.
- **Voltage interruptions:** A momentary loss of voltage that is typically brought on by faults or the tripping of safety features in the power distribution system.
- **DC offset:** A direct current (DC) component that is constant or slowly varying is superimposed on the alternating current (AC) voltage waveform, which is a power quality problem known as DC offset in voltage. This may happen as a result of several operational and voltage-related power quality problems. Undesirable effects of DC offset are transformer saturation, overheating in motors, and equipment malfunctions.
- **Voltage harmonics:** The presence of non-sinusoidal components in the voltage waveform is commonly referred to as harmonic distortion. Non-linear loads, such as variable speed drives, can introduce harmonics into the system, which can lead to overheating in transformers and motors.

1.3.2 Current-based PQ issues

Nonlinear loads are a common cause of power quality problems in source currents in electrical systems. Devices and equipment that draw non-sinusoidal current waveforms from the power source are referred to as nonlinear loads. Typically, this is due to the

electronic switching components that are already present in these devices and equipment. These loads have the potential to cause several power quality issues, particularly current harmonics.

- **Current Harmonics:** Transient pulses or surges of current are drawn by nonlinear loads, which can distort the current waveform. Harmonic currents, which are multiples of the fundamental frequency, represent this distortion. Harmonic currents can cause several problems, including Overheating of conductors and transformers and reduced power factor, leading to lower apparent power and potential penalties from utilities.
- **Voltage Distortion:** Harmonic currents from nonlinear loads can cause voltage distortion in the power system. The ideal sinusoidal waveform can be altered and deviated from by this voltage distortion, which also includes waveform distortion and harmonic distortion. Voltage distortion can damage delicate equipment connected to the same system, lead to faults, or reduce the equipment's lifespan.
- **Poor Power Factor:** Typically, nonlinear loads have a low power factor, which causes them to consume more apparent power than actual power. Higher electricity prices may arise from this, and power factor improvement efforts may be necessary.

1.4 State of Art in Power Quality

Due to increase of nonlinear loads in the distribution system causes undesirable effects on modern distribution systems. These nonlinear loads cause current-related power quality issues such as poor power factor, current harmonics, and reactive power demand. These current related PQ issues are mitigated through shunt active power filter (SAPF) also considered as distribution static compensator (DSTATCOM). Different control schemes are utilized for SAPF. Unit template or PLL-less synchronization technique is used to extract the synchronizing signals. But unit template method is not suitable for distorted grid conditions. The SAPF will work satisfactorily under distorted grid conditions by employing PLL schemes such as SOGI, EPLL, MAF-PLL, CCF PLL, MCCF, and so on. Voltage source converters (VSC) based on photovoltaics (PV) fulfill the two distinct functions of bidirectional active power transfer to the grid and load in grid-connected systems. Grid current balancing, harmonic reduction, reactive power

balancing, and raising the supply side power factor to unity can all be accomplished by controlling them. The PV source can be connected directly to the VSC at its DC link using the single-stage design or integrated through a DC-DC boost converter using the double-stage configuration. The most common MPPT techniques utilized are incremental conductance (InC) and Pertub & Observer (P&O). These MPPT techniques are meant to extract the maximum power from the PV array.

The PV source and nonlinear loads are additionally linked to the grid at the point of common coupling (PCC) via a voltage source converter. These power electronic-based loads are favored because they are more efficient and smaller. The nonlinear loads consume reactive power, which lowers the quality of the electricity and introduces harmonics into the system, increasing losses. To address the aforementioned problems, SAPF is built and programmed to perform power factor correction, reactive power compensation, and harmonic mitigation. In order to enhance the power quality in distribution systems, it is advised to adhere to several international standards based on IEEE and IEC. IEEE-519 requirements for grid current harmonic mitigation should be followed. The IEEE-519 standard specifies that the grid current's total harmonic distortion shall be less than 5%. Additionally, when PV systems are connected to the grid, the IEEE-1547 standard states the permissible harmonic content that can be injected.

The Shunt APF is developed in MATLAB Simulink for single-phase and three-phase distribution systems. Varying loads are carried out to investigate the performance of the proposed system. The two-level inverter is considered for single-phase and three-phase distribution systems. Comparing two-level inverters to more sophisticated multilevel inverters, two-level inverters are more straightforward in terms of design and control. This simplicity may lead to less expensive manufacture, simpler maintenance, and faster deployment. Two-level inverters are suitable for low-to-moderate power applications in single-phase distribution systems, making them a good choice for various residential and small commercial setups. The SAPF's performance is also influenced by how precisely the control algorithm extracts the reference current and compensates for the harmonics produced by the load. The Literature review mentions many time and frequency domain algorithms, such as Synchronous Reference Frame Theory, Instantaneous Reactive Power Theory, Second Order Generalised Integrator, etc. These algorithms are time-based conventional ones. Other time-domain algorithms, like

Composite and model observer-based algorithms, Kernel incremental learning methods, and others, perform well but call for fine-tuning of some parameters, intensive arithmetic, and additional filters. Additionally, some frequency-domain methods, including the Fourier transform and Kalman filter, have been employed to manage the SAPF and distribution static compensator (DSTATCOM). The newly developed control algorithms for shunt active power compensation in distribution systems need to be investigated, according to a thorough literature analysis on power quality issues and methods for mitigating them. The ability of these control algorithms to correct power quality issues in PV integrated grid-connected systems under a variety of linear, and non-linear circumstances must also be examined. In-depth research is required for performance study of control algorithms for grid-connected single-phase and three-phase systems. Two-leg SAPF topology is used in single-phase grid-connected systems, whereas three-phase three-wire topology is used in three-phase distribution systems. Both of these topologies are standard and have been tested in the past. The shunt APF with conventional and advanced control scheme is utilized for current related PQ issues. Poor power factor, harmonics in the source current, load imbalance, and reactive power imbalance are the current-based power quality issues. Control methods adopted for Shunt Active Power Filters address these PQ issues. The PV-integrated DC link capacitor meets the load demand in cases of variable PV and during load perturbations are also examined. All of these systems' performances are thoroughly described, along with detailed test results that include experimental ones.

Series active filters are used in distribution systems to reduce problems with power quality and enhance the overall efficiency of the electrical network. Numerous issues, including harmonic distortion, voltage sags, swells, flickers, and other disruptions, can be solved by using these filters. Distribution systems' harmonic distortion can be significantly decreased by using a series of active power filters. They identify harmonic currents using advanced control algorithms and real-time monitoring, inject equal but opposing currents to cancel the harmonics out, and the result is a cleaner supply voltage. Series active power filters can aid voltage quality by reducing voltage sags, swells, and flickers in addition to harmonic mitigation. To stabilize the voltage levels within predetermined limits, they can inject or absorb reactive power. There have been reported in the literature control methods for the DVR based on synchronous reference frame

theory (SRFT), Adaline-based fundamental extraction, instantaneous symmetrical component theory, energy-optimized control, PQR instantaneous power theory, symmetrical component estimation, etc. The control schemes such as SRFT, IRPT, SOGI, Hermite ANN, Bernoulli's polynomial-based ANN, q-LMF, ε − NSRLMMN are utilized for fundamental load compensation.

An advanced and comprehensive power quality solution called the Unified Power Quality Conditioner (UPQC) is utilized in distribution systems to simultaneously address several power quality problems. In order to solve issues such as voltage sag, swell, harmonics, flicker, and unbalance, it includes both series and shunt active power filters. State-of-the-art UPQCs employ advanced control algorithms that ensure optimal operation under varying load and network conditions. These algorithms are capable of real-time monitoring and quick response to maintain power quality. Some of the UPQC control schemes discussed in this thesis work are SRFT, MAF-SRF, and Mittag-Leffler ANN. Also, the developed control scheme for a series of active power filters in a three-phase distribution system needs to be investigated. The voltage-related PQ issues are mitigated using series SAPF (DVR). The performance of the DVR is investigated under voltage-related PQ issues such as voltage sag, swell, voltage harmonics, and voltage imbalance. Another custom power device is UPQC which is utilized to mitigate PQ issues related to both voltage and current. The UPQC and DVR are integrated with PV source analysis and performance under varying PV solar irradiance, varying load, and distorted grid is investigated in this thesis work.

Distribution systems frequently employ phase-locked loops (PLLs), particularly when it comes to the distribution of electrical power. PLLs play a key role in the generation and control of synchronous signals, the monitoring and regulation of voltage and frequency, and the maintenance of the stability and dependability of the electrical grid in distribution systems. Different distributed energy resources, including solar photovoltaic (PV) systems and wind turbines, are integrated into modern power distribution systems. These DERs are synchronized with the grid using PLLs, providing that the power generated is in-phase with the voltage and frequency of the grid.

PLLs are essential for keeping the electrical grid's frequency and voltage stable. They continuously check the grid's voltage and frequency, and when deviations are detected, they give feedback to the control systems so that they can change the power

output of generators or active compensators like STATCOMs and DVR. The literature study focuses development of various PLLs, and Synchronous Reference Frame Theory (SRFT) is the most basic PLL. SRF-PLL is widely used and functions well under typical circumstances. However, this PLL does not reliably track frequency and phase angle when the grid is distorted. Finding alternatives to SRFT-based PLLs is therefore crucial. For handling various grid anomalies, orthogonal signal generator (OSG) based PLL has been widely used and implemented in recent years. Additionally, compared to SRF-PLL, its tracking capability is quite good and accurate. Generalized sinusoidal integrator (SOGI-PLL) is the most widely used OSG-PLL, and other PLLs that have been discussed in the literature include the Discrete Fourier Transform, Notch, Second Order Generalised Integrator Fuzzy Logic Controller, and Cascaded Generalised Integrator (CGI) PLL. PLL control schemes such as SRFT, SOGI, MAF, and FAMAF PLL are developed and discussed in this thesis work.

1.5 Thesis Structure

The content of the thesis work has been divided into the following chapters:

Chapter 1: This chapter deals with the introduction of power quality (PQ), PQ standards, classification of PQ problems, and mitigation of PQ issues.

Chapter 2: This chapter deals with the extensive literature survey on PQ issues, effects, and mitigation techniques. Also, shunt APF, Series APF, and UPQC-based control scheme literature is discussed. Synchronization techniques for DSTATCOM, DVR, and UPQC (conventional and advanced control) under various grid abnormalities are discussed.

Chapter 3: This chapter discusses the design of a single-phase shunt active power filter for grid-connected PV system. The proposed control scheme for single-phase DSTATCOM is discussed and examined under normal and distorted grid conditions. The proposed control scheme is simulated in MATLAB Simulink and experimentally validated using hardware setup using dSpace 1104, OPAL-RT real-time simulator, Power quality analyzer, and Digital storage oscilloscope (DSO). The performance of the proposed control scheme is compared with the conventional control scheme.

Chapter 4: This chapter discusses the design of a three-phase shunt active power filter grid-connected PV system. The proposed control scheme for three-phase DSTATCOM is discussed and examined. The proposed control scheme is simulated in MATLAB Simulink and experimentally validated using hardware setup using dSpace 1104, OPAL-RT real-time simulator, Power quality analyzer, and Digital storage oscilloscope (DSO). The performance of the proposed control scheme is compared with the conventional control scheme.

Chapter 5: This chapter discusses the design of a three-phase series active power filter grid-connected PV system. The proposed control scheme for three-phase DVR is discussed and examined. The proposed control scheme is simulated in MATLAB Simulink and experimentally validated using hardware setup using OPAL-RT real-time simulator, power quality analyzer, and Digital storage oscilloscope (DSO). The performance of the proposed control scheme is compared with the conventional control scheme.

Chapter 6: This chapter discusses the design of a three-phase unified power quality compensator (UPQC) grid-connected PV system. The proposed control scheme for the three-phase UPQC is discussed and examined. The proposed control scheme is simulated in MATLAB Simulink and experimentally validated using hardware setup using OPAL-RT real-time simulator, power quality analyzer, and Digital storage oscilloscope (DSO). The performance of the proposed control scheme is compared with the conventional control scheme.

Chapter 7: This chapter discusses weak grid-connected systems that experience voltage sag, swell, harmonics, and DC offset. Different PLLs are created for synchronisation and tested with weak and non-ideal single-phase grids. The discussion includes the Phase Locked Loop (PLL) techniques such as Synchronous Reference Frame Theory (SRFT-PLL), SOGI-PLL, and FAMAF PLL. A hardware prototype created in the lab under various grid conditions is used to study the performance analysis of the proposed PLL in MATLAB Simulink. The steady state and dynamic performance analyses for precisely identifying the phase angle and generating the sinusoidal unit template under weak grid conditions are addressed in detail.

Chapter 8: Conventional and adaptive control algorithms, grid synchronization methods, control algorithms for DSTATCOM, DVR, and UPQC, and the integration of PV to the grid in single-phase and three-phase systems are all summarised in this chapter. The last chapter also includes a presentation of the work's future scope.

CHAPTER 2

LITERATURE SURVEY

2.1 General

The previous chapter gives a detailed introduction to the power quality issues, their effects, and mitigation techniques. It includes a variety of problems, including changes in voltage, frequency, harmonics, and disturbances. Increased energy expenses, equipment damage, and service interruptions can all result from poor power quality. The grid-connected system with and without PV integration is discussed in the previous chapter. The system configuration of grid-connected VSC with its control schemes is discussed in this chapter. Various Literature is reviewed for grid synchronization with conventional and advanced control schemes. The grid-connected VSC is controlled to achieve reactive power balance, harmonic reduction, and power factor correction.

In this chapter, an extensive literature survey on load compensation control schemes for shunt active power filters concerning current generation is discussed. This chapter deals with custom power devices (CPDs) such as shunt active power filter, series active power filter, and unified power quality compensator and their control scheme for generating reference switching signals for their respective IGBT switches. It is necessary to investigate the performance of conventional and proposed control schemes for CPDs under distorted grid conditions. The PV integration with the existing grid is also discussed.

2.2 Literature Survey on PQ issues, Effects, and Mitigation techniques

High levels of harmonics have been introduced into an electrical supply system as a result of the growing reliance on power electronics-based devices at the utilization level. The electrical supply system is contaminated by the large number of consumer electronics that operate as nonlinear loads and draw nonsinusoidal currents. At the point of common coupling (PCC), which is coupled to other loads, power quality (PQ) problems become evident. The functionality of connected loads and their lifespan is impacted by problems including voltage harmonics, surge, sag/dip, swell, and others [1-4]. Due to the increase of nonlinear load, the reactive power demand and losses increase. Various negative

consequences on electrical systems and connected equipment can be caused by poor power quality. Due to high penetration of nonlinear loads in the system causes large reactive power demand, as well as injects the current and voltage harmonics. This results in a poor power factor and makes the source current non-sinusoidal [5-6]. Consequently, this chapter studies and analyses a comprehensive assessment of numerous PQ issues, mitigation techniques, and distinct international standards.

The International Electrotechnical Commission (IEC) and the Institute of Electrical and Electronics Engineers (IEEE) are two established organizations that create and disseminate standards for electrical and electronic technologies. The quality, interoperability, and safety of many electrical and electronic systems are greatly influenced by these standards. This standard outlines the prerequisites for integrating distributed energy resources (DERs) safely and reliably into the electrical power system. The IEEE 519 standard specifies recommendations for reducing harmonic distortion and regulating harmonics in electrical power networks [7-8]. The IEC is a global organization that creates and disseminates electrotechnology standards. Internationally renowned and frequently embraced by numerous nations are IEC standards [9-10].

Electrical waveforms having harmonics, which are non-sinusoidal, can damage power systems and affect the functionality of electrical and electronic equipment. Numerous methods and technologies are used to reduce harmonics and enhance power quality. Some of the harmonic mitigation techniques are passive filter, active filter, variable frequency drives, and phase shifting transformer. But in this research work active filters will be discussed. For reducing harmonics in electrical power systems, passive harmonic filters are a popular and economical solution. They function by giving particular harmonic frequencies a low-impedance path to follow, effectively redirecting and lowering harmonic currents in the system. Inductors, capacitors, and resistors are common passive electronic parts found in passive harmonic filters [11-14]. Some of the advantages of passive filters are cost-effectiveness, reliability, low maintenance, and compact size. There are some limitations of limited tuning, Limited range, and resonance risk. Many applications can benefit from passive harmonic filters, especially when tackling known and specific harmonic problems.

Active filters or other methods might be more appropriate for systems with dynamic and shifting harmonic spectra or for applications needing a wider spectrum of

harmonic mitigation [15]. The active filters considered for PQ mitigation are configured in shunt and series. The shunt active power filter also known as DSTATCOM is used for mitigating current related PQ issues [16-17]. The series active power filter such as DVR is used to mitigate voltage-related PQ issues [18-19]. Electrical systems' harmonic distortion can be efficiently reduced using active power filters, which are essential in contexts with non-linear loads. They eliminate the undesirable harmonics and produce cleaner electricity by introducing equal and opposite harmonics. A system's power factor can be enhanced by using active power filters, bringing it closer to unity (1.0). Reactive power demand is decreased by a higher power factor, which can lead to cheaper electricity bills and distribution system losses. The researchers discuss various control schemes for DSTATCOM. The UPQC has served the combine objectives of both shunt and series active power filters [20]. The UPQC can mitigate both current and voltage-related PQ issues [21].

2.3 Literature Survey Control algorithm of Shunt APF

The efficient performance of a grid-connected shunt active power filter usually depends on its control scheme. Various control schemes are designed to extract the fundamental load current through load compensation and thus generate the reference source current. Literature reviews on the design configuration of shunt APF are thoroughly discussed in various research papers [22-23]. The mostly conventional schemes such as synchronous reference frame theory (SRFT), IRPT, SOGI, and unit template base control schemes are utilized for PQ mitigation techniques [24-25]. However, due to their slow response and poor dynamic performance, other advanced control schemes are required. An adaptive neuro-fuzzy interference system LMS control scheme is utilized for load compensation and mitigates the current related power quality issues as presented by M. Badoni, A. Singh, and B. Singh [26]. The proposed control scheme is found to be effective under steady-state and dynamic load conditions. P. Chittora and A. Singh developed an efficient controller based on a multiple complex coefficient filter (MCCF), and second-order generalized integrator (SOGI) to mitigate PQ issues under normal and weak grid conditions [27]. A. Gharmi et. al. presented a sliding mode control for three-phase shunt APF [28]. The implementation of the sliding-mode controller enhances tracking performance characteristics, and power quality, and reduces reactive power demand. P.

Chittora et al. introduce Chebyshev Function expansion ANN-based shunt compensation in a three-phase grid-connected system. ANNs provide a tool for approximating random functions, which can be used for solving a specific problem quickly. Developing neural network topologies without hidden layers is essential since ANNs employ a lot of hidden layers to increase accuracy, which consumes a lot of computational work [29-31]. Utilizing Chebyshev polynomials, such a single-layer functional link ANN eliminates the hidden layer [32]. The proposed ChANN method performs superbly in terms of convergence, minimal processing effort needed, and sinusoidal source currents. In [33-34] a notch filter-based control scheme is introduced to extract the fundamental load current which is used to generate the reference source current. In [35], the authors proposed a backstepping controller with self-tuning filter for single-phase SAPF. The control scheme is designed for two loops, one is an inner loop and another is an outer loop. The disadvantages of conventional LPF-based load compensation are corrected using a self-tuning filter.

Various adaptive control schemes based on real-time training are discussed in literature such as Levenberg Marquardt [36-37]. Another adaptive filter based on the N-LMS control scheme is implemented for grid synchronization and PQ improvement. The proposed N-LMS control scheme provides the estimated component free from negative sequence components and low-order harmonics [38]. The LMS [39], Leaky-LMS [40], variable LMS [41-42], Least mean fourth [43-44], leaky least mean fourth [45-46], LMS-LMF [47], normalized LMF [48], quantum LMF (q-LMF) [49], and Weiner Filter [50].

The orthogonal polynomials can also be used for the extraction of fundamental active load components and for generating the reference source current for generating switching signals for single and three-phase grid-connected systems. Some of the orthogonal polynomial methods are Hermite polynomial-based ANN (HeANN) [51], Bernoulli's polynomial-based ANN (BePANN) [52], and Lagurre based polynomial [53] for mitigating the PQ issues in grid-connected inverter system. Ppaer [54] presents the control system of an active shunt compensator for quick harmonic compensation. In order to lessen the injection of non-sinusoidal currents into the ac mains, it is linked in shunt to the distribution system. An instantaneous quantity-based time domain control technique is typically used to operate an active shunt compensator. These algorithms operate under both ideal and non-ideal assumptions, and include p-q theory [55], I cosφ [56], nonlinear

control algorithm [57], direct power control [58], model predictive control [59], instantaneous reactive power theory [60], etc. Other control algorithms include the CFT (Character of Triangle Function) control algorithm [61], which is based on the character of the distorted load currents' triangle function; the adaptive filter-based control algorithm [62], which necessitates numerous approximations for the estimation of the fundamental component of load currents; and the composite observer-based control algorithm [63]. Digital signal processors, or DSPs, are used to handle control variables in the active filter technology application [64]. In order to account for power factor, paper [65] examined the effectiveness of the synchronous detection and I cosφ control algorithms and suggested that the latter performed better. Implementing synchronous detection algorithms using analogue circuits and various approaches, such as same power, equal current, and equal resistance, has been covered by paper [66]. According to paper [67], this technique can be used to rectify power factor in non-ideal ac mains, although the performance is not ideal, particularly when the supply system is distorted. Another modification of the synchronous detection approach [68]. Although the simulation produces the expected results, the harmonic control is not attained to the desired degree.

2.4 Literature Survey Control algorithm of Series APF

Electrical systems and connected devices can be significantly impacted by voltage-related power quality problems. Power quality difficulties can be caused by many issues, such as internal problems with a facility, the utility grid, or a mix of the two. Many power quality researchers demonstrate that DVR has been successfully employed to address the power quality issues in the distribution network. Some of the voltage-related PQ issues are voltage sag, swell, flicker, noise, voltage unbalance, and voltage harmonics [70]. Two topologies are used for DVR configuration, Battery-supported DVR and another capacitor-supported DVR. In [71] capacitor capacitor-supported DVR is considered for mitigating voltage-related PQ issues with the use of a genetic algorithm (GA). The GA optimization is used to tune the value of the PI controller. The Dual P-Q theory has been proposed to generate the instantaneous reference voltage signal to compensate for the load voltage with direct power flow control [72]. The adaptive neuro-fuzzy inference system is used to regulate the gain of the PI controller of capacitor-supported DVR [73]. A SOGI-based control of DVR is used to mitigate the voltage sag, swell, and interruptions

in a grid-connected PV system. It used a unit vector template (UVT) to enhance the effectiveness of grid-connected renewable energy resources [74].

According to [75], the DVR has been utilized to reduce harmonic distortion successfully. Sundarabalan and Selvi [76] have reported on the usage of DVR for mitigation in recent research studies. Using the real coded genetic algorithm optimized fuzzy logic controller, DVR was used to correct both balanced and unbalanced voltage sag/swell in the load side for the DG system under various fault scenarios. The series-injected DVR voltage is synchronized with the grid terminal voltage during in-phase compensation to restore the load voltage magnitude. When energy-optimized compensation is used, the DVR recovers the load voltage magnitude while minimizing the need for active power. The size of the injected voltage, the phase leap, and how the active power is used all affect how these techniques behave [77-79].

2.5 Literature Survey Control algorithm of UPQC

Unified Power Quality Compensators (UPQC) have many different control methodologies, technological advances, and power quality applications. A literature review on UPQC control might provide insightful information. Using an adaptive method, the Firefly Algorithm (FFA) and Recurrent Neural Network (RNN) control strategies are investigated. UPQC control pulses are optimised using FFA, and the optimisation parameter is trained using an RNN. Based on the source side and load side factors, the series and shunt Active Power Filters (APF) produce the best control pulses. In addition to its capacity to raise the PQ in the distribution system, this strategy is capable of injecting active power into the grid [80]. Various control strategies for UPQC to mitigate PQ issues are investigated such as ADALINE [81], modified P-Q theory [82], sliding mode control (SMC) [83], Enhanced PLL-based SRF [84], modified generalized integrator (GI) [85], adaptive neuro-fuzzy inference system (ANFS) [86]. A moving average filter (MAF) based SRF is utilized to extract the fundamental load current and generate the reference source current in a three-phase grid-connected PV inverter. The series compensator compensates for the grid side power quality problems such as grid voltage sags/swells. The compensator injects voltage in-phase/out-of-phase with the point of common coupling (PCC) voltage during sag and swell conditions, respectively [87].

In grid-side converter (GSC) systems, the crucial parameters such as amplitude, frequency, and phase of grid voltage should be measured and controlled for grid-tied applications [88]. Frequency variations have a greater impact on traditional equipment that does not employ electronics or on relatively inexpensive electronic devices in most circumstances [89]. PLL is a standard synchronization method that requires power fluctuations to be sustained since their instability affects the resultant reference signal. To increase steady-state performance during poor grid conditions, conventional PLL uses a feedback loop-filter (LF) to monitor the frequency and phase. A great challenge associated with the PLL is obtaining a fast and accurate estimation of phase angle and frequency estimation under abnormal grid conditions in grid-tied PV UPQC [90-92].

Neural network-based soft computing techniques are increasingly in demand for creating adaptive control methods in the PQ domain. By using the weight update equations, the least mean square algorithm (LMS) in [93] adaptively estimates the reference signal needed for converter switching. A varied step-size LMS-based technique (VSSLMS) is proposed in [94] to address the issue of low convergence rate caused by fixed-step size. In order to extract the amplitude of the distorted load current and innovate the performance, a leakage component is added to the current LMS algorithm in another technique based on leaky LMS (LLMS) that is discussed [95]. Furthermore, in a PV grid integrated system, altering the leakage factor offers more accurate power frequency estimates and effective control [96], [97].

2.6 Literature Survey synchronization techniques

The estimation of synchronizing signals from source voltage and the calculation of the fundamental load component from the load current signal are both necessary steps in the control algorithms used for shunt compensation, series compensation, and hybrid compensation. The unit template approach is the easiest way to create the synchronizing signal, but it can only be used when the source voltage is ideal [98, 99]. However, if there are power quality issues with the grid voltage, such as noise, distortion, and DC-offset, then new and improved techniques are needed to estimate the synchronizing signals. Researchers have also suggested several PLL approaches, some of which do not perform well under less-than-ideal source conditions. The most common PLL is a synchronous reference frame (SRF), it provides better performance under ideal grid conditions but

shows poor performance under distorted grid conditions [100,101]. Another common synchronization technique is generalized integrator-based PLLs such as SOGI, EPLL, TOGI, and ROGI. The conventional SOGI estimates the phase and frequency information under normal and distorted grid conditions [102-104]. The frequency adaptive SOGI PLL has the limitations of implementation complexity, tuning sensitivity, and reduced stability. While frequency fixed SOGI PLL is proposed to ensure stability and simple implementation [105,106]. SOGI PLL does not perform satisfactorily under the highly distorted grid and DC offset condition. An enhanced 3P-EPLL in combination with multiple delayed signal cancellation (DSC) filters has been proposed to accurately estimate the grid synchronous information even under non-ideal grid settings. In order to get rid of the input dc offsets and even-order harmonics, a DSC operator is set at each 3P-EPLL input [107]. Another more stable enhanced phase-locked loop (Ms-EPLL) technique, a modified version of EPLL is discussed and applied in a three-phase grid integrated PV system [108,109]. A type 3 modified notch filter-based type 3 SOGI-PLL with the inherent capacity to reject dc offset and reduce phase errors has been proposed by authors in [110].

The use of a sliding Fourier transform-based PLL for the synchronization of a three-phase grid-interactive SPV system has been demonstrated by Mansour et al. [111]. The PLLs can be divided into three categories: 1) power-based PLLs, 2) orthogonal signal generation PLLs, and 3) adaptive filter-based PLLs. Xu et al. [112] have provided an outline of a comparative study of numerous PLLs. The most recent issues with PLLs, according to a significant amount of literature, include phase error minimization and dc offset. For SOGI to operate effectively under variable frequency conditions, SOGI-FLL has been proposed [113-114]]. In order to determine the frequency of the input signal, the FLL block is realized. In the event of a DC-offset in the source voltage, SOGI-FLL does not provide satisfactory results due to its poor filtering capability. To reject the DC offset in grid voltage, a modified SOGI-FLL has been presented [115, 116]. Additionally, it has been noted that in steady-state circumstances on a heavily distorted grid, the frequency estimated by the FLL exhibits variable degrees of oscillation.

For grid synchronization, several cascaded fixed-tuned notch filters or FIR filter designs based on an adjustable sample rate have also been published [117, 118]. Due to the execution of additional algorithms on the same digital signal processor, the adaptive

sampling method implementation could be complicated. Under ideal circumstances, three-phase systems can use an enhanced phase-locked loop (PLL) [119]. To reject the detrimental effects of disturbances, however, some in-loop filters can be included in the enhanced PLL at the penalty of added complexity [120]. Advanced methods are typically divided into two categories. One is a prefiltering-based solution, which uses control techniques such as complex-coefficient filters [121], dual SOGI [122], delayed signal cancellation (DSC) operators [123], and others before the PLL loop. Adaptive notch filter [124], MA filter [125], dq-frame DSC operator [126], and other particular filters are used in the phase control loop of the SRF-PLL as part of an additional approach called in-loop filtering. However, the in-loop filtering method results in a slower response since it adds a temporal delay to the PLL control loop.

The cascaded DSC (CDSC) operator's design is adaptable since different operator configurations can be used with different input voltages. The predicted harmonic components [127–130] determine how many DSC operators should be included in the CDSC string. Under grid disturbances and surroundings with fluctuating frequency, the SRF-PLL based on the adaptive CDSC prefilter generates precise and quick responses [131]. The phase and frequency estimation include interdependent loops where they are simultaneously influenced by each other, making parameter tweaking delicate and difficult. In order to employ the Park transformation in the phase detector, it also necessitates the assessment of trigonometric functions (sine and cosine). Additionally, a square root operation is performed to preserve the quadrature-axis component of the Park transformation insensitive to changes in the amplitude. In order to apply the sine, cosine, and square root operations, Taylor infinite series must be used, which requires a significant amount of computational work to implement on a digital signal processor. Artificial neural networks (ANN) play a unique function in estimating power system parameters. They have been applied to the detection of harmonics, symmetry phase components, and more [132, 133]. Back-propagation techniques and repeated training of neurons for accurate weight estimation were used in some of the earliest ANN systems. Online and supervised training algorithms have emerged as superior substitutes for offline training techniques. Furthermore, if real-time implementation algorithms based on ANN methodologies are to replace the conventional PLL, they should be quick, accurate, and roughly converge within a few cycles. Adaline is made up of a single neuron that

processes input from various sources and produces a single output after properly training the weights that are involved. Because the Adaline-based PLL is straightforward and training can be done online, it is possible to train for and monitor sudden changes in voltage amplitude, phase angle, and frequency.

Various PLLs are discussed in the literature [134-144] such as Synchronous Reference Frame Theory (SRFT) PLL. This PLL is commonly used and works well under normal conditions. However, this PLL suffers from frequency and phase angle tracking in distorted grid conditions. It is necessary to overcome the disadvantage of SRFT PLL hence Decoupled Double Synchronous Reference Frame (DDSRF-PLL) is proposed. It uses double decoupled SRFT PLL which obtains the positive and negative sequence from grid voltage but introduces time delays which causes sluggish dynamic response.

2.7 Research Gaps

The following research gaps are noted according to the findings of the comprehensive literature review:

1. An advanced and adaptive control scheme is required for load compensation and generating reference source current for CPDs.
2. Extensive investigation is required for grid-connected PV systems under distorted grid conditions.
3. Extensive investigation is required for non-PLL and PLL in grid-connected CPDs.
4. It is necessary to address synchronization methods that take into account a polluted grid, a weak grid, and various loading situations. Also necessary is an accurate evaluation of these based on simulation and experimental research.

2.8 Objective of Research work

1. Design, control, and performance investigation of single and three-phase grid-connected PV systems under normal and distorted grid conditions.
2. Design of advanced control schemes for shunt APF, series APF and UPQC.
3. Performance comparison of advanced control scheme with conventional control scheme of CPDs.
4. Investigation of PQ problems under distorted grid condition

5. Experimental verification of the proposed control scheme under different loading and distorted grids.

2.9 Conclusion

This chapter includes thorough reviews of the literature on a range of power quality (PQ) problems, and their solutions. Under abnormal and distorted grid situations, several time and frequency domain adaptive control methods have also been addressed to estimate the basic component of load current and to generate the reference current. We show various grid synchronization PLLs to address various grid irregularities. Single-stage grid-connected PV systems control schemes have also been covered. An extensive literature survey has been done on CPD's control scheme. The extensive investigation has led to the identification of research gaps and the formulation of research objectives.

CHAPTER 3

DESIGN AND CONTROL OF SINGLE-PHASE SHUNT ACTIVE POWER FILTER FOR GRID CONNECTED PV SYSTEM

3.1 Design of Single-Phase Grid-Connected Shunt Active Power Filter

This chapter deals with the design of a single-phase shunt active powerFig.3. 1 filter (SAPF) with PV integration at the distribution level. The proposed Single-phase SAPF configuration consists of voltage source converter (VSC) with two legs and four switches. The VSC comprises insulated gate bipolar transistors (IGBTs) based switches with antiparallel diodes and a DC link capacitor as shown in Fig. 3.1. The proposed system is simulated in MATLAB Simulink software. The VSC is designed to operate in current operating mode, thus also known as current controlled VSC. The simulation model of a single-phase grid-connected PV system consists of an interfacing inductor, VSC, a solar PV array, nonlinear loads, and a ripple filter. The designed rating of experimental VSC. A small experimental prototype is developed in the laboratory to verify the simulated performance of SAPF. The developed system is controlled by a digital signal processor (DSP). The designing of these quantities is required:

1. DC-link bus voltage
2. DC-link Capacitor
3. Interfacing Inductor
4. PV array
5. Sensors circuits
6. Hysteresis current controller

3.1.1 Calculation of DC-link Bus Voltage

During PWM operation, the minimum required AC voltage across the ac input of VSC of DSTATCOM decides the value of DC link Bus Voltage. The DC bus voltage is required to inject the reactive power into the grid. The DC link bus voltage must be greater than the standard applied grid voltage. The peak amplitude of applied grid voltage is given by Eq. (3.1).

$$V_P = \sqrt{2}v_s \quad (3.1)$$

where, V_P is the peak amplitude of the grid voltage and v_s is the RMS value of applied grid voltage. For the 230V, 50Hz simulation system, and 40V, 50Hz experimental system, the DC-link bus voltage is given by Eq. (3.2) and Eq. (3.3) respectively

$$V_{dc(ref)} > V_{dc(min)} = \sqrt{2}v_s = \sqrt{2} \times 230 = 325.57V \quad (3.2)$$

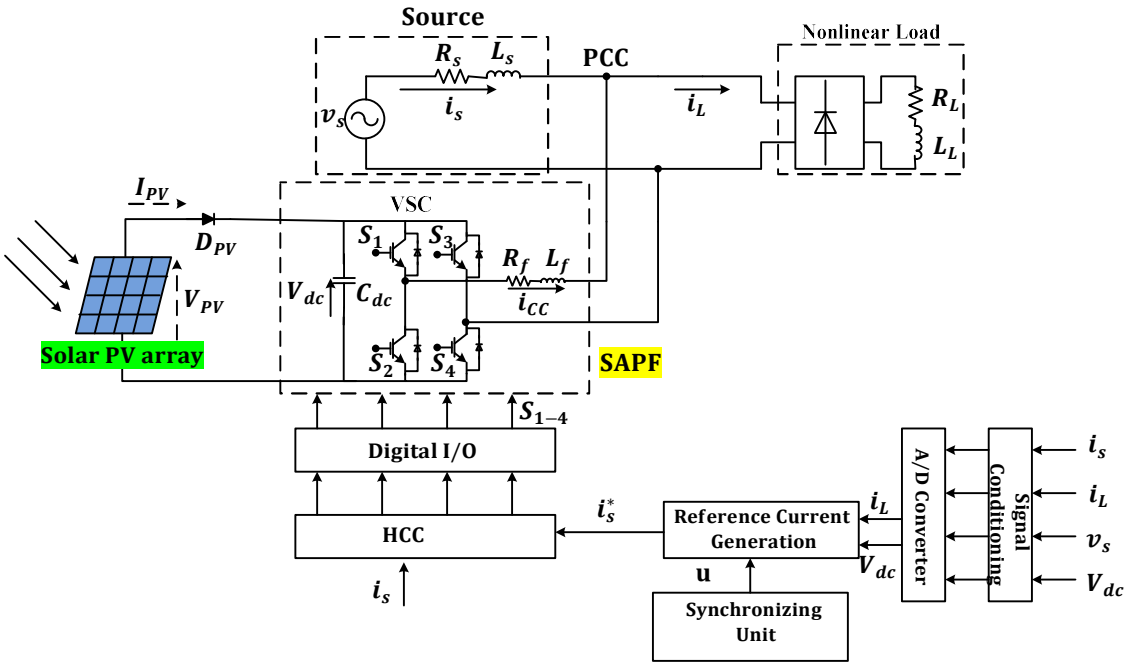

Fig. 3.1 System Configuration Diagram of Single-phase Single-stage grid-connected PV System

and for experimental study.

$$V_{dc(ref)} > V_{dc(min)} = \sqrt{2}v_s = \sqrt{2} \times 40 = 56.56V \quad (3.3)$$

The DC-link bus voltage reference ($V_{dc(ref)}$) must be greater than the minimum DC link bus voltage ($V_{dc(min)}$). In the Simulation system, the DC-link reference voltage is considered 400V and in the experimental system, the DC-link reference voltage is 80V.

3.1.2 Calculation of DC-link Capacitor

In single-stage single-phase grid-connected PV system has a DC link capacitor at the input port of VSC. The simulation and experimental value of the DC link Capacitor is calculated using (3.5) and (3.6) using [69]. DC link voltage of the VSC is affected by grid voltage. The value of DC link Capacitance must be able to sustain the DC link voltage fluctuations.

$$C_{dc} = \frac{v_s \tau i_{cc} a k_1}{\frac{1}{2}(V_{dc(ref)}^2 - V_{dc(min)}^2)} \quad (3.4)$$

where $V_{dc(ref)}$ is the DC link bus voltage, $V_{dc(min)}$ is the minimum DC link voltage, τ is the time constant, a is the overloading factor, k_1 is the gain constant and i_{cc} is the VSC's compensating current. Let $a = 1.2$, $i_{cc} = 25A$, $V_{dc(ref)} = 400V$, $V_{dc(min)} = 375.27\,V$, $\tau = 0.02s$, and $k_1 = 0.3$. The DC link capacitance for simulation is given by

$$C_{dc} = \frac{v_s \tau i_{cc} a k_1}{\frac{1}{2}(V_{dc(ref)}^2 - V_{dc(min)}^2)} = 1527.6\mu F \quad (3.5)$$

and it is taken as $C_{dc} = 2000\ \mu F$ (simulation). For experimental setup, $v_s = 40V$, $i_{cc} = 15A$, $a = 1.2$, $V_{dc(min)} = 56.56V$, $V_{dc(ref)} = 80V$, $\tau = 0.02s$, and $k_1 = 0.3$. The value of DC link capacitance for experimental setup is given by

$$C_{dc} = \frac{v_s \tau i_{cc} a k_1}{\frac{1}{2}(V_{dc(ref)}^2 - V_{dc(min)}^2)} = 2699.19\mu F \quad (3.6)$$

Based on the availability $C_{dc} = 4700\mu F$ was used in experiments.

3.1.3 Calculation of Interfacing Inductor

An interfacing inductor is utilised to filter the current ripples. The selection of an inductor with a proper inductance value must be considered. It is very evident that the larger the value of inductance, the better the filtering, but with increased power loss.

$$L_f = \frac{\sqrt{3} m V_{dc(ref)}}{12 a f_{sw} \Delta I_{cr}} \quad (3.7)$$

Here, 'L_f' is the interfacing inductor, 'm' is the modulation index, 'f_{sw}' is the switching frequency and ΔI_{cr} is the current ripple which is considered 5% of the maximum current. The value of L_f for simulation is calculated by (3.8) and for experimental setup, it is calculated by (3.9).

$$L_f = \frac{\sqrt{3} m V_{dc(ref)}}{12 a f_{sw} \Delta I_{cr}} = \frac{\sqrt{3} * 1 * 400}{12 * 1.2 * 10 * 1000 * 1.5} = 3.20mH \quad (3.8)$$

$$L_f = \frac{\sqrt{3} m V_{dc(ref)}}{12 a f_{sw} \Delta I_{cr}} = \frac{\sqrt{3} * 1 * 80}{12 * 1.2 * 10 * 1000 * 1.5} = 0.64mH \quad (3.9)$$

The experimental value of the interfacing inductor is considered slightly higher than the calculated value and it is taken as 2mH.

Table 3.1: Parameter Values used in Simulation and Experimental

Element	**Parameters**	**Simulation Values**	**Experimental Values**
Supply side	Source	230V(rms),50Hz	40V(rms),50 Hz
Shunt Active Power Filter	DC link capacitor	C_{dc}=2000μF	C_{dc}=4700μF
	Interfacing filter inductor	L_f=3.2mH	L_f=2mH
	Proportional gain	K_P=2	K_P=0.05
	Integral gain	K_i=5	K_i=0.5
	Switching Frequency	F_s=5kHz	F_s=5kHz
Loads	1-Ø diode rectifier	----	----
	R-L Load	R_L=40Ω and L_L=90mH	R_L=40Ω and L_L=90mH

3.1.4 Modelling and Design of PV array

Photovoltaic (PV) module modeling is an important aspect of solar energy system design and analysis. PV modules are the key components of solar panels that convert sunlight into electricity. Modelling of PV modules involves understanding their electrical behavior, and performance characteristics, and predicting their output under various operating conditions. Some of the Keypoints regarding the modelling of PV modules includes:

1. Electrical Characteristics
2. Single Diode Model
3. Model Parameters
4. Temperature Effects
5. Irradiance Effects
6. Modelling Software
7. Validation and Accuracy

PV modules exhibit both current-voltage (I-V) and power-voltage (P-V) characteristics. These characteristics describe how the module's electrical output varies with changes in sunlight intensity and temperature. The most common model used for PV module simulation is the single-diode model. The module can be represented by a single diode connected in parallel with a current source. The model considers parameters such as short-circuit current (I_{SC}), open circuit voltage (V_{OC}), maximum power point voltage (V_{mp}), maximum power point current (I_{mp}), and fill factor (FF). Some of the model parameters such as diode ideality factor, series resistance, shunt resistance, and temperature coefficients must be determined. The performance of the PV module is influenced by varying temperatures and irradiance.

Several software tools are available for modeling PV modules, such as MATLAB/Simulink, PVsyst, PVLIB, and SAM (System Advisor Model). These tools provide comprehensive modeling capabilities, allowing users to simulate PV module performance under different environmental conditions. A single PV module cannot generate a large amount of power. Thus, it is required to connect these PV modules in series or parallel to achieve desired voltage and current levels. The number of PV modules connected in series or parallel constitutes PV strings. These PV strings together are Known as PV arrays.

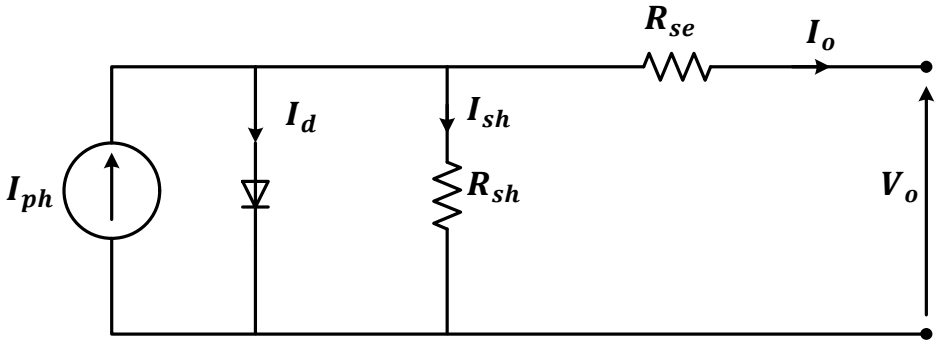

Fig.3.2 Circuit diagram of Practical single diode model of PV cell

The circuit diagram of the PV cell with shunt and series resistance is shown in Fig. 3.2. The output current I_O is calculated by applying Kirchhoff's current law,

$$I_o = I_{ph} - I_d - I_{sh} \tag{3.10}$$

$$I_o = I_{ph} - I_0\left[\exp\left(\frac{V_o + I_0 R_{se}}{a}\right) - 1\right] - \frac{V_o + I_0 R_{se}}{R_{sh}} \tag{3.11}$$

In equation (3.11), I_{ph} represents the photon current, I_d represents the diode current, I_{sh} is the leakage current in parallel resistor, R_{se} is the resistor connected in series, R_{sh} is the resistor connected in the shunt, a is the ideality factor and V_o is the terminal voltage.

$$a = \frac{N_{se} A k T}{q} \tag{3.12}$$

where q is the electron charge (1.602×10^{-19}), N_{se} is the number series cell in the PV array, k is Boltzmann's constant (1.381×10^{-23}), T is the cell temperature in Kelvin. The ideality factor for silicon polycrystalline module is 1.3. The photon current is given by

$$I_{ph} = \frac{I_r}{I_{r(ref)}}\left(I_{ph(ref)} + \mu_{sc}\Delta T\right) \tag{3.13}$$

$$\Delta T = T_C - T_{C\,(ref)} \tag{3.14}$$

The photon current($I_{ph(ref)}$) at standard test condition (STC) is approximately equal to the short circuit current at STC ($I_{sc(ref)}$) in A/K, ($I_{ph(ref)} \approx I_{sc(ref)}$). Here, $I_{r(ref)}$ is irradiance at STC which is 1000 W/m^2 and the PV cell temperature ($T_{C\,(ref)}$) at STC is 298K and μ_{sc} is the temperature coefficient of short circuit current. Diode current (I_d) is directly proportional to the reverse saturation current (I_o) which is expressed by Eq. (3.15),

$$I_d = I_o\left[\exp\left(\frac{V_O + I_O R_{se}}{a}\right) - 1\right] \tag{3.15}$$

$$I_o = \frac{I_{sc(ref)}}{\exp\frac{V_{oc(ref)}}{a} - 1}\left(\frac{T_c}{T_{C(ref)}}\right)^3 \exp\left[\left(\frac{q\in_g}{Ak}\right)\left(\frac{1}{T_{c(ref)}} - \frac{1}{T_c}\right)\right] \tag{3.16}$$

where, $V_{oc(ref)}$ is the open circuit voltage of the PV module at STC, $\in_g$ is the energy band gap which is 1.2 eV for silicon-based PV cells. For the PV array, the PV array current I_{PV} is expressed by Eq. (3.17).

$$I_{PV} = N_P I_{ph} - I_o\left[\exp\left(\frac{V_{PV} + I_O R_{se}\left(\frac{N_S}{N_P}\right)}{a}\right) - 1\right] - \frac{V_{PV} + I_O R_{se}\left(\frac{N_S}{N_P}\right)}{R_{sh}\left(\frac{N_S}{N_P}\right)} \tag{3.17}$$

where, N_s and N_P is the number of modules connected in series and parallel of a PV array respectively. For the simulation model, Zytech Engineering Technology ZT190S is selected for performance analysis. The parameters of PV module are shown in Table 3.2.

Table 3. 2: PV module Parameters at STC (Zytech Engineering Technology ZT190S)

Parameters	**Rating**
Maximum Power (P_{max})	190.15 W
No. of cells per module	72
Open circuit voltage (V_{oc})	44.86 V
Short-circuit current (I_{sc})	5.5 A
Voltage at maximum power point (V_{mp})	37.73 V
Current at maximum power point (I_{mp})	5.5 A
Temperature coefficient of V_{oc}	-0.364
Temperature coefficient of I_{sc}	0.102
Shunt resistance of a cell (R_{sh})	179.26 Ω
Series resistance of a cell (R_{se})	0.2794 Ω

The output current and voltage of the PV module depend on environmental conditions. The output power and current of the PV module vary with P-V and I-V curves. The output power and current of the PV module increase with the increase in irradiance (100W/m^2, 500W/m^2, 1000W/m^2) at a fixed temperature of 25℃. But if temperature increases ($25℃, 35℃, 45℃$) and irradiance is constant (1000W/m^2), the output power and current decreases. The P-V and I-V curve of the selected Zytech Engineering Technology ZT190S module is shown in Fig. 3.3. The P-V and I-V curve shows the open circuit voltage, and maximum power point (MPP). The MPP is the combination of voltage and current at which the PV module or array produces the maximum power output. The MPPT algorithm ensures that the PV system works at or near the MPP by continuously tracking and modifying the operating point. This maximizes power output and optimizes energy harvesting. The voltage at MPP is known as the maximum voltage (V_{mp}) while current at MPP is also known as maximum current (I_{mp}). There are two methods of connectivity between PV array and utility viz single-stage grid-tied PV system and

double-stage grid-tied PV system. In this research work, a single-stage grid-tied PV system is utilized. A single-stage grid-connected photovoltaic (PV) system, also known as a single-stage grid-tied PV system, is a form of PV system that links the PV array directly to the utility grid without the requirement for an intermediate energy storage system. It works by converting the direct current (DC) electricity supplied by the PV modules into alternating current (AC) power that is synchronized with the utility grid's voltage and frequency.

The process of designing a PV array from PV modules involves determining the configuration, sizes, and arrangement of the modules to generate the necessary power output and meet certain system requirements.

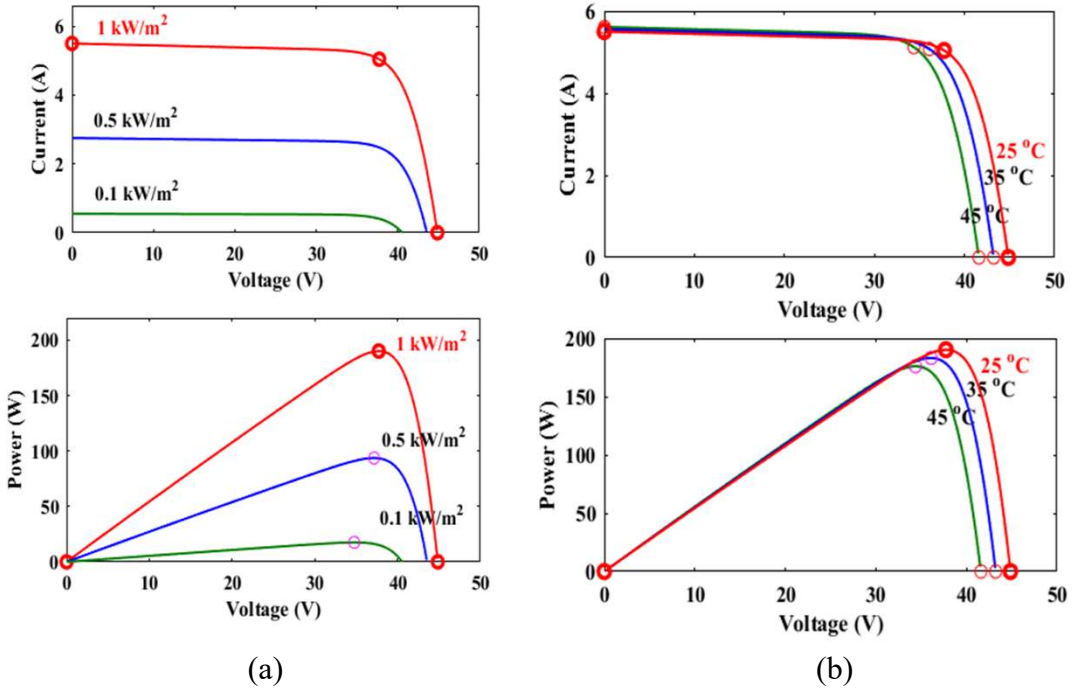

Fig.3. 3 P-V and I-V curve of PV module (a) 25℃ and at specified irradiance (b) 1000 W/m^2 and at specified temperatures

It is important to determine the PV array arrangement based on available space, shading concerns, system voltage, and desired performance. The following are examples of frequent configurations:

1**. Series Connection**: Modules are linked in series to enhance system voltage while retaining current. This design is appropriate when there is little shade and larger voltages are required.

2. **Parallel Configuration**: Modules are linked in parallel to keep the system voltage constant while boosting current. This arrangement is useful when there is shade and preserving the overall system voltage is critical.

3. **Combination:** To obtain the necessary system voltage and current, a combination of series and parallel connections can be used.

In a single-stage PV system, there is no DC-DC boost converter. The PV array voltage should be higher than the reference DC link voltage of the voltage source converter (VSC). The MPPT technique must be capable of generating the maximum voltage at MPP. The minimum number of series-connected PV modules required is calculated by (3.18)

$$N_S = \frac{V_{dc(min)}}{V_{mp}} = \frac{325.57}{37.73} = 8.61 \quad (3.18)$$

Thus, the number of series-connected PV modules is selected as 11. The parameters of the PV string or array are given in Table 3.3 and the P-V and I-V curves of the PV array are shown in Fig. 3.4.

Table 3.3: PV array Parameter at standard test condition (Zytech Engineering Technology ZT190S)

Parameters	Value
No. of series PV modules (N_S)	11
No. of parallel PV modules (N_P)	1
Maximum Power (P_{mp})	2092 W
Open circuit voltage (V_{OC})	493.5 V
Short circuit current (I_{SC})	5.5 A
Voltage at MPP (V_{mp})	415 V
Current at MPP (I_{mp})	5.04 A

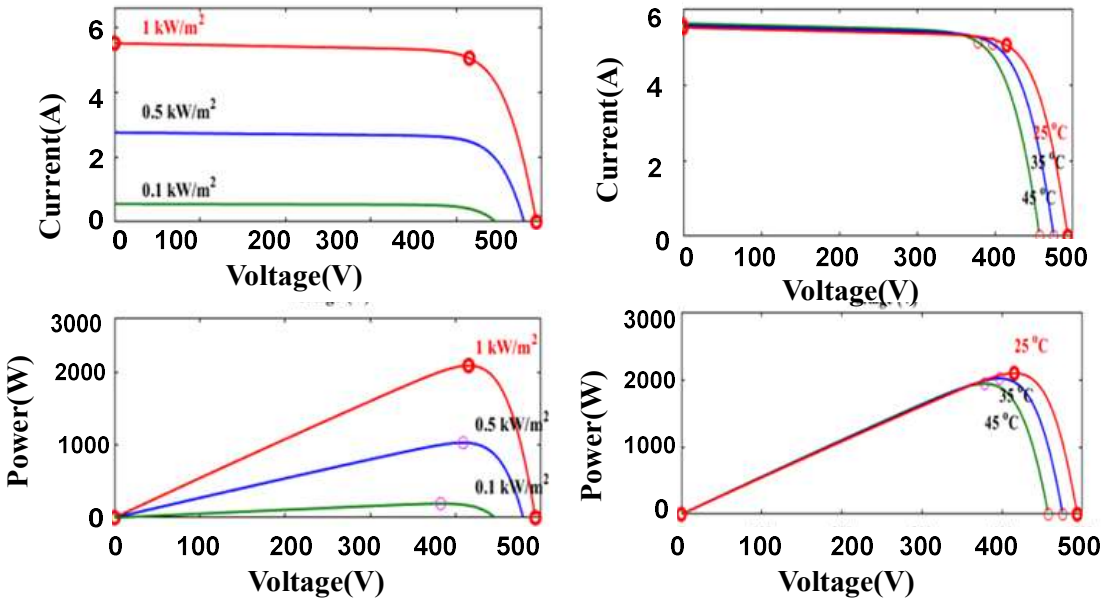

(a) (b)

Fig.3.4 P-V and I-V curve of PV array (a) 25℃ and at specified irradiance (b) 1000 W/m^2 and at specified temperatures

3.1.5 Design of current and voltage sensors

Sensors are essential in monitoring and identifying numerous electrical parameters in the shunt active power filter (SAPF) experimental setup. APFs are used in electrical systems to reduce harmonics and improve power quality.

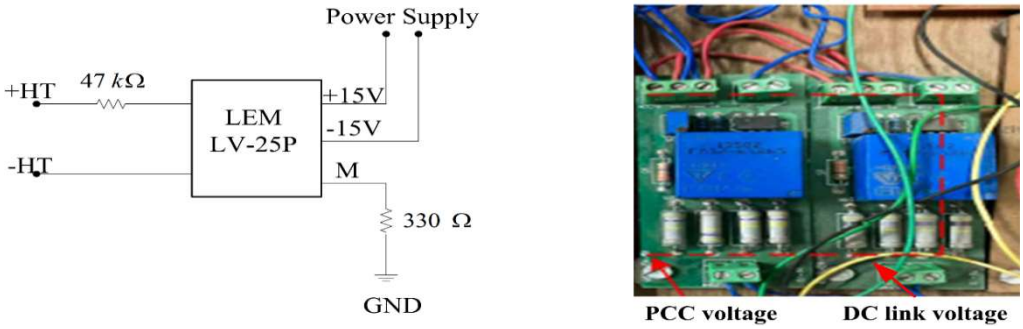

(a) (b)

Fig.3.5 (a) Circuit diagram of voltage sensor (b) Photograph of DC link voltage and PCC voltage sensors

The sensors in an APF experimental setup can provide the APF controller with the necessary feedback and control signals. Various voltage and current parameters are required to be sensed for controlling the shunt active power filter to mitigate power quality issues.

The DC link voltage, PCC voltage, source current, compensating current, and load current are sensed through voltage and current sensors. The sensed voltage and current

are given to ADC channels of dSpace. A voltage sensor (LEM LV-25P) is used for measuring PCC voltage and another voltage sensor is used for measuring DC link voltage. The circuit diagram and photograph of voltage sensors are shown in Fig. 3.5 (a-b). Two voltage sensors have been used for measuring PCC voltage and DC link voltage. A DC supply of +/-15V supply is required to operate the voltage sensor. The output signal of the voltage sensor is fed into the buffer circuit. After buffering the output using OPAM (OP07), the resultant signal is given to the designed control scheme with the help of ADC of dSpace.

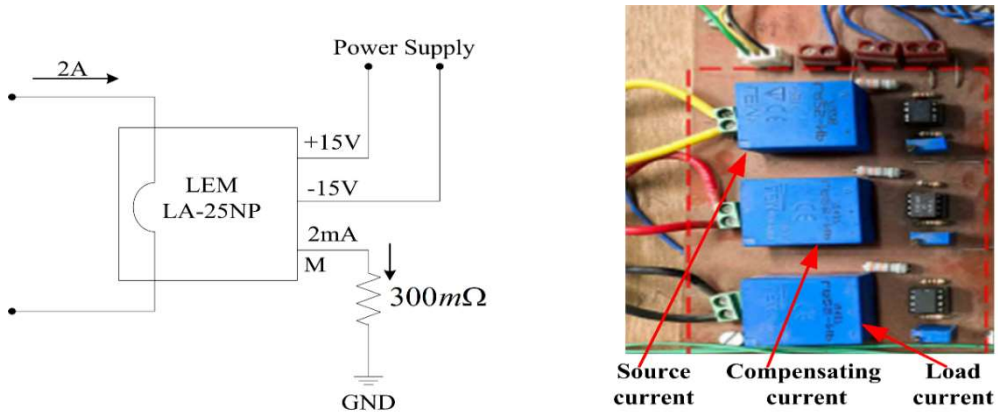

(a) (b)

Fig.3.6 (a) Circuit diagram of current sensor (b) Photograph of source current, load current, and compensating current sensors

Three LEM LA-25P are used for sensing source, load, and compensating current. The LEM LA-25P is a Hall effect sensor that operates at $\pm 15V$ DC supply. The output of the sensors is fed into the ADC channel of dSpace. Fig. 3.6 (a)-(b) show the circuit diagram of the current sensor and a photograph of the current sensors.

3.1.6 Design of voltage amplifier circuit for gating signals

The output signal obtained from the PWM port of dSpace is 5V. The IGBT switches of VSC require 15V for switching operation. The process of regulating the 5V to 15V requires a gating circuit. The gating circuit consists of suitable resistors, hex Inverter 7406N, and 2N2222 N-P-N transistors. The circuit diagram and actual practical photograph of the gating circuit are shown in Fig. 3.7 (a-b).

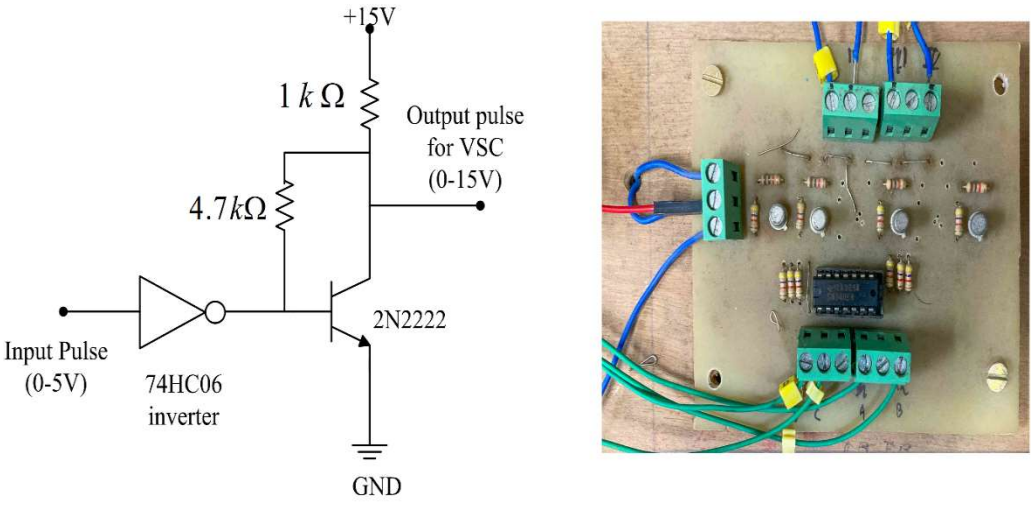

Fig.3.7 (a) Circuit diagram of gating circuit for IGBTs switches (b) Photograph of developed gating circuit

3.1.7 Experimental Hardware setup

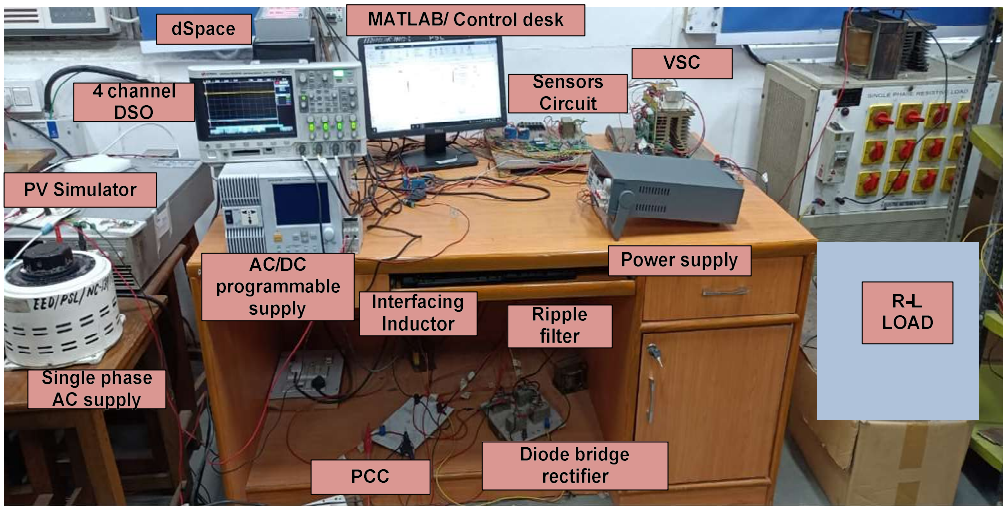

Fig.3.8 Photograph of Experimental set-up

Figure 3.8 depicts the experimental setup for a grid-connected PV system using the Chroma 62100H-600S (PV simulator). The PV simulator exhibits qualities similar to a rooftop PV panel. To implement the proposed control method on hardware, the controller dSpace 1104 controller is used. LEM LV-25P and LA-25P HALL effect transducers are used in the sensor circuit. The experimental results' waveforms are obtained using a Keysight DSOX2014A oscilloscope and a HIOKI PQ3100 power analyzer. Keithley triple channel DC supply provides power to the VSC driving circuit and sensor circuits. In the proposed system, a GwInstek APS-1102A programmable AC/DC supply is also

used to generate distorted voltage signals. The suggested grid-connected PV distribution system has been experimentally tested with a nonlinear R-L load.

3.2 Control Scheme for single-phase grid-connected SAPF under normal and polluted grid

A single-phase shunt active power filter (SAPF) is used in a single-phase electrical system to reduce harmonic distortions, enhance power factor, and control voltage. In order to eliminate harmonic currents and enhance power quality, the control strategy for a single-phase SAPF a controller for detecting the load current, isolating harmonic components, and producing compensatory currents. Some of the conventional control schemes that are discussed below are Synchronous Reference Frame Theory (SRFT), Instantaneous Reactive Power Theory (IRPT), and Complex Coefficient Filter (CCF). The describe section below the mathematical formulation and description of the SRFT conventional control technique.

3.2.1 Synchronous Reference Frame Theory (SRFT)

Synchronous Reference Frame Theory (SRFT) based control schemes for controlling DSTATCOM are discussed in many papers [24]. The SRFT is based on Park's and Clarke's transformation. The main objective of SRFT control is to generate the fundamental component of load current. The SRF control scheme generates the reference supply current from the nonlinear load current. This section describes the control block for the SRF-based control scheme which will generate the switching signals for VSC of DSTATCOM. The nonlinear load current is first transformed into its alpha and beta Clarke components. The alpha component ($i_{L\alpha}$) is in the same phase as the actual load current while beta component is 90° phase shift delayed to the actual load current. The $i_{L\alpha}$ and $i_{L\beta}$ signals are transformed into Park's d-q component (I_d and I_q). Both the components are passed through LPF to extract the DC components I'_{Fd} and I'_q and filtered out all non-DC components from the load current. When a grid-connected PV system is considered, the feed-forward PV current (I_{PVff}) is subtracted from the addition of filtered fundamental load current (I'_{Fd}) and switching loss component I_{loss}.

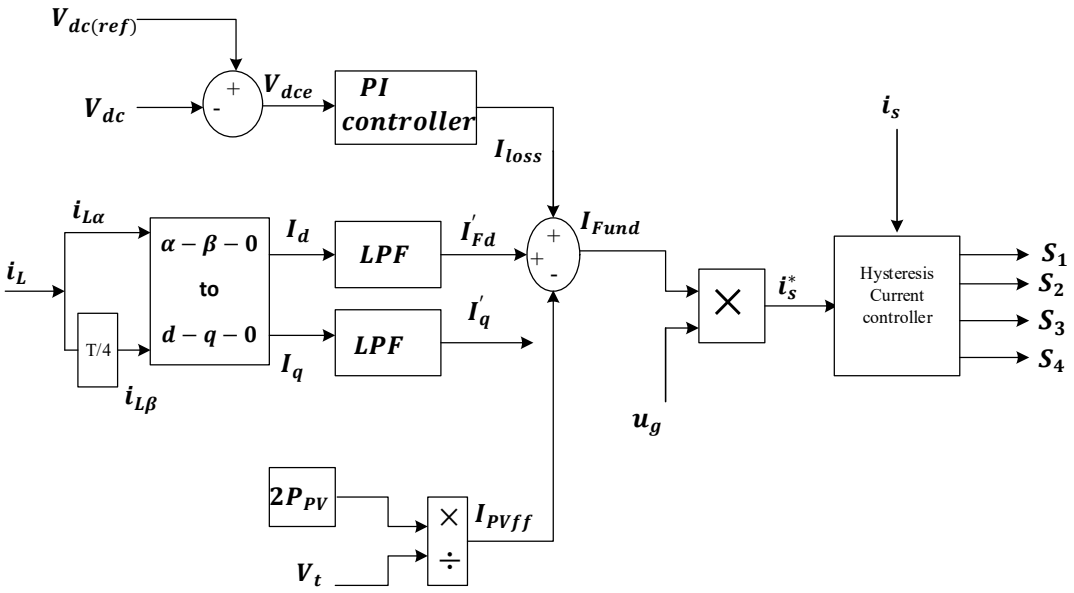

Fig.3.9 SRF-based Control Scheme for Single-phase grid-connected PV DSTATCOM

The I_{loss} is the loss component which is necessary to adjust the DC capacitor' voltage. The resultant component is the total fundamental current component is I_{Fund}. The resultant fundamental current is multiplied by the synchronizing signal obtained from single-phase PLL. Park transformation is used to obtain the fundamental load component given by

$$\begin{bmatrix} I_d(t) \\ I_q(t) \end{bmatrix} = \begin{bmatrix} \sin\theta & -\cos\theta \\ \cos\theta & \sin\theta \end{bmatrix} \begin{bmatrix} i_\alpha(t) \\ i_\beta(t) \end{bmatrix} \tag{3.19}$$

The switching loss component I_{loss} is calculated as

$$I_{loss}(n) = I_{loss}(n-1) + k_P\{V_{dce}(n) - V_{dce}(n-1)\} + k_i V_{dce}(n) \tag{3.20}$$

where, V_{dce} is the DC link voltage error given by Eq. (3.21)

$$V_{dce}(n) = V_{dc(ref)}(n) - V_{dc}(n) \tag{3.21}$$

The peak amplitude of voltage (V_t) is then obtained by taking the square root of the sum of the square of $v_{s\alpha}$, and $v_{s\beta}$, which is then used to create the synchronizing unit's in-phase template (sin) for generating reference current.

$$v_{s\alpha} = V_m \sin\omega t \tag{3.22}$$

$$v_{s\beta} = V_m \sin\left(\omega t - \frac{\pi}{4}\right) \tag{3.23}$$

$$V_t = \sqrt{v_{s\alpha}^2 + v_{s\beta}^2} \tag{3.24}$$

$$u = \frac{v_{s\alpha}}{V_t} = \sin\theta \tag{3.25}$$

The reference source current (i_s') is calculated by multiplying the resultant total fundamental current component with the synchronizing signal ($\sin\theta$), given by Eq. (3.26),

$$i_s^* = (I_{Fund} * \sin\theta) = (I_{Fd}' + I_{loss} - I_{PVff}) * (\sin\theta) \tag{3.26}$$

By comparing the currents coming from the actual source and the reference source, the hysteresis current controller (HCC) creates four switching signals for driving the IGBTs of VSC.

3.2.2 Instantaneous Reactive Power Theory (IRPT)

An approach to controlling the reactive power in a power distribution system is called Instantaneous Reactive Power Theory (IRPT)-based control of the DSTATCOM (Distribution Static Compensator). The control strategy is based on the concept of "instantaneous reactive power" (also known as "p-q theory" or "instantaneous power theory"). It involves measuring the instantaneous values of voltage and current at the point of connection (PC), and then calculating the reactive power (Q) and active power (P) components in real-time.

The IRPT control scheme determines the necessary compensation based on the computed values of P and Q. In order to achieve the intended reactive power compensation, the algorithm then creates proper control signals for the DSTATCOM to inject or absorb reactive power as necessary. By regulating the reactive power, voltage stability, and power quality will be improved. The single-phase AC supply and load current are sensed by real-time sensors and used to calculate the instantaneous active and reactive power. The source voltage (v_s) and load current (i_L) are transformed into alpha-beta components ($v_{s\alpha}, v_{s\beta}, i_{L\alpha}$ and $i_{L\beta}$).

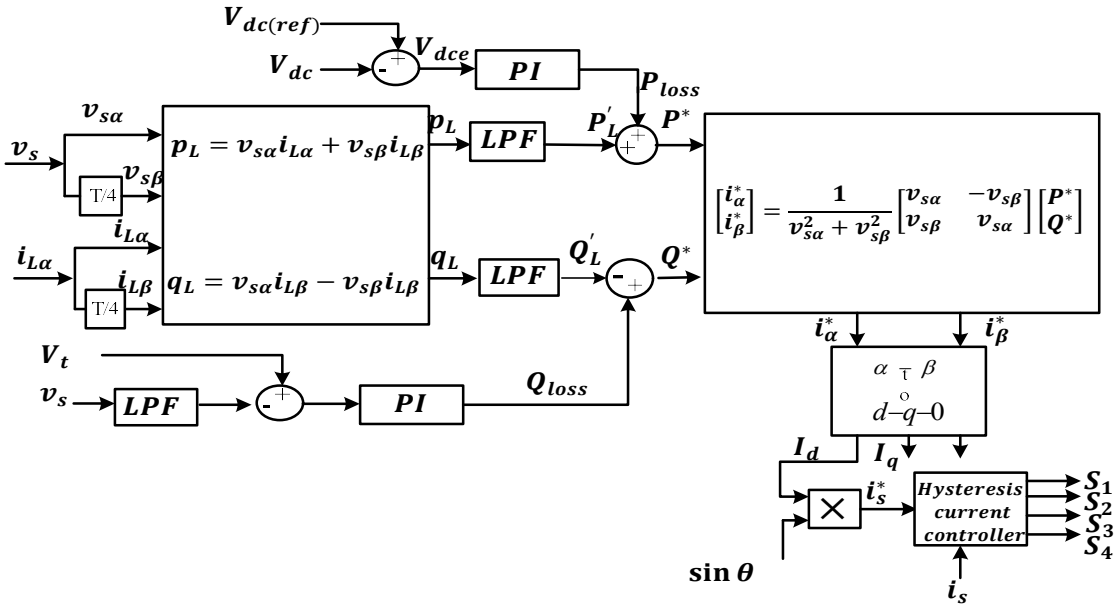

Fig.3.10 Block diagram of IRPT-based control scheme of Single-phase grid connected DSTATCOM

The instantaneous active (p_L) and reactive power (q_L) flowing into the load side are calculated as

$$p_L = v_{s\alpha}i_{L\alpha} + v_{s\beta}i_{L\beta} \tag{3.27}$$

$$q_L = v_{s\alpha}i_{L\beta} - v_{s\beta}i_{L\alpha} \tag{3.28}$$

The signals p_L and q_L consists of non-DC components. These components are filtered out using LPFs to extract the DC component of both obtained power P_L' and Q_L'. The fundamental active power P_L^* is added to the instantaneous active power loss component (P_{Loss}) which is required to adjust the DC link voltage of the DC capacitor. While the reactive power required to maintain the Point of common voltage (Q_{Loss}) power loss component is added with instantaneous reactive power (q_L). The fundamental active power (P^*) and reactive power (Q^*) are obtained by

$$\left.\begin{aligned} P^* &= p_L + P_{Loss} \\ Q^* &= q_L + Q_{Loss} \end{aligned}\right\} \tag{3.29}$$

The reference alpha-beta component (i_α^*) and (i_β^*) are calculated from fundamental active power (P_L^*) and reactive power (Q_L^*) and expressed as

$$\begin{bmatrix} i_\alpha^*(t) \\ i_\beta^*(t) \end{bmatrix} = \frac{1}{v_{s\alpha}^2 + v_{s\beta}^2} \begin{bmatrix} v_{s\alpha} & v_{s\beta} \\ v_{s\beta} & -v_{s\alpha} \end{bmatrix} \begin{bmatrix} P^* \\ Q^* \end{bmatrix} \tag{3.30}$$

$$\begin{bmatrix} I_d(t) \\ I_q(t) \end{bmatrix} = \begin{bmatrix} \sin\theta & -\cos\theta \\ \cos\theta & \sin\theta \end{bmatrix} \begin{bmatrix} i_\alpha^*(t) \\ i_\beta^*(t) \end{bmatrix} \quad (3.31)$$

These alpha-beta components (i_α^*, i_β^*) are transformed into d-q components (I_d, I_q). The peak amplitude of voltage (V_t) is then obtained by taking the square root of the sum of the square of $v_{s\alpha}$ and $v_{s\beta}$, which is then used to create the synchronizing unit's in-phase template ($\sin\theta$ or u_p) for generating reference current as discussed in Eq. 3.32 to Eq.3.35.

$$v_{s\alpha} = V_m \sin\omega t \quad (3.32)$$

$$v_{s\beta} = V_m \sin\left(\omega t - \frac{\pi}{4}\right) \quad (3.33)$$

$$V_t = \sqrt{v_{s\alpha}^2 + v_{s\beta}^2} \quad (3.34)$$

$$u_p = \frac{v_{s\alpha}}{V_t} = \sin\theta \quad (3.35)$$

The fundamental direct component I_d is multiplied by the synchronizing signal $\sin\theta$ to obtain reference supply current or source current. This obtained reference source current is compared with the actual or sensed source current in the PWM current controller or HCC, to obtain switching signals for the VSC of DSTATCOM.

$$i_s^* = (I_d * \sin\theta) \quad (3.36)$$

3.2.3 Hermite function-based ANN control Technique

In this chapter, a single-phase grid-connected PV system with a Hermite Function-based ANN (HeANN) control scheme is discussed and developed under both ideal and polluted grid voltage conditions. The schematic diagram of the proposed system with HeANN control scheme is shown in Fig. 3.11.

The input, hidden, and output layers are all part of the multilayer network comprising the proposed system's ANN structure, which is depicted in Fig. 3.12. The functional expansion employing Hermite polynomials serves as the buried layer.

These higher-order functional neural networks, which are used for image denoising, channel equalisation, and noise processing, are based on nonlinear function expansions. Examples include the Chebyshev functional expansion (ChANN) [32], Legendre Functional Neural Network (LANN), Trigonometric Functional Expansion, and

Hermite Expansion [51]. Shunt active power filtering is applied using some of these techniques in both three-phase and single-phase systems [31-35].

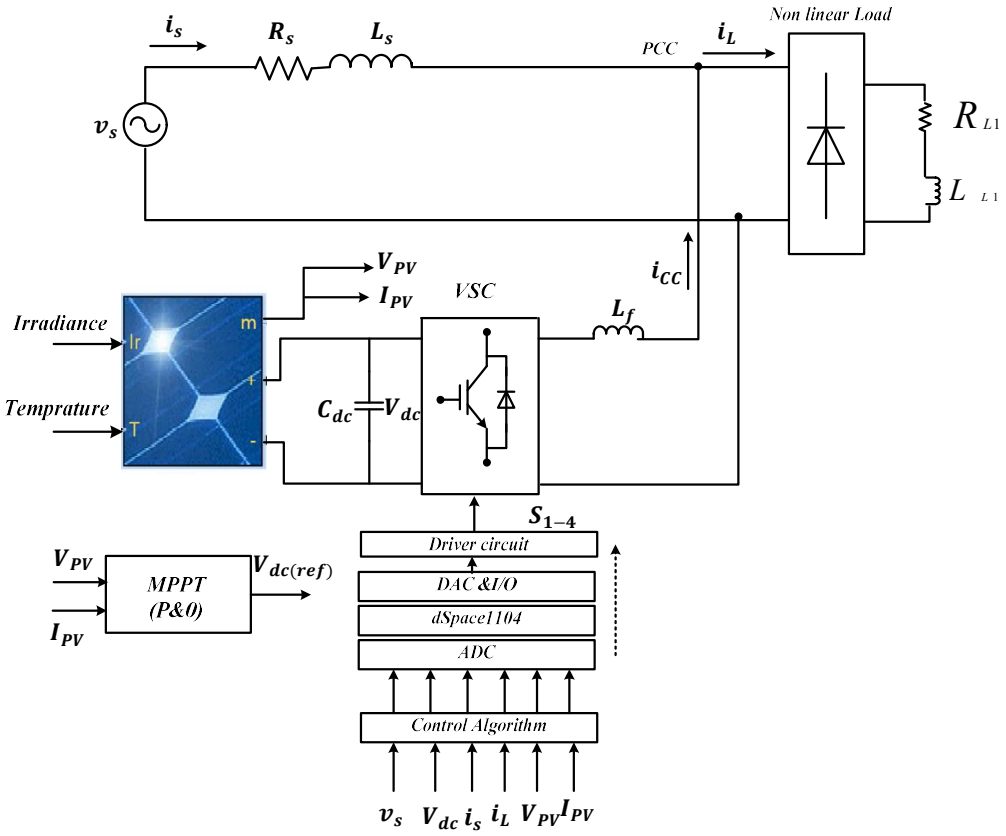

Fig.3.11 Schematic of single-phase grid-connected PV system

Hermite polynomials (HeP) were first introduced by Pierre-Simon Laplace in 1810, and Pafnuty Chebyshev improved on the research in 1859. The Hermite polynomials are named for Charles Hermite, who published a treatise on polynomials in early 1864. Hermite Polynomials accurately anticipated the data points given for estimate. The method is used in the study of partial differential equations, the least squares approximation, and quantum harmonic oscillators.

As a control technique, the Hermite expansion-based Artificial Neural Network (HeANN) is used to reduce PQ problems in single-phase grid-linked PV systems. The HeANN differs from traditional neural networks in that it is based on the functional expansion of nonlinear inputs and has one hidden layer. HeANN's weights undergo online training to achieve quick convergence and quick dynamic response. For load compensation and reference source current, the Hermite function expansion-based control

technique is used. Three key factors active power demand of the load, switching loss calculation handled by the grid, and feedforward PV component are used to determine the reference source current. HeANN's weights are adjusted with LMS, giving the controller its adaptive nature. Using a hysteresis current controller (HCC), the reference source current and the actual source current are compared. The switching signals for VSC will be generated by the HCC.

The structure is made up of an output layer, a functional expansion, and input signals $(x_1, x_2, x_3 \ldots\ldots, x_n)$. The functional expansion functions $(\emptyset_m(x_n)$ as a hidden layer of the NN, expanding the bounds of the inputs to effectively comprehend the network. Through the LMS method, the proposed NN's weights are modified in real-time.

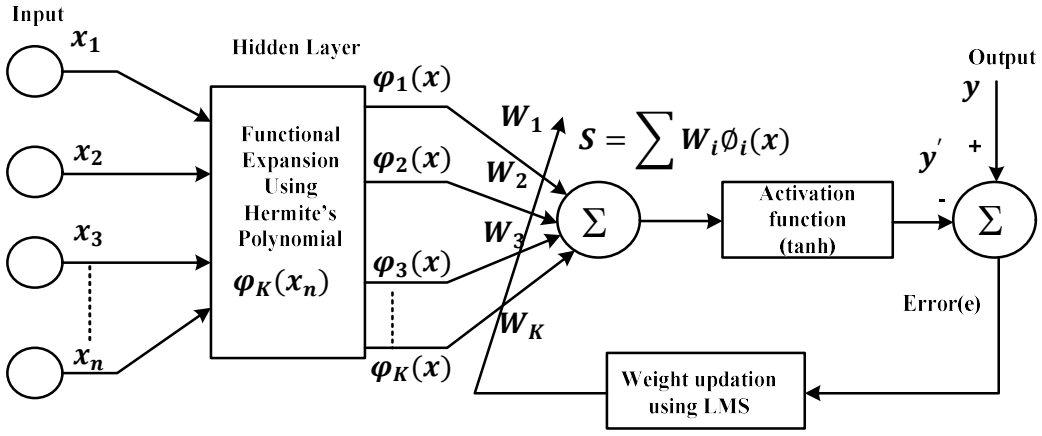

Fig.3.12 Structure of Single-layer neural network with functional expansion layer

The computational complexity and time are reduced by the functional expansion. The relationship between input and output variables is expressed as

$$y'(n) = f(s) \tag{3.37}$$

$$S(n) = \sum_{i=1}^{K} W_i \emptyset_i(X) \tag{3.38}$$

where $X = [x_1, x_2, x_3, \ldots\ldots, x_n]$ denotes the Hermite functional expansion of the input variable and $W_i(n) = [W_1 W_2 W_3 \ldots\ldots W_K]$ represent the weights coefficient of Hermite Function based NN, $y'(n)$ denotes the calculated or the estimated quantity as a function of the input variable, and S is the summation of the product of weights w_{ji} and functionality expanded input vector $\emptyset_i(X)$. The computed sum is passed through the activation function, which is nonlinear in this article i.e., hyperbolic tangent function to calculate the estimated output signal y'.

$$y' = \tan h\,(s) \tag{3.39}$$

The learning method is utilized to update the weights through the Least Means Square (LMS) and reduce the error 'e'.

$$e(n) = y(n) - y'(n) \tag{3.40}$$

$$W(n) = W(n-1) + \mu e(n)\sin\theta \tag{3.41}$$

where $y(n)$ is the actual output, $y'(n)$ is the estimated output signal, $e(n)$ is the calculated error at every instant of time 'n', μ is the step size and, $\sin\theta$ is the PLL's synchronizing signal.

First four Hermite Polynomials are shown in Eq. (3.42),

$$\left.\begin{aligned} H_0(x) &= 1 \\ H_1(x) &= 2x \\ H_2(x) &= -2 + 4x^2 \\ H_3(x) &= 12 - 48x^2 + 16x^4 \end{aligned}\right\} \tag{3.42}$$

These polynomials represent the ANN's function expansion block, which uses load current (i_L) as an input variable to calculate the active load current component. The corresponding load components can be presented as

$$\left.\begin{aligned} I_{L0}(x) &= 1 \\ I_{L1}(x) &= 2i_L \\ I_{L2}(x) &= -2 + 4i_L^2 \\ I_{L3}(x) &= -12i_L + 8i_L^3 \end{aligned}\right\} \tag{3.43}$$

$$I_{LFavg} = [I_{L0(x)} \quad I_{L1}(x) \quad I_{L2}(x)] \tag{3.44}$$

The weighted sum of the load current with the Hermite function extended yields the fundamental active load component. Its output is added up and then put through a tanh activation function. The proposed ANN's weights are updated online via LMS. It restricts the output to a range between 0 and 1. The scaling factor for the load current is 0.01.

$$I_{LFest} = I_{LFavg}^{T} W \tag{3.45}$$

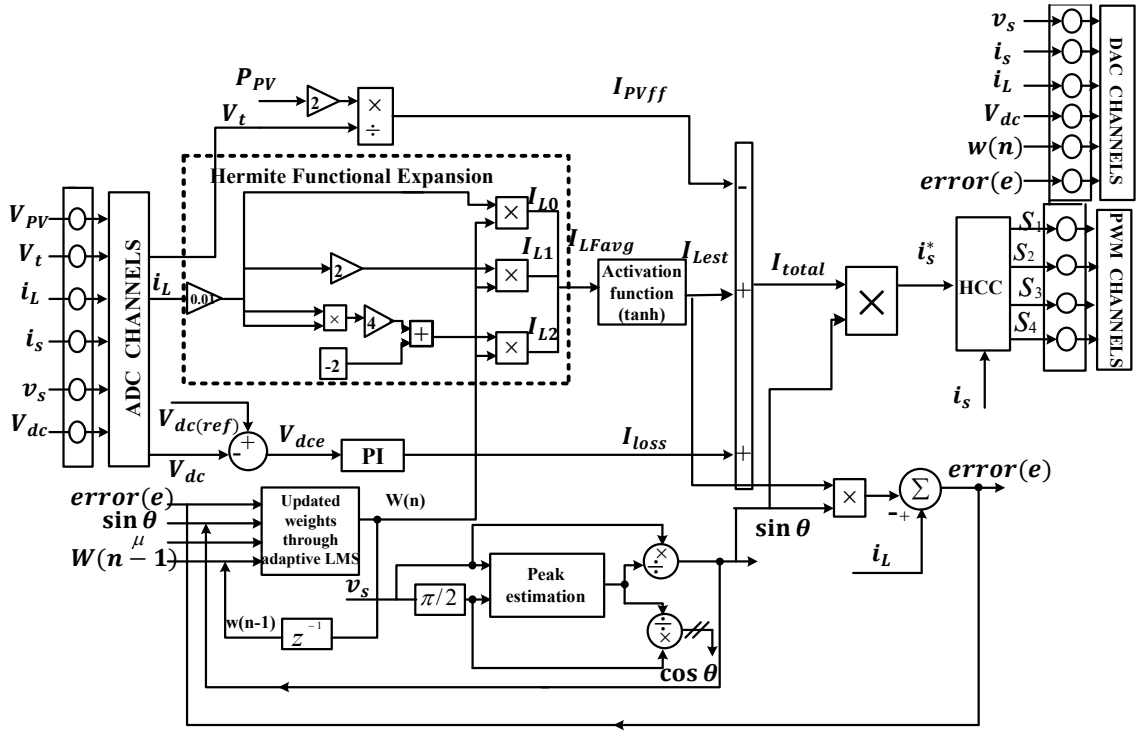

Fig.3.13 Control scheme based on HeANN for single-phase grid-connected PV system.

The error is calculated as

$$e = y - y' \tag{3.46}$$

$$e = i_L - I_{Lest}\sin\theta \tag{3.47}$$

$$e = i_L - I_{LFavg}^T W\sin\theta \tag{3.48}$$

The weight 'W' is updated to reduce the error while simultaneously minimizing the mean square error (MSE). The worst dynamic state, or load unbalancing, has been considered in the paper that has been proposed. The weight is updated by using the Gradient Descent technique given by Widrow and Hoff,

$$W(n) = W(n-1) - \frac{\mu}{2}\nabla I_{Lest}e(n) \tag{3.49}$$

where $\nabla I_{Lest}e(n) = \frac{\partial e(n)}{\partial I_{Lest}}$ denotes the gradient of the error.

$$MSE = E[e^2] = (i_L - I_{Lest}\sin\theta)^2 \tag{3.50}$$

Differentiate Equation (3.50),

$$\frac{\partial E(e^2)}{\partial I_{Lest}} = -2\sin\theta \underbrace{(i_L - I_{Lest}\sin\theta)}_{e} = 2e\sin\theta \tag{3.51}$$

$$W(n) = W(n-1) - \frac{\mu}{2}(-2e\sin\theta) \tag{3.52}$$

$$W(n) = W(n-1) + \mu e\sin\theta \tag{3.53}$$

The updated weight ($W(n)$) is calculated by adding the previous weight ($W(n-1)$) and product of step size (μ), error (e), and sine template ($\sin\theta$). The step size considered for the adaptive LMS algorithm is selected between 0 and 1. The weight ($W(n)$) is updated accordingly to the load change or any other dynamic changes. The voltage from the single-phase source is split up into its 'α-β' components. Through a T⁄4 phase shift in the source voltage, the quadrature signal is obtained. The squared and added signals are both in phase and quadrature. The peak amplitude of voltage (V_t) is then obtained by taking the square root of the sum of the square of $v_{s\alpha}$ and $v_{s\beta}$, which is then used to create the synchronizing unit's in-phase template ($\sin\theta$) for generating reference current. There mathematical operation is shown in Eq. (3.54) to Eq. (3.57).

$$v_{s\alpha} = V_m \sin\omega t \tag{3.54}$$

$$v_{s\beta} = V_m \sin\left(\omega t - \frac{\pi}{4}\right) \tag{3.55}$$

$$V_t = \sqrt{v_{s\alpha}^2 + v_{s\beta}^2} \tag{3.56}$$

$$u = \frac{v_{s\alpha}}{V_t} = \sin\theta \tag{3.57}$$

The proposed HeANN control system yields the switching signals for VSC. High-frequency operation of the power converter switches results in switching loss (I_{loss}) in the system. By operating a PI controller across the difference between the dc-link voltage (V_{dc}) and reference dc-link voltage ($V_{dc(ref)}$), the switching loss is determined. The PI controller receives the dc error signal (V_{dce}) as an input, and produces the loss component (I_{loss}). The grid supply compensates for the proposed system's switching loss. The proposed control scheme's loss component is stated as

$$I_{loss}(n) = I_{loss}(n-1) + K_P\{V_{dce}(n) - V_{dce}(n-1)\} + K_I V_{dce}(n) \tag{3.58}$$

where, K_P and K_I are the proportional and integral gain constants of the PI controller. Due to the integration of PV with the proposed system, its active contribution must be computed. The active power component of PV is shown by its feedforward component (I_{PVff}).

$$I_{PVff} = \frac{2P_{PV}}{V_t} \tag{3.59}$$

The computed total current I_{total} is expressed as

$$I_{total} = I_{Lest} + I_{loss} - I_{PVff} \tag{3.60}$$

This total current is further utilized to produce the reference current (i_s^*) and it is expressed as

$$i_s^* = I_{total} * \sin\theta \quad (3.61)$$

This reference current (i_s^*) is compared with the actual source current(i_s) into an HCC-based PWM controller and produces four switching signals (S_{1-4})for VSC to operate as a shunt active power filter (SAPF).

3.2.4 Bernoulli Polynomial based ANN (BePANN) control Technique

This technique uses for higher-order functional neural networks based on polynomials include speech recognition, picture processing, and communication systems. To reduce the present PQ issues present in single-phase grid-connected PV inverters, Bernoulli's Polynomial expansion-based ANN is used for load compensation. The functional expansion block, which differs from any other typical ANN, is known as the hidden layer of the ANN. BePANN allows for more accurate and less oscillatory fundamental component extraction. This element will be used to produce reference source current. BePANN's mathematical expression and use in grid-connected PV systems are discussed below.

Jacob Bernoulli combines the Bernoulli coefficient and the Bernoulli numbers. They work using the Euler-MacLaurin formula and series expansion of functions. The first four of Bernoulli's Polynomials are as follows

$$B_0(t) = 1,\ B_1(t) = t - \frac{1}{2},\ B_2(t) = t^2 - t + \frac{1}{6},\quad B_3(t) = t^3 - \frac{3}{2}t^2 + \frac{1}{2}t \quad (3.62)$$

At t=0, the Bernoulli's numbers will be

$$B_0 = 1,\ B_1 = \frac{-1}{2}, B_2 = \frac{1}{6}, B_3 = 0$$

Bernoulli's Polynomial satisfied these conditions [52], which are

(a) $B'_K(t) = KB_{K-1}(t), \quad (K \geq 1)$

(b) $\Delta_t B_K(t) = Kt^{K-1}, \quad (K \geq 0)$

(c) $B_K = B_K(0) = B_K(1), \quad (K \neq 1)$

(d) $B_{2m+1} = 0, \quad (m \geq 1)$

In the proposed research article, the Bernoulli's Polynomial (BeP) is used for load compensation. The load current $i_{Ln}(x)$ is expanded into its intermediate components $I_{L0}(x), I_{L1}(x), I_{L2}(x)$ and so on. The BeP represents the function expansion block of

ANN as shown in Fig.3.14, the input signal is the load current i_L and the output of the BePANN is the fundamental active load current component. The weight component of the proposed ANN is updated and trained online through adaptive LMS. The intermediate component or expanded load components are given by Eq (3.63)

$$\left.\begin{aligned} I_{L0}(x) &= 1 \\ I_{L1}(x) &= i_L - \frac{1}{2} \\ I_{L2}(x) &= i_L^2 - i_L + \frac{1}{6} \\ I_{L3}(x) &= i_L^3 - \frac{3}{2}i_L^2 + \frac{1}{2}i_L \end{aligned}\right\} \quad (3.63)$$

In the proposed research article, the first three terms are considered. The non-linear functional expansion of load current is expanded into three terms (dominant),

$$I_{LF} = [I_{L0(x)} \quad I_{L1}(x) \quad I_{L2}(x)]^T \quad (3.64)$$

$$I_{Lest} = I_{LF}^T . W = W^T I_{LF} \quad (3.65)$$

For simplification, the load current i_L is scaled down by 0.01. The average fundamental load current I_{LFavg}, is passed through the activation function 'tanh' which will limit the output in the range -1 and 1.

The error is calculated as

$$e = y - y' \quad (3.66)$$

$$e = i_L - I_{Lest}\sin\theta \quad (3.67)$$

The error is minimized by updating the weights 'W' so that MSE is also minimised. In the proposed article the worst dynamic condition i.e., load change has been considered. The weight is updated by using the Gradient Descent technique given by Widrow and Hoff

$$W(n) = W(n-1) - \frac{\mu}{2}\nabla I_{Lest} e(n) \quad (3.68)$$

where $\nabla I_{Lest} e(n) = \frac{\partial e(n)}{\partial I_{Lest}}$ denotes the gradient of the error.

$$MSE = E[e^2] = (i_L - I_{Lest}\sin\theta)^2 \quad (3.69)$$

Differentiate Equation (3.69)

$$\frac{\partial E(e^2)}{\partial I_{Lest}} = -2\sin\theta \underbrace{(i_L - I_{Lest}\sin\theta)}_{e} \quad (3.70)$$

$$W(n) = W(n-1) - \frac{\mu}{2}(-2e\sin\theta) \quad (3.71)$$

$$W(n) = W(n-1) + \mu e\sin\theta \quad (3.72)$$

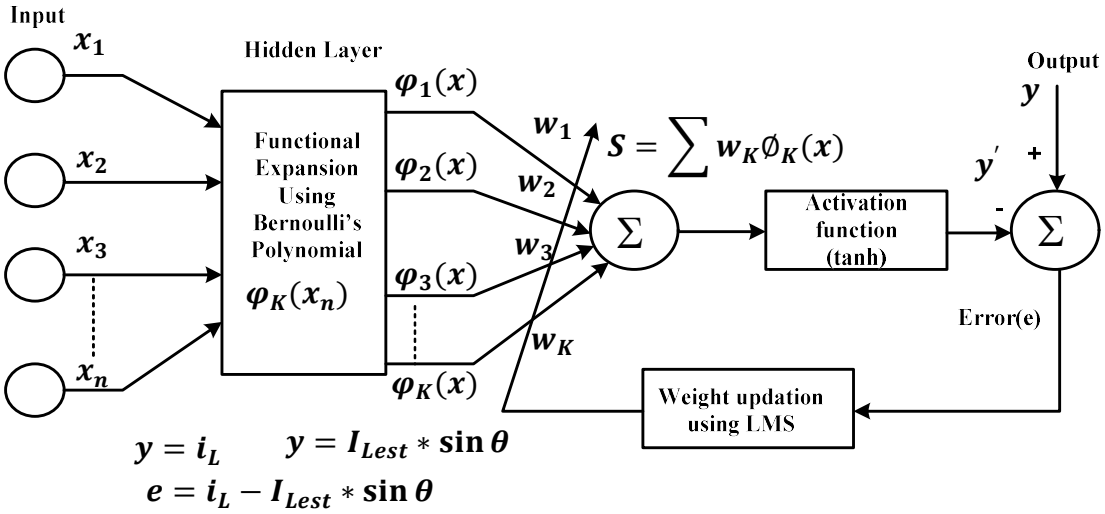

Fig.3.14 Structure of Single-layer neural network with Bernoulli's Polynomials.

The updated weight $(W(n))$ is calculated by adding the previous weight $(W(n-1))$ and product of step size (μ), error (e), and sine template $(\sin\theta)$. The step size considered for the adaptive LMS algorithm is between 0 and 1. The weight $(w(n))$ is updated accordingly to the load change or any other dynamic changes.

The load current i_L is functionally expanded by using higher order Bernoulli's polynomial. The load current expansion through Bernoulli's Function is expressed by the expanded load current components I_{L0}, I_{L1}, I_{L2}. The total current I_{total} is constituted from the average fundamental current I_{LFavg}, PV feedforward current (I_{PVff}) and dc switching loss component (I_{loss}).

$$v_s(t) = V_m \sin(\underbrace{\omega_i t + \varphi_i}_{\theta_i}) \tag{3.73}$$

The voltage error (e_v) is the difference between the in-phase voltage component and the source voltage (v_s).

$$e_v(t) = v_s(t) - v_\alpha(t) \tag{3.74}$$

The quadrature component (v_β) of the source voltage signal is expressed by

$$v_\beta(t) = \omega_n \int v_\alpha(t)\, dt \tag{3.75}$$

where, ω_n is the natural frequency of SOGI PLL [83]. The Laplace transform of quadrature component of source voltage,

$$v_\beta(s) = \omega_n \frac{v_\alpha(s)}{s} \tag{3.76}$$

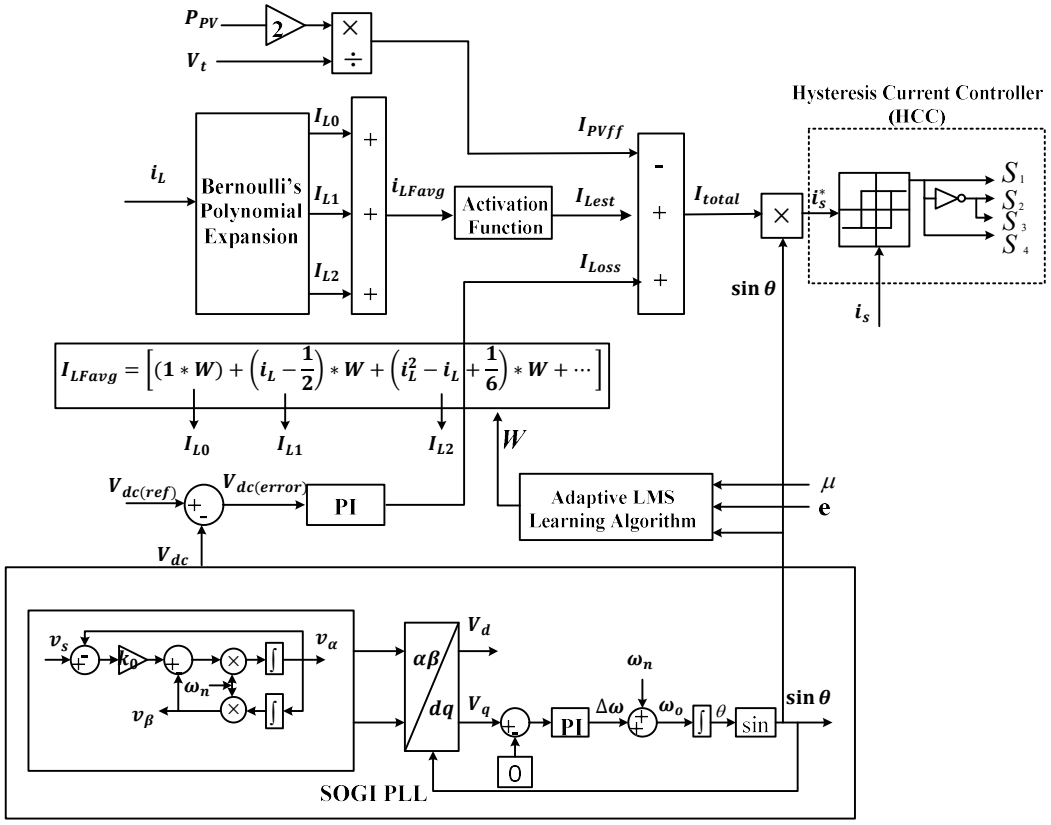

Fig.3. 15 Control scheme for single-phase grid-connected PV inverter based on BePANN.

From Fig. 3.15, the in-phase component of source voltage is obtained using SOGI and expressed as

$$v_\alpha(t) = \int \omega_n\left[K_0 e_v(t) - v_\beta(t)\right]dt \tag{3.77}$$

$$v_\alpha(t) = \int \omega_n K_0[v_s(t) - v_\alpha(t)] - \omega_n \int v_\beta(t)\, dt \tag{3.78}$$

The Laplace Transform of the above equation is given by

$$v_\alpha(s) = \omega_n K_0 \left[\frac{v_s(s)}{s} - \frac{v_\alpha(s)}{s}\right] - \omega_n \frac{v_\beta(s)}{s} \tag{3.79}$$

The transfer function of the in-phase component is expressed as

$$D(s) = \frac{v_\alpha(s)}{v_s(s)} = \frac{K_0\omega_n s}{s^2 + K_0\omega_n s + \omega_n^2} \tag{3.80}$$

The transfer function of the Quadrature component is expressed as

$$Q(s) = \frac{v_\beta(s)}{v_s(s)} = \frac{K_0\omega_n^2}{s^2 + K_0\omega_n s + \omega_n^2} \tag{3.81}$$

Therefore, the transfer function for SOGI is written as

$$\frac{D(s)}{Q(s)} = \frac{v_\alpha(s)}{K_0 e_v(s)} = \frac{\omega_n s}{s^2 + \omega_n^2} \tag{3.82}$$

The main objective of SAPF is to generate an equal and opposite current harmonics waveform present in load current from Shunt connected VSC, that will cancel out the harmonics and thus make the source current or grid current sinusoidal. The reference source current requires the synchronizing signal ($\sin\theta$), load fundamental current (I_{Lest}), PV feedforward current (I_{PVff}) and switching loss current (I_{loss}). The synchronizing is obtained through SOGI PLL. The average fundamental load current (i_{LFavg}) is expressed as

$$I_{LFavg} = \left[(1 * W) + \left(i_L - \frac{1}{2}\right) * W + \left(i_L^2 - i_L + \frac{1}{6}\right) * W + \cdots\cdots\cdots\right] \quad (3.83)$$

The total fundamental load current is obtained by passing the average fundamental load current through the activation function ($\tan h$).

$$I_{Lest} = (\tan h) * I_{LFavg} \quad (3.84)$$

The switching losses occur in VSC which is compensated by the DC link capacitor. The switching loss is estimated by calculating the DC link voltage error ($V_{dc(error)}(n)$) and regulating it to zero using a PI controller. The DC link voltage error is the difference between the sensed DC link voltage and the reference DC link voltage.

$$V_{dc(error)}(n) = V_{dc(ref)}(n) - V_{dc}(n) \quad (3.85)$$

The output of the PI controller is expressed as

$$I_{loss}(n) = I_{loss}(n-1) + K_P\{V_{dc(error)}(n) - V_{dc(error)}(n-1)\} + K_I V_{dc(error)}(n) \quad (3.86)$$

The peak amplitude of voltage (V_t) is then obtained by taking the square root of the sum of the square of $v_{s\alpha}$ and $v_{s\beta}$, which is then used to create the synchronizing unit's in-phase template ($\sin\theta$) for generating reference current using Eq. (3.86) to Eq. (3.89).

$$v_{s\alpha} = V_m \sin\theta \quad (3.87)$$

$$v_{s\beta} = V_m \sin\left(\theta - \frac{\pi}{4}\right) \quad (3.88)$$

$$V_t = \sqrt{v_{s\alpha}^2 + v_{s\beta}^2} \quad (3.89)$$

$$u = \frac{v_{s\alpha}}{V_t} = \sin\theta \quad (3.90)$$

The reference source current (i_s^*) is obtained by multiplying the total net current (I_{total}) with synchronizing signal ($\sin\theta$).

$$i_s^* = (I_{total} * \sin\theta) = (I_{Lest} + I_{loss} - I_{PVff}) * (\sin\theta) \quad (3.91)$$

The hysteresis current controller (HCC) is used to generate the four switching signals for driving the IGBTs of the VSC by comparing the actual source current (i_s) with the reference source current (i_s^*).

3.3 Simulation Results

3.3.1 Performance Analysis with SRFT control scheme

Synchronous Reference Frame Theory-based control scheme is designed and tested under stable and balanced operating conditions, load increment. At t=0.3s, the linear load is added to the connected load as shown in Fig.3.16. to fulfill the load demand, the source current increase at t=0.3s up to t=0.5s. Similarly, to fulfill the reactive power requirement, the compensating current is also increased. The DC link voltage settle at 400V with a small peak of $\pm$1V. The power analysis of the SRFT control scheme under load change for a single-phase grid-connected system is shown in Fig.3.17.

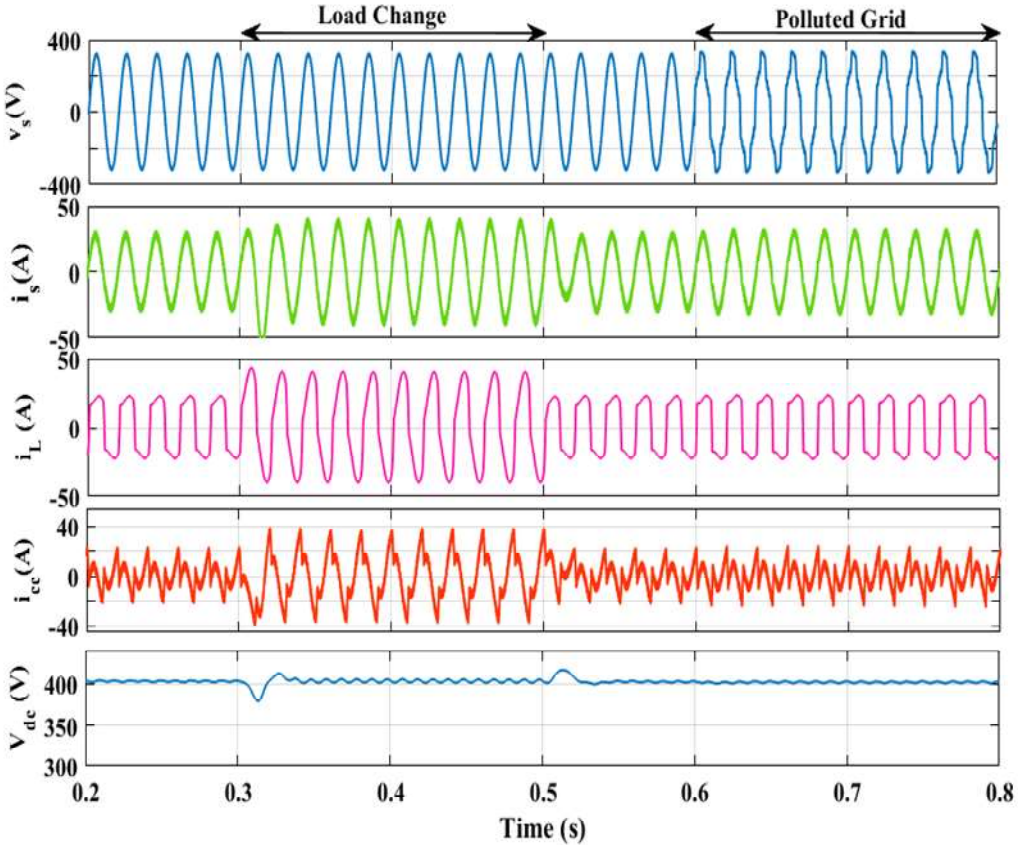

Fig.3.16 Performance Analysis of SRFT under load change and polluted grid

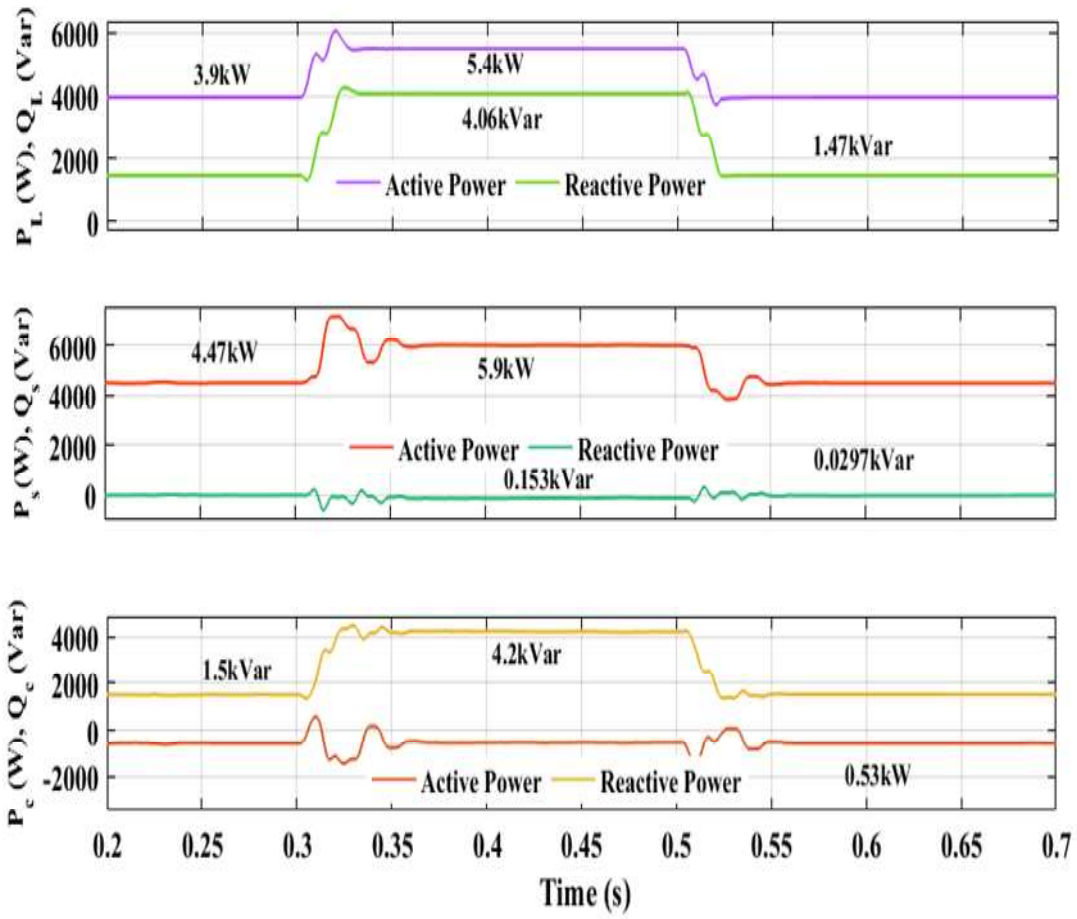

Fig.3.17 Power analysis with SRFT control scheme of single-phase grid-connected system.

Under steady-state conditions, only nonlinear load is connected in a system. The active power demand of the load (P_L) is 3.9kW while reactive power demand (Q_L) is 5.4kW under steady-state condition (till t=0.3s). The active power demand of the load is fulfilled by the source's active power (P_S) while the remaining power of the source is fed into the VSC and the reactive power demand of load is fulfilled by VSC's power (Q_C). Under dynamic load conditions, the linear load is connected to the system the power requirement is increased to 5.4kW and reactive power demand is 4.06kW. The additional active power demand is fulfilled by source power while the reactive power demand of load is fed by VSC.

The FFT analysis of the single-phase grid-connected system with nonlinear load under normal grid conditions is shown in Fig. 3.18. The THD of source voltage, load current and source current are 2.03%, 32.88%, and 3.2% respectively.

The dynamic performance with SRFT control is tested under the condition of irradiance change. At t=0.2s to 0.3s, the irradiance is fixed at 1000W/m^2. The load is a combination of both linear and nonlinear load which is constant throughout the time interval. The load active and reactive power demand during 1000W/m^2 are 5.4kW and 4.06kVar respectively. The active power generated by the VSC in a PV-integrated single-phase system is actively controlled to match the active power requirements of the loads and to contribute to the grid as needed.

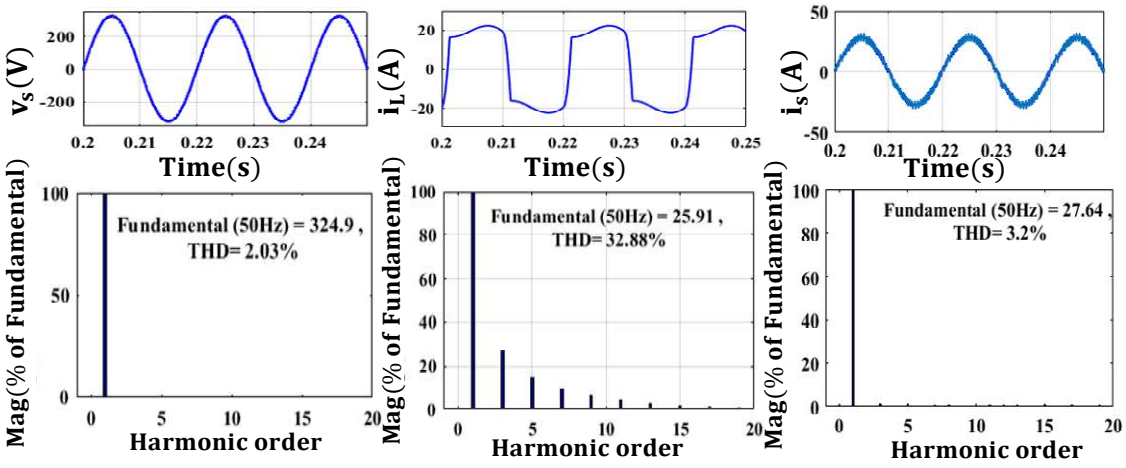

(a) (b) (c)

Fig.3.18 FFT analysis of (a) source voltage (b) load current (c) source current under the single-phase grid-connected system with SRFT control scheme.

The PV's active power is utilized to fulfill the load's active power demand while the surplus power is fed into the source or exported from the source to fulfill the remaining load power demand. While the reactive power demand of load is provided by VSC's reactive power (4.2kVar). As the irradiance is decreased to 500W/m^2, the PV current is also decreased as shown in Fig.3.20(b). In this case, the source current must be increased to generate the required power. The active power demand of load (5.4kW) is fulfilled by PV power (1.026kW) and the remaining power is fulfilled by the source's active power (4.92kW). When 0W/m^2 of solar radiation is taken into account, SAPF operation without PV integration is meant. PV doesn't provide active power during this nighttime scenario, thus the source current rises and the source power rises to satisfy the 5.4kW total load requirement. Only PQ issues are mitigated by the SAPF, and no active power transfer occurs at this time to meet the 5.4kW load demand.

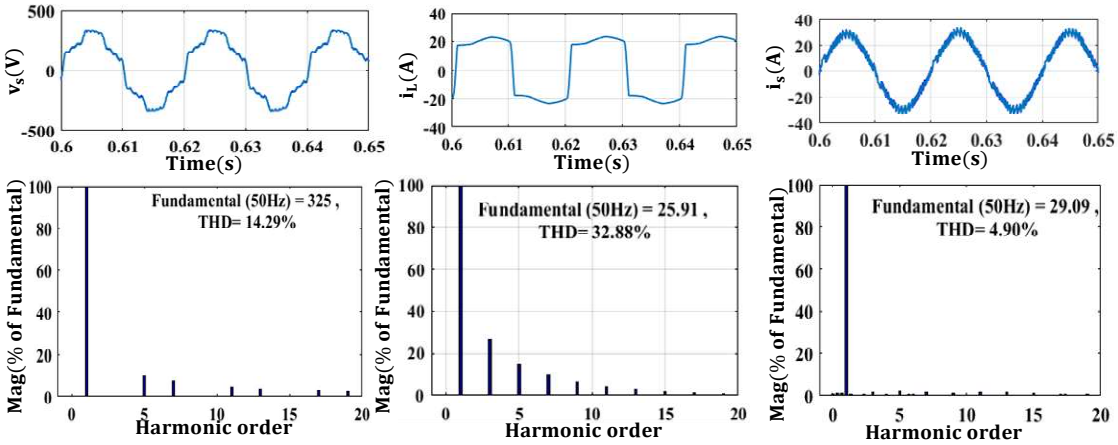

(a) (b) (c)

Fig.3.19 FFT analysis of (a) source voltage (b) load current (c) source current under polluted grid with SRFT control scheme.

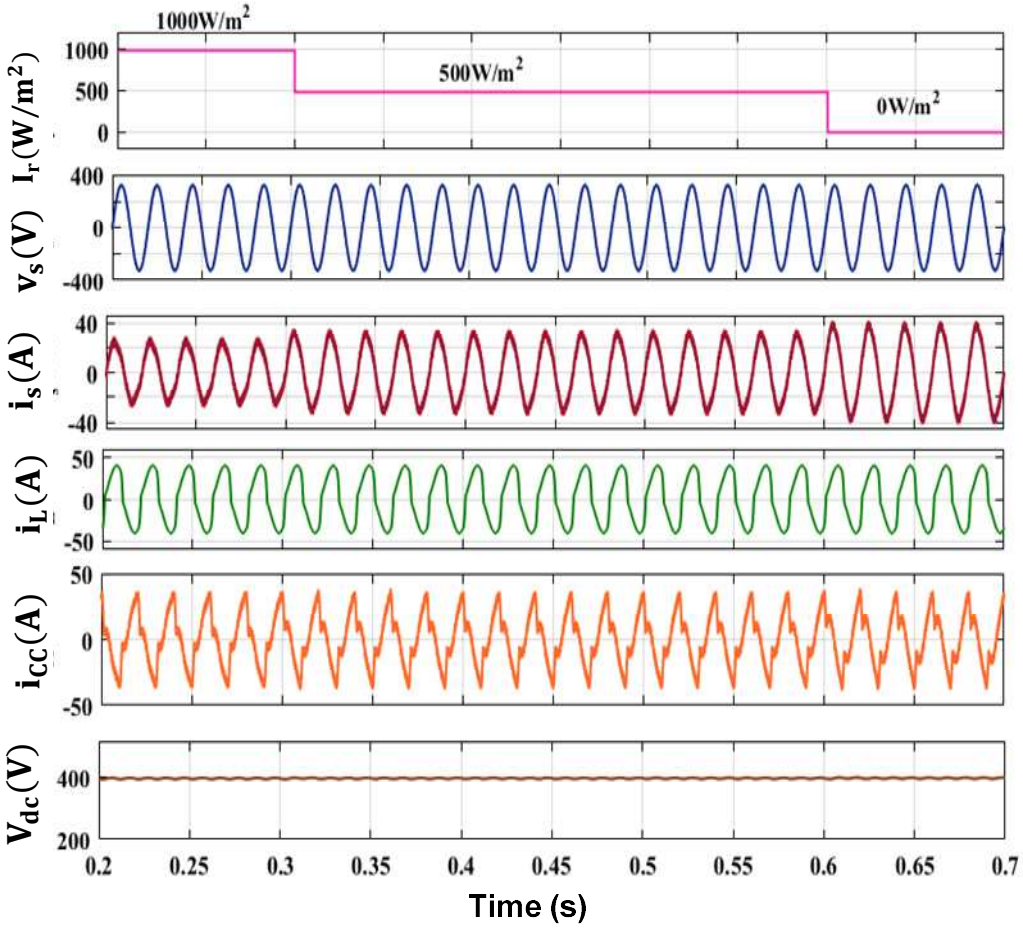

(a)

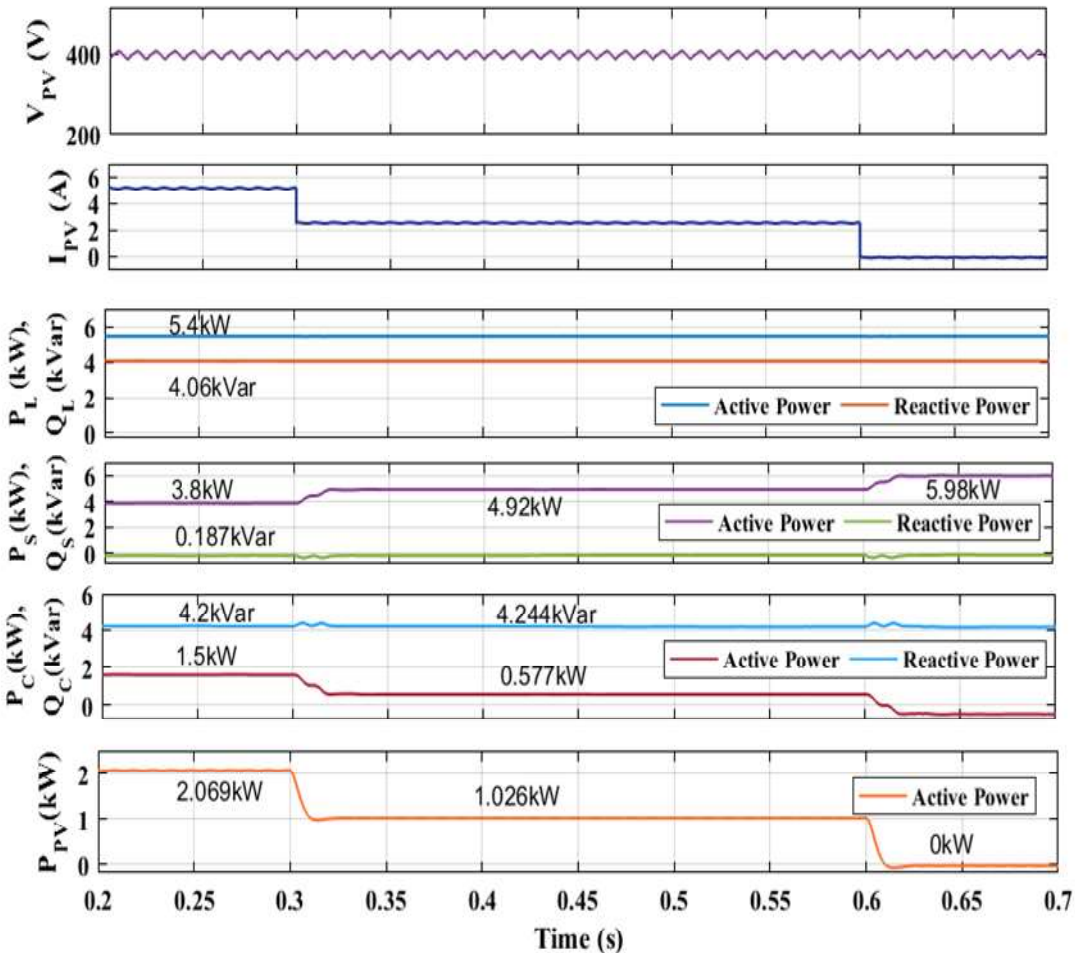

(b)

Fig.3.20 (a) Performance analysis of single-phase grid-connected PV system under Irradiance change (b) Power analysis under irradiance change.

3.3.2 Performance Analysis with IRPT control scheme

When implementing an Instantaneous Reactive Power Theory (IRPT) based control scheme in a grid-connected system with the addition of loads, the control strategy needs to adapt to the changes in the system's power requirements. The system operates in a steady state at a fixed irradiance of 1000W/m^2. At t=0.3s, the linear load is added into the system increasing the load current (i_L). As the load is increased the source's current (i_s) is also increased as shown in Fig.3.21. The DC link voltage (V_{dc}) is regulated at 400V with very small variation for less than one cycle. The compensating current is increased to fulfill the reactive power demand of the load.

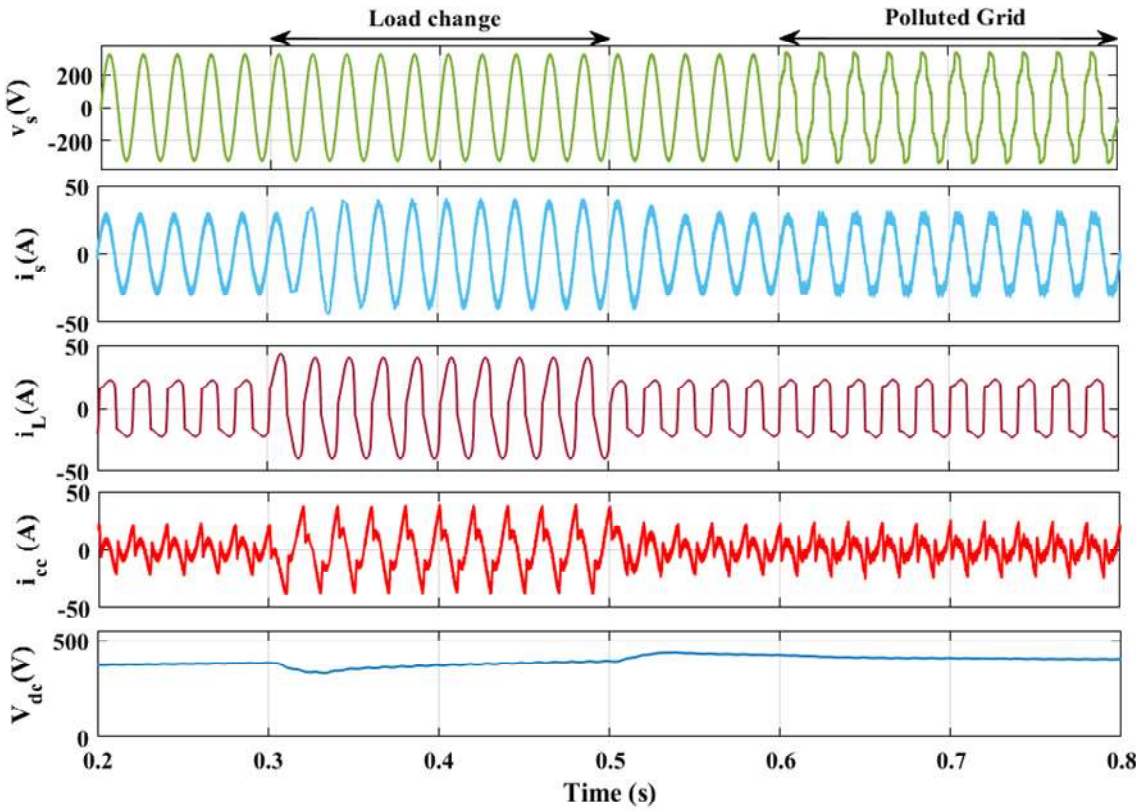

Fig.3.21 Performance analysis of IRPT control scheme under load change and polluted grid.

The dynamic performance of IRPT control is tested under the condition of irradiance change. At t=0.2s to 0.3s, the irradiance is fixed at 1000W/m^2. The load is a combination of both linear and nonlinear load which is constant throughout the time interval. The load active and reactive power demand during 1000W/m^2 are 3.9kW and 1.47kVar respectively. The active power generated by the VSC in a PV-integrated single-phase system is actively controlled to match the active power requirements of the loads and to contribute to the grid as needed. The PV's active power is utilized to fulfill the load's active power demand while the surplus power is fed into the source or exported from the source to fulfill the remaining load power demand. While the reactive power demand of load is provided by VSC's reactive power (1.47kVar). As the irradiance is decreased to 500W/m^2, the PV current is also decreased as shown in Fig.3.22. In this case, the source current must be increased to generate the required power. The active power demand of the load (5.4kW) is fulfilled by PV power (1.026kW) and the remaining power is fulfilled by the source's active power (4.93kW). At night, irradiance goes to 0W/m^2, and the total

load's active power demand (3.9kW) is fulfilled by the source' active power. The DC link voltage (V_{dc}) is stable and regulated at 400V.

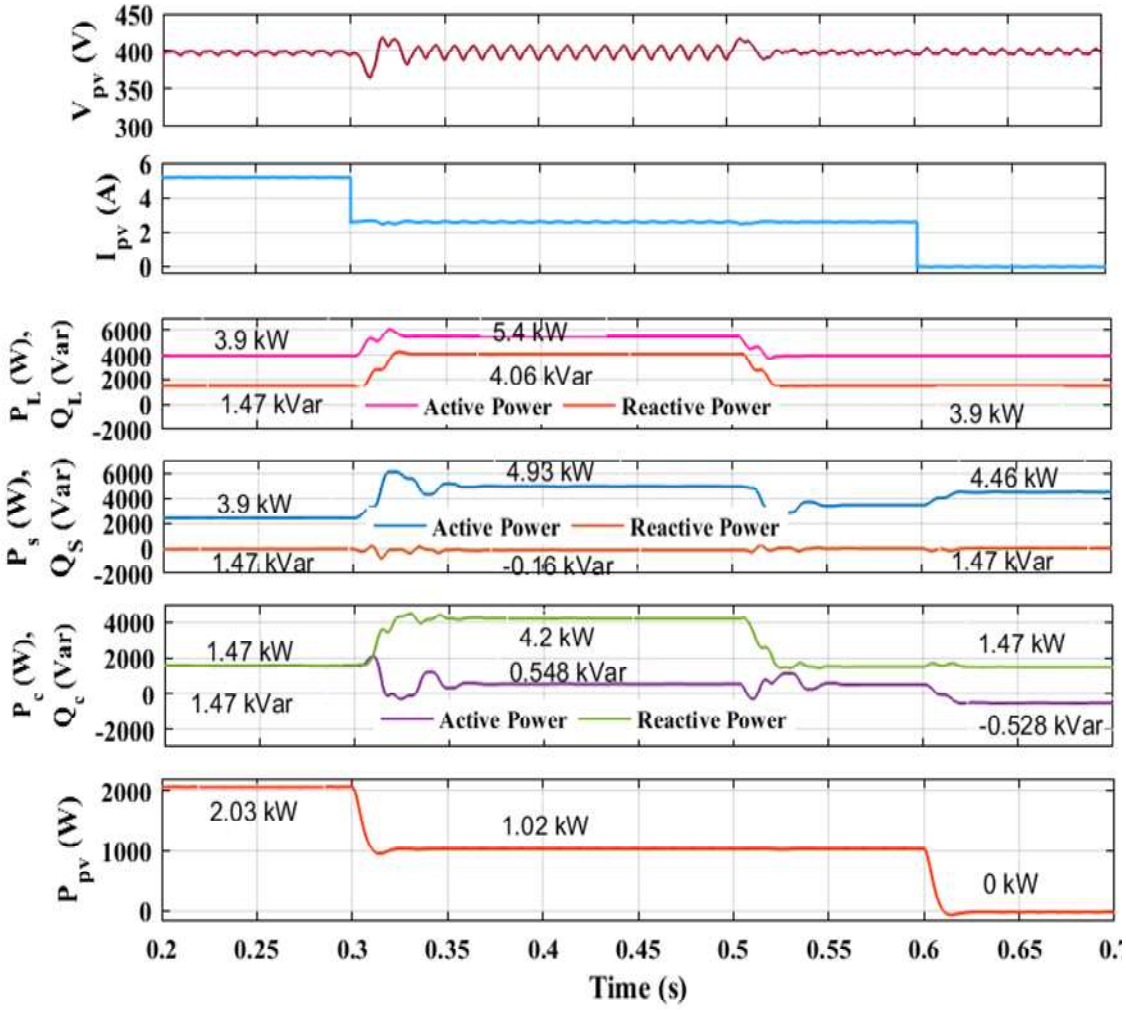

Fig.3.22 Power analysis of the proposed system with IRPT control scheme under irradiance change.

The FFT analysis of the proposed system with IRPT control scheme is shown in Fig.3.23. The THD of the source voltage (v_s), load current (i_L), source current (i_s) are 0.15%, 32.88%, and 4.81%, respectively. The FFT analysis of the proposed system with IRPT control scheme is shown in Fig.3.24. The THD of the source voltage (v_s), load current (i_L), source current (i_s) are 14.28%, 32.88%, and 4.89%, respectively.

.

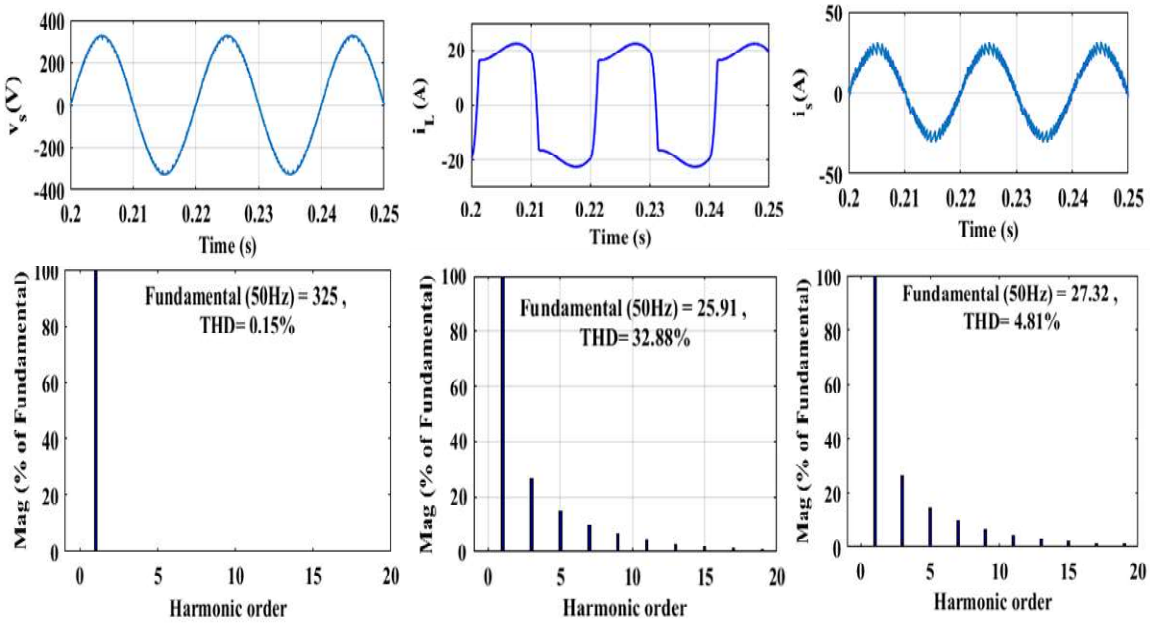

Fig.3.23 THD of source voltage, load current, and source current under normal grid.

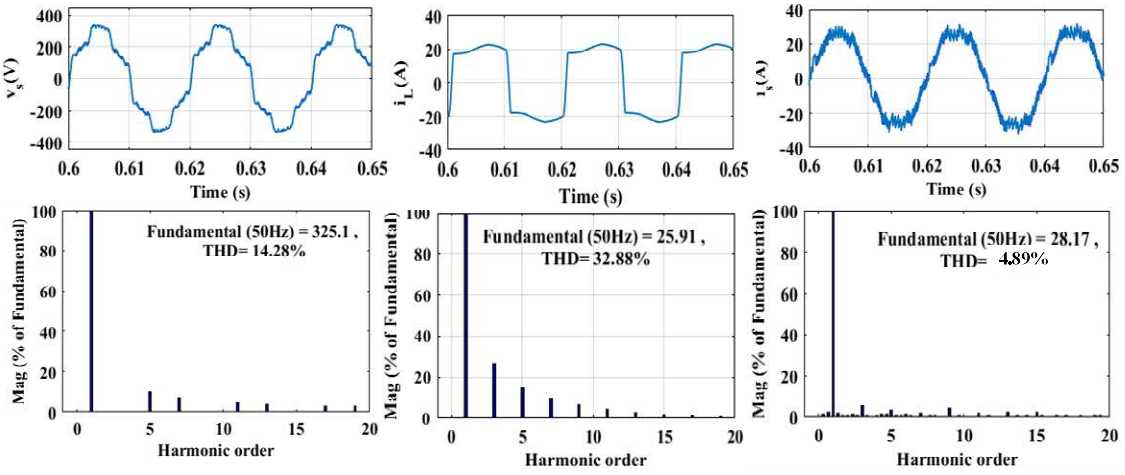

Fig.3.24 THD of source voltage, load current, and source current under the polluted grid.

3.3.3 Performance Analysis with HeANN control scheme under normal and polluted grid

The performance of the proposed system is shown in Fig.3.25 having the signal source voltage (v_s), source current (i_s), and dc-link voltage (V_{dc}). At t=0.3s, the load is increased. The dynamic performance of the proposed control technique with load change is shown below in Fig. 3.25. The source current is in phase with the source voltage and SAPF injects the compensating current to oppose the load current harmonics injected into the supply.

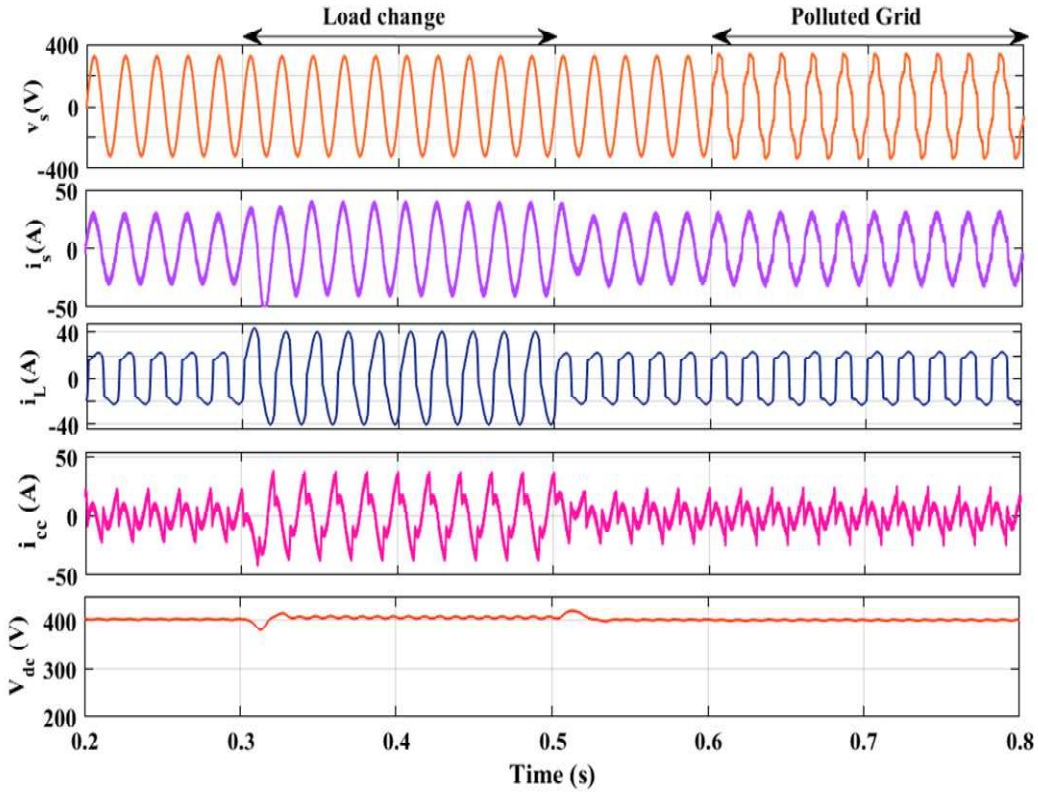

Fig.3.25 Performance analysis of HeANN under normal and polluted conditions in a single-phase grid-connected PV system at 1000W/m^2.

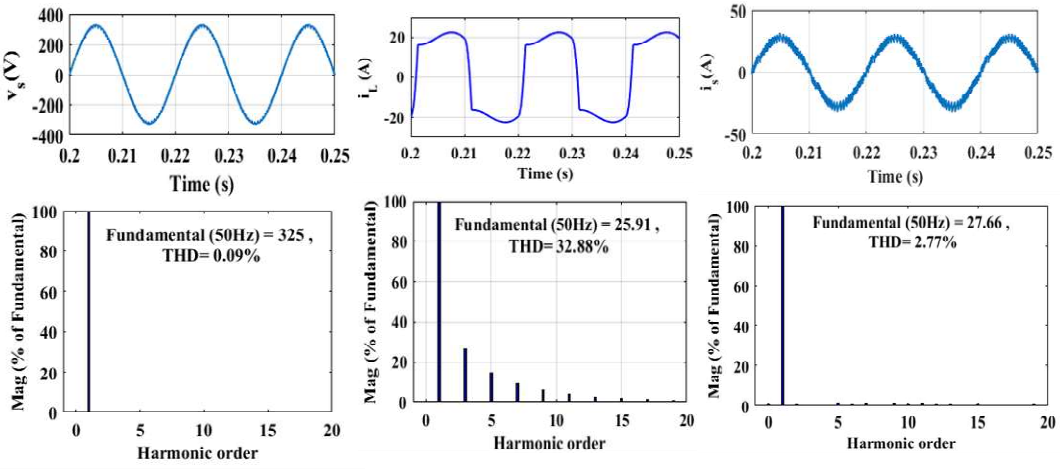

(a) (b) (c)

Fig.3.26 FFT analysis of proposed systems with HeANN control scheme under normal grid (a) source current (b) load current

Fig. 3.26 (a-b) shows the FFT analysis of source current and load current under load change conditions without PV integration. The THD of the source current is 2.77% and the load current is 32.88%.

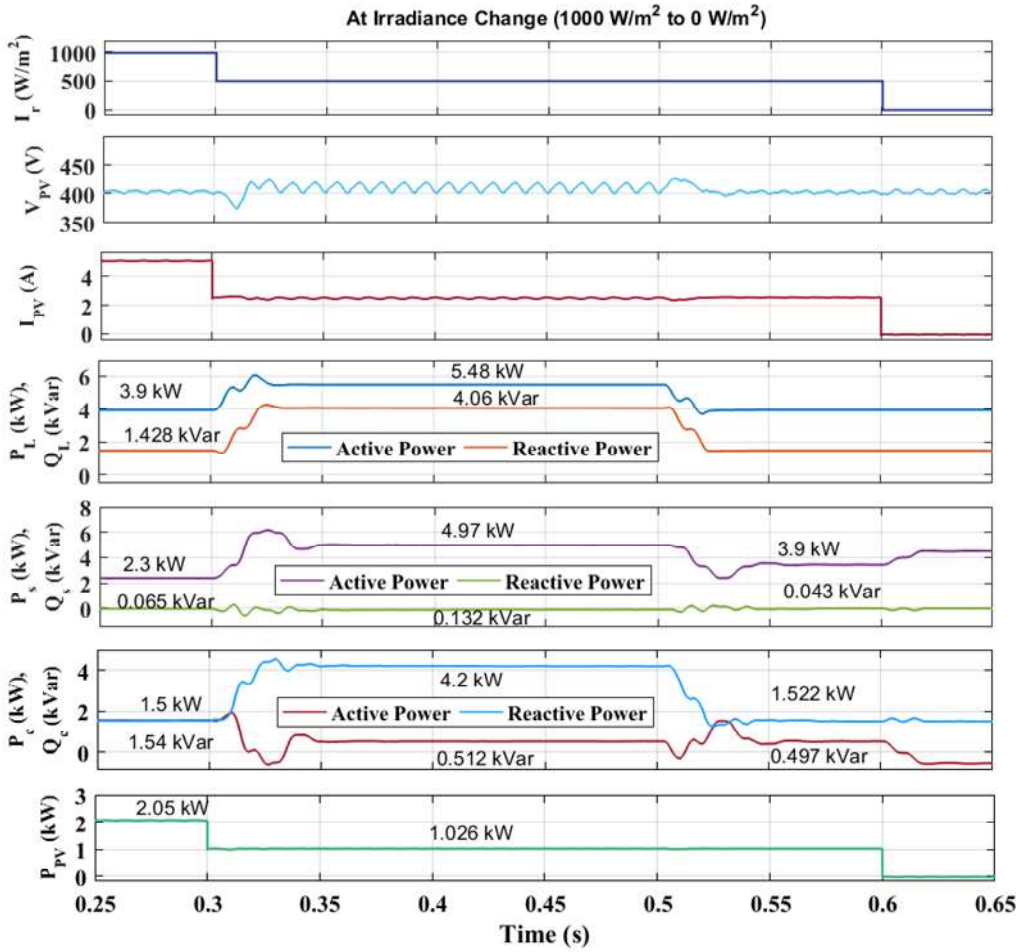

Fig.3.27 Dynamic Performance of the single-phase grid-connected PV system with varying irradiance

The system's performance is also investigated under varying solar irradiance as depicted in Fig. 3.27 with the waveforms of signal active load power (P_L), reactive load power (Q_L), source active power (P_s), source reactive power (Q_S), compensator's active and reactive power (P_C, Q_C). The solar irradiance of the PV array is changed at t = 0.3s, the irradiance is 1000 W/m^2. The source current is reduced as PV will insert its power into the system. The PV will be able to generate its maximum power into the system as the irradiance of the PV array is 1000 W/m^2. The PV array provides its maximum power of 2.05kW to the system. The load's active power demand of 3.9kW is partially fulfilled by the PV while the remaining power is provided by the source's active power. Also, the reactive power demand of the load (1.428kVar) is fed by the VSC. The dc-link voltage is maintained constant at 400V with a very small variation of +5V which is settled within two cycles.

The FFT analysis of the proposed system with IRPT control scheme is shown in Fig.3.28. The THD of the source voltage (v_s), load current (i_L), source current (i_s) are 14.29%, 32.88%, and 4.90%, respectively come under the favorable limit of IEEE-519 standards.

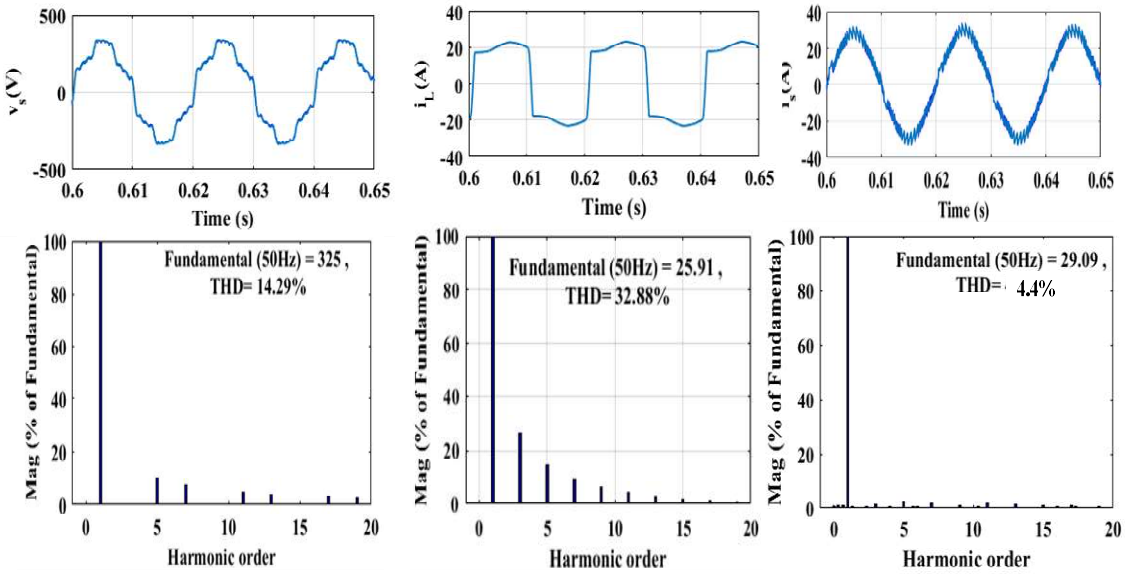

Fig.3.28 FFT analysis under polluted grid with HeANN control.

It is also necessary to investigate the control algorithm's performance on its intermediate signals. The load current is scaled down by dividing it by 0.01. The intermediate signals of the proposed control algorithm for load compensation are shown in Fig. 3.29. The load current expansion through Hermite's Function is expressed by the expanded load current components I_{L0}, I_{L1}, I_{L2}. All these components are summed to get the fundamental average load current I_{LFaug}. The updated weight (W) of the proposed algorithm is regularly updated through LMS to reimburse for load disturbance and solar irradiance change. The total load current I_{total} is composed of PV's feed-forward current (I_{PV}), dc-link loss's component (I_{loss}) and estimated fundamental load current (I_{Lest}). The weight signal and error signal increase as the load current increases. At t = 0.3s, the linear load (R-L) connected to the system, and thus total load current increases. The weight through LMS is also updated and gets increased as the load current increases. Also, the expanded load current through Hermite expansion is increased as the load increases.

3.3.4 Performance Analysis with BePANN control scheme Under normal grid and polluted grid

The dynamic performance of grid-connected PV SAPF under the control of BePANN is tested using MATLAB Simulink and verified with the experimental results. The PV is disconnected from the system. A linear R-L load is added into the system which already has a nonlinear R-L load at t=0.3s to 0.5s.

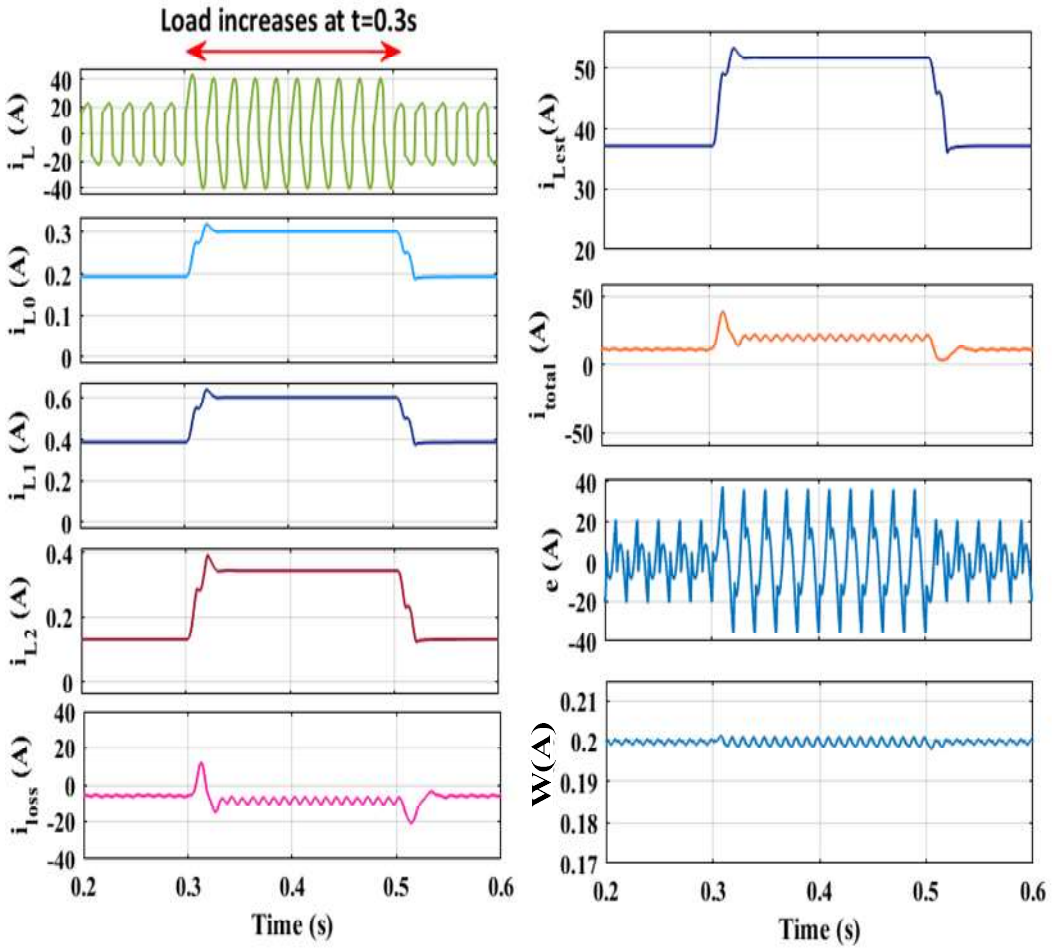

Fig.3.29 Intermediate signals/waveforms of control technique based on HeANN

The source current increases when the load increases to fulfill the load demand. The source current is sinusoidal at a polluted grid as shown in Fig. 3.30, the compensating current is also increased due to load increase, for fulfilling the load's reactive power demand. The DC link is maintained to its reference value to its PI voltage controller with a small voltage fluctuation at load increase and polluted grid.

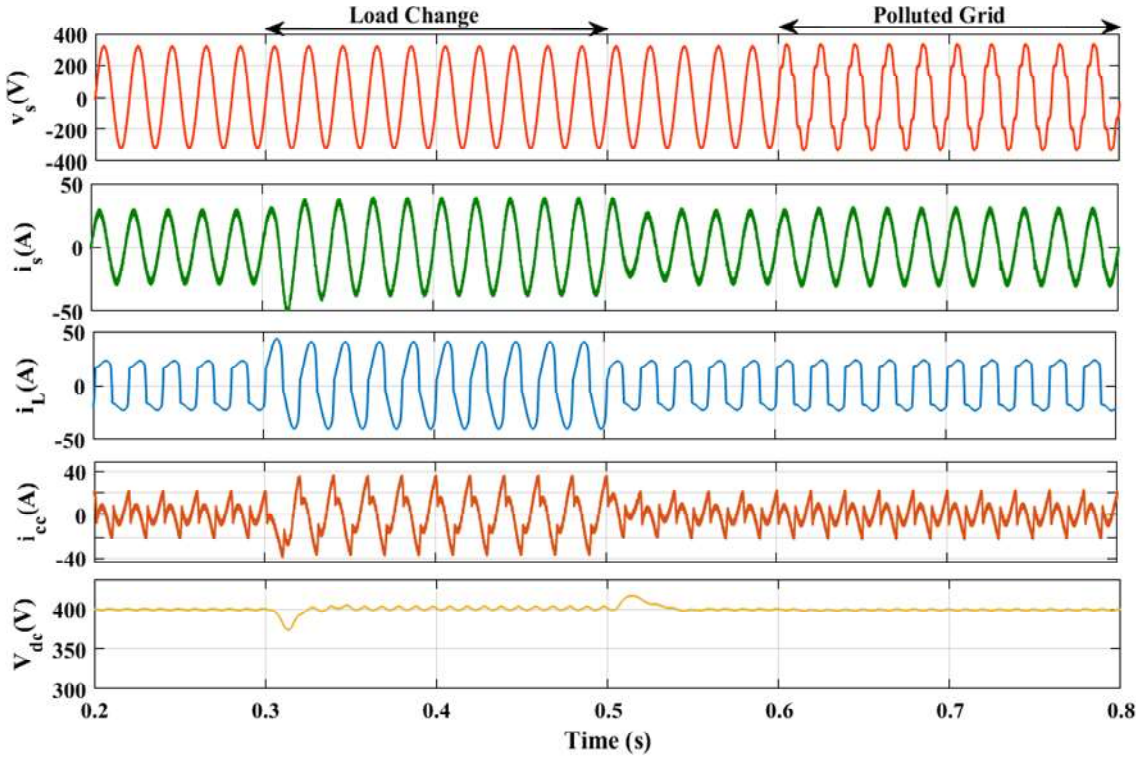

Fig.3.30 Dynamic performance of proposed grid connected SAPF with BePANN control scheme under load change and distorted grid.

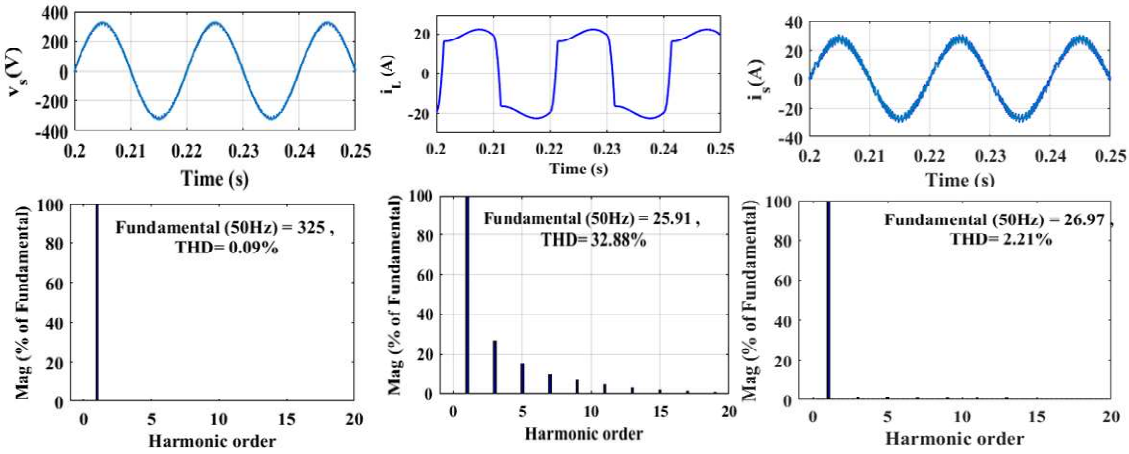

(a) (b) (c)

Fig. 3.31 FFT analysis of source voltage, load current, and source current with BePANN

It is seen in Fig. 3.31, that the THD of source voltage, load current, and source current are 0.09%, 32.88%, and 2.21% respectively with the BePANN control scheme.

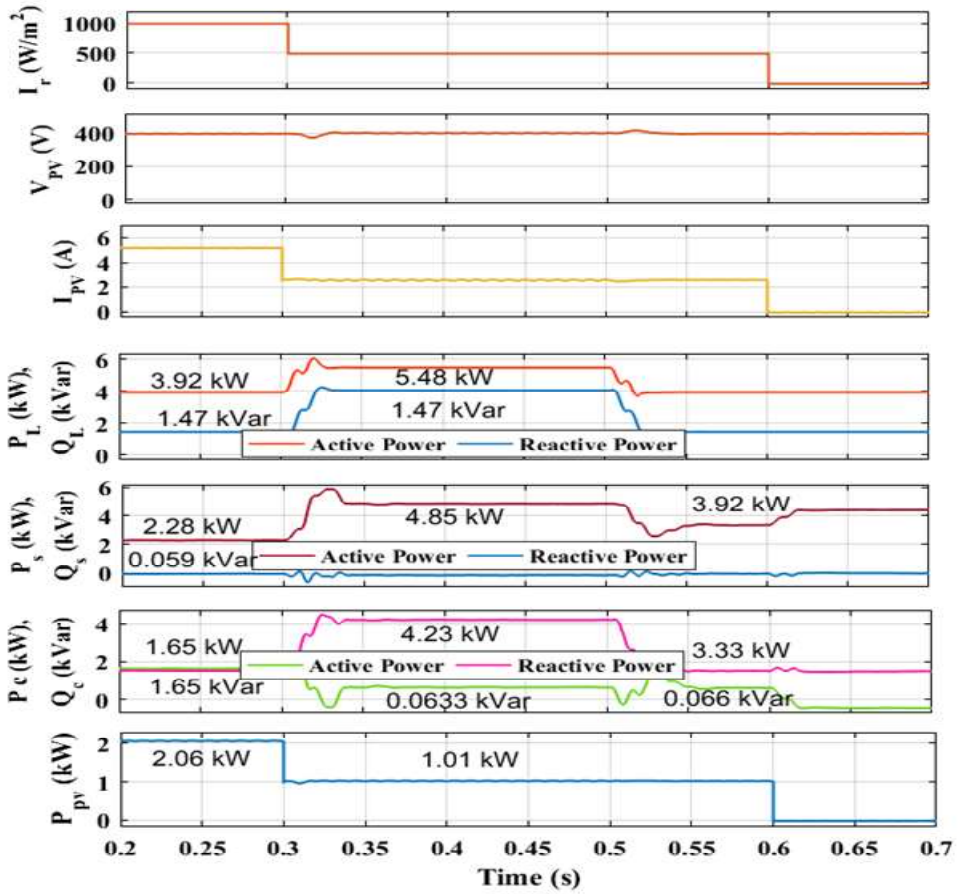

Fig. 3.32 Dynamic Performance analysis under varying solar irradiance with BePANN.

The performance of the proposed system under varying solar irradiance is shown in Fig. 3.32. The solar PV irradiance is 1000W/m^2 at t=0.2 to 0.3s. During 1000W/m^2 irradiance, the PV array current, and voltage at 400V and 5.1A respectively. The PV current decreases when solar irradiance decreases to 500W/m^2. The active and reactive power demand of load are 5.48kW and 1.47kVar respectively, where 1.01kW of active power demand is fulfilled by solar PV and the remaining power of 4.47kW is fed by source power. The reactive power demand of load is fully provided by VSC. At t=0.6s, night condition is created by maintaining solar irradiance to zero. During night conditions, the load's active power demand is provided by grid while the VSC provides the reactive power demand of the load.

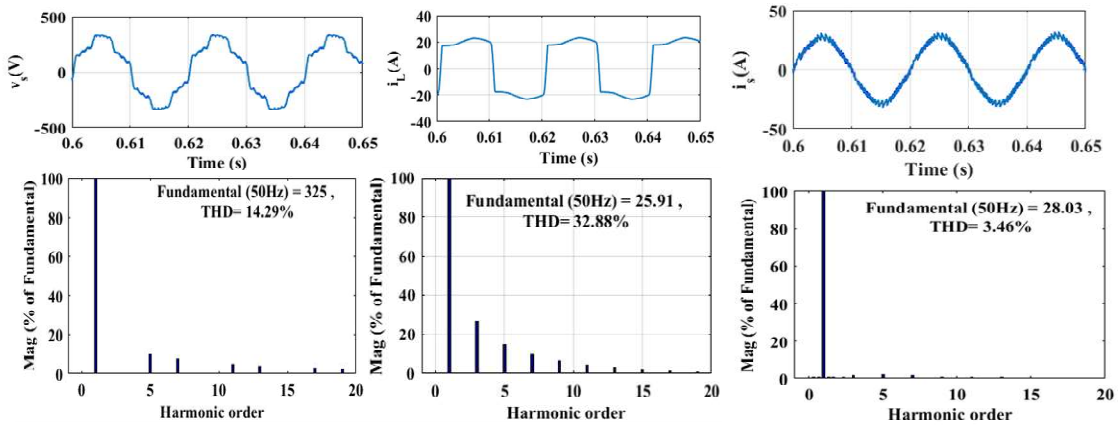

(a) (b) (c)

Fig. 3.33 FFT analysis of source voltage, load current, and source current under distorted grid condition with BePANN

The THD of the source voltage, load current, and source current under distorted grid conditions with the BePANN control scheme are 14.29%, 32.88%, and 3.46% which is under IEEE-519:2014 standards as shown in Fig.3.33. This FFT analysis shows the effectiveness of the proposed control scheme under normal, varying solar irradiance and distorted grid.

The intermediate waveforms of the proposed system with the BePANN control scheme under load change conditions are shown in Fig. 3.34. The load increased at t=0.3s, due to which load current (i_L), load current expansion component through Bernoulli's Polynomial (I_{L0}, I_{L1}, I_{L2}) get increased. The calculated error (e) and weight (W), and estimated fundamental load component (I_{Lest}) are shown in Fig. 3.34. The adaptive LMS algorithm is used to update the weight (W) of the load component with the change in load or any other variations in the system. The step size (μ) is chosen as 5e-6. The load current is scaled down by 0.01 for easy operation.

3.4 Experimental Results

The hardware prototype of a single-phase grid-connected non-linear load system developed in the lab using dSPACE 1104 with and without PV interfaced systems is discussed in this section along with the experimental results of the developed system with Synchronous Reference Frame Theory (SRFT), Instantaneous reactive power theory (IRPT), Hermite function-based ANN (HeANN), and Bernoulli Polynomial based ANN (BePANN) based controller for SAPF. A 300W maximum power Chroma EN50530 PV array is connected to the inverter's DC connection. Results for the hardware are obtained

using a power analyzer and a DSO. To evaluate the efficacy of these control algorithms, performance analysis is carried out under various non-linear, and mixed loading circumstances.

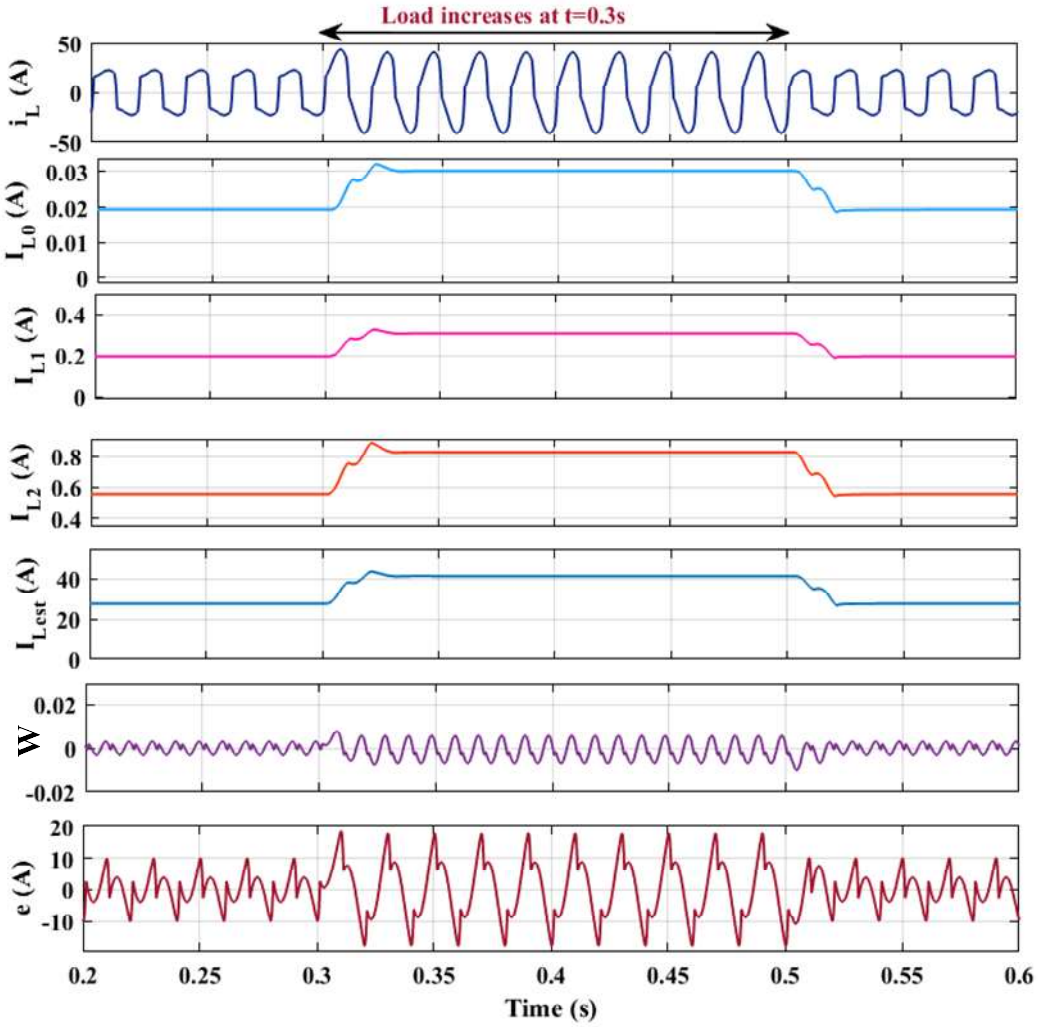

Fig. 3.34 Intermediate waveform of proposed BePANN controller under load change.

3.4.1 Performance Analysis with SRFT control scheme

The single-phase shunt APF is experimentally at 40V, 50Hz supply feeding both linear and nonlinear loads. The conventional SRFT control is utilized for extracting fundamental load current and generating the switching signals. The SRFT-based control scheme is modeled in dSpace 1104 on a hardware prototype developed on single-phase grid-connected systems. The steady-state performance of grid-connected SAPF with SRFT control scheme is shown in Fig. 3.35. The waveforms of source voltage, source current, and load current are shown in Fig. 3.35(a-b). The THD of source voltage, source

current, and load current are 1.84%, 4.9%, and 32.45% respectively shown in Fig. 3.35(c-d)

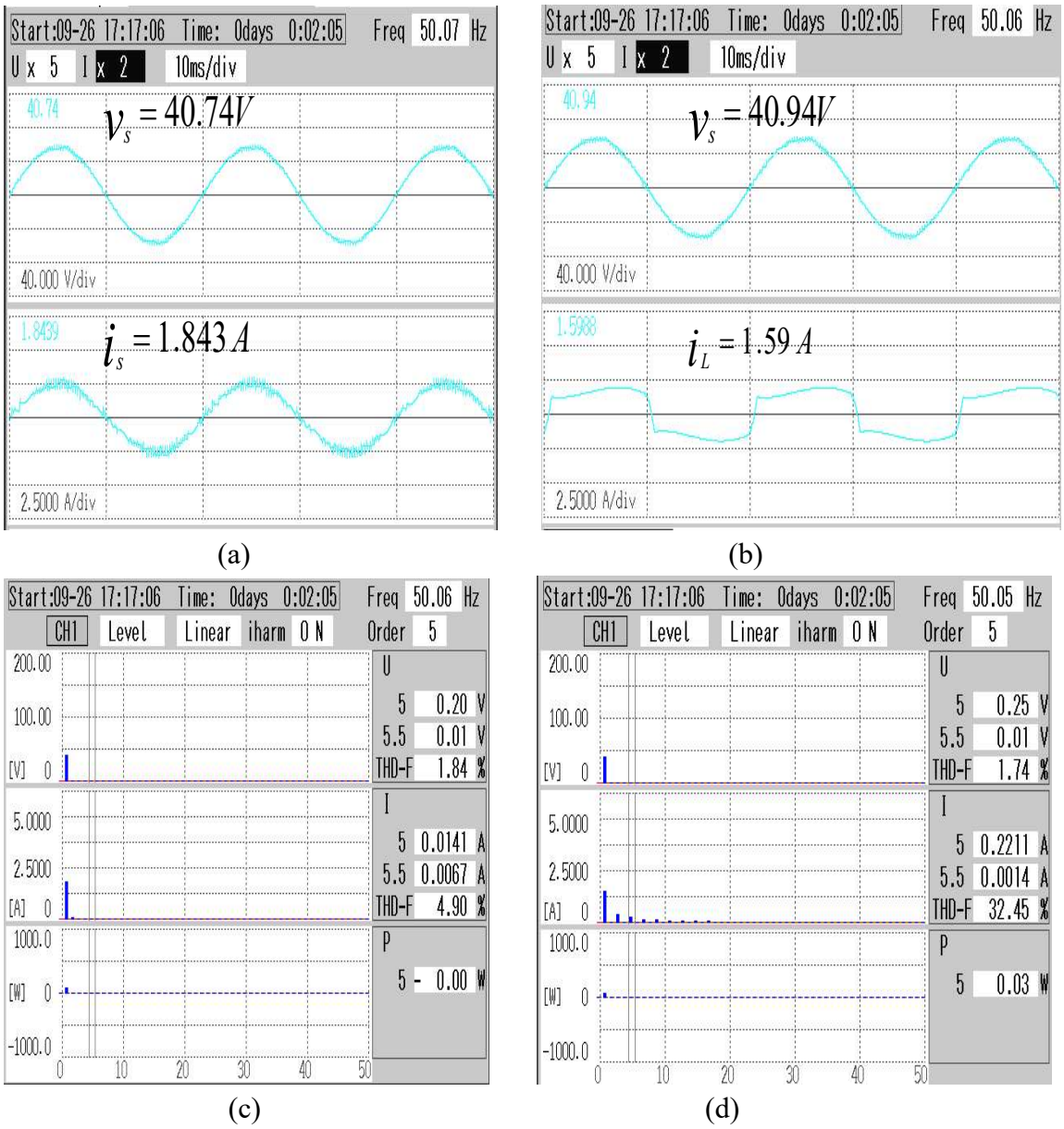

Fig. 3.35 Steady state performance analysis of SRFT controller under nonlinear load (a) waveform of source voltage (v_s) and source current (i_s) (b) waveforms of source voltage (v_s) and load current (i_L) (c) THD of source current (b) THD of load current

The load requires an active power of 60.32W and a reactive power of 25.95Var. The load active power demand is fulfilled by source active power which is 72.64W. The remaining source active power 12.32W meets the switching losses. The reactive power demand of the load is met by the compensator's reactive power as shown in Fig.3.36.

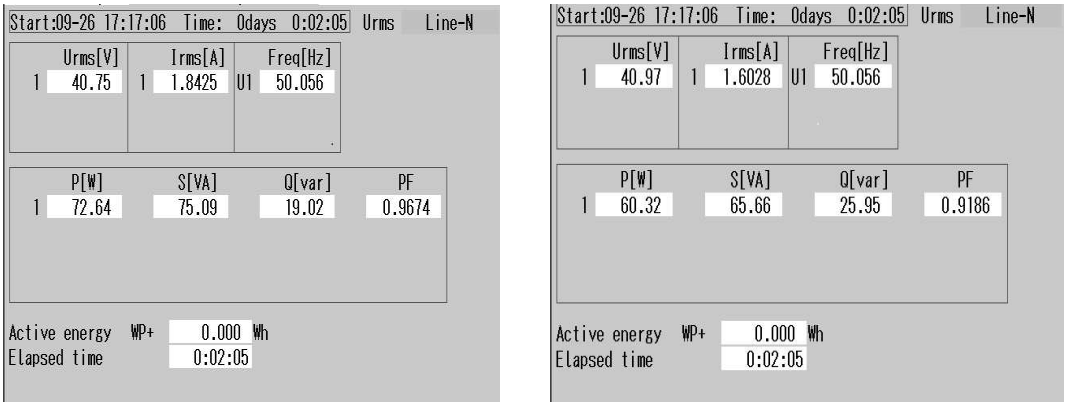

(a) (b)

Fig. 3.36 Steady-state power analysis of SRFT controller with nonlinear load (a) source side power (b) load side power

The dynamic performance of the SRFT control scheme is shown in Fig. 3.37. Initially, only nonlinear loads are connected to the system. The source voltage (v_s) and source current (i_s) are in the same phase. The DC link voltage is regulated to 80V. At some instant of time, linear loads are included, which also increases the source current and slight change in DC link voltage. The source current increases to fulfill the load active power demand as shown in Fig. 3.37(a). The reference source current (i_s^*) generated through the SRFT control scheme is compared with the actual source's current (i_s) to get the switching signals for IGBTs' switches. The compensating current (i_{cc}) is also increased with the load increase as shown in Fig.3.37(b).

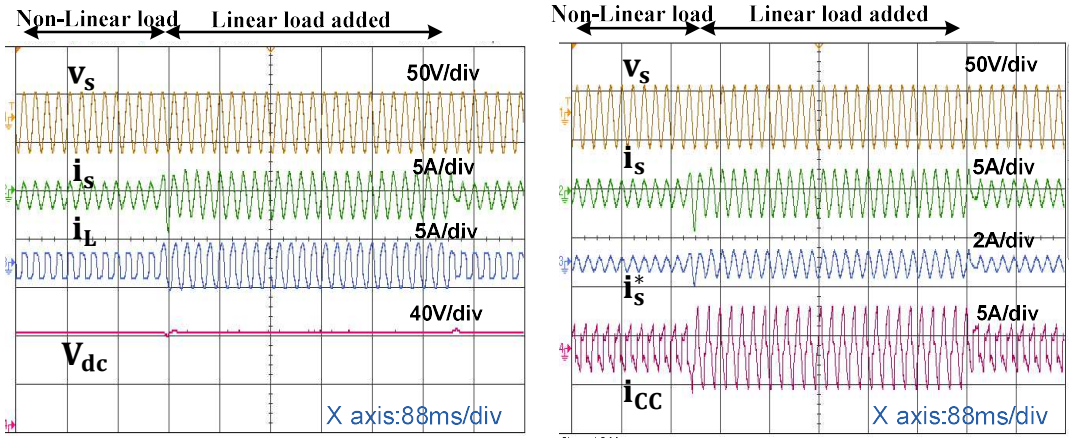

(a) (b)

Fig. 3.37 Dynamic performance of the proposed system with conventional SRFT control scheme under load change (a) Experimental waveforms of source voltage (v_s), source current (i_s), load current (i_L) and DC link voltage (V_{dc}) (b) v_s, i_s , i_s^*, and compensating current (i_{cc}).

The intermediate signals with an increase of load with the SRFT control scheme are shown in Fig. 3.38. The fundamental active component of load current (I_{FD}) is also

increased. The total current is increased (I_{Fund}) with an increase in load. The synchronizing signal (sinθ) is obtained through conventional PLL. The synchronizing signal is the sinusoidal during load change.

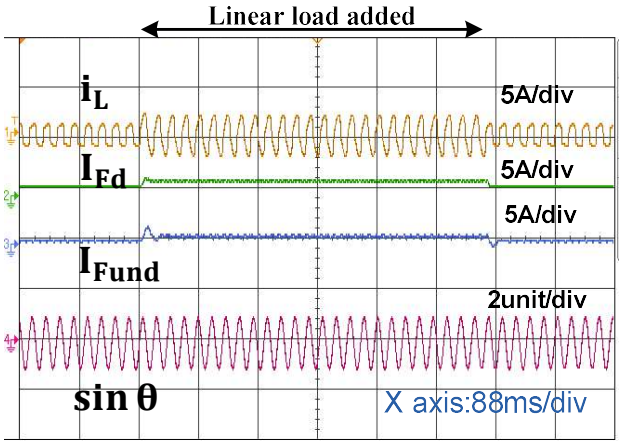

Fig. 3.38 Intermediate signals of SRFT control scheme under load change.

3.4.2 Performance Analysis with IRPT control scheme

The steady-state performance of the proposed single-phase grid-connected PV system with the IRPT control scheme is shown in Fig.3.39(a-d). The source voltage and source current are in the same phase with a magnitude of 40.7V and 1.83 A respectively. The load current has a THD of 32.45%, while the THD of the source current is 4.72% which is under IEEE-519 standards.

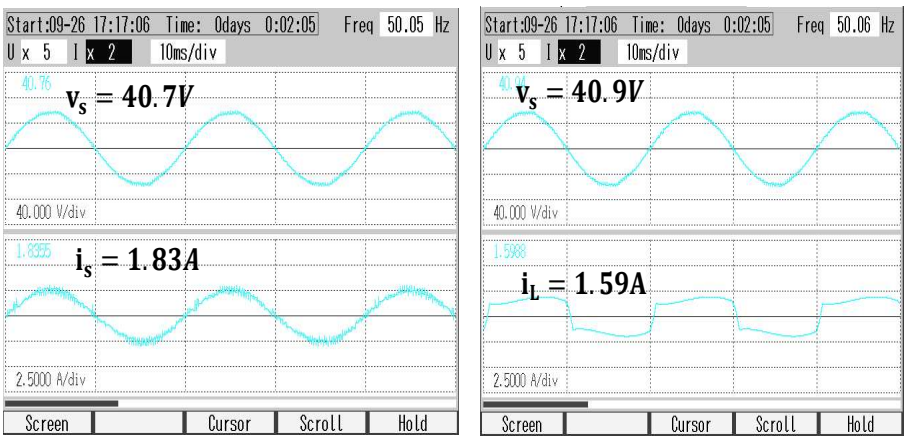

(a) (b)

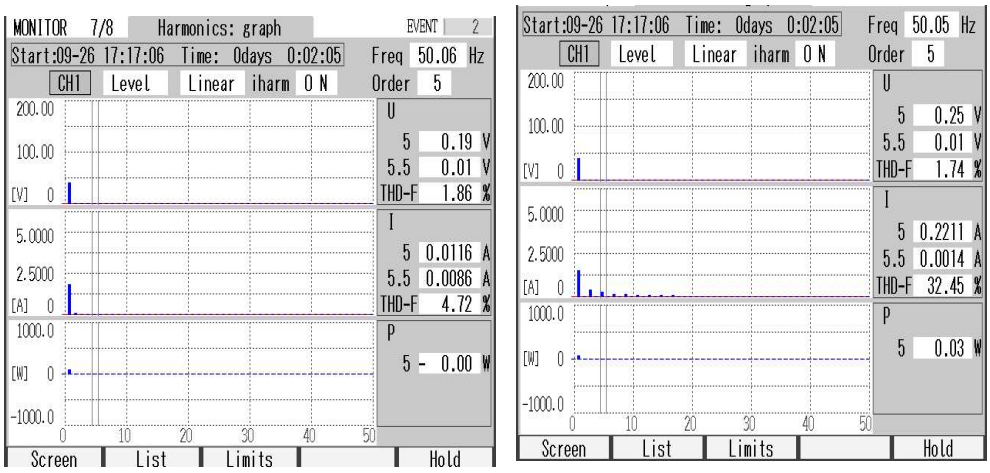

(c) (d)

Fig. 3.39 Steady state performance analysis of IRPT controller under nonlinear load (a) waveform of source voltage (v_s) and source current (i_s) (b) waveforms of source voltage (v_s) and load current (i_L) (c) THD of source current (b) THD of load current

The dynamic performance of the proposed system with IRPT control scheme is given in Fig. 3.40. At some instant of time the load is disconnected from the system, thus source current decreases to maintain the constant source power supply. The signals source voltage (v_s), source current (i_s), compensating current (i_{cc}), and DC link voltage (V_{dc}) is shown in Fig 3.40 (a) under the condition of load disconnect. The DC link voltage is maintained at its reference voltage (80V) with the PI voltage controller. The reference source's current i_s^* is in the same phase as the sensed source current, and VSC supplies the compensating current with load change as shown in Fig.3.40(b). The intermediate signals of the IRPT control scheme are shown in Fig. 3.40(c). The fundamental active power (P^*), reactive power (Q^*), and alpha-beta current components (i_α^*, i_β^*) are increasing with the increase of connected load.

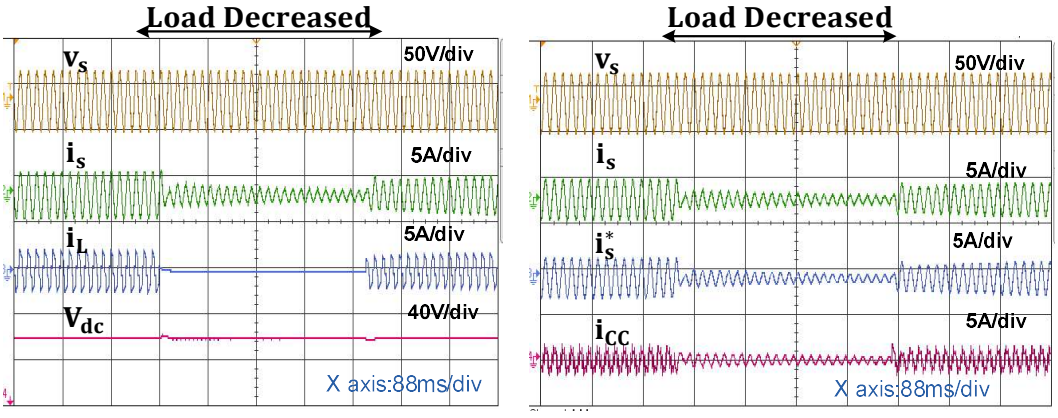

(a) (b)

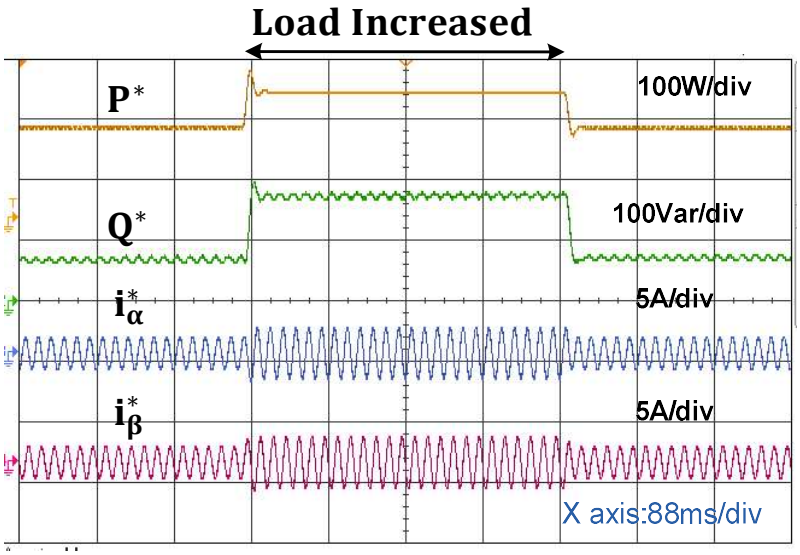

(c)

Fig. 3.40 Dynamic Performance analysis with IRPT control scheme with the waveforms of (a) v_s, i_s, i_L and V_{dc} under load disconnection (b) v_s, i_s, i_s^* and i_{cc} under load disconnection (c) intermediate signals P^*, Q^*, and i_α^*, i_β^* of IRPT control under load-increased conditions.

3.4.3 Performance Analysis with HeANN control scheme

Fig. 3.41 (a) shows the waveform source voltage and source current (v_s and i_s) under steady-state conditions, both are in the same phase. The THD in the source current is 4.33% which is under IEEE-519 standards, while the source voltage's THD is 0.17% as shown in Fig.3.41 (b). Also, the waveforms of source voltage and load current (v_s and i_L) is given in Fig. 3.41(c) having magnitude of 40.57V and 2.3A. The THD of load current is 33.58%. The THD of source current without compensation is almost equal to the THD of load current and it decreases to 4.33% with SAPF compensation of the proposed system.

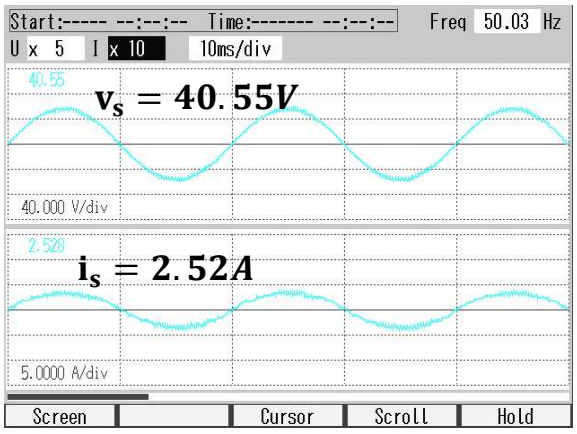

(a)

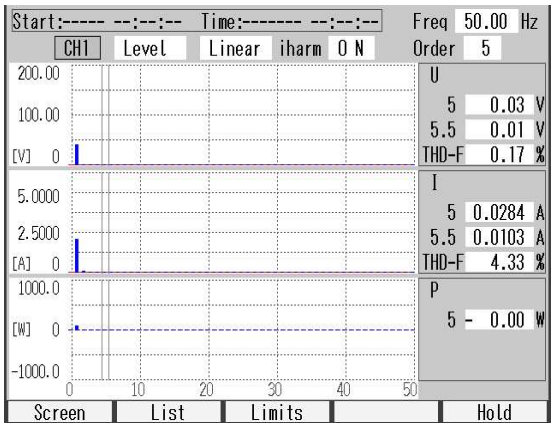

(b)

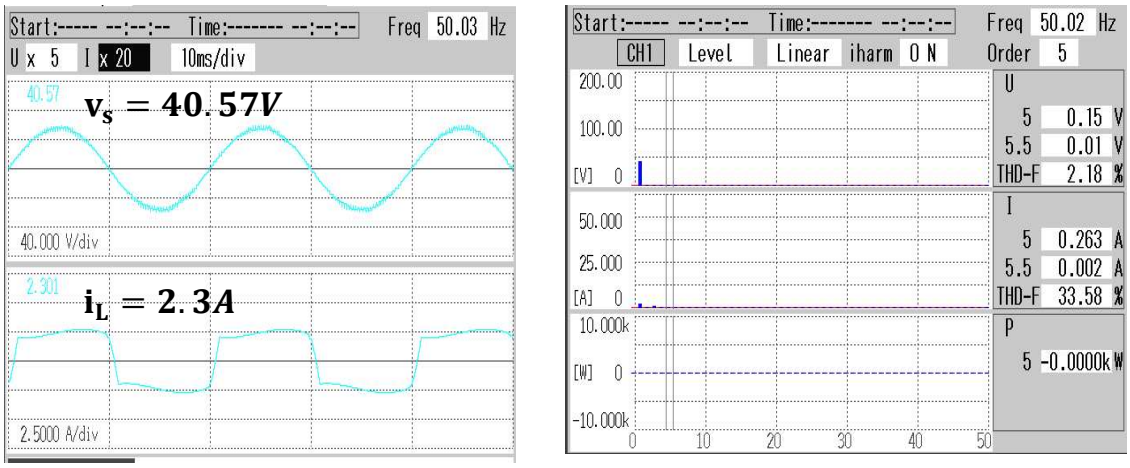

(c) (d)

Fig. 3.41 Steady state performance analysis of HeANN controller under nonlinear load (a) waveform of source voltage (v_s) and source current (i_s) (b) THD of source current (c) waveforms of source voltage (v_s) and load current (i_L) (d) THD of load current without PV interconnection

The power analysis of the proposed system under HeANN control algorithm is shown in Fig. 3.42. The load active power demand is 93.7W and reactive power demand is 38.1 Var. The grid generates active power of 99.4W which is given to load to fulfil load active power demand. The VSC produces compensating current which can fulfil the reactive power demand of load, and meet switching losses. The power factor of the source side is 0.96.

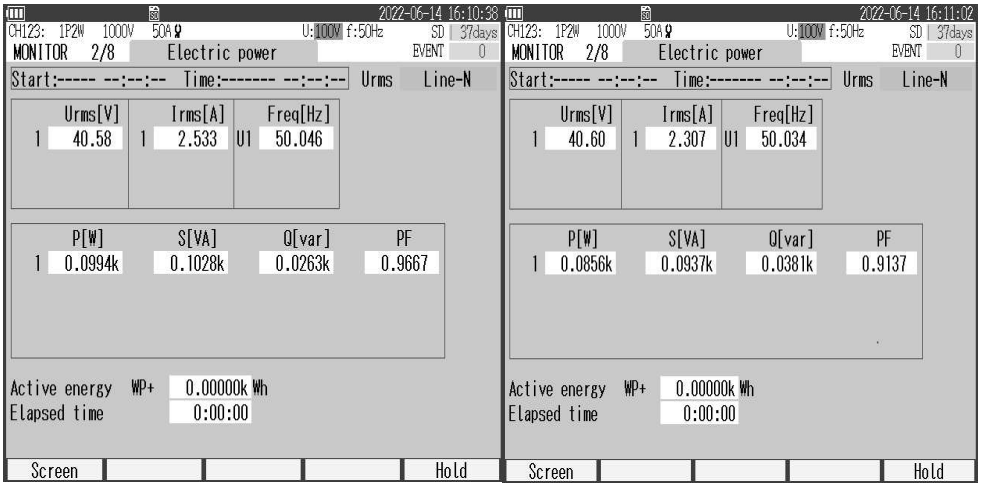

(a) (b)

Fig. 3.42 Power Analysis of the proposed system under steady-state conditions (a) grid power (b) load power

The performance of the proposed control algorithm under PV and grid integration is shown in Fig. 3.43 (a). The signals v_s, i_s, i_L, V_{dc} are shown in Fig. 3.43(a) when PV is connected with the system and load is also decreased. The source current is out of phase

which indicates that the PV array delivers active power to load and in case of any surplus power, it is fed to the grid. The DC-link voltage is increased to support the active power transfer to the system through a PV array. The PV simulator used in the proposed system is Chroma 62100H-600s which feeds 100 W approximately. It is observed that the load requires 33.5W of active power and 12.1Var of reactive power. After fulfilling the load demand the remaining power of PV is given to the grid which is 44.3W and the switching losses of the VSC which is 22.2W. The Power analysis under PV and grid integration is shown in Fig. 3.43(c-d).

The dynamic performance of the proposed controller is tested under load increment. Fig. 3.44(a) shows the waveform of signals v_s, i_s, i_L and V_{dc}. When the load increases, the source current increases to fulfill the load's active power demand. At the same time, the DC-link voltage is slightly decreased but after some time it will come to its reference value. In Fig. 3.44(b), the intermediate signals of the LMS weight updating method are shown. The fundamental load average current ($I_{LF(avg)}$), weight (W), and error (e) signals increase as the load increases. The intermediate signals of HeANN load compensation are shown in Fig. 3.44(d) with the load increases. The signals $I_{LF(avg)}$,I_{L0},I_{L1}, are fundamental load average current, first load current expansion term, and second load current expansion term obtained through Hermite Expansion respectively.

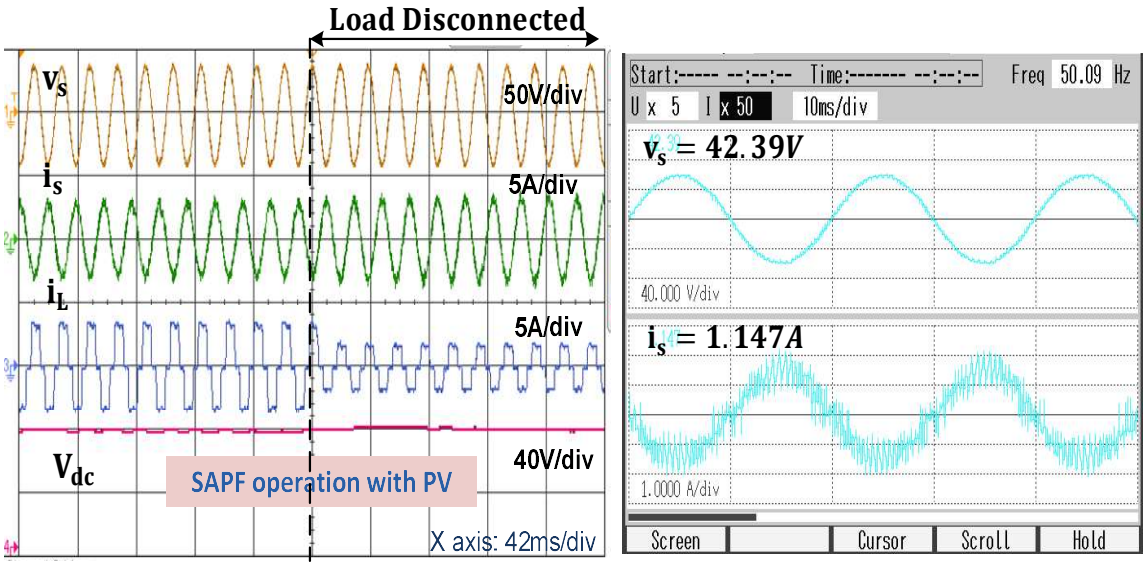

(a) (b)

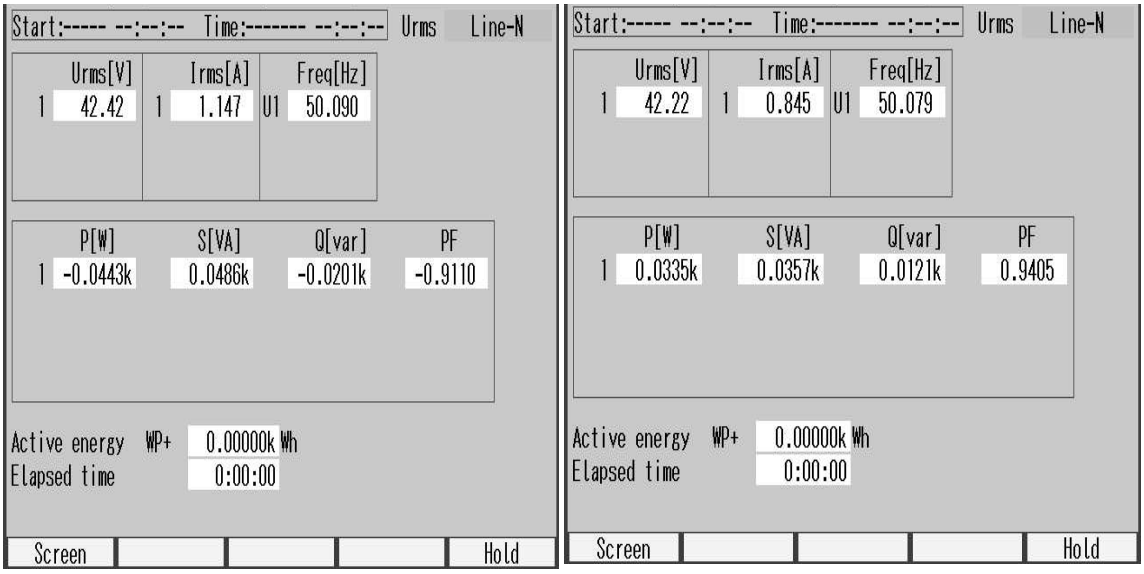

(c) (d)

Fig.3.43 Performance analysis of the proposed system with PV integration (a) Waveforms of v_s, i_s, i_L and V_{dc} in DSO (b) waveform of v_s, i_s in Power analyser (c) source power (d) load power

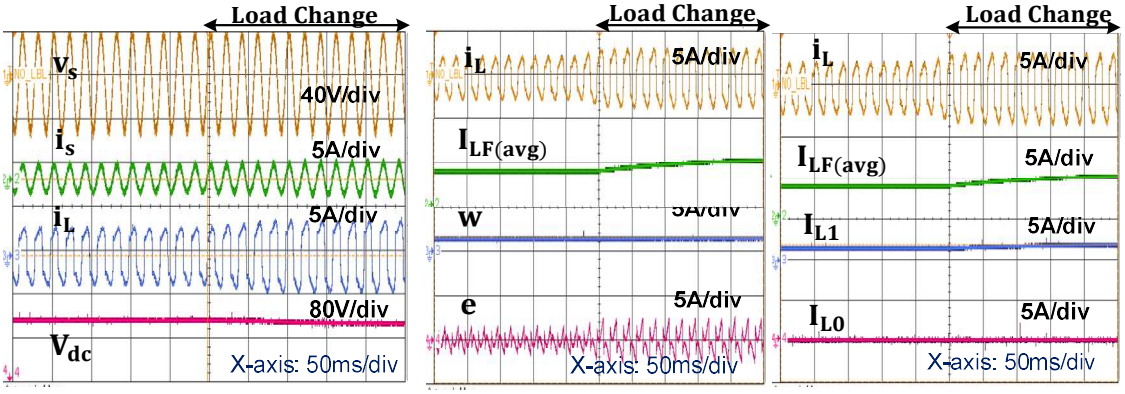

(a) (b) (c)

Fig. 3.44 Dynamic Performance of the Proposed system under load change with HeANN control algorithm (a) Experimental waveforms of supply voltage (v_s), source current (i_s), load current (i_L) and DC link voltage (V_{dc}) (b)Intermediate signals of HeANN with waveforms of i_L, $I_{Lf(avg)}$, W, e (c) i_L, $I_{Lf(avg)}$, I_{L1}, I_{L0}.

3.4.4 Performance Analysis with BePANN control scheme

Fig. 3.45 (a) shows the waveform source voltage, source current (v_s and i_s) and source voltage, load current (v_s and i_L) under steady-state conditions. The THD in the source current is 4.20% which is under IEEE-519 standards, while the source voltage's THD is 0.16% as shown in Fig.3.45 (c). Also, the waveforms of source voltage and load current (v_s and i_L) having a magnitude of 40.57V and 2.3A. The THD of load current is 33.58%. The THD of source current without compensation is almost equal to the THD of load current and it decreases to 4.20% with SAPF compensation of the proposed system.

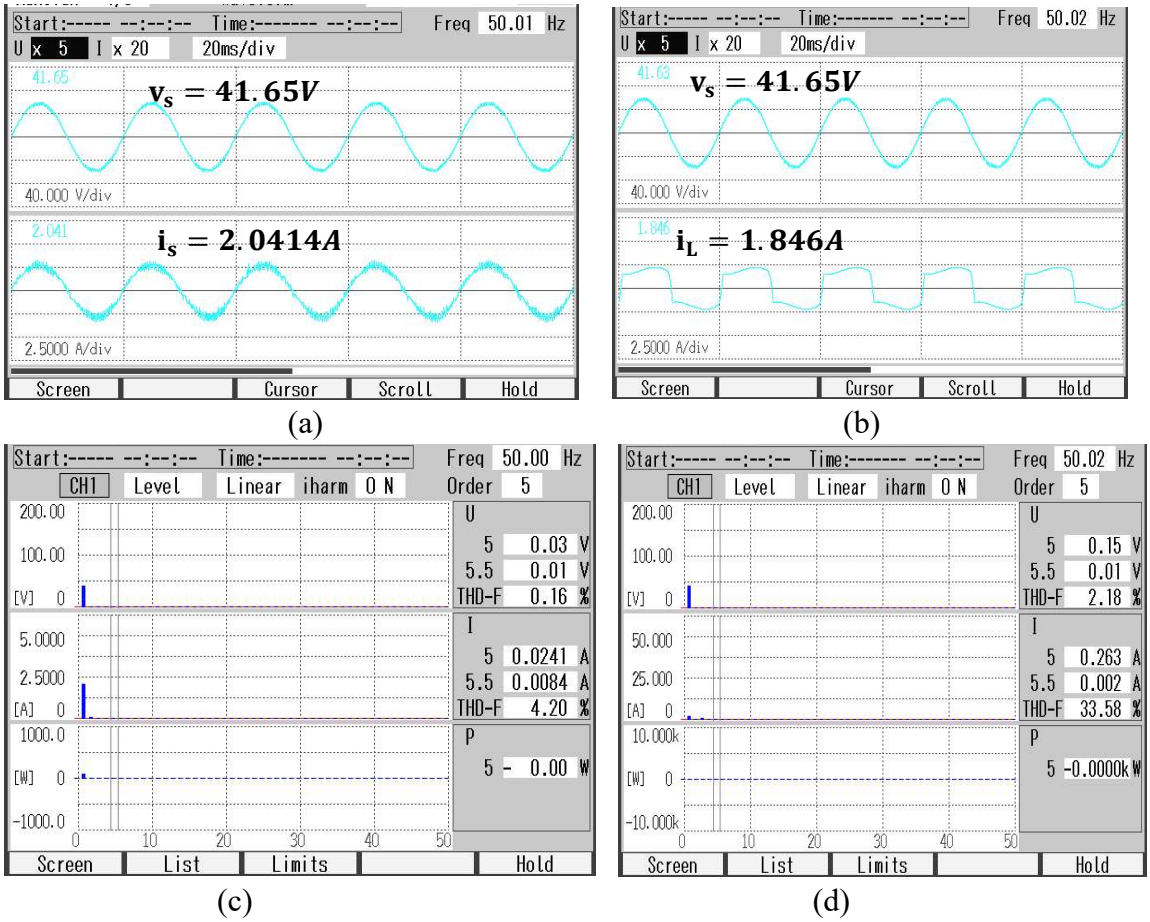

Fig. 3.45 (a) Waveform of signal (v_s *and* i_s) (b) Waveform of (v_s *and* i_L) (c) THD of source current (d) THD of load current with BePANN controller

The dynamic performance of the proposed single-phase SAPF with the BePANN control scheme is shown in Fig. 3.46 (a-d). At some instant of time load is increased due to which the source current increases. The total fundamental load current (I_{Lest}) is also increased with an increase in load current. The DC link voltage (V_{dc}) is maintained to its reference value with the effect of the PI controller as shown in Fig. 3.46 (a). It is also evident from Fig. 34.6(b) that PV is connected with the VSC. In this condition, the source current and source voltage have some phase shift and the load is decreased at some instant in time. The DC link voltage is maintained at a constant magnitude. Another set of signals such as source voltage, source current, load current, and DC link voltage with an increase in load are shown in Fig. 3.47(c). The compensating current (i_{CC}) is also increased to support reactive power compensation as shown in Fig. 3.46(d) with load increase condition.

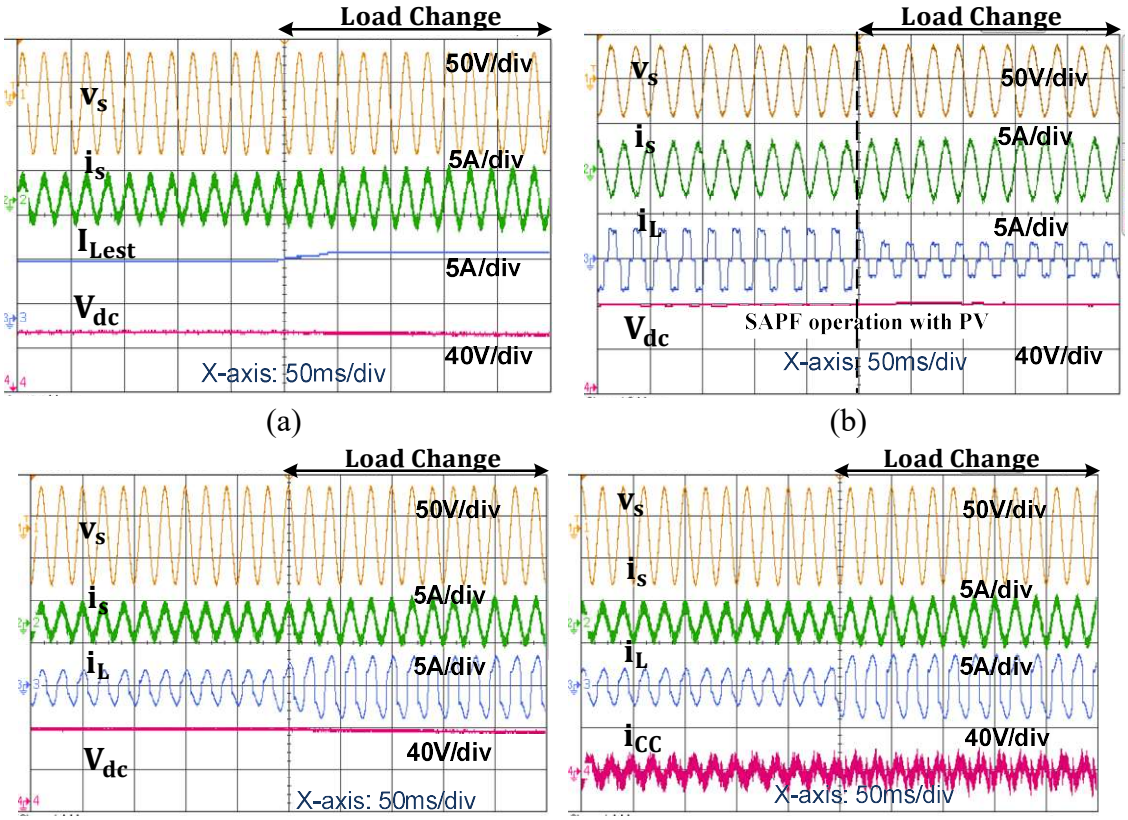

Fig. 3.46 Experimental waveforms of the proposed system with BePANN control scheme under (a) load change ($v_s, i_s, I_{Lest}, V_{dc}$) (b) with PV integration (v_s, i_s, i_L, V_{dc}) (c) load change (v_s, i_s, i_L, V_{dc}) (d) load change (v_s, i_s, i_L, i_{CC})

3.5 Comparative Performance analysis of control schemes of single-phase shunt active power filter

The performance of the BePANN is contrasted with that of methods called SRFT, IRPT, and HeANN control technique. These methods are all used for load compensation under the same system parameters. From each algorithm, the fundamental active load component under load change conditions is extracted and compared for weight convergence in terms of oscillations, sampling time, PLL needs, settling time, convergence rate, and THD in source current. Table 3.4 and Fig. 3.47 are displayed to provide a more accurate comparison of performance.

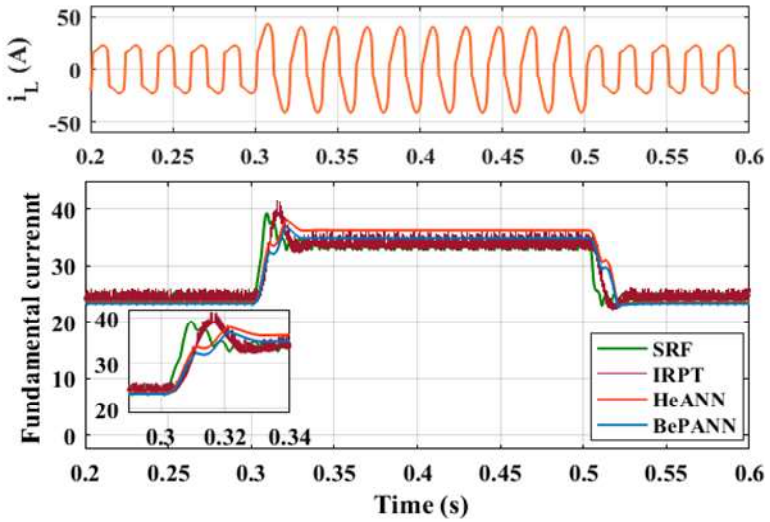

Fig. 3.47 Simulation-based Performance comparison of fundamental current under varying load during t=0.3s to 0.5s with SRFT, IRPT, HeANN, and BePANN

Table 3. 4: Comparison of SRFT, IRPT, HeANN and BePANN Control Schemes

S.No.	**Features**		**SRFT**	**IRPT**	**HeANN**	**BePANN**
1.	PLL Required	Normal and load change	Required	Required	Not Required	Not Required
		Distorted Grid	Required	Required	Required	Required
2.	Transformation required		Yes	Yes	No	No
3.	Convergence		Slower ($3\sim4\ cycles$	Slower (3 $\sim4\ cycles$	**Faster** (1 $\sim2\ cycles$)	**Faster** (1 $\sim2\ cycles$)
4.	Oscillations in fundamental weights		More	More	No	No
5.	THD of current (Simulation)	Source Current	4.09%	5.33%	**2.77%**	2.88%
		Load Current	32.88%	32.88%	32.88%	32.88%

6.	THD of current (Experimental)	Source Current	4.90%	4.72%	4.33%	**4.20%**
		Load Current	32.45%	32.45%	33.58%	33.58%
7.	Error		Moderate	More	Less	Less
8.	DC link voltage oscillations		4V to 5V	4V to 4.5V	2V to 3V	2V to 3V
9.	Sampling time		$60\mu s$	$60\mu s$	$50\mu s$	$50\mu s$

It is seen from Table 3.4, that the proposed HeANN and BePANN control schemes perform much better than conventional SRFT and IRPT control schemes for the proposed single-phase grid-connected PV system. All the mentioned control schemes can mitigate current related PQ issues and perform reactive power compensation. The THD of source current with proposed BePANN with experimental setup is 4.20%, and 2.77% with HeANN in simulation performance. The Convergence of fundamental load components under load change is faster with HeANN and BePANN around 1 to 2 cycles as compared to SRFT and IRPT.

3.6 Conclusion

This chapter focuses on the design and implementation of four control algorithms for shunt compensation in PV integrated single-phase grid-connected systems: SRFT, IRPT, HeANN, and BePANN controllers. Both experimental setup in the lab and models created using Matlab Simulink are used to test the performance. Variations in solar irradiation and load changes are addressed in the performance study. The functional NN algorithms' performance compared with that of the conventional algorithms such as SRFT and IRPT. Since the proposed HeANN and BePANN algorithms are based on functional series expansion, they are easy to use and need less processing power. It has been determined that a few terms from these expansion series are adequate and appropriate. Moreover, these functional NNs have been made adaptive. The LMS algorithm performs the algorithms' real-time training. PLL synchronisation and Park-Clark transformation techniques, which are required for conventional techniques like SRFT, are no longer necessary. To achieve the optimal response, the SRFT and IRPT algorithms need transformation blocks and gain constant adjustment. Lastly, the tracking performance of

each algorithm under dynamic load variations is examined in order to carry out a fair comparison of all the methods. The THD of source current with proposed BePANN with experimental setup is 4.20%, and 2.77% with HeANN in simulation performance. The performance of the newly proposed HeANN and BePANN algorithms is better for SAPF operation. Furthermore, under PV integration, these methods function quite satisfactorily.

CHAPTER 4

DESIGN AND CONTROL OF THREE-PHASE SHUNT ACTIVE POWER FILTER FOR GRID CONNECTED PV SYSTEM

4.1 Design of three-phase grid-connected shunt active power filter

The three-phase grid-connected PV system is utilized to mitigate current harmonics and reactive power compensation. Harmonic currents may penetrate the electrical system through non-linear loads like rectifiers, variable frequency drives, and other power electronic equipment. Harmonics can cause equipment overheating, voltage distortions, and interference with sensitive electronics. The detrimental impacts of harmonics can be successfully reduced by SAPF, which can detect and inject equal and opposite harmonic currents to cancel out the harmonics. The capacity of conventional power factor correction techniques, such as capacitors and inductors, to offer reactive power compensation under variable and non-linear load situations is constrained. A SAPF may change the injected reactive current to match the system requirements and maintain the appropriate power factor. This allows for dynamic reactive power compensation control.

Unbalanced loads can result in an unequal distribution of power among the phases in three-phase systems. Voltage imbalances, greater losses, and decreased system effectiveness may result from this. To balance the loads over the three phases, a SAPF can track load imbalances and inject the proper current. The system configuration of a three-phase single-stage grid-connected PV system is shown in Fig. 4.1. The PV array is connected to a DC link capacitor without a DC-DC converter. An MPPT technique is required to obtain the reference DC link voltage. A VSC is connected in parallel with the nonlinear load. The VSC is responsible for generating the compensating current and fed into the grid. These compensatory currents are produced by the VSC and have the same amplitude and the opposite phase as the harmonic grid currents. The SAPF effectively balances out the harmonic currents by injecting these compensatory currents into the grid, producing a smoother sinusoidal current waveform.

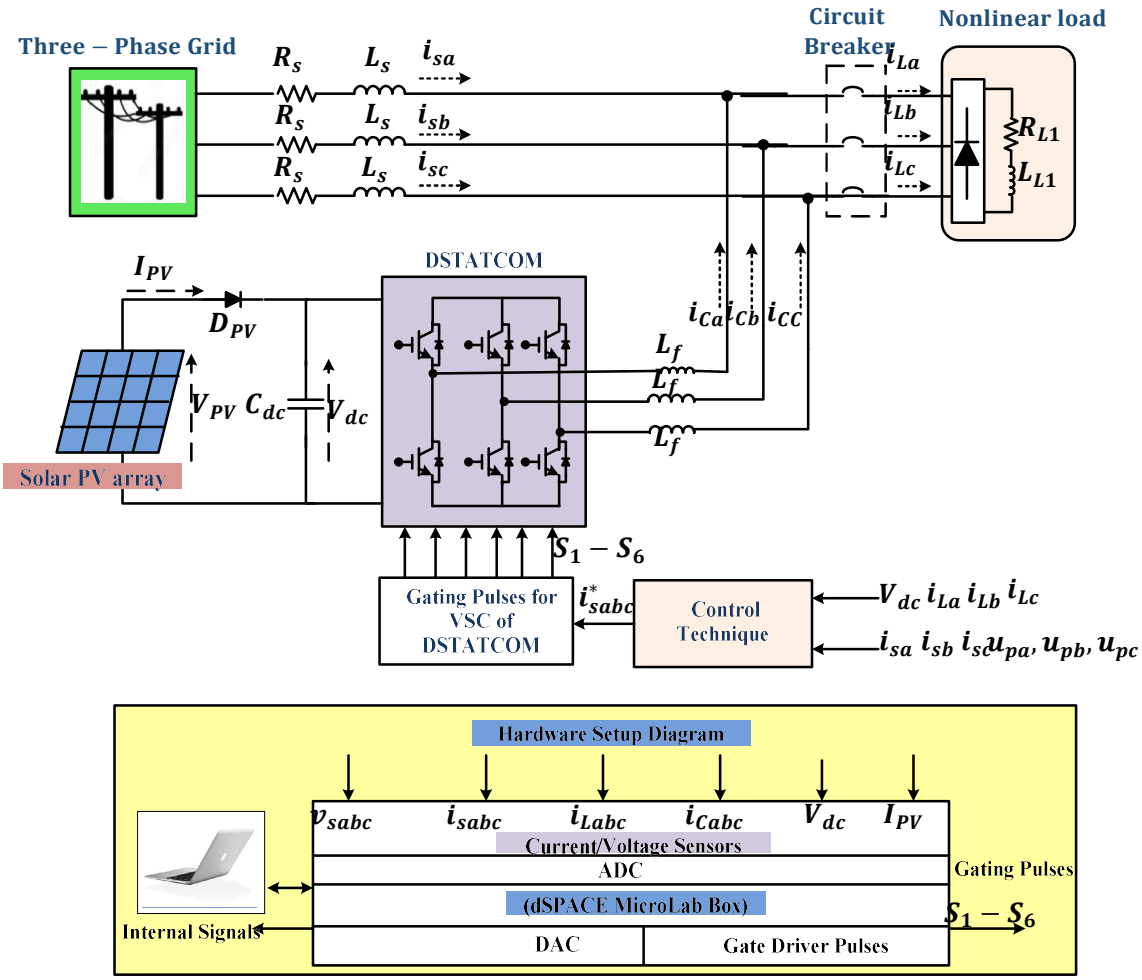

Fig. 4.1 Proposed three-phase grid-connected PV SAPF system

4.1.1 Calculation of DC link voltage

The supply voltage for simulation is considered as 400V (v_{L-L}) at 50Hz frequency, while for experimental validation the supply voltage is chosen 40V (v_{L-L}), 50Hz. The DC link voltage is calculated [69] using Eq. (3.19),

$$V_{dc(ref)} > V_{dc(min)} = \frac{2\sqrt{2}}{\sqrt{3}} v_{L-L} = \frac{2\sqrt{2}}{\sqrt{3}} \times 400 = 653.19V \quad (4.1)$$

The reference DC link voltage $V_{dc(ref)}$ should be greater than the minimum DC link voltage $V_{dc(min)}$, and thus it is considered 800V for simulation. The experimental DC link voltage is calculated using Eq. (4.2),

$$V_{dc(ref)} > V_{dc(min)} = \frac{2\sqrt{2}}{\sqrt{3}} v_{L-L} = \frac{2\sqrt{2}}{\sqrt{3}} \times 40 = 65.31V \quad (4.2)$$

The reference DC link voltage $V_{dc(ref)}$ should be greater than the minimum DC link voltage $V_{dc(min)}$, and thus it is considered 80V for experimental setup.

4.1.2 Calculation of DC link capacitor

The designed value of the DC link capacitor [69] is calculated using Eq. (4.3),

$$C_{dc} = \frac{6k_1 v_{ph} a i_{cc} \tau}{V_{dc(ref)}^2 - V_{dc(min)}^2} = \frac{6\times0.4\times230.94\times1.2\times25\times0.02}{(800^2 - 653.19^2)} = 1558.7\mu F \quad (4.3)$$

where, $V_{dc(ref)}$ is the DC link bus voltage, $V_{dc(min)}$ is the minimum DC link voltage, τ is the time constant, a is the overloading factor, k_1 is the gain constant and i_{cc} is the VSC's compensating current. Let $a = 1.2$, $i_{cc} = 25A$, $V_{dc(ref)} = 800V$, $V_{dc(min)} = 653.19\,V$, $\tau = 0.02s$, and $k_1 = 0.4$. The value of DC-link capacitance $C_{dc} = 1558.7\ \mu F$ and it is chosen as 1650 µF (simulation).

4.1.3 Calculation of Interfacing Inductor

The interfacing inductor plays an important role in harmonic filtering and provides isolation between the PV array and the grid. Due to variable solar irradiation and other environmental factors, the output of the PV array may exhibit various variations and harmonics. These variations are filtered by the interface inductor, which also lowers the harmonic content of the current supplied into the grid. The value of the interfacing inductor can be calculated using Eq. (4.4),

$$L_f = \frac{\sqrt{3} m V_{dc(ref)}}{12 a f_{sw} \Delta I_{cr}} \quad (4.4)$$

Here, 'L_f' is the interfacing inductor, 'm' is the modulation index, 'f_{sw}' is the switching frequency and ΔI_{cr} is the current ripple which is considered 5% of the maximum current. The value of L_f for simulation is calculated by (4.5) and for experimental setup, it is calculated by (4.6).

$$L_f = \frac{\sqrt{3} m V_{dc(ref)}}{12 a f_{sw} \Delta I_{cr}} = \frac{\sqrt{3}\times1\times800}{12\times1.2\times10\times1000\times1.5} = 7.6mH \quad (4.5)$$

$$L_f = \frac{\sqrt{3} m V_{dc(ref)}}{12 a f_{sw} \Delta I_{cr}} = \frac{\sqrt{3}\times1\times80}{12\times1.2\times10\times1000\times1.5} = 0.76mH \quad (4.6)$$

4.1.4 Design of PV array

There is no DC-DC boost converter in a single-stage PV system. The voltage of the PV array should be higher than the voltage of the voltage source converter (VSC)'s reference DC link. The highest voltage at MPP and reference DC voltage of the PV

array must be produced by the MPPT method. Eq. (4.7) calculates the necessary minimum number of series-connected PV modules.

$$N_S = \frac{V_{dc(min)}}{V_{mp}} = \frac{653.19}{37.73} = 17.31 \quad (4.7)$$

Thus, the number of series-connected PV modules selected is 22. The parameters of the PV string or array are given in Table 4.1.

Table 4.1: PV array Parameter at standard test condition (Zytech Engineering Technology ZT190S)

Parameters	Value
No. of series PV modules (N_S)	22
No. of parallel PV modules (N_P)	1
Maximum Power (P_{mp})	4184 W
Open circuit voltage (V_{OC})	986.9 V
Short circuit current (I_{SC})	5.5 A
Voltage at MPP (V_{mp})	830.1 V
Current at MPP (I_{mp})	5.04 A

4.1.5 Experimental Hardware setup

The prototype three-phase grid-connected PV inverter comprises grid current and voltage sensors viz. LEM-LA25P and LEM-LV25P. The sensors are used to sense the three-phase grid current, load current, compensating current, dc-link voltage, and grid voltage. The experimental setup is shown in Fig. 4.2. The dSPACE/Microlab Box consists of analog-to-digital conversion (ADC) and digital-to-analog conversion (DAC) pins. The sensor outputs are analog in nature and are to be converted into digital signals through an ADC port. The switching signals for VSC are generated by HCC. The PV simulator used in the experimental setup is Chroma 62100H-600S. The grid supply is fed by a three-phase variable AC supply. An external DC supply is utilized for supplying the sensors circuit and gating circuit. A Keysight digital storage oscilloscope (DSO) is used to monitor and capture the dynamic response of the system. The steady-state performance of the proposed system is monitored and captured through the Hioki power analyzer. A personal computer (PC) and MATLAB are used to build the model and dSPACE is used to process the control algorithm.

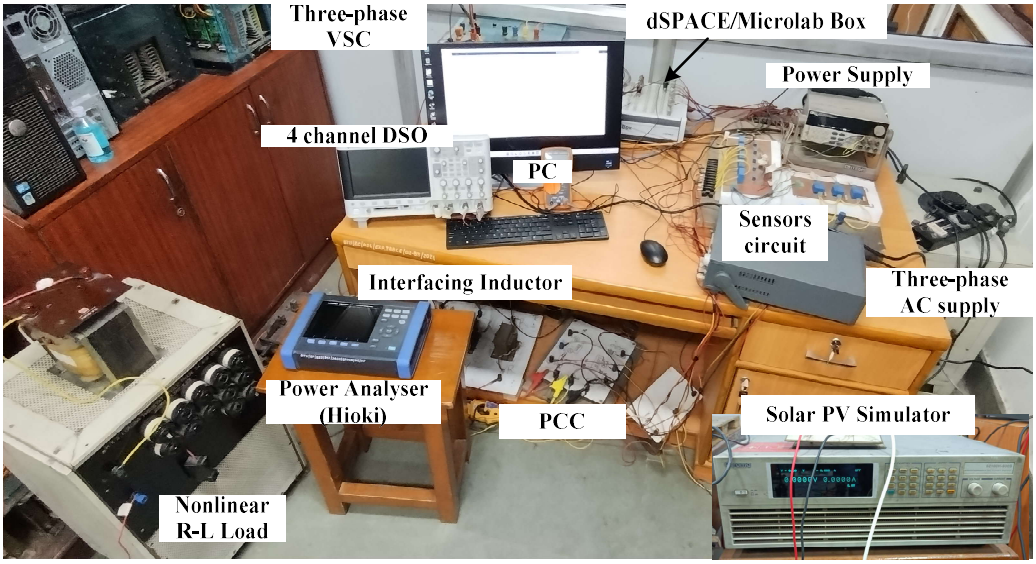

Fig. 4.2 Experimental Setup of a three-phase grid-connected PV system

4.2 Control Schemes for Three-phase grid-connected shunt active power filter

A three-phase shunt active power filter (SAPF) is used in a three-phase electrical system to reduce harmonic distortions, enhance power factor, and control voltage. To eliminate harmonic currents and enhance power quality, the control strategy for a three-phase SAPF typically encompasses detecting the load current, isolating harmonic components, and producing compensatory currents. Some of the conventional control schemes which are discussed below are Synchronous Reference Frame Theory (SRFT), ε −Normalized Sign Regressor Least Mean Mixed Norm (ε − NSRLMMN), and Quantum Least Mean Fourth (q-LMF). The below section describes the mathematical formulation and description of the conventional control technique.

4.2.1 Synchronous Reference Frame Theory (SRFT)

This technique is often used in distribution systems to improve power quality by compensating for reactive power and harmonics. In this context, the SRFT control scheme is used to generate a reference supply current for the DSTATCOM to mitigate the effects of nonlinear load currents. The control block mentioned below is responsible for generating switching signals for the three-phase Voltage Source Converter (VSC) of the DSTATCOM. These switching signals control the operation of the three-phase VSC to provide the required compensation and maintain the desired voltage and current waveforms.

Typically, the control block in an SRFT-based control scheme consists of controller that analyze the input signals (usually load current) and calculate the reference current components in the synchronous reference frame. These reference current components are then compared with the actual load current components in the same reference frame. The difference between the reference and actual current components is used to generate the control signals for the VSC, which will adjust its switching patterns accordingly to generate the required compensating currents. The three-phase nonlinear load current consists of balanced load components and harmonic components. The three-phase nonlinear load current of each phase is given in Eq. (4.8) to (4.10). The terms I_{Fund_a}, I_{Fund_b}, and I_{Fund_c} are the fundamental component of each phase of load current and $H_n(t)$ is the harmonic component.

$$i_{La}(t) = I_{Fund\_a}\sin(\omega t) + H_n(t) \tag{4.8}$$

$$i_{Lb}(t) = I_{Fund\_b}\sin\left(\omega t - \frac{2\pi}{3}\right) + H_n(t) \tag{4.9}$$

$$i_{Lc}(t) = I_{Fund\_c}\sin\left(\omega t + \frac{2\pi}{3}\right) + H_n(t) \tag{4.10}$$

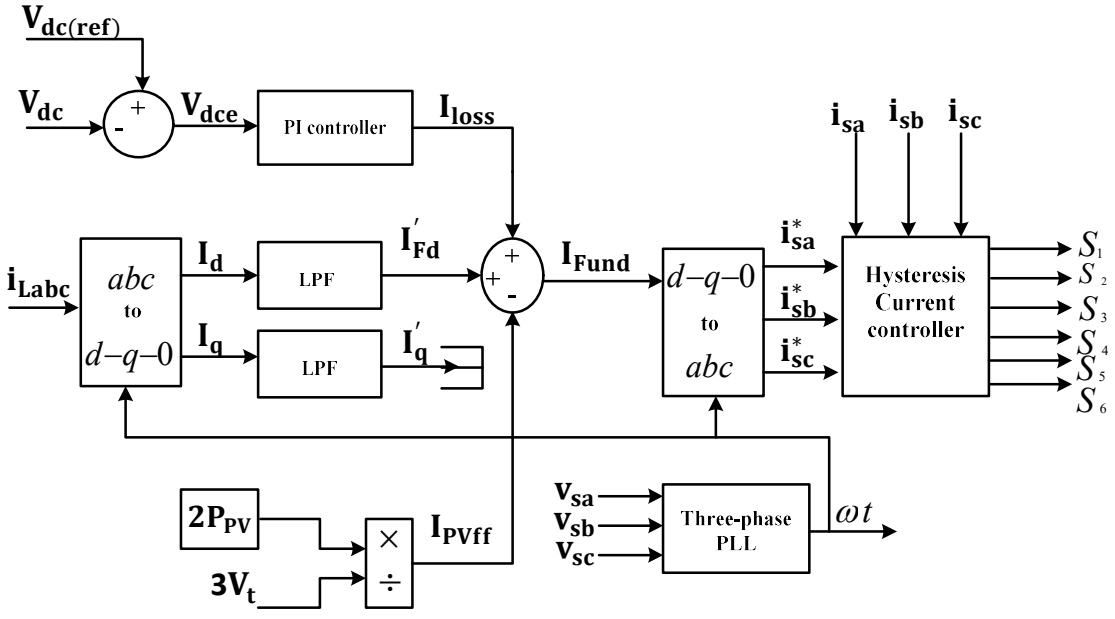

Fig. 4.3 Control of three-phase grid-connected Shunt APF based on conventional SRFT

Applying the Park Transformation for a-b-c to d-q-0 which depends on the dq frame alignment at t=0, when the rotating frame is aligned with the phase A axis,

$$\begin{bmatrix} I_d \\ I_q \\ I_0 \end{bmatrix} = \frac{2}{3}\begin{bmatrix} \cos(\omega t) & \cos\left(\omega t - \frac{2\pi}{3}\right) & \cos\left(\omega t + \frac{2\pi}{3}\right) \\ -\sin(\omega t) & -\sin\left(\omega t - \frac{2\pi}{3}\right) & -\sin\left(\omega t + \frac{2\pi}{3}\right) \\ 1/2 & 1/2 & 1/2 \end{bmatrix}\begin{bmatrix} i_{La} \\ i_{Lb} \\ i_{Lc} \end{bmatrix} \quad (4.11)$$

Three-phase PLL is used to generate the synchronizing signals. The active current (I_d) and reactive current (I_q) consists of some AC components that are filtered by a Low Pass Filter (LPF). The d-axis and q-axis current consists of the fundamental and harmonic components which is given by Eq (4.12) and (4.13),

$$I_d = I'_{Fd} + I'_{FdAC} \quad (4.12)$$

$$I_q = I'_q + I'_{qAC} \quad (4.13)$$

This control strategy involves compensating for reactive power by supplying the direct current (DC) component of the direct-axis load current. Along with compensating for reactive power, the control strategy also ensures that the DC bus voltage is maintained. The control strategy takes losses (I_{loss}) into account and provides the necessary compensation to overcome them. The loss component is given by Eq. (4.14)

$$I_{loss}(n) = I_{loss}(n-1) + K_p[V_{dce}(n) - V_{dce}(n-1)] + K_i V_{dce}(n) \quad (4.14)$$

Where $V_{dce}(n) = V_{dc(ref)}(n) - V_{dc}(n)$ is the error between actual and reference DC link voltage at the n^{th} instant of sampling and K_p, K_i are the PI controller's proportional and integral gain constant. In the case of a PV integrated system, another important term feed forward PV current (I_{PVff}) is subtracted from the d-axis load current component and loss component.

$$I_{Fund} = I'_{Fd} + I_{loss} - I_{PVff} \quad (4.15)$$

By applying reverse Park transformation, the reference source current is obtained which is given by Eq (4.16),

$$\begin{bmatrix} i^*_{sa} \\ i^*_{sb} \\ i^*_{sa} \end{bmatrix} = \begin{bmatrix} \cos(\omega t) & -\sin(\omega t) & 1 \\ \cos\left(\omega t - \frac{2\pi}{3}\right) & -\sin\left(\omega t - \frac{2\pi}{3}\right) & 1 \\ \cos\left(\omega t + \frac{2\pi}{3}\right) & -\sin\left(\omega t + \frac{2\pi}{3}\right) & 1 \end{bmatrix}\begin{bmatrix} I_{Fund} \\ 0 \\ I_0 \end{bmatrix} \quad (4.16)$$

4.2.2 ε − NSRLMMN Adaptive control Technique

Adaptive filters can self-adjust. The cost function and objective function are determined using the error signal. As illustrated in Fig. 4.4 the error signal value must be

reduced to zero by minimizing this cost function. Commonly, the cost function is the mean square of the error signal. The most effective Winer solution is the only minimum solution for the cost function. This solution can be arrived by equating the derivative of Eq (4.17) to zero. According to the LMMN algorithm, the convex cost function [48] is given by

$$J(n) = E\left[\delta\left(e(n)\right)^2 + (1-\delta)\left(e(n)\right)^4\right] \tag{4.17}$$

$$W(n+1) = W(n) + \mu[x(n)]^T e(n)\,[\delta(1-\delta)\left(e(n)\right)^2] \tag{4.18}$$

where δ is the mixing parameter, e(n) is the estimated error between the actual and estimated output at the n^{th} instant, and $x(n)$ is the input signal vector which is defined as $x(n) = \left[x_1, x_2, \ldots\ldots\ldots\ldots, x_M\right]^T$, where M is the size of the filter. The proposed $\boldsymbol{\varepsilon}$ - NSRLMMN algorithm has been described in Eq. (4.19) and Eq. (4.20) and it employs the Steepest Descent technique for determining the derivative of the cost function.

$$e(n) = d(n) - W^T(n)x(n) \tag{4.19}$$

The following recursion can control the weight update equation for the -NSRLMMN algorithm as given by Eq (4.20),

$$W(n+1) = W(n) + \frac{\mu}{\varepsilon + ||x(n)||_H^2}\,\text{sign}[x(n)]^T e(n)[\delta + (1-\delta)\left(e(n)\right)^2] \tag{4.20}$$

where W(n+1) is the updated weight vector, J is the cost function, μ is the step-size, ε is a small positive constant used for regularization purposes, $||x(n)||_H^T = x(n)H[x(n)][x(n)]^T$ and H[x(n)] is a positive-definite Hermitian matrix-valued function of x(n). The normalization of the LMF and LMS protects the algorithm from divergence when input power increases.

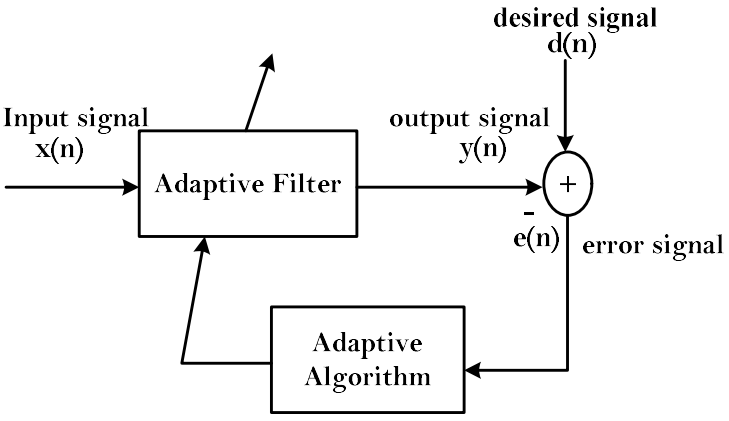

Fig. 4.4 Basic Model of Adaptive control technique

It might be challenging to choose the step size for any adaptive filtering system. However, the step size limit of ε-NSRLMS and ε-NSRLMF have been combined to determine the step size in [48]. The step size was determined by combining the step size limits of ε-NSRLMS and ε-NSRLMF.

$$\left.\begin{matrix} 0 < \mu_{\varepsilon\, NSRLMS} < 2 \\ 0 < \mu_{\varepsilon\, NSRLMF} < \mu_{upper} \end{matrix}\right\} \tag{4.21}$$

The step size for the proposed algorithm has been chosen as

$$0 < \mu_{\varepsilon\, NSRLMMN} < 2\delta + (1-\delta)\mu_{\text{upper}} \tag{4.22}$$

It is adequately justified that by selecting the appropriate value of the mixing parameter, either 1 or 0, the suggested algorithm may be converted to ε-NSRLMS and ε-NSRLMF. The expression for Eq. (4.20) will be changed to a weight update expression for ε-NSRLMS for δ = 1 and a weight update expression for ε-NSRLMF for δ = 0 respectively. The control scheme of a three-phase grid-connected inverter based on ε-NSRLMMN is shown in Fig. 4.5.

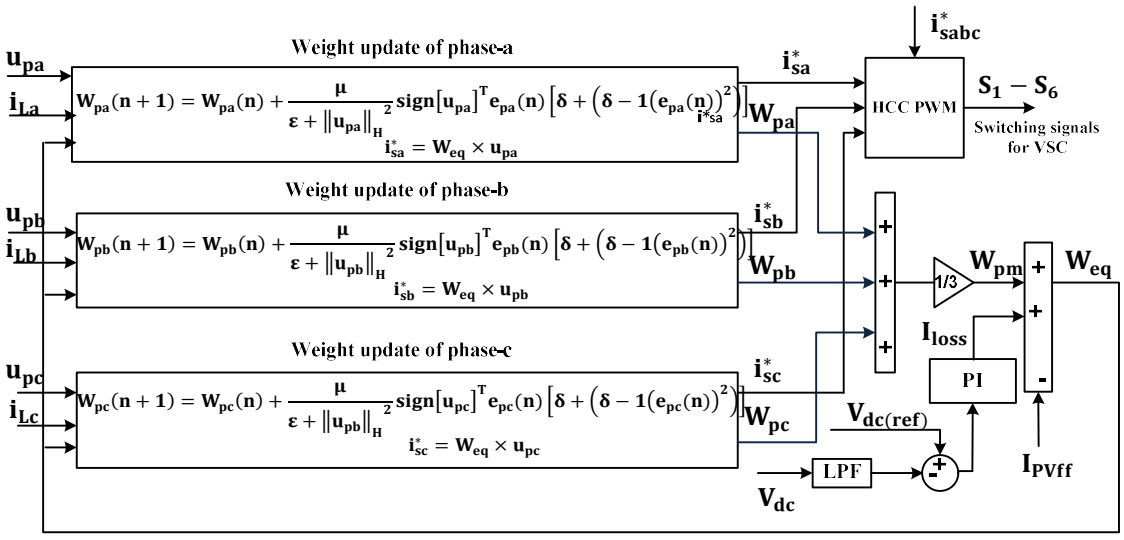

Fig. 4.5 Control scheme of three-phase grid-connected inverter based on ε-NSRLMMN

The fundamental current $(W_{pa}(n+1), W_{pb}(n+1), W_{pc}(n+1))$ are obtained using the ε-NSRLMMN control algorithm is given by

$$W_{pa}(n+1) = W_{pa}(n) + \frac{\mu}{\varepsilon + \left\|u_{pa}\right\|_H^2} \text{sign}\left[u_{pa}\right]^T e_{pa}(n)\left[\delta + (1-\delta)\left(e_{pa}(n)\right)^2\right] \tag{4.23}$$

$$W_{pb}(n+1) = W_{pb}(n) + \frac{\mu}{\varepsilon + \left\|u_{pb}\right\|_H^2} \text{sign}\left[u_{pb}\right]^T e_{pb}(n)\left[\delta + (1-\delta)\left(e_{pb}(n)\right)^2\right] \tag{4.24}$$

$$W_{pc}(n+1) = W_{pc}(n) + \frac{\mu}{\varepsilon + ||u_{pc}||_H^2} \operatorname{sign}\left[u_{pc}\right]^T e_{pc}(n)[\delta + (1-\delta)\left(e_{pc}(n)\right)^2] \quad (4.25)$$

The error signal e_{pa}, e_{pb}, e_{pc} for each phase is given by

$$e_{pM\,(n)} = \begin{bmatrix} i_{La}(n) - u_{pa}(n)W_{pa}(n) \\ i_{Lb}(n) - u_{pb}(n)W_{pb}(n) \\ i_{Lc}(n) - u_{pc}(n)W_{pc}(n) \end{bmatrix} \quad (4.26)$$

where, u_{pa}, u_{pb}, u_{pc} are the in-phase template, μ is the step-size, δ is the mixing parameter, W_{pa}, W_{pb}, W_{pc} are the fundamental weight of each phase. The in-phase template is calculated by

$$u_{pa} = \frac{v_{sa}}{V_t}, u_{pb} = \frac{v_{sb}}{V_t}, u_{pc} = \frac{v_{sc}}{V_t} \quad (4.27)$$

The average fundamental load current is given by Eq. (4.28),

$$W_{pm} = \frac{1}{3}(W_{pa} + W_{pb} + W_{pc}) \quad (4.28)$$

The terminal voltage (V_t) is expressed as

$$V_t = \sqrt{v_{sa}^2 + v_{sb}^2 + v_{sc}^2} \quad (4.29)$$

The proposed three-phase SAPF does not require PLL under normal grid conditions as unit templates determined in Eq. (4.27) work well and load balancing but in case of weak grid conditions, an appropriate PLL is required. Thus, the proposed system is PLL less system. The output of the PI voltage controller is the loss current which meets its losses at the DC link voltage of VSC. The loss current (I_{loss}) is expressed as

$$I_{loss}(n+1) = I_{loss}(n) + K_i V_{dce}(n+1) + K_p(V_{dce}(n+1) - V_{dce}(n)) \quad (4.30)$$

Where, the DC link voltage error (V_{dce}) is the error between the actual DC link voltage ($V_{dc}^*(n)$) and reference DC link voltage ($V_{dc}^*(n)$), $V_{dce}(n) = V_{dc}^*(n) - V_{dc}(n)$ at n^{th} instant of switching. The total current $\left(W_{eq}\right)$ is expressed as

$$W_{eq} = W_{pm} + I_{loss} \quad (4.31)$$

The reference source current ($i_{sa}^*, i_{sb}^*, i_{sc}^*$) for each phase is calculated as

$$i_{sa}^* = W_{eq} * u_{pa};\ i_{sb}^* = W_{eq} * u_{pb};\ i_{sc}^* = W_{eq} * u_{pc} \quad (4.32)$$

The reference source current ($i_{sa}^*, i_{sb}^*, i_{sc}^*$) with respective actual current (i_{sa}, i_{sb}, i_{sc}) are fed to the HCC to generate the switching signals for three-phase VSC.

4.2.3 q-LMF based adaptive control Technique

The fundamental component of a nonlinear load current is identified in the proposed study using a q-LMF-based control technique. An appropriate step size with the mathematical model is used to construct the control strategy. The proposed q calculus-based LMF can be utilized to enhance the functionality of the conventional LMF while preserving the stability of the algorithm [49] by utilizing an additional control parameter q. The proposed control method also produces values for adaptive weights. The suggested q-LMF algorithm behaves like a standard LMF if q = 1. The algorithm's behaviour, however, can completely change depending on how the q parameter is changed. Limitless calculus is another name for quantum calculus. A function's differential is written as

$$d_q\big(f(x)\big) = f(qx) - f(x) \tag{4.33}$$

The derivative of Eq. (4.33) is given as

$$D_q\big(f(x)\big) = \frac{d_q(f(x))}{d_q(x)} = \frac{f(qx)-f(x)}{(q-1)x} \tag{4.34}$$

The aforementioned formula fits the classical derivative if q approaches 1. For 'm' variables, the q-gradient of the function f(x) is represented as

$$\nabla_{q,w} f(x) \triangleq \left[D_{q1,x1} f(x), D_{q2,x2} f(x), \dots \dots \dots D_{qn,xm} f(x)\right]^T \tag{4.35}$$

where $q = \left[q_1, q_2, q_{3\dots\dots\dots\dots}, q_m\right]^T$

The conventional LMF algorithm is expressed as

$$W(n+1) = W(n) - \frac{\mu}{4}\nabla_W J(W) \tag{4.36}$$

where ‘μ’ is the step size or learning rate, J(w) is the cost function for the proposed q-LMF algorithm, and it is expressed as $J(W) = e^4(n)$. Here, e(n) is defined as the calculated error between actual output (d) and calculated output $(W^T(n)x(n))$ at the n^{th} instant. Also, x(n) is denoted as the input signal which is expressed as $x(n) = \left[x_1, x_{2,\dots\dots\dots\dots\dots}, x_M\right]^T$ and ‘W’ is the weights vector, and 'M' is the length of the filter. A flow chart for step size optimization is shown in Fig. 4.6, which explains the procedure to choose the step size value in the proposed q-LMF control scheme.

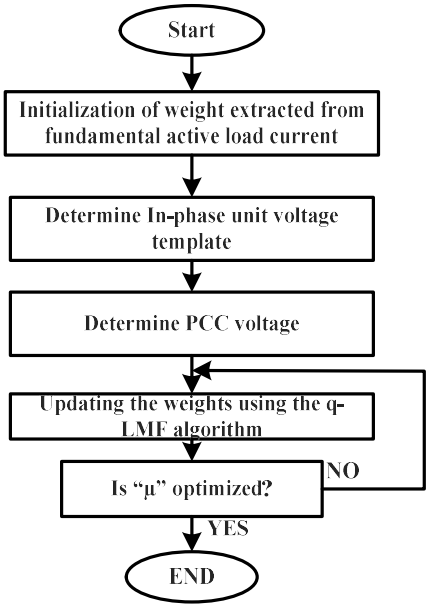

Fig. 4.6 Flow chart for step size optimization

The proposed q-LMF algorithm is obtained by replacing the conventional gradient with the q-gradient [49] as shown in Eq. (4.38).

$$e(n) = d(n) - W^{T}(n)x(n) \tag{4.37}$$

$$W(n+1) = W(n) - \frac{\mu}{4}\nabla_{q,W}J(W) \tag{4.38}$$

$$\nabla_{q,w}J(W) = -4E\,(q_K^3 + q_K^2 + q_K^2 + 1)x_K(n)e^3(n) \text{ for } K = 1, 2, 3, \ldots..M \tag{4.39}$$

$$\nabla_{q,w}J(w) = -4E[Gx(n)e^3(n)] \tag{4.40}$$

where q_k is the quiescent value at kth instant of time, where G is a diagonal matrix,

$$\text{diag}(G) = \left[\left(\frac{q_1^3+q_1^2+q_1+1}{4}\right), \left(\frac{q_2^3+q_2^2+q_2+1}{4}\right), \ldots\ldots\ldots\ldots, \left(\frac{q_M^3+q_M^2+q_M+1}{4}\right)\right]^{T} \tag{4.41}$$

System ergodicity of the system $\nabla_{q,W}J(W)$ can be expressed as $\nabla_{q,W}J(W) \approx -4Gx(n)e^3(n)$. Equation (4.42) will be expressed as

$$W(n+1) = W(n) + \mu Gx(n)e^3(n) \tag{4.42}$$

$$W(n+1) = \begin{bmatrix} W_{pa}(n+1) & W_{pb(n+1)} & W_{pc}(n+1) \end{bmatrix}^{T} \tag{4.43}$$

$$W(n) = \begin{bmatrix} W_{pa}(n) & W_{pb}(n) & W_{pc}(n) \end{bmatrix}^{T} \tag{4.44}$$

$$e(n) = \begin{bmatrix} i_{La}(n) - u_{pa}(n)W_{pa}(n) \\ i_{Lb}(n) - u_{pb}(n)W_{pb}(n) \\ i_{Lc}(n) - u_{pc}(n)W_{pc}(n) \end{bmatrix} \tag{4.45}$$

While for *q*-LMF, the value of *q* can be chosen according to the requirement q = 2, 3, 4……..

For q =2, $G = [3.5 \quad 3.5 \quad 3.5]^T$. Hence, the G matrix is dependent on the choice of q, where, u_{pa}, u_{pb}, u_{pc} are the in-phase template, μ is the step-size, δ is the mixing parameter, W_{pa}, W_{pb}, W_{pc} are the fundamental weight of each phase. The in-phase template is calculated by

$$u_{pa} = \frac{v_{sa}}{V_t}, u_{pb} = \frac{v_{sb}}{V_t}, u_{pc} = \frac{v_{sc}}{V_t} \tag{4.46}$$

The average fundamental load current is given by Eq. (4.46),

$$W_{pm} = \frac{1}{3}(W_{pa} + W_{pb} + W_{pc}) \tag{4.47}$$

The terminal voltage (V_t) is expressed as

$$V_t = \sqrt{v_{sa}^2 + v_{sb}^2 + v_{sc}^2} \tag{4.48}$$

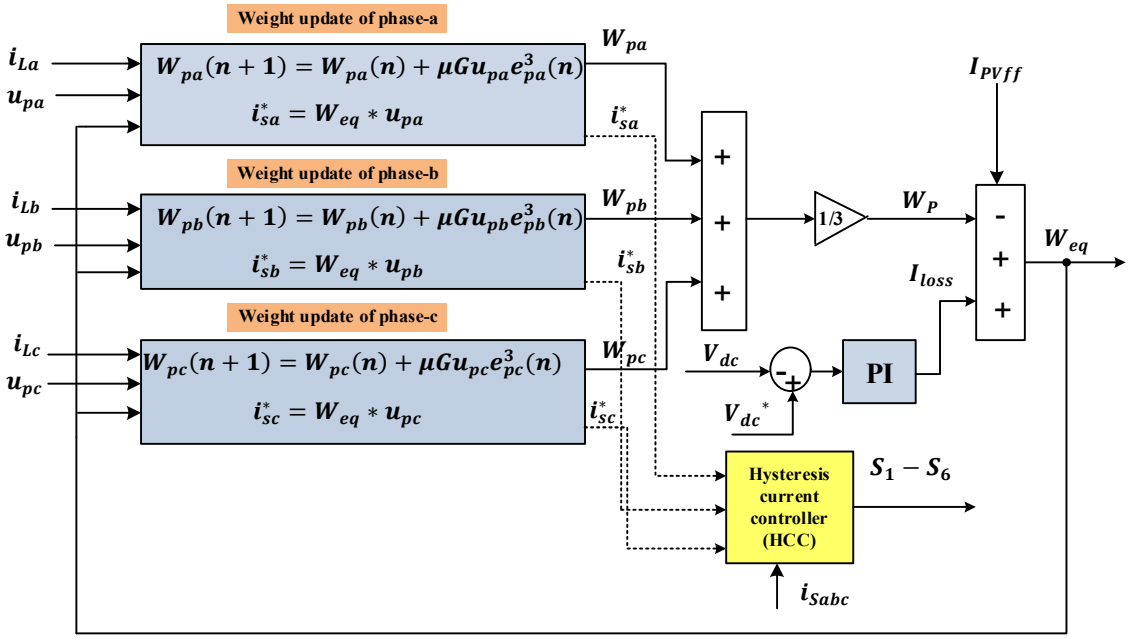

Fig. 4.7 Control scheme of three-phase grid-connected inverter based on q-LMF.

The proposed three-phase SAPF does not require PLL under normal grid conditions and load balancing but in case of weak grid conditions, an appropriate PLL is required. Thus, the proposed system is PLL less system. The output of the PI voltage controller is the loss current which meets its losses at the DC link voltage of VSC. The loss current (I_{loss}) is expressed as

$$I_{loss}(n+1) = I_{loss}(n) + K_i V_{dce}(n+1) + K_p(V_{dce}(n+1) - V_{dce}(n)) \tag{4.49}$$

where, the DC link voltage error (V_{dce}) is the error between the actual DC link voltage ($V_{dc}^{*}(n)$) and reference DC link voltage ($V_{dc}^{*}(n)$), $V_{dce}(n) = V_{dc}^{*}(n) - V_{dc}(n)$ at n^{th} instant of switching. The total current (W_{eq}) is expressed as

$$W_{eq} = W_{pm} + I_{loss} - I_{PVff} \tag{4.50}$$

The reference source current ($i_{sa}^{*}, i_{sb}^{*}, i_{sc}^{*}$) for each phase is calculated as

$$i_{sa}^{*} = W_{eq} * u_{pa};\ i_{sb}^{*} = W_{eq} * u_{pb};\ i_{sc}^{*} = W_{eq} * u_{pc} \tag{4.51}$$

The reference source current ($i_{sa}^{*}, i_{sb}^{*}, i_{sc}^{*}$) with respective actual current (i_{sa}, i_{sb}, i_{sc}) are fed to the HCC to generate the switching signals for three-phase VSC.

4.3 Simulation Results

4.3.1 Performance Analysis of Synchronous Reference Frame Theory (SRFT)

The Synchronous Reference Frame Theory-based control scheme is performed well under stable and balanced operating conditions. While it comes under load unbalancing, the performance of the control scheme can be affected. Load unbalancing occurs due to uneven distribution of loads or variations in the characteristics of the load connected. The load is disconnected at phase 'a' from t=0.4s to 0.5s. The source current remains sinusoidal under load unbalancing.

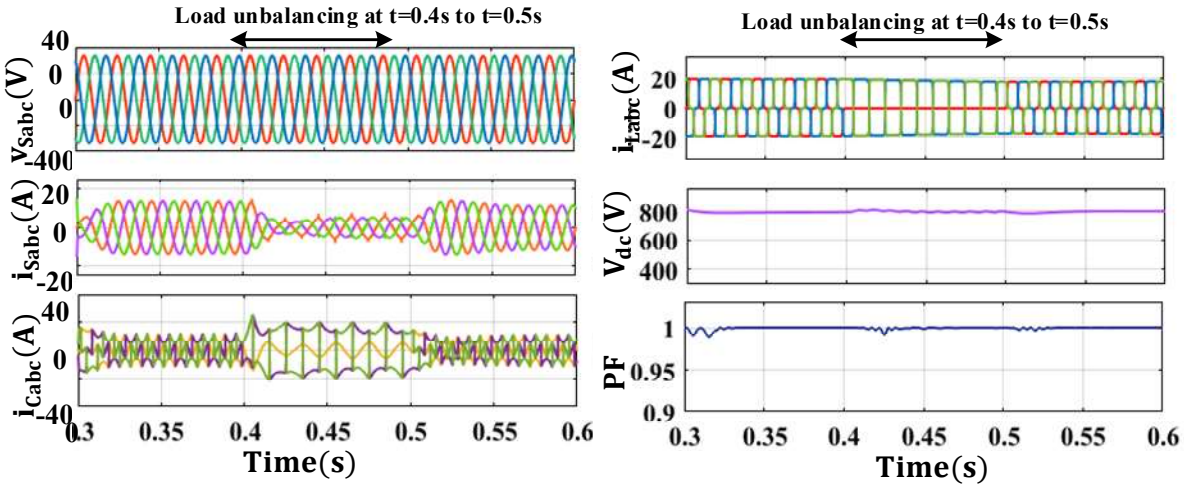

Fig. 4.8 Steady-state and dynamic performance of the three-phase grid-connected system with SRFT control scheme under the normal grid and load unbalancing.

The DC link voltage remains stable due to its PI voltage controller with a small voltage increase at t=0.4s. The power factor (PF) is 0.98 under load unbalancing while unity PF is observed under a normal grid. The compensating VSC current is fed to the PCC to support the reactive power demand and cancel out the harmonics of the load current. The

waveforms of signal source voltage (v_{sabc}), source current (i_{sabc}), compensating current (i_{Cabc}), load current (i_{Labc}), DC link (V_{dc}) voltage and PF. The THD of the source current under steady state condition is 2.46% having a magnitude of 11.66A with SRFT control scheme, while THD of load current is 27.06% having a magnitude of 19.44A as shown in Fig. 4.9. The THD of source current is within the limit of IEEE-519:2014 standards.

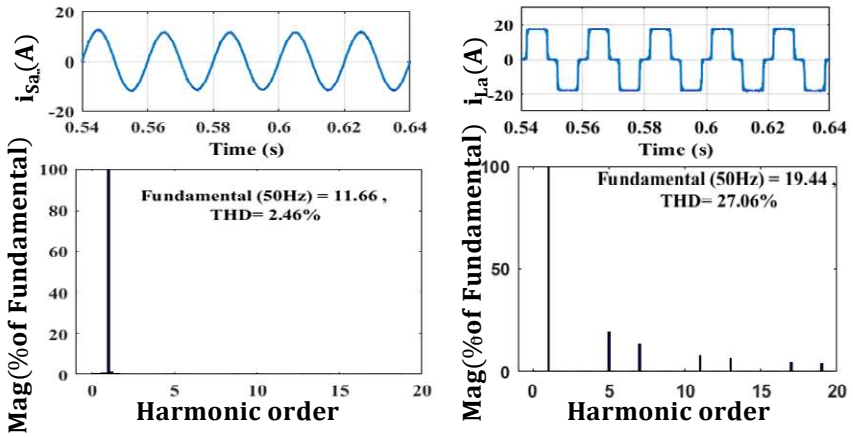

(a) (b)

Fig. 4.9 FFT analysis of proposed system with SRFT control under normal grid (a) source current (b) load current

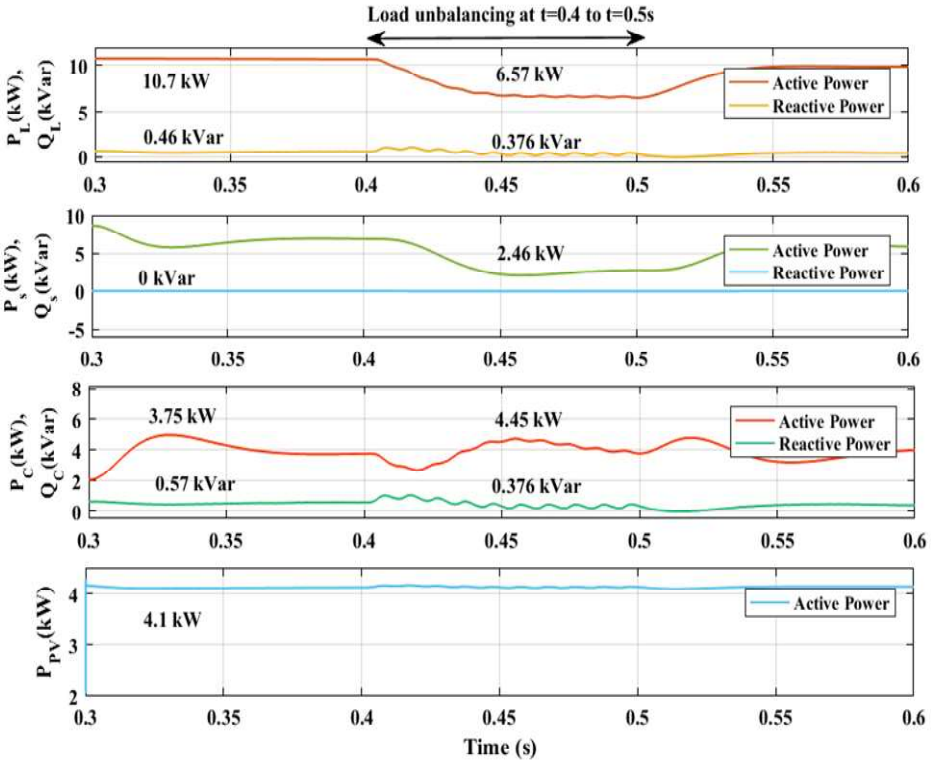

Fig. 4.10 Power analysis with SRFT control scheme under Load unbalancing from t=0.4 to 0.5s.

Power analysis under steady-state and load unbalancing when a load of Phase 'a' disconnected is shown in Fig. 4.10. The active power demand before load unbalancing is 10.7kW and the reactive power demand is 0.46kVar. A PV array is also interconnected at input of the VSC with the three-phase grid connected VSC at 1000W/m^2 irradiance. The PV array will support the load's active power demand of 4.1kW while the remaining active power demand is fulfilled by the grid's power 6.6kW. The VSC is able to provide the reactive power compensation and supports the reactive power demand of load i.e., 0.57kVar before load unbalancing. At load unbalancing, the active power demand of load is decreased to 6.7kW which is partially supported by grid and PV power.

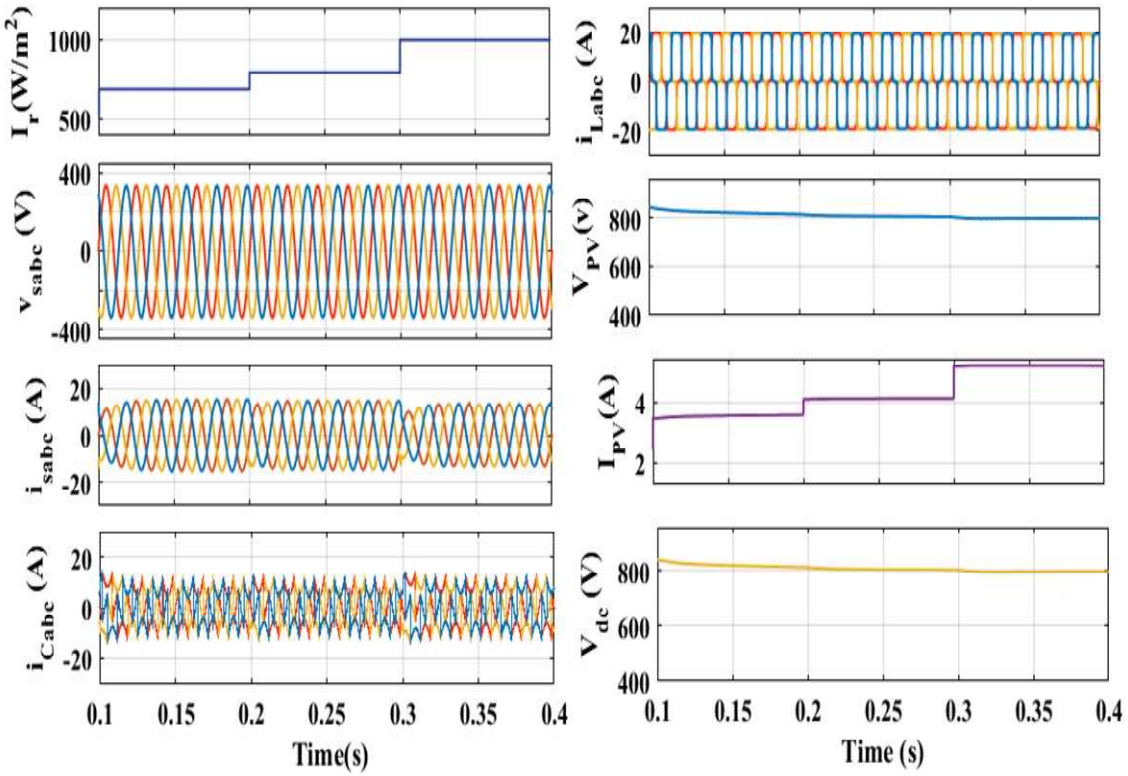

Fig. 4.11 Performance analysis of the proposed system with SRFT control scheme under varying solar irradiance, i.e., 600W/m^2 to 1000W/m^2.

The performance of a three-phase grid-connected PV system with an SRFT control scheme is shown in Fig.4.11. At irradiance of 600W/m^2, the PV array will not be able to deliver its full capacity power, and at this time source current increases to support the power demand of the connected load. The PV array voltage is constant with decreasing PV current. At t=0.2s, the irradiance is increased to 800W/m^2 due to which the PV current increases and source current reduces because the maximum power demand is fulfilled by the PV array. The DC link voltage is maintained at 800V with a small deviation due to

changing irradiance. The Power analysis under varying solar irradiance is shown in Fig. 4.12 having the waveforms of load power (P_L, Q_L), source power (P_s, Q_s), VSC power (P_C, Q_C) and PV power (P_{PV}).

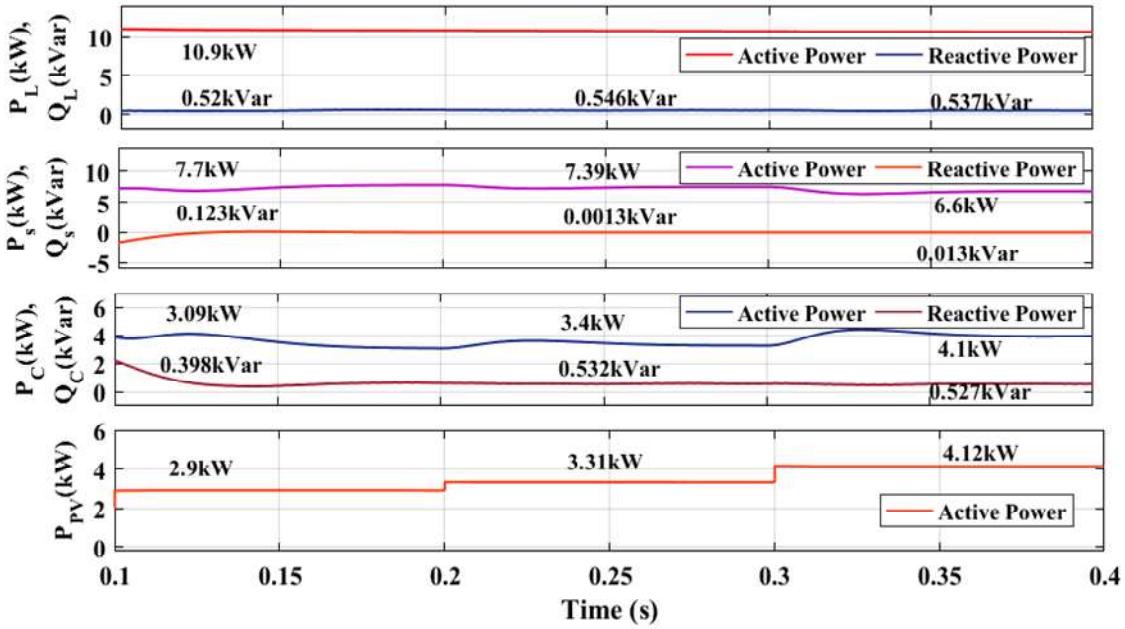

Fig. 4.12 Power analysis under irradiance change with SRFT controller.

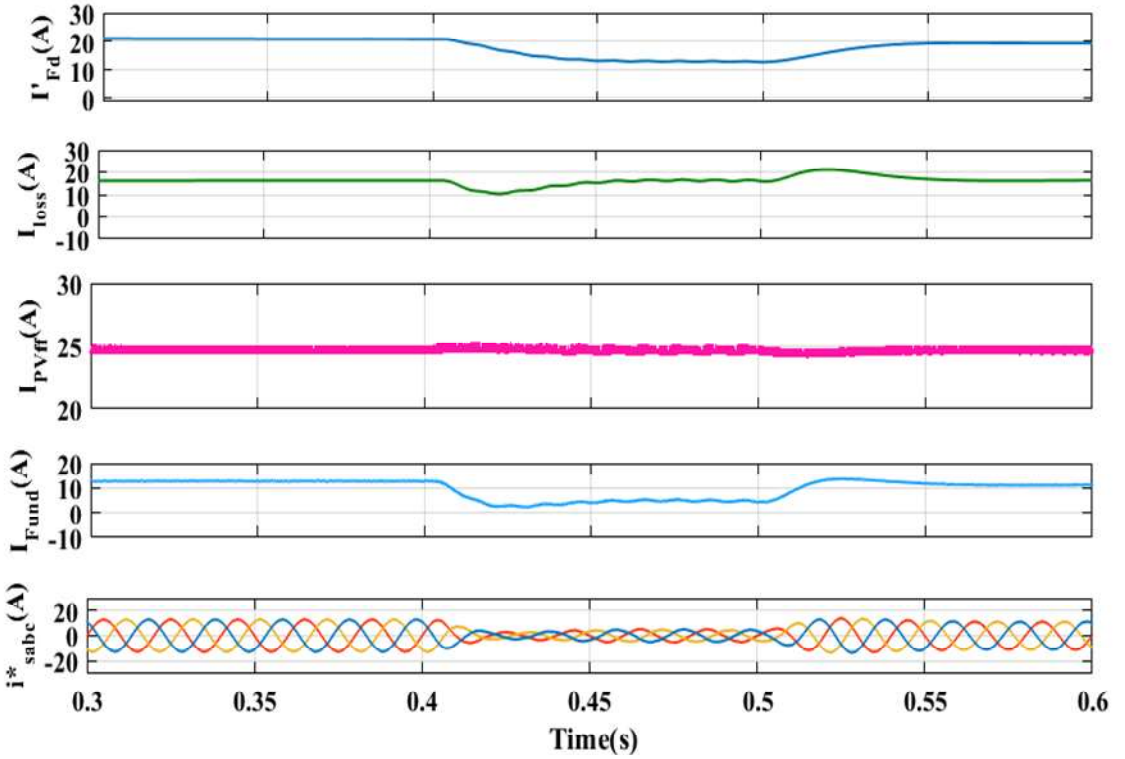

Fig. 4.13 Intermediate signals of SRFT control scheme for the proposed system under load unbalancing.

The intermediate signals of the SRFT control scheme for PQ improvement and reactive power compensation are shown in Fig. 4.13. The direct axis component (I'_{Fund}) of three-phase load current (i_{Labc}) is decreased with a decrease in load. Similarly, the total fundamental current (I_{Fund}) is decreasing with a decrease in load during load unbalancing. The reference source's current (i^*_{sabc}) also decrease due to load unbalancing and the power balance between source, load and compensator is maintained.

4.3.2 Performance Analysis of ε − NSRLMMN Adaptive control Technique

The performance of the three-phase grid-connected PV-SAPF system with the proposed ε − NSRLMMN control scheme under the condition of load unbalancing from t=0.4s to 0.5s is shown in Fig. 4.14. The source voltage is ideal while under load unbalancing, the source current (i_{sabc}) decreases to maintain the power balance among source, load, and PV. The VSC provides compensating current (i_{Cabc}) to cancel out the load current harmonics and fulfill the reactive power compensation. The DC link voltage (V_{dc}) is maintained at 800V due to its PI control.

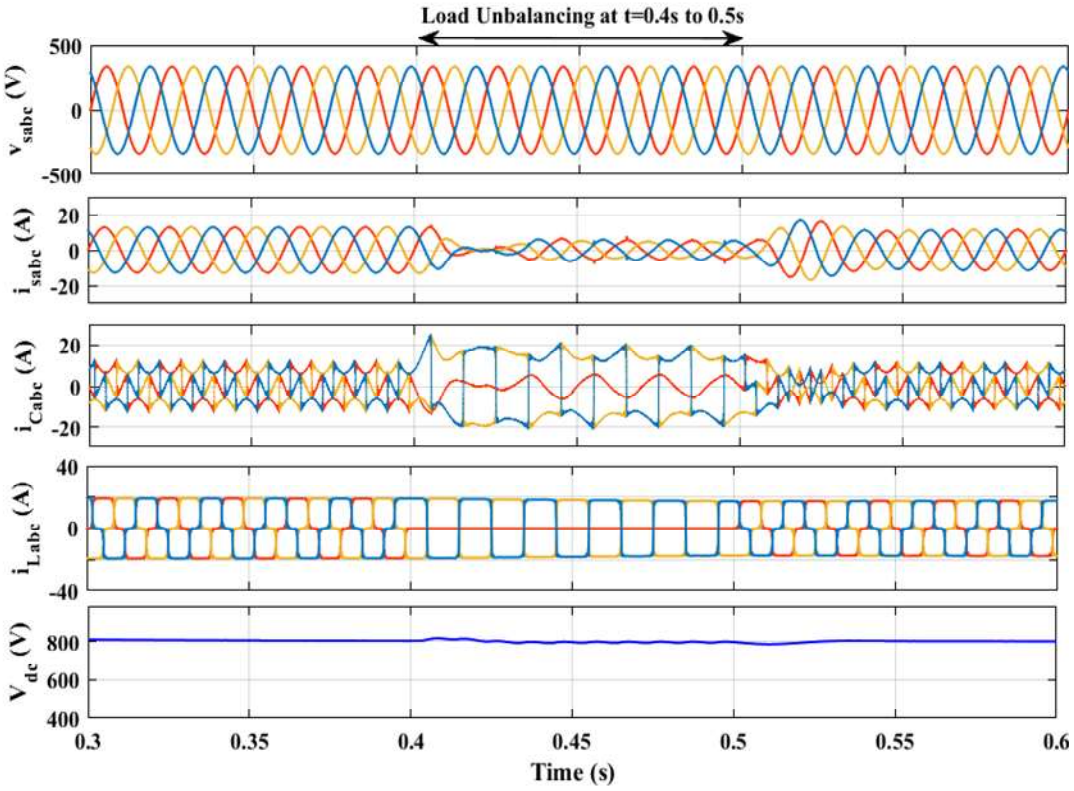

Fig. 4.14 Simulation results of proposed three-phase grid connected PV-SAPF under load unbalancing with $\varepsilon - NSRLMMN$

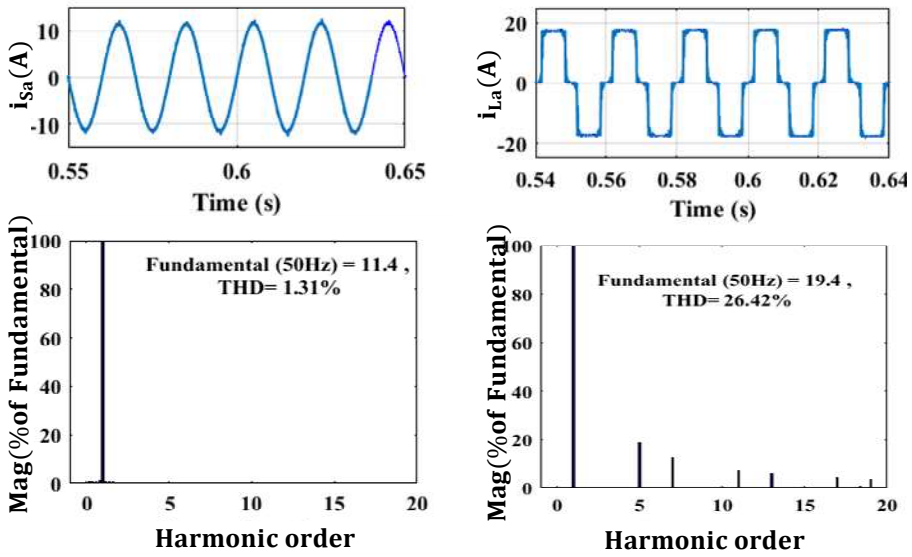

Fig. 4. 15 FFT analysis of source current and load current with $\varepsilon - NSRLMMN$ control technique.

The FFT analysis of source current and load current with $\varepsilon - \text{NSRLMMN}$ is shown in Fig. 4.15(a-b). The magnitude of the source current under steady-state conditions is 11.4A with the THD of the source current being 1.31%, while the magnitude of the load current is 19.4A with a THD of 26.42%. The power analysis under the condition of load unbalancing is shown in Fig. 4.16. The load's active power demand is 6.7kW under load unbalancing which is partially fulfilled by the PV array and the remaining required power is fed by source power. The reactive power demand of load is completely fulfilled by VSC (Q_C).

The performance of a three-phase grid-connected PV system with $\varepsilon - \text{NSRLMMN}$ control scheme is shown in Fig. 4.17. The dynamic response of the system under varying solar irradiance depicts the waveforms v_{sabc}, i_{sabc}, i_{Cabc}, and i_{Labc} . At irradiance of 600W/m^2, the PV array will not be able to deliver its full capacity power, and at this time source current increases to support the power demand of the connected load. The PV array voltage is constant with decreasing PV current. At t=0.2s, the irradiance is increased to 800W/m^2 due to which the PV current increases and the source current reduces because the maximum power demand is fulfilled by the PV array. The DC link voltage is maintained to 800V with a small deviation due to changing irradiance. The Power analysis under varying solar irradiance is shown in Fig. 4.18 having the waveforms of load power (P_L, Q_L), source power (P_s, Q_s), VSC power (P_C, Q_C) and PV power (P_{PV}).

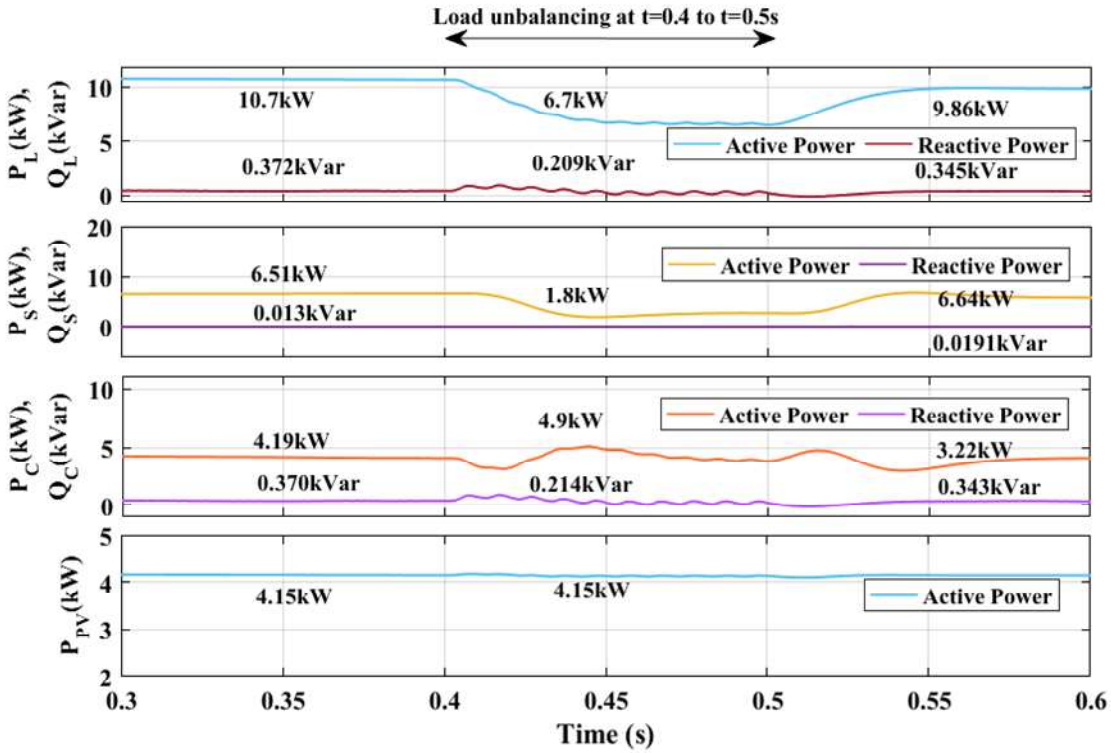

Fig. 4.16 Power analysis of proposed three-phase SAPF under load unbalancing with ε − NSRLMMN control scheme

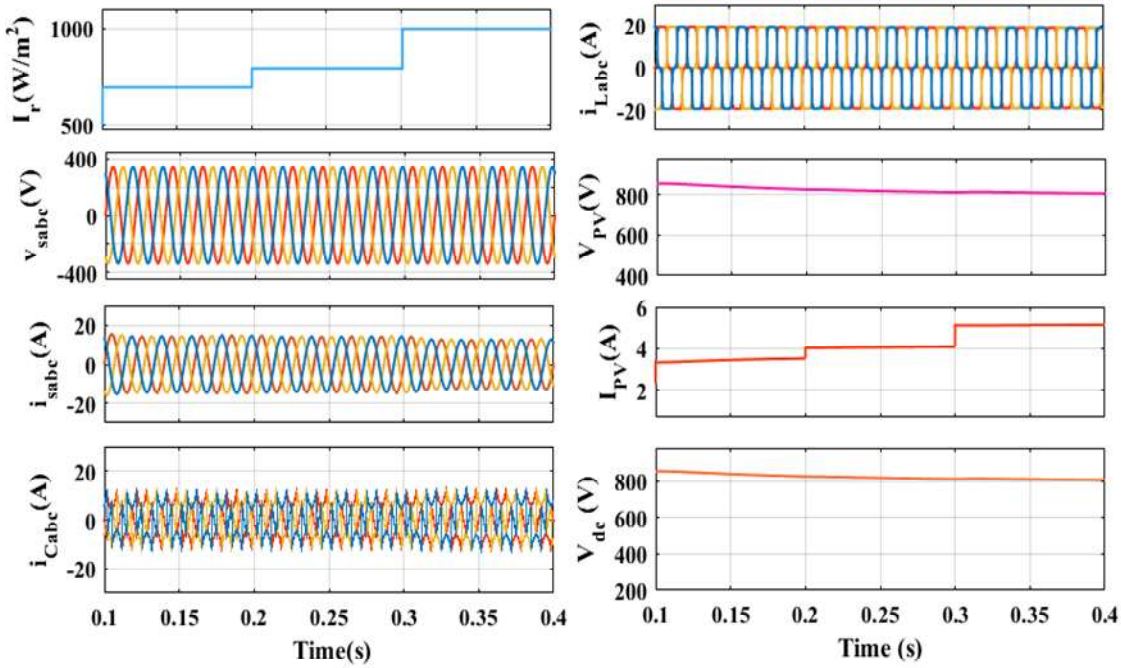

Fig. 4.17 Simulation results under irradiance change with ε − NSRLMMN control scheme.

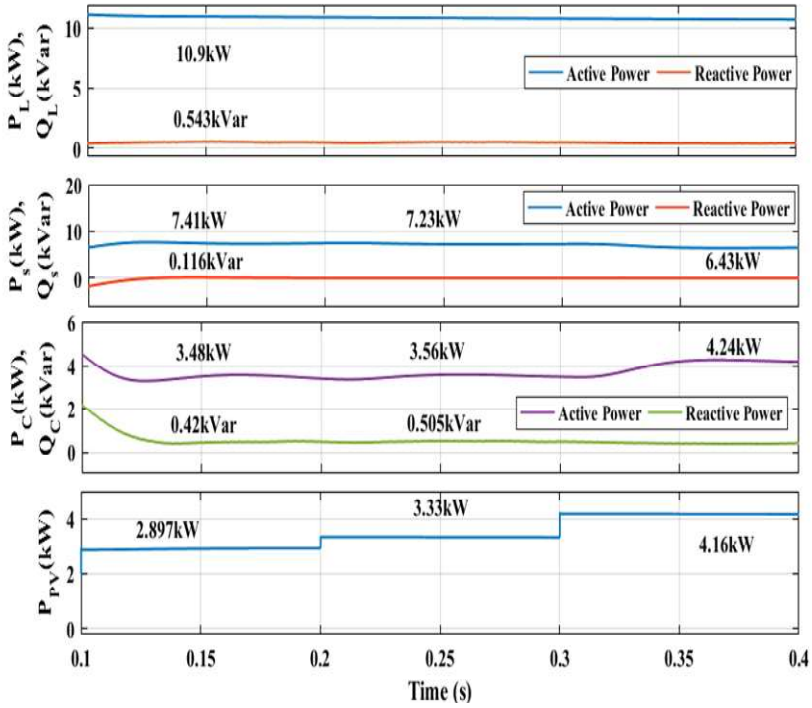

Fig. 4.18 Power analysis under irradiance change with ε − NSRLMMN control scheme

The intermediate signals of ε − NSRLMMN control scheme under load unbalancing are shown in Fig. 4.19. The error signal (e_{pa}) has magnitude zero when phase 'a' load is disconnected from the proposed system. The fundamental load current (W_{pa}) is decreased with a decrease in load from t=0.4 to 0.5s. The switching loss component, and total fundamental current used to generate the reference source current are shown in Fig. 4.19. The error signal oscillates near zero and the weight of the active component waveform shifts with load unbalance and subsequently settles down to its original value. The total weight of the fundamental active component (W_{eq}), the output of the dc-link PI controller (I_{loss}).

4.3.3 Performance Analysis of q-LMF-based Adaptive control Technique

The effectiveness of the grid-connected SAPF is monitored through the signal source voltage (v_{sabc}), source current (i_{sabc}), compensating current (i_{Cabc}), load current (i_{Labc}) and DC link voltage (V_{dc}). The proposed q-LMF current extraction method is utilized for evaluating the behavior of SAPF under both steady-state and dynamic conditions. The load from phase 'a' is disconnected from t=0.4s to 0.5s. The source current reduces due to a decrease in the load connected to the system, while the DC link voltage is maintained at its nominal value of 800V as shown in Fig. 4.20.

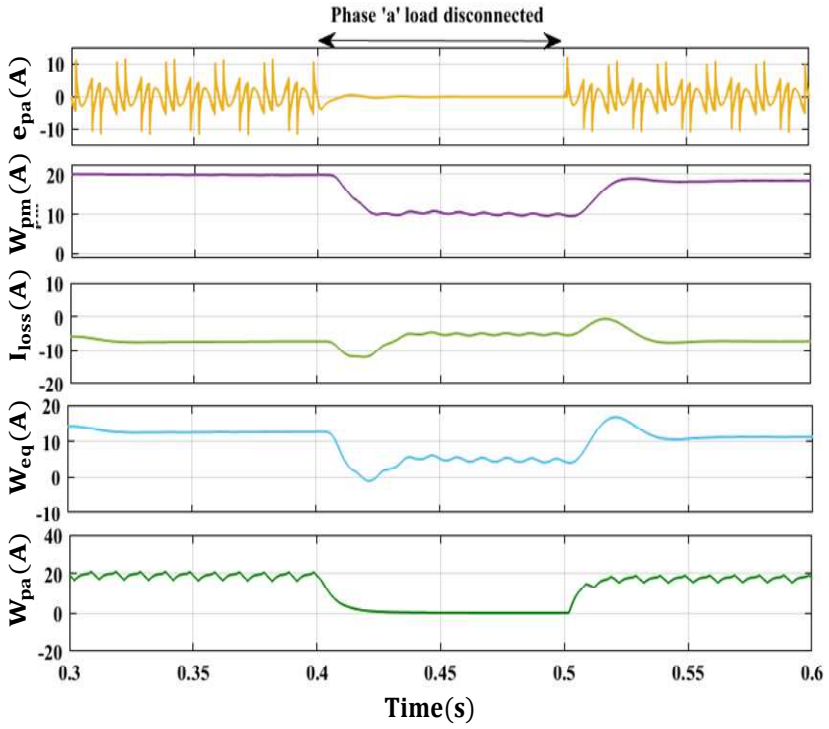

Fig. 4.19 Intermediate signals under load unbalancing with ε − NSRLMMN control scheme

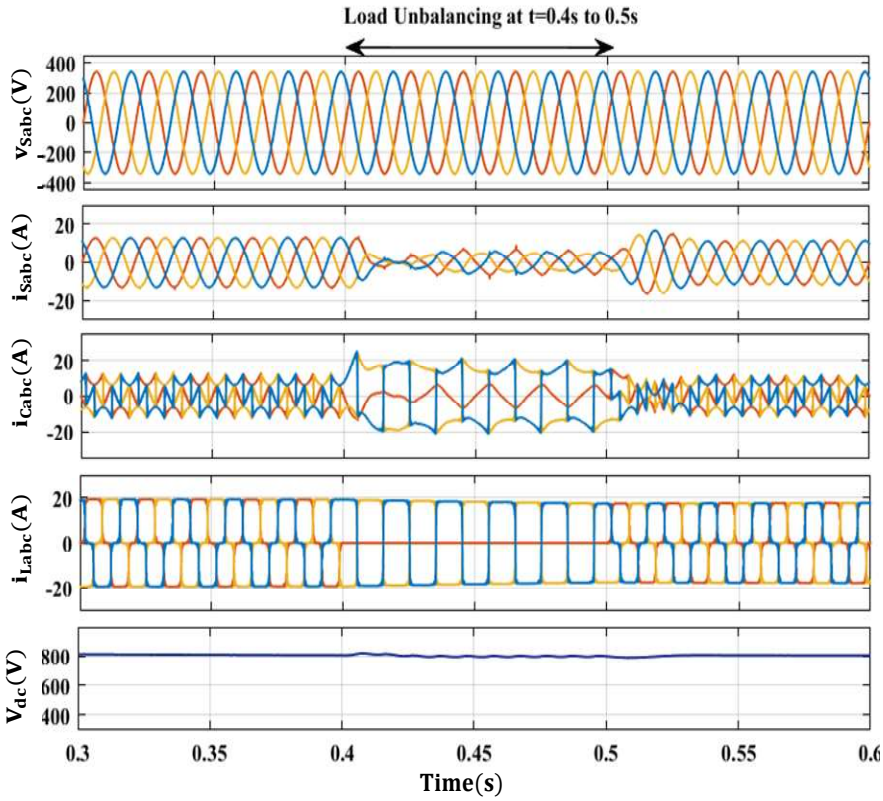

Fig. 4.20 Dynamic Performance of grid-connected PV-SAPF under load unbalancing with q-LMF control scheme.

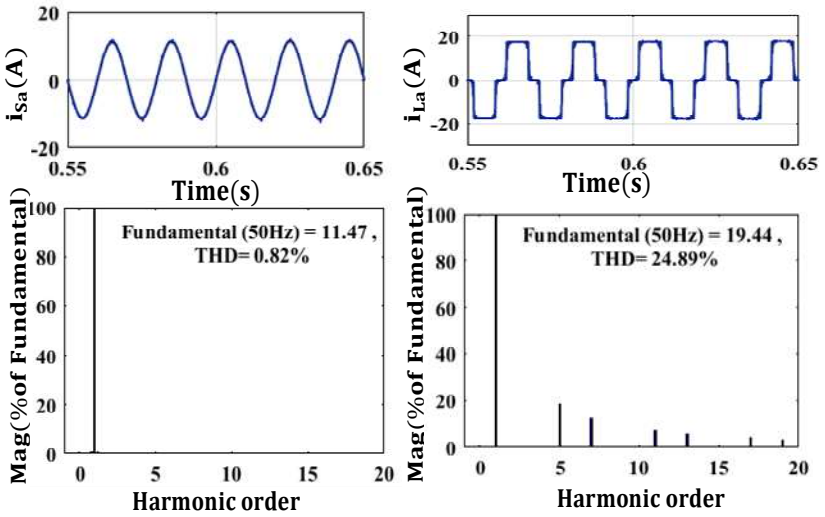

(a) (b)

Fig. 4.21 FFT analysis of (a) source current and (b) load current with q-LMF control scheme

The THD of the source current is 0.82% with a peak magnitude of 11.47A and the THD of load current is 24.89% with the 19.4A magnitude with the proposed q-LMF control scheme which shows its effectiveness among conventional and adaptive control schemes in Fig. 4.21.

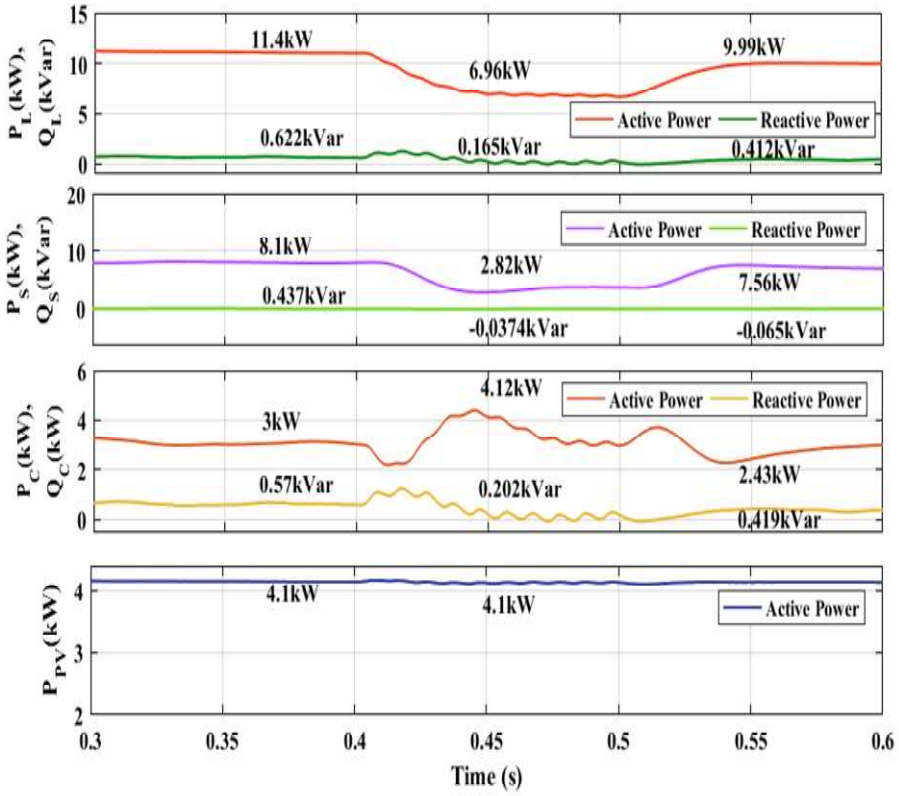

Fig. 4.22 Power analysis of three-phase grid-connected PV-SAPF under load unbalancing with q-LMF control scheme.

The load's active power demand before load unbalancing is 11.4kW and reactive power is 0.622kVar which is partially fulfilled by PV array and source's active power. At t=04s, the

load's active power demand is decreased to 6.96kW and is fed by 4.1kW of PV power and 2.82kW of source power. The reactive power load demand is fulfilled by VSC which is meant for reactive power compensation as shown in Fig. 4.22.

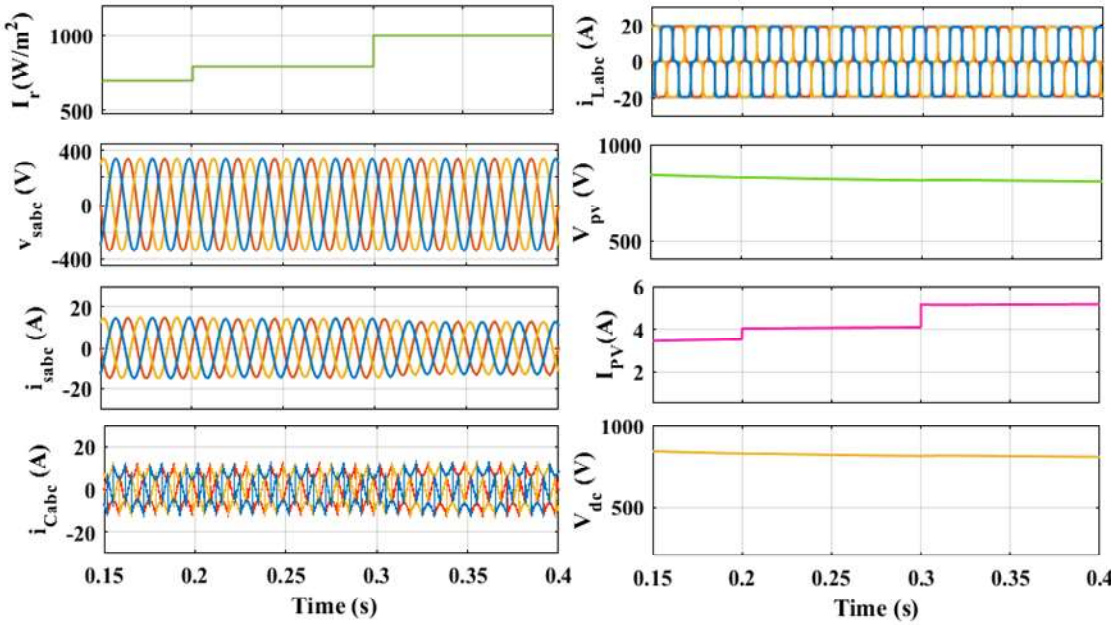

Fig. 4.23 Dynamic performance analysis under varying solar irradiance with the effectiveness of q-LMF control scheme.

The effectiveness of the proposed three-phase grid-connected SAPF with varying solar irradiance is shown in Fig. 4.23. The irradiance varies from 600W/m^2 to 1000W/m^2, the source current remains sinusoidal with varying magnitude according to the irradiance of the solar PV array. The source current increases due to low PV array irradiance and to fulfill the load's active power demand. The DC link voltage is maintained at 800V due to its PI-controlling action.

The intermediate signals of proposed q-LMF control scheme under the condition of load unbalancing is shown in Fig. 4.24. The calculated error (e_{pa}) for phase 'a' weight is decreased and oscillates to zero as the load decreased or is disconnected. The cubic power of error (e_{pa}^3) is three times of phase 'a' error component is also shown in Fig. 4.24. The total effective weight (W_p) is decreased when load unbalancing occurs and its convergences to its final steady-state value with the effect of the q-LMF control scheme.

Figure 4.25 (a) shows the fundamental active weight component waveform under steady-state conditions. It depicts that the fundamental weight signal converges fast with q-LMF based algorithm. Fig. 4.25(b) shows the response of the average weight of the fundamental

component of load current (W_p) when subjected to load unbalancing in phase 'a' for the proposed q-LMF-based control algorithm. Studies demonstrate that by adding a second regulating term, 'q' to the traditional LMF, the suggested q-LMF improves its performance.

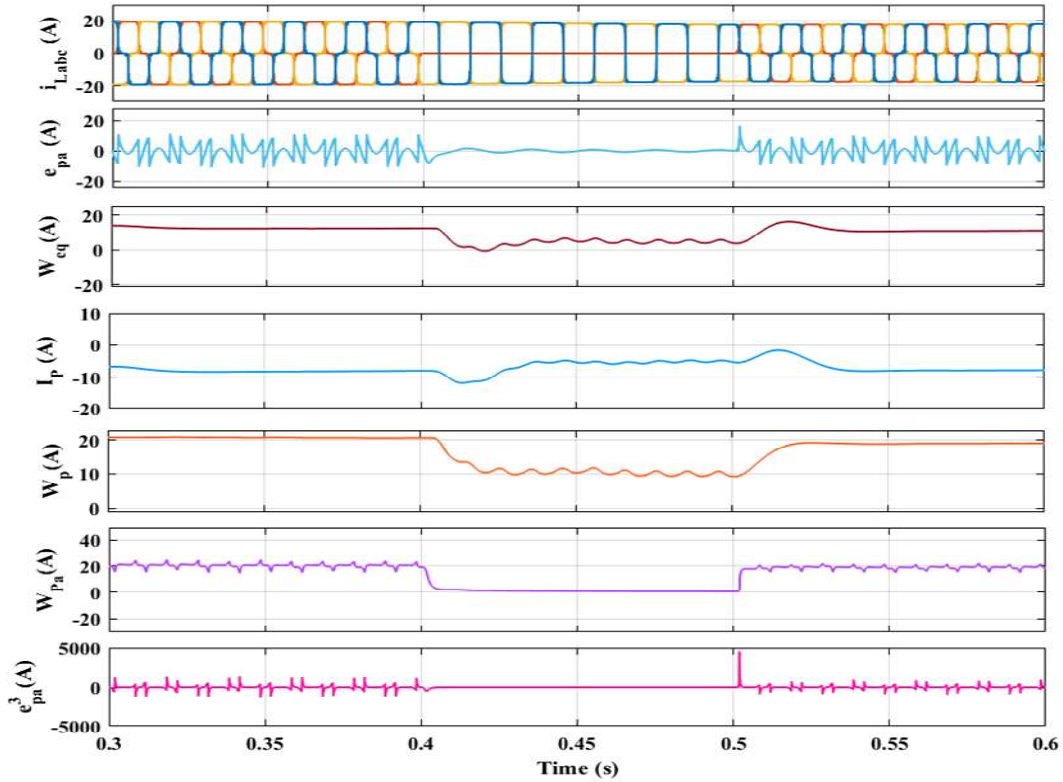

Fig. 4.24 Intermediate signals of proposed q-LMF control scheme under load unbalancing.

To evaluate the proposed algorithm, step size has been chosen $\mu = 0.01$ for LMS, LMF, and q-LMF with different values of q = 1, 2, 3. In terms of steady-state error and convergence rate measurements, Fig.4.25(b) demonstrates that the q-LMF performs better than the traditional LMF and LMS. The proposed algorithm converges faster as compared to the conventional LMF and LMS. The average component with the LMS technique takes the maximum time to reach the steady state compared to LMF and the proposed q-LMF. As shown in Fig. 4.25(b), it is visible that the oscillations with the LMS technique are less as compared to LMF and the proposed one, but it causes the maximum error.

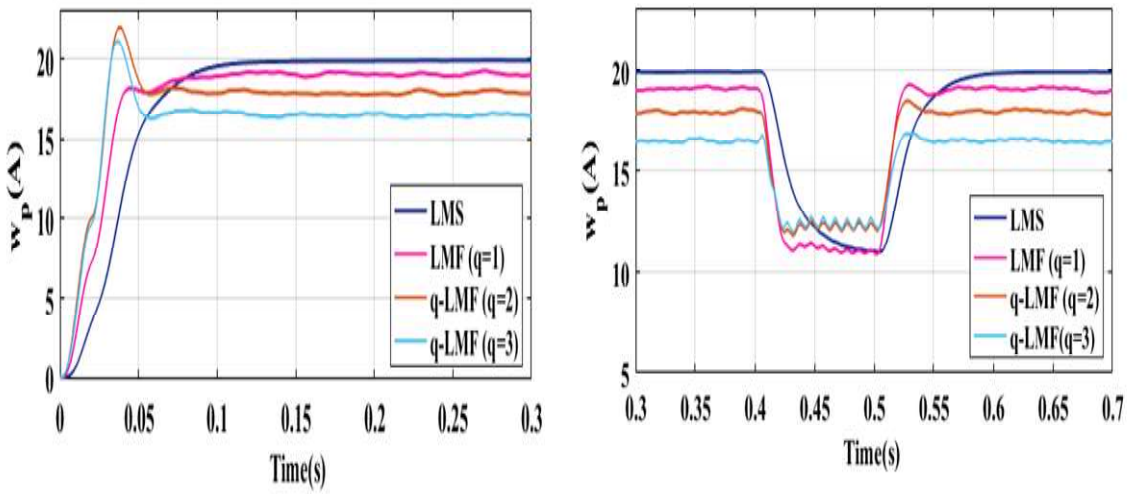

(a) (b)

Fig. 4.25 Response of fundamental weight signal (w_p) for conventional LMF, LMS, and proposed q-LMF (at q = 2, q = 3) at (a) steady state (b) dynamic load condition

When q = 2, the signal converges at t = 0.72s, and when q = 1 (Conventional LMF) signal converges at t = 0.73s. At q = 3, the fundamental active component of load current has fast convergence compared to q = 1 and 2 but with a small steady-state error. It has been noticed that the q-LMF algorithm's response changes when the q parameter changes. From Fig. 4.25, it is clearly shown that by increasing the value of q, faster learning is achieved with a significant final error. At a higher value of q, the signal converges faster but with a large steady-state error.

4.4 Experimental Results

The proposed system is put into application with a research lab prototype model. The proposed system uses LEM LA 25P and LEM LV 25P current and voltage sensors to measure load current, source current, PCC voltage, compensatory current, and DC-link voltage. The ADC of the dSPACE/ Microlab Box must be used to convert analogue sensor outputs to digital signals. The hysteresis current controller produces the switching signals for the voltage source converter. Three-phase variable ac power is provided by the electricity grid. A DC power source established for scientific purposes serves as the backup power for sensor and gating circuits. Using a Keysight digital storage oscilloscope (DSO), the dynamic performance has been examined. Using a power analyzer of the Hioki brand, the system's steady-state performance was evaluated. The algorithms have been processed using the personal computer as well as the dSPACE 1202.

4.4.1 Performance Analysis of Synchronous Reference Frame Theory (SRFT)

The experimental investigation of the proposed SAPF on a three-phase system with conventional SRFT control is shown in Fig. 4.26. The SAPF operation is performed on a 40V, 50Hz supply. Fig. 4.26(a) shows the waveforms of phase 'a' source voltage (v_{sa}), source current (i_{sa}), load current (i_{La}) and DC link voltage (V_{dc}) under load unbalance by disconnecting the load from phase 'a' of the proposed system.

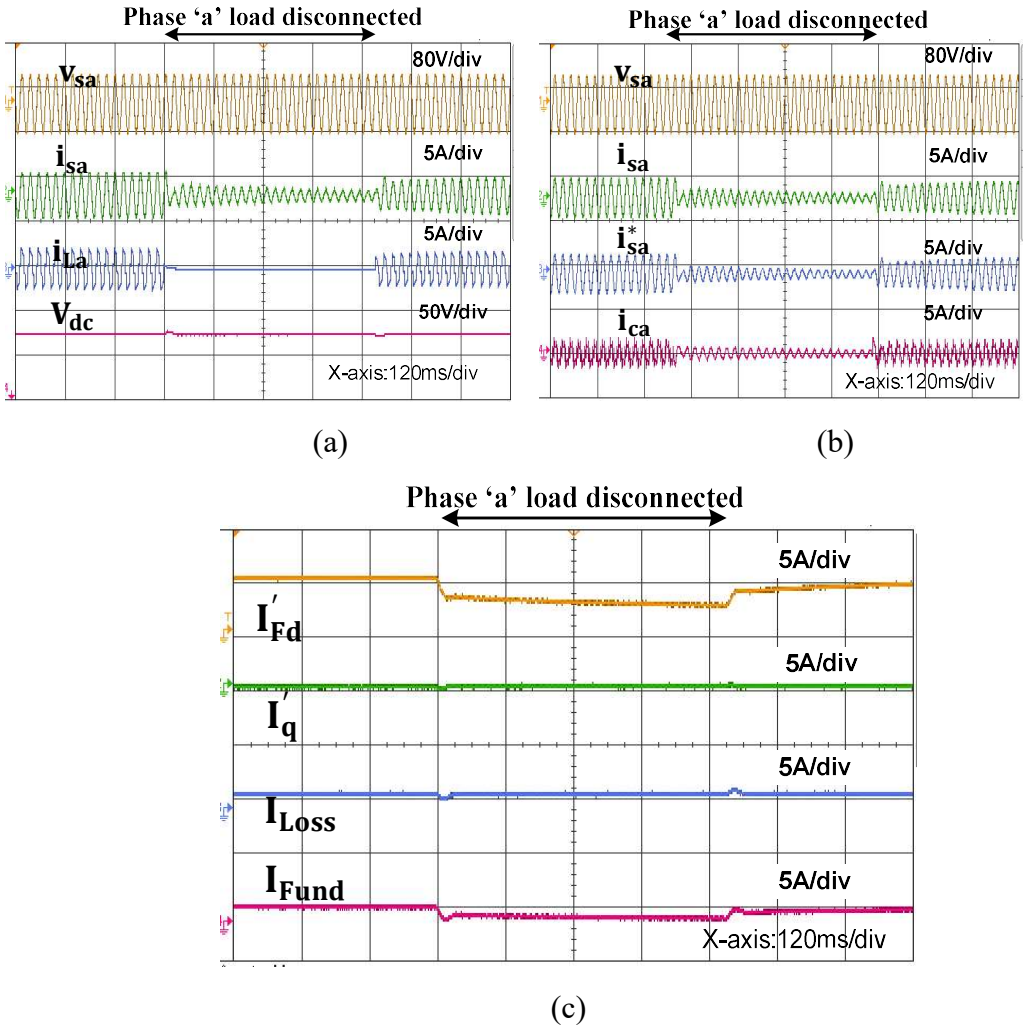

Fig. 4.26 Dynamic performance of the proposed system under load unbalancing with SRFT control scheme (a) Waveforms under load unbalancing (phase 'a' disconnected) (a) $v_{sc}, i_{sc}, i_{LC}, V_{dc}$ (b) $v_{sc}, i_{sc}, i^*_{sc}, i_{ca}$ (c) Intermediate signals I'_{Fd}, I_q, I_{loss}, I_{Fund}

The source current is sinusoidal under load unbalance and DC link voltage is maintained at its nominal value of 80V with a small voltage dip. While the reference source current (i^*_{sa}) and compensating current (i_{Ca}) decreases with load disconnection. Fig. 4.26(c) shows the intermediate signals of the SRFT control scheme with waveforms of the fundamental component of load current (I'_{Fd}), quadrature component of load

current (I'_q), DC link loss component (I_{loss}), and total current component (I_{Fund}). The fundamental component is estimated accurately and it is decreasing with load change. The SAPF operation with the SRFT control scheme is tested experimentally and the steady-state performance is shown in Fig. 4.27(a-d). The waveforms of the source voltage (v_{sabc}), source current (i_{sabc}), load current (i_{Labc}), THD of source current and THD of load current are seen in Fig. 4.27. It is found that the source current is sinusoidal and balanced having a THD of 4.60%. While the THD of load current is 21.15%.

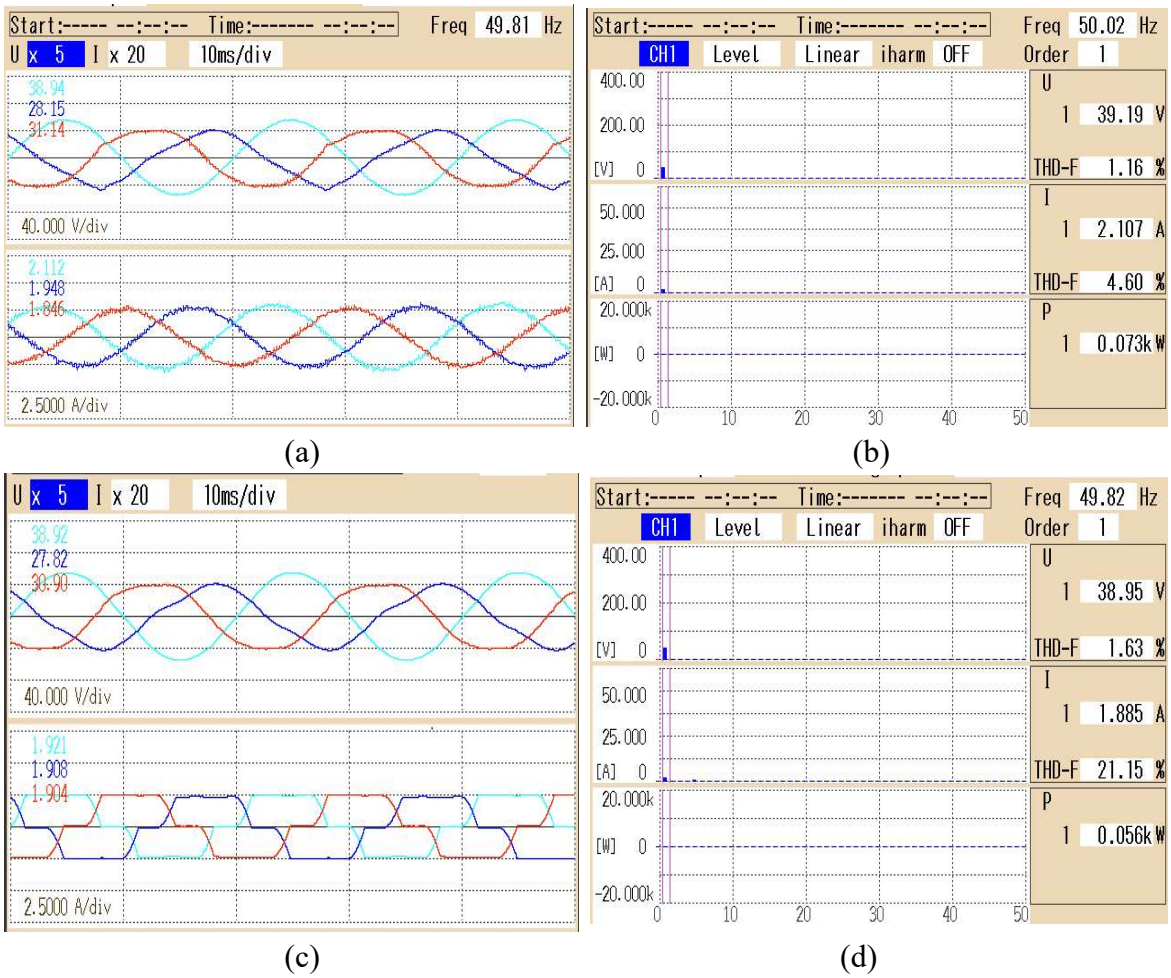

Fig. 4.27 Steady-state analysis of SRFT control scheme with nonlinear loads (a) source voltage and source current waveform (b) THD of source current (c) source voltage and load current (d) THD of load current.

4.4.2 Performance Analysis of ε − NSRLMMN adaptive control Technique

The experimental steady-state performance of SAPF on the proposed three-phase grid system with ε − NSRLMMN control scheme is shown in Figure 4.28(a-b). The waveforms of source voltage (v_{sa}), source current (i_{sa}), load current (i_{La}), and dc-link voltage (V_{dc}) are depicted in Fig. 4.28(a). The source current is sinusoidal and in phase

with the source voltage and thus power factor is near unity. Similarly, the waveforms of signals source voltage (v_{sa}), source current (i_{sa}), load current (i_{La}) and compensating current (i_{ca}) are shown in Fig. 4.28(b).

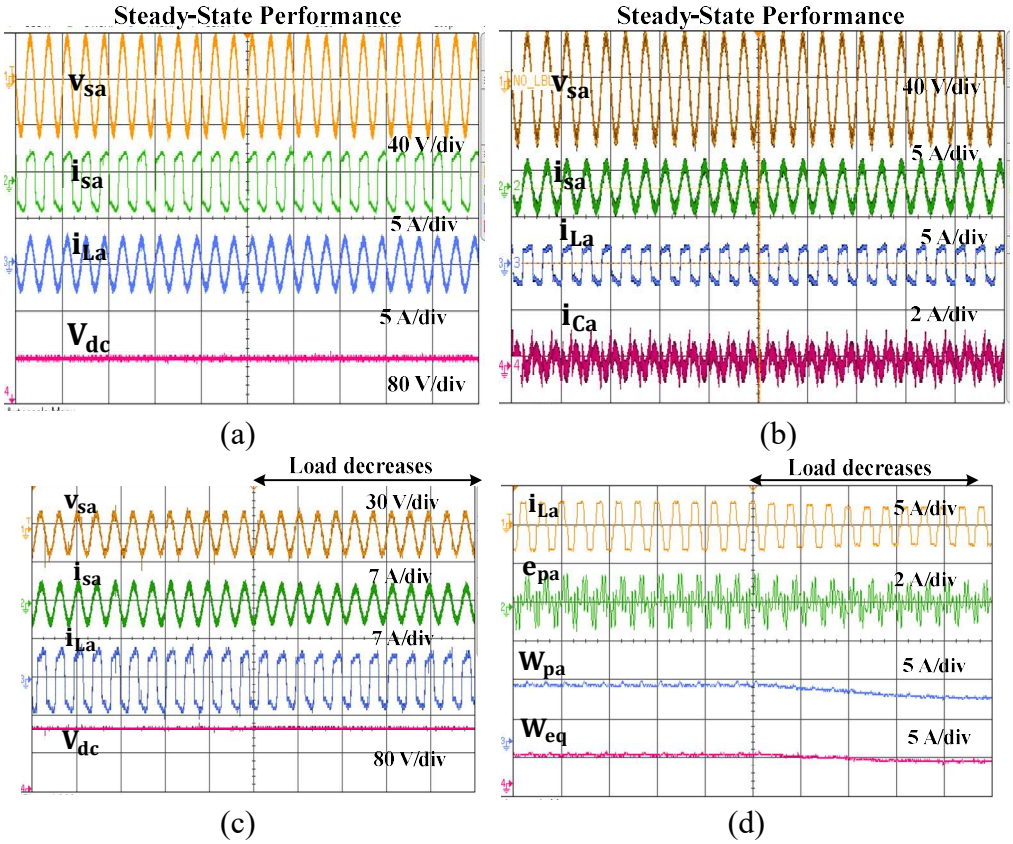

Fig.4.28 Dynamic Performance of SAPF with proposed $\varepsilon - NSRLMMN$ control algorithm (a) Steady-state performance with waveforms of phase-a having source voltage (v_{sa}), source current (i_{sa}), load current (i_{La}) and dc-link voltage (V_{dc}) (b) waveforms of having source voltage (v_{sa}), source current (i_{sa}), load current (i_{La}) and compensating current (i_{ca}) (c) dynamic performance of the system with load change (d) intermediate signals of $\varepsilon - NSRLMMN$ control algorithm

The dynamic performance of the proposed control algorithm is shown in Fig. 4.28(c-d) under load change. The load is decreased at some instant of time. With the decrease in load, the source current also reduces to maintain the load's active power demand. When the load decreases, the DC-link voltage increases momentarily but settles to its steady state value within a few cycles. The intermediate signals of the adaptive ε − NSRLMMN control algorithm are shown in Fig. 4.28(d). When load current decreases (i_{La}), thus decreasing the weight of phase-a (W_{pa}), and equivalent weight (W_{eq}) are founds decrease.

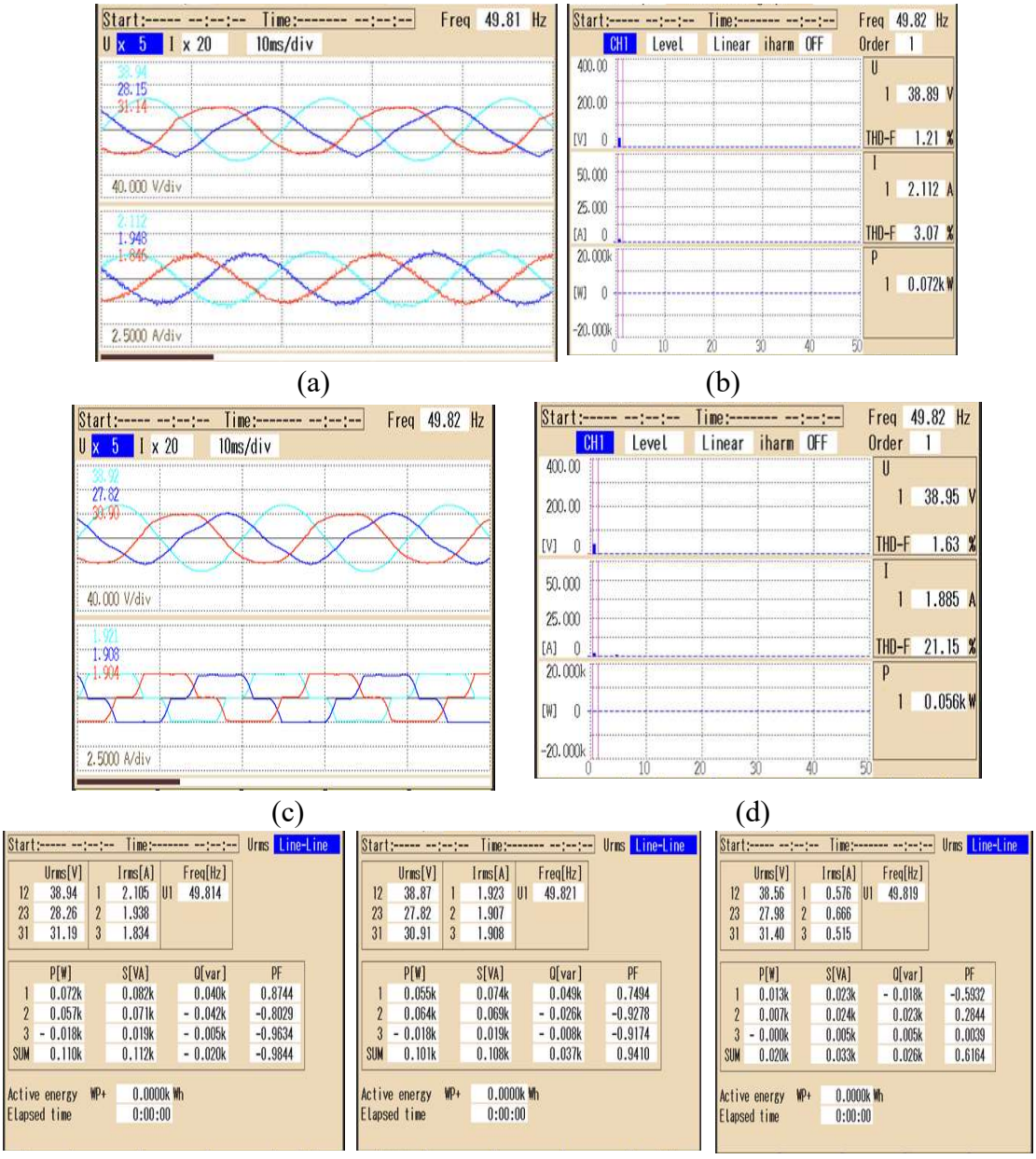

Fig. 4.29 Experimental results of SAPF with power analyser (a) waveform of v_{sabc} and i_{Labc} (b) THD of i_{La} (c) waveform of v_{sabc} and i_{sabc} (d) THD of i_{sa} (e) power generated by the grid or source (f) power demand of load (g) power generated by VSC.

The waveforms of source voltage, source current, and load current are shown in Fig. 4.29 (a-b). Figure 4.29(c-d) shows the waveforms of source voltage and source current and the THD of the source current is 3.07 % which is under IEEE-519 standard. While the THD of load current is 21.15 % shown in Fig. 4.29(b). The active power generated by the grid is 110 W and the load demands the active power of 101 W and reactive power demand of

37 Var as shown in Fig. 4.29(e-f). The entire reactive power demand of load is fulfilled by VSC.

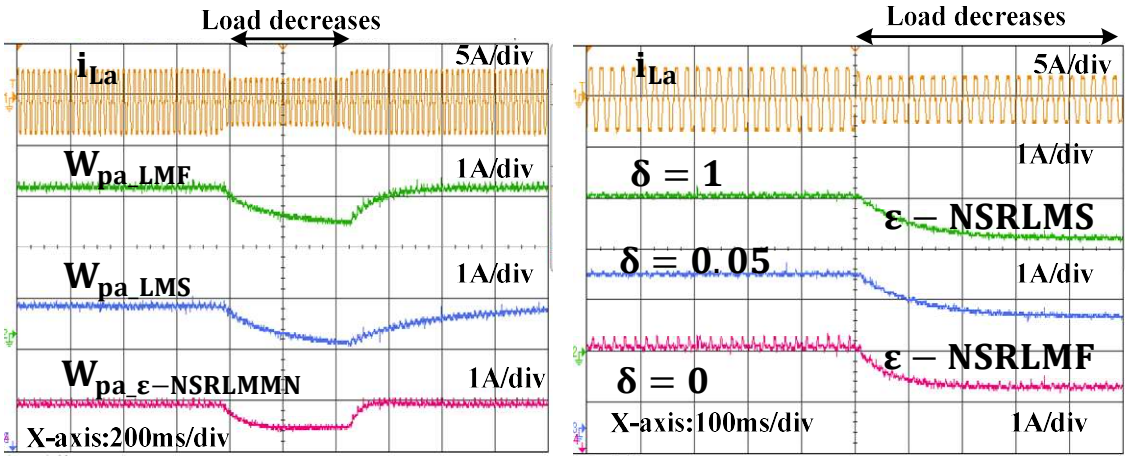

Fig. 4.30 Experimental results (a) Comparative convergence analysis of the active weight of phase-a of ε-NSRLMMN, LMF and LMS (b) Comparison of normalized active weight of phase- a learning curves of ε-NSRLMMN algorithm for different value of δ under dynamic condition

The convergence analysis of fundamental weight obtained through various adaptive LMF, LMS and ε-NSRLMMN is investigated under load change condition as shown in Fig.4.30(a). The active weight for phase-a convergences fast with proposed ε-NSRLMMN algorithm as compared to other two algorithms (LMS and LMF) without oscillations. The normalized active weight with different learning rate is shown in Fig. 4.30(b).

4.4.3 Performance Analysis of q-LMF based adaptive control Technique

Dynamic response of the proposed system with q-LMF control scheme is shown in Fig. 4.31. Fig. 4.31(a) shows the dynamic response of the system under load increase. The waveform of signals of phase 'a' source voltage (v_{sa}), source current (i_{sa}), load current (i_{La}) and DC link voltage (V_{dc}) are shown in Fig. 4.31(a). The source current decreases as the decrease in load to maintain the supply power constant. At the same time, the DC link voltage regulates its reference value due to the effectiveness of the PI controller. The DC link voltage slightly decreases with an increase in load for almost a cycle; after that, its regulates to its reference 80V, as shown in Fig. 4.31(a). The reference source current (i_{sa}^{*}) is sinusoidal and follows the sensed source current due to the proposed q-LMF control and HCC as shown in Fig. 4.31(b).

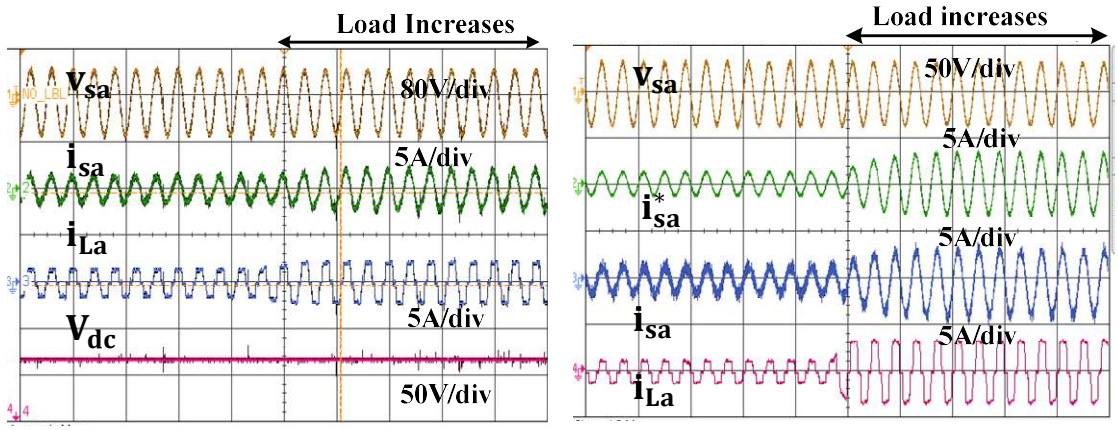

(a) (b)

Fig. 4. 31 Dynamic response of the proposed system having waveforms of signals $v_{sa}, i_{sa}, i_{La}, and\ V_{dc}$ (b) source voltage (v_{sa}), reference source current (i^*_{sa}), actual source current (i_{sa}), and load current (i_{La}) of phase-a under load unbalancing

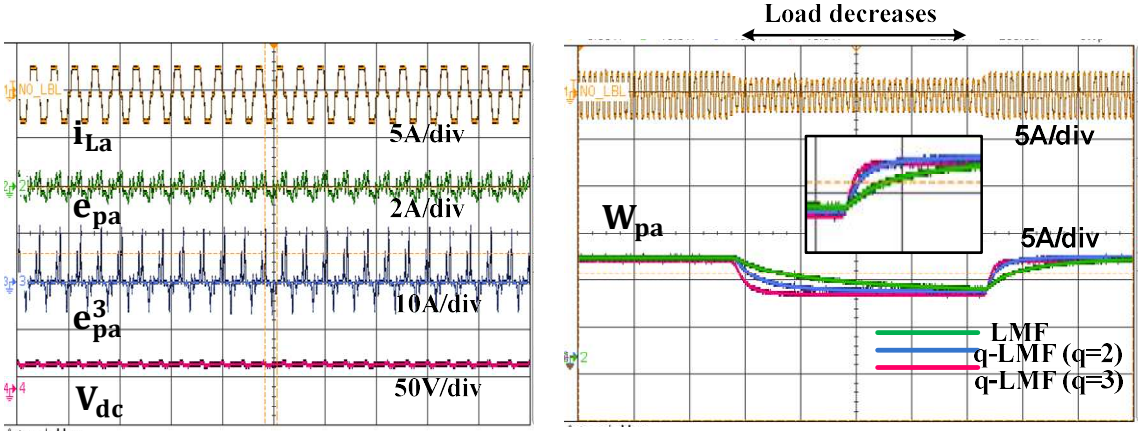

(a) (b)

Fig. 4.32 Intermediate signals of the proposed q-LMF-based control scheme with the waveforms of (a) $i_{La}, e_{pa}, e^3_{pa}, and\ V_{dc}$ (b) fundamental weight W_{pa} under load change.

The intermediate signals of the proposed control scheme based on q-LMF are shown in Fig. 4.32(a). The effectiveness of q calculus-based LMF on fundamental active load components under load unbalancing is shown in Fig. 4.32(b). The conventional LMF takes more time to converge under load unbalancing and reach a steady state. The conventional LMF takes around 4.5 cycles to reach the steady state position, while with q-LMF with q=2, G=3.5, the fundamental active load component takes 1 to 1.5 cycles to converge. When q=3, the fundamental active components converge the fastest but a small steady-state error is also obtained. When q=2, both convergence rate and steady-state performance are optimized. Thus, it is established from Fig. 4.32(b) that increasing the value of 'q' results in fast convergence but also results in a large steady-state error. These results also match the findings of simulation studies. Figures 4.33(a) and (b) show the

representations of source voltage and source current with current THD levels. The THD of the source current is achieved to be 2.99% with SAPF compensation and follows the IEEE 519 standards, while the THD of the source voltage is only 1.15%. Fig. 4.33(c) and (d) show the source voltage waveform and load current with their THD, respectively. The THD of load current is 21.63%.

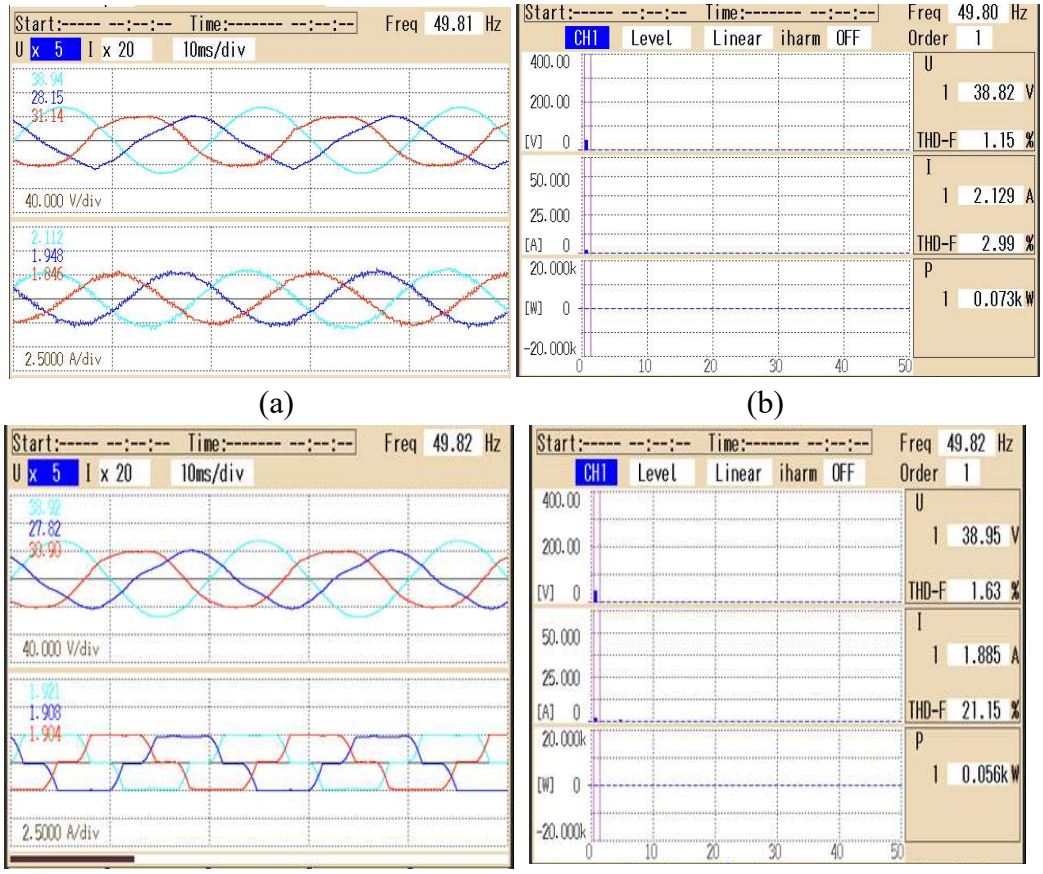

(a) (b)

(c) (d)

Fig. 4.33 Power analyser results of (a) waveforms of the source voltage and current (b) THD of source current (c) waveforms of source voltage and load current (d) THD of load current with q-LMF control scheme.

4.5 Comparative Performance analysis of control schemes of three-phase shunt active power filter

The performance of the q-LMF is contrasted with SRFT, and the ε − NSRLMMN control technique. These methods are all used for load compensation under the same system parameters. From each algorithm, the fundamental active load component under load unbalance conditions is extracted and compared for weight convergence in terms of oscillations, sampling time, PLL need, settling time, convergence rate, and THD in source

current. Table 4.2 and Fig. 4.34 are displayed to provide a more accurate comparison of performance among the mentioned control schemes.

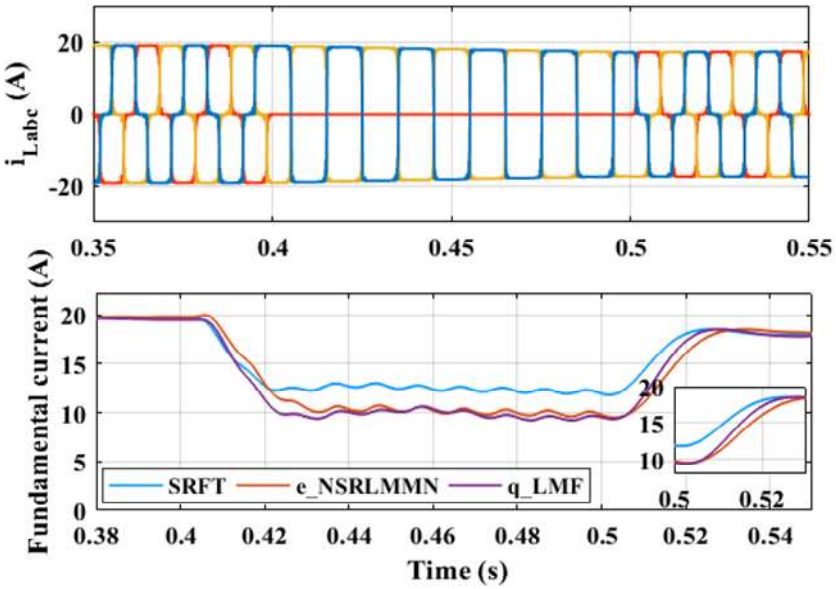

Fig. 4.34 Simulation-based Performance comparison of fundamental current under varying load during t=0.3s to 0.5s with SRFT, q-LMF, and $\varepsilon - NSRLMMN$

It is seen from Table 4.2, that the proposed q-LMF and ε − NSRLMMN control schemes perform much better than conventional SRFT control scheme-based SAPF for the proposed three-phase grid-connected PV system. All the mentioned control schemes can mitigate current related PQ issues and perform reactive power compensation. The THD of source current with proposed q-LMF with experimental setup is 2.99%, and 3.07% with ε − NSRLMMN. The convergence of fundamental load components under load change is faster with q-LMF and ε − NSRLMMN around 1 to 2 cycles as compared to SRFT.

Table 4. 2: Comparison of SRFT, $\varepsilon - NSRLMMN$, and q-LMF Control Schemes

S.No.	**Features**	**SRFT**	**ε − NSRLMMN**	**q-LMF**
1.	PLL Required	Required	Not Required	Not Required
2.	Transformation required	Yes	No	No
3.	Convergence	Slower (2 cycles)	Slower (3 cycles)	**Faster** (1.5 cycles)

4.	Oscillations in fundamental weights		More	Moderate	Less
5.	THD of current (Simulation)	Source Current	2.46%	1.31%	**0.82%**
		Load Current	27.06%	26.4%	24.89%
6.	THD of current (Experimental)	Source Current	4.60%	3.07%	**2.99%**
		Load Current	21.15%	21.15%	21.63%
7.	Error		More	Moderate	Less
8.	DC link voltage oscillations		8V to 7V	4V to 5V	2V to 3V
9.	Sampling time		$60\mu s$	$50\mu s$	$50\mu s$

4.5 Conclusions

The design, mathematical modelling, and analysis of three-phase SRFT, ε − NSRLMMN, and q-LMF algorithms for SAPF control and PV integration in three-phase grid-connected systems are covered in this chapter. Using MATLAB Simulink software, the results were obtained, and hardware investigations were used to validate them. Tests were conducted on three-phase systems with and without PV integration, under situations of load unbalancing and variable solar irradiation. This chapter presents a thorough control analysis of the developed systems. The system that performs best with q-LMF is followed by ε − NSRLMMN and SRFT. In both steady state and dynamic state settings, the SRFT approach results demonstrate continuous persistent oscillations. The algorithms q-LMF and e-NSRLMMN rely on adaptive control. Algorithms trained in real time can respond quickly and track changes more quickly in a variety of loading and radiation scenarios. The q-LMF behaves in both steady state and dynamic states with nearly no oscillations and a very quick transient response. The limitations of traditional time domain algorithms are addressed by the real-time adaptive methods q-LMF and e-NSRLMMN. However,

the gain parameters must be adjusted for SRFT algorithms. The outcomes of the simulation and the hardware agree.

CHAPTER 5

DESIGN AND CONTROL OF SERIES ACTIVE POWER FILTER FOR GRID CONNECTED PV SYSTEM

5.1 Design of three-phase grid-connected DVR

The growth of sustainable energy now heavily depends on the integration of renewable energy sources into the current electrical system. Due to their abundance and favorable effects on the environment, photovoltaic (PV) systems are among the most extensively used types of renewable energy generation. The stability and dependability of the electrical grid may be jeopardized by the intermittent nature of solar power output. Innovative approaches, like the coupling of three-phase grid-connected PV systems with dynamic voltage restorers (DVRs), have been developed to address these problems. To reduce voltage sags, swells, and transients in the electrical grid, advanced power electronic devices known as dynamic voltage restorers are used. When working under unusual circumstances, they are particularly effective at keeping the source's voltage within the established limits. DVRs continuously check the source voltage and react to voltage fluctuations quickly by injecting or absorbing reactive power to get the voltage back to normal. A battery energy storage system (BESS) is a system that stores electrical energy in batteries for later use. By injecting or absorbing active and reactive power, BESS can respond quickly to grid disruptions and aid in grid stabilization. To improve the VSC's capacity to respond to grid voltage disturbances, the BESS is integrated with it. The DVR recognizes the disturbance when a voltage sag or transient happens and swiftly injects or absorbs reactive power to reduce the voltage deviation. The BESS can simultaneously offer more active and reactive power support. A battery is needed at the VSC's DC bus due to the DVR injects active power if the injected voltage and current are in phase.

DVRs can compensate for voltage fluctuations caused by the intermittent nature of solar power generation, ensuring consistent and stable power delivery to the grid or source. A three-phase, three-wire AC supply, IGBT switches, short-circuit impedance, and three single-phase transformers make up the proposed system. The three-phase DVR

with BESS at the DC side is linked to important loads, as seen in Fig. 5.1. Even when PQ problems arise at the supply end, the DVR is controlled to adjust the voltage across the load (v_{Labc}) with rated magnitude. With a series transformer, which will introduce compensating voltage ($v_{cabc(inj)}$) into the line, the suggested three-phase DVR is connected to a three-phase line. To filter the ripples in the injected voltage, a second ripple filter made up of capacitance and resistance is connected across the series transformer (T_r). In Fig. 5.1, the terminal voltage at the PCC is depicted as v_{sa}, v_{sb}, v_{sc} three-phase, 400V, 10KVA, 50Hz system is comprised. The maximum voltage required by the critical loads will determine the voltage rating of the VSC. If the BESS DVR system is used, the voltage injected per phase is equal to 20% of the phase voltage.

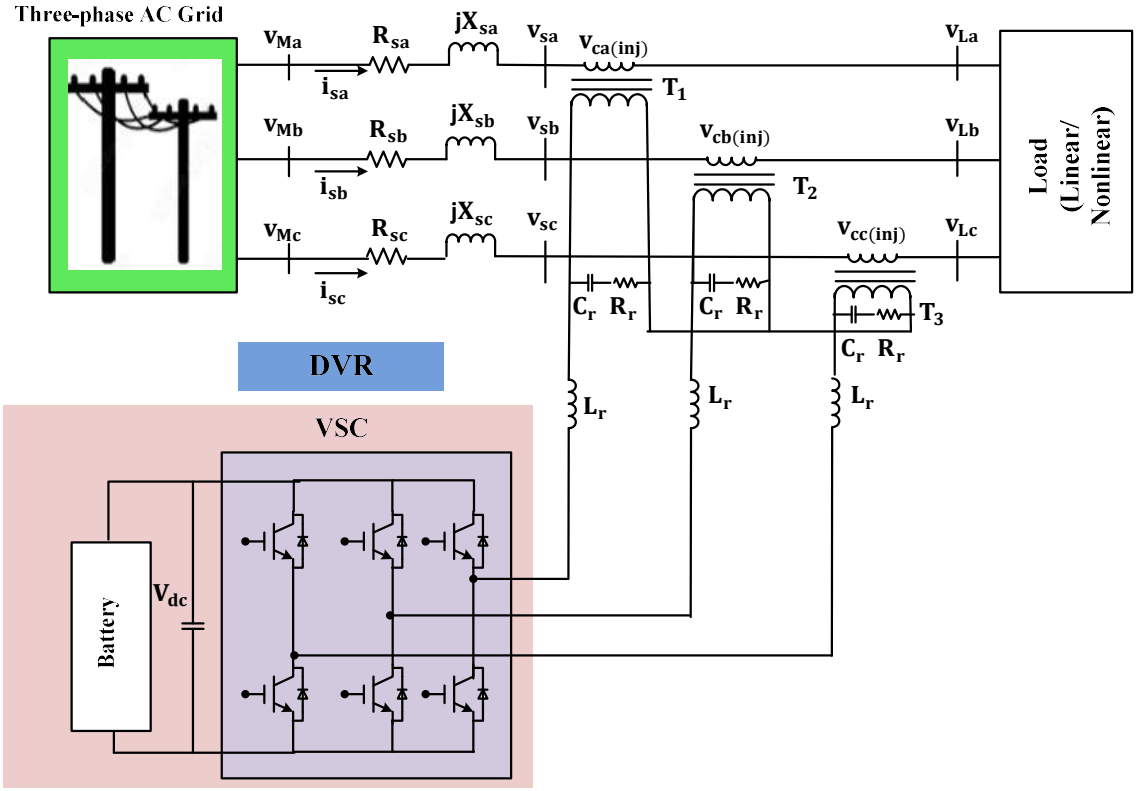

Fig. 5.1 Schematic diagram of a three-phase battery-supported DVR system

5.1.1 Rating of Injection Transformer of DVR

Several factors have been considered for selecting the rating of series injection transformer DVR capacity, voltage sag requirement, calculation of required DVR current, select DVR rating. The DVR capacity depends on specific applications and the level of voltage support needed. The value of DVR capacity is selected as 10kVA. The maximum

voltage sag on source voltage per phase that the DVR will mitigate is calculated as $230.9 \times 0.8 = 184.72V$. The required DVR's current rating is calculated as

$$\sqrt{3}v_{Sa}i_{Sa} = 10000 \quad (5.1)$$

$$i_{Sa} = 25A$$

The series injection voltage required to be injected per phase is given by Eq. (5.2)

$$v_{ca(inj)} = \sqrt{v_{sa}^2 - v_{sag(max)}^2} = \sqrt{230.9^2 - 184.72^2} = 138.54V \quad (5.2)$$

Transformer capacity (kVA), $S = \frac{3 \times V_{Ca(inj)} I_{sa}}{1000} = 10.39kVA$ (5.3)

Table 5. 1: Parameter Values used in Simulation and Experimental

Element	**Parameters**	**Simulation Values**	**Using OPALRT**
Supply side	Source	415V(rms),50Hz	415V(rms),50 Hz
Series Active Power Filter	Lithium-ion Battery	260V, 1.2Ah	260V, 1.2Ah
	Interfacing filter inductor	L_r=3.2mH	L_r=2mH
	Ripple Filter	$R_r = 1\Omega$, $C_r = 31.8\mu F$	$R_r = 1\Omega$, $C_r = 31.8\mu F$
	Transformer Rating	10kVA	10kVA
	Switching Frequency	f_s=5kHz	f_s=5kHz
Loads	3-Ø diode rectifier	----	----
	R-L Load	R_L=30Ω and L_L=5mH	R_L=30Ω and L_L=5mH

5.1.2 Interfacing Inductor of the VSC of DVR

The KVA rating of the series injection transformer will be the same as the KVA rating of VSC, i.e.,10.39 kVA. For BESS DVR, the DC voltage is considered 300V. The interfacing inductor L_r is calculated [] as

$$L_r = \frac{n\times(\sqrt{3/2}mV_{DC})}{6a_{sw}\Delta I_s} = 0.946mH \approx 1mH \quad (5.4)$$

where n is the transformation ratio of the series injection transformer, m is the modulation index, f_{sw} is the switching frequency and ΔI_s is the ripple current of DVR. A ripple filter is designed to filter the switching frequency ripples that occur due to a series injection transformer. The expression for ripple filter which consists of series resistance (R_r) and series capacitor (C_r) is given as

$$\frac{f_s}{2} = \frac{1}{2\pi R_r C_r} \quad (5.5)$$

For, $R_r = 1\Omega, C_r = 31.8\mu F$

5.1.3 Capacity of BESS

The duration of the compensation period and the depth of the voltage sag affect the BESS for the DVR's capacity. Additionally, the BESS needs to have enough power to compensate for voltage sags. The size of the BESS's capacity is determined by the amount of time and power needed to compensate for voltage sags, the depth of discharge, and the battery's efficiency. The minimum capacity of BESS depends on the required power during voltage sag conditions. The minimum capacity of BESS is calculated as

$$Cap_{min\,(Wh)} = \frac{Power\,(W)\times Duration(h)}{DoD(\%)\times Efficiency(\%)} \quad (5.6)$$

where DoD is the depth of discharge. These technologies have an approximate efficiency range of 92% to 96% and a Depth of Discharge (DOD) range of 80% to 100% for lithium-ion batteries.

5.2 Control Technique of three-phase grid connected DVR

The BESS is used to inject or absorb active power into the source based on the source voltage conditions. When the source voltage is low, the BESS can inject power to support the source, and when the source voltage is high, it can absorb excess power. The DVR

function immediately injects or absorbs active and reactive power to quickly restore the voltage to its nominal value in the event of voltage sags or swells. This calls for quick action, which can be accomplished with various control strategies.

Continuous monitoring of PCC voltage is required with a PLL synchronization technique. When the voltage injected by a DVR is in-phase with the current, it means that the DVR is not only compensating for the voltage magnitude but also for the real power. In this scenario, the DVR does not just correct voltage distortions (sags, swells, or harmonics) but also contributes real power to the system. The series active power filter also known as DVR injects compensating voltage in series with the grid voltages. The DVR will inject the required voltage to maintain the load voltages across critical loads when voltage-related PQ issues such as voltage sag, voltage swell, voltage unbalance, voltage flicker, and harmonics occur in the grid. The gating pulses for VSC's switches are obtained through the PWM control.

5.2.1 Synchronous Reference Frame Theory (SRFT) Control Technique

The control scheme for the proposed DVR is shown in Fig. 2. The control scheme for the three-phase DVR is based on a Synchronous Reference Frame based controller. The sensed load voltages (v_{Labc}) and sensed PCC voltage (v_{sabc}) are utilized to get the switching signals of IGBT switches.

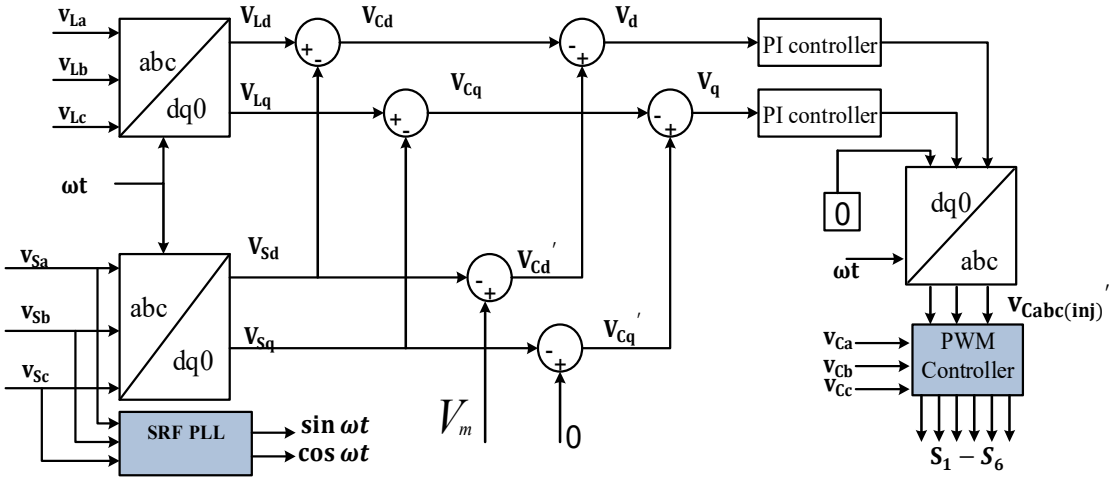

Fig. 5.2 Block Diagram of proposed SRF-based control scheme for BESS-DVR.

The load voltages (v_{La}, v_{Lb}, v_{Lc}) are transformed into its rotating reference frame component (d-q-0) component using Park transformation. The synchronizing signals

$(\sin \omega t\,, \cos \omega t)$ are obtained using conventional three-phase PLL. The PLL is suitable for generating the synchronizing signals accurately under voltage disturbances viz. sag, swell, unbalance, and so on. The Park conversion for load voltages is given by Eq. (5.7),

$$\begin{bmatrix} V_{Ld} \\ V_{Lq} \\ V_{L0} \end{bmatrix} = \frac{2}{3} \begin{bmatrix} \cos \omega t & -\sin \omega t & 1/2 \\ \cos\left(\omega t - \frac{2\pi}{3}\right) & -\sin\left(\omega t - \frac{2\pi}{3}\right) & 1/2 \\ \cos\left(\omega t + \frac{2\pi}{3}\right) & \sin\left(\omega t + \frac{2\pi}{3}\right) & 1/2 \end{bmatrix} \begin{bmatrix} V_{La} \\ V_{Lb} \\ V_{Lc} \end{bmatrix} \tag{5.7}$$

Similarly, the Park transformation of source voltages is given by Eq. (5.8)

$$\begin{bmatrix} V_{sd} \\ V_{sq} \\ V_{s0} \end{bmatrix} = \frac{2}{3} \begin{bmatrix} \cos \omega t & -\sin \omega t & 1/2 \\ \cos\left(\omega t - \frac{2\pi}{3}\right) & -\sin\left(\omega t - \frac{2\pi}{3}\right) & 1/2 \\ \cos\left(\omega t + \frac{2\pi}{3}\right) & \sin\left(\omega t + \frac{2\pi}{3}\right) & 1/2 \end{bmatrix} \begin{bmatrix} V_{sa} \\ V_{sb} \\ V_{sc} \end{bmatrix} \tag{5.8}$$

The direct component of the series injected voltage (V_{cd}) is the difference between direct component actual load voltages (V_{Ld}) needed at the load side and supplied source voltages (V_{sd}). The expression of injected voltage is given by Eq. (5.9),

$$V_{cd} = V_{Ld} - V_{sd} \tag{5.9}$$

Similarly, the quadrature component of the series injected voltage (V_{Cq}) is given by Eq. (5.10),

$$V_{Cq} = V_{Lq} - V_{sq} \tag{5.10}$$

V_m is the reference value of amplitude of load voltage which is constant under voltage disturbance at the source side, i.e., sag, swell, unbalance, and so on. Under the condition of voltage swell at the source side, the direct component of the source voltages (V_{sd}) will increase and become greater than the reference load voltage (V_m). Thus, the resultant series injecting voltage (V'_{Cd}) will decrease as compared to pre-swell conditions. The expression for resultant reference series injecting voltage (V'_{Cd}) is given by Eq. (5.11) and (5.12),

$$V'_{Cd} = V_m - V_{sd} \tag{5.11}$$

$$V'_{Cq} = V_{sq} \tag{5.12}$$

The voltage errors between a d-q-0 component of actual series injected voltage and d-q-0 components of reference series injected voltages $(V_d \text{ and } V_q)$ are passed through two PI controllers for voltage regulation [18]. Applying reverse Park's transformation to obtain reference series injected voltage in a-b-c frame which is given by

$$\begin{bmatrix} v'_{Ca} \\ v'_{Cb} \\ v'_{Cc} \end{bmatrix} = \begin{bmatrix} \cos \omega t & \sin \omega t & 1 \\ \cos\left(\omega t - \frac{2\pi}{3}\right) & \sin\left(\omega t - \frac{2\pi}{3}\right) & 1 \\ \cos\left(\omega t + \frac{2\pi}{3}\right) & \sin\left(\omega t + \frac{2\pi}{3}\right) & 1 \end{bmatrix} \begin{bmatrix} V_d \\ V_q \\ V_0 \end{bmatrix} \tag{5.13}$$

The PWM controller will generate the switching signals $(S_1 - S_6)$ for DVR when the actual series injected voltage (v_{Cabc}) is compared with reference series injected voltage (v'_{Cabc}). The PWM controller has a fixed switching frequency of 10 kHz.

5.2.2 Multiple second and third order generalized integrator (MSTOGI) SRF-based control scheme

5.2.2.1 Switching Signal Generation

The control scheme for the proposed DVR is shown in Fig.5.3. The control scheme for the three-phase DVR is based on a Synchronous Reference Frame based controller with MSTOGI PLL (MSTOGI-SRF). The sensed load voltages (v_{Labc}) and sensed PCC voltage (v_{sabc}) are utilized to get the switching signals of IGBT switches. The load voltages (v_{La}, v_{Lb}, v_{Lc}) are transformed into its rotating reference frame component (d-q-0) component using Park transformation. The synchronizing signals $(\sin \omega t, \cos \omega t)$ are obtained using MSTOGI PLL. The MSTOGI PLL is suitable for generating the synchronizing signals accurately under voltage disturbances viz. sag, swell, flicker, noise, unbalance, harmonics, and so on. The fundamental load voltage and source voltage is obtained using Park conversion for load voltages is given by Eq. (5.14)

$$\begin{bmatrix} V_{Ld} \\ V_{Lq} \\ V_{L0} \end{bmatrix} = \frac{2}{3} \begin{bmatrix} \cos \omega t & -\sin \omega t & 1/2 \\ \cos\left(\omega t - \frac{2\pi}{3}\right) & -\sin\left(\omega t - \frac{2\pi}{3}\right) & 1/2 \\ \cos\left(\omega t + \frac{2\pi}{3}\right) & \sin\left(\omega t + \frac{2\pi}{3}\right) & 1/2 \end{bmatrix} \begin{bmatrix} v_{La} \\ v_{Lb} \\ v_{Lc} \end{bmatrix} \tag{5.14}$$

Similarly, Park transformation of source voltages is given by Eq. (5.15)

$$\begin{bmatrix} V_{sd} \\ V_{sq} \\ V_{s0} \end{bmatrix} = \frac{2}{3}\begin{bmatrix} \cos\omega t & -\sin\omega t & 1/2 \\ \cos\left(\omega t - \frac{2\pi}{3}\right) & -\sin\left(\omega t - \frac{2\pi}{3}\right) & 1/2 \\ \cos\left(\omega t + \frac{2\pi}{3}\right) & \sin\left(\omega t + \frac{2\pi}{3}\right) & 1/2 \end{bmatrix}\begin{bmatrix} v'_{sa} \\ v'_{sb} \\ v'_{sc} \end{bmatrix} \quad (5.15)$$

The direct component of the series injected voltage (V_{cd}) is the difference between direct component actual load voltages (V_{Ld}) needed at the load side and supplied source voltages (V_{sd}). The expression for injected voltage (or DVR voltage) is given by Eq. (5.16),

$$V_{Cd} = V_{Ld} - V_{sd} \quad (5.16)$$

Similarly, the quadrature component of the series injected voltage (V_{Cq}) is given by Eq. (5.17),

$$V_{Cq} = V_{Lq} - V_{sq} \quad (5.17)$$

V_m is the reference value of amplitude of load voltage which is constant under voltage disturbance at the source side, i.e., sag, swell, unbalance, and so on. Under the condition of voltage swell at the source side, the direct component of the source voltages (V_{sd}) will increase and become greater than (V_m). Thus, the resultant series injecting voltage (V'_{Cd}) will decrease as compared to pre-swell conditions. The expression for resultant series injecting voltage (V'_{Cd}) is given by Eq. (5.18) and (5.19),

$$V'_{Cd} = V_m - V_{sd} \quad (5.18)$$

$$V'_{Cq} = V_{sq} \quad (5.19)$$

The voltage errors between a d-q-0 component of actual series injected voltage and d-q-0 components of reference series injected voltages $(V_d \text{ and } V_q)$ are passed through two PI controllers for voltage regulation. Applying reverse Park's transformation to obtain reference series injected voltage in a-b-c frame which is given by

$$\begin{bmatrix} v'_{Ca} \\ v'_{Cb} \\ v'_{Cc} \end{bmatrix} = \begin{bmatrix} \cos\omega t & \sin\omega t & 1 \\ \cos\left(\omega t - \frac{2\pi}{3}\right) & \sin\left(\omega t - \frac{2\pi}{3}\right) & 1 \\ \cos\left(\omega t + \frac{2\pi}{3}\right) & \sin\left(\omega t + \frac{2\pi}{3}\right) & 1 \end{bmatrix}\begin{bmatrix} V_d \\ V_q \\ V_0 \end{bmatrix} \quad (5.20)$$

The PWM controller will generate the switching signals $(S_1 - S_6)$ for DVR when the actual series injected voltage (v_{Cabc}) and reference series injected voltage (v'_{Cabc}). The PWM controller has a fixed switching frequency of 10 kHz.

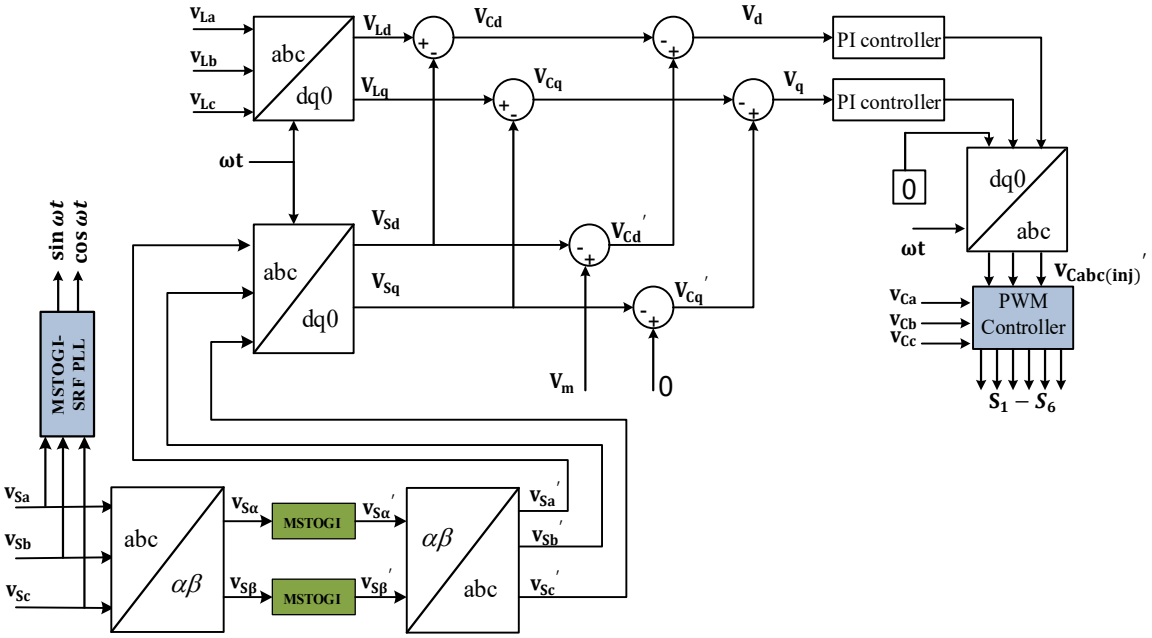

Fig. 5.3 Block Diagram of proposed MSTOGI-SRF-based control scheme for BESS-DVR.

5.2.2. MSTOGI SRF PLL for Grid Synchronization

A precise PLL result not only reduces total harmonic distortion (THD) but also improves source current waveform quality, ensuring grid currents remain in phase with source voltages and therefore improving the stability of grid-connected systems. However, substantial power quality issues in grid-connected systems such as voltage waveform distortions, harmonics, voltage frequency changes, and so on, degrade PLL performance. It is important to utilize accurate phase locking under nonideal grid voltage conditions. Despite conventional SRF PLL being used quite frequently, MSTOGI is a better PLL scheme. Conventional SRF PLL is widely used due to its fast dynamic response and its simple structure, but under voltage-related PQ issues, it provides errors while estimating the fundamental frequency. MSTOGI PLL is quite effective in grid synchronization under voltage harmonics, sag, swell, and voltage imbalance. The MSTOGI is a combination of SOGI and TOGI.

Fig.5.3 shows the block diagram of the proposed MSTOGI-SRF-based PLL. The three-phase source voltages are converted into the αβ components using Clark Transformation. The transformation gives $v_{s\alpha}$ and $v_{s\beta}$ component. Both $v_{s\alpha}$ and $v_{s\beta}$ are fed into the MSTOGI block to generate corresponding signals $S_{\alpha}, S_{q\alpha}, S_{\beta}, S_{q\beta}$. The signals $S_{q\beta}$ is subtracted from S_{α} to obtain fundamental positive sequence component $S_{\alpha P}$.

Another signal $S_{q\alpha}, S_{\beta}$ are added to obtain quadrature fundamental positive sequence $S_{\beta P1}$. These two orthogonal signals are converted into dq0 components of source voltages. These signals are further fed to SRF PLL for grid synchronization and estimating the angular frequency (ωt). The synchronizing frequency ω is feedback to MSTOGI to make it frequency adaptive. The angular frequency ω_c is added to increase the speed of PLL. The generalized structure of SOGI as shown in Fig.5.4, has two orthogonal signals u_1 and u_2, which have equal magnitude and 90° phase shift. While signals S_{α} and $v_{s\alpha}$ have the same magnitude and phase. The transfer functions of SOGI [106] are expressed below

$$G_1(s) = \frac{u_1}{v_{s\alpha}} = \frac{k\omega_0 s}{s^2+k\omega_0 s+\omega_0^2} \tag{5.21}$$

$$G_2(s) = \frac{u_2}{v_{s\alpha}} = \frac{k\omega_0^2}{s^2+k\omega_0 s+\omega_0^2} \tag{5.22}$$

By combining the effect of both SOGI and TOGI [106], a resultant MSTOGI is obtained. The transfer functions of MSTOGI [106] are given by Eq. (5.23) and (5.24),

$$G_3(s) = \frac{S_{\alpha}}{v_{s\alpha}} = \frac{k\omega_0(s^2+\omega_0^2)}{(s+\omega_0)(s^2+k\omega_0 s+\omega_0^2)} \tag{5.23}$$

$$G_4(s) = \frac{S_{q\alpha}}{v_{s\alpha}} = \frac{k\omega_0 s(\omega_0-s)}{(s+\omega_0)(s^2+k\omega_0 s+\omega_0^2)} \tag{5.24}$$

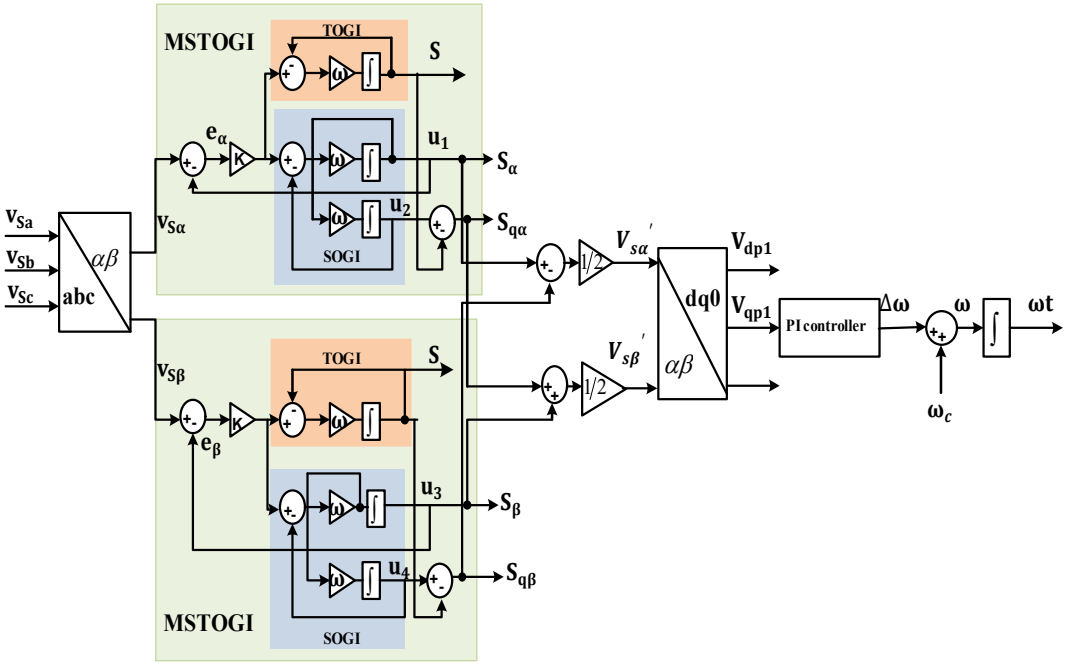

Fig. 5.4 Block Diagram of proposed MSTOGI PLL for grid synchronization.

5.3 Simulation Results

5.3.1 Performance analysis of SRFT based control of DVR

The performance of the proposed SRFT control scheme of a three-phase grid-connected DVR is investigated under various disturbances at grid supply or supply voltage. The various disturbances that are considered, are voltage sag, swell, and imbalance. The transient response of DVR is shown in this section with the following cases:

Case I: Balanced Voltage Sag of 20% in the source voltages

Case II: Balanced Voltage Swell of 20% in the source voltages

Case III: Voltage unbalanced with 20% sag in source voltages (Phase 'a')

Case I: Voltage Sag at the Source side

One of the most prominent voltage-related PQ issues is voltage sag. In this case scenario, a voltage sag of 20% is applied in the source voltages (v_{sabc}). At t=0.3s to 0.4s, a voltage sag is applied for 5 cycles in source voltages. The load voltages must be balanced and sinusoidal with the desired magnitude even during voltage sag conditions. The PCC voltage (v_{sabc}), load voltages (v_{Labc}), series injecting compensating voltage (v_{Cinj}), grid current (i_{sabc}), a direct component of load and source voltages (V_{Ld} and V_{sd}), and battery DC voltage (V_{dc}) is shown in Fig. 5.5. During voltage sag condition at t=0.2 to 0.3s, the signal V_{sd} is decreased but load voltages have constant magnitude due to series compensating voltage. The required load voltages at voltage sag condition are fed by a series injection transformer at PCC. The grid current is sinusoidal at voltage sag condition due to its control technique. The Battery supported DVR shows DC voltage having a very small variation of 2V.

Case II: Voltage Swell at the source side

Another most common disturbance at source voltages is voltage swell. At t=0.45 to 0.55s, voltage swell is developed at source voltages which is a 20% increase of source voltages for 5 cycles. Before t=0.45s the system is operating at steady-state. The voltage swell is cleared after 5 cycles. The battery DC voltage is slightly increased due to the transient effect but gets stable within 1 cycle. The direct component of source voltages is

increased but load voltages are maintained to their rated value. The response of the proposed system under voltage swell conditions is depicted in Fig.5.6.

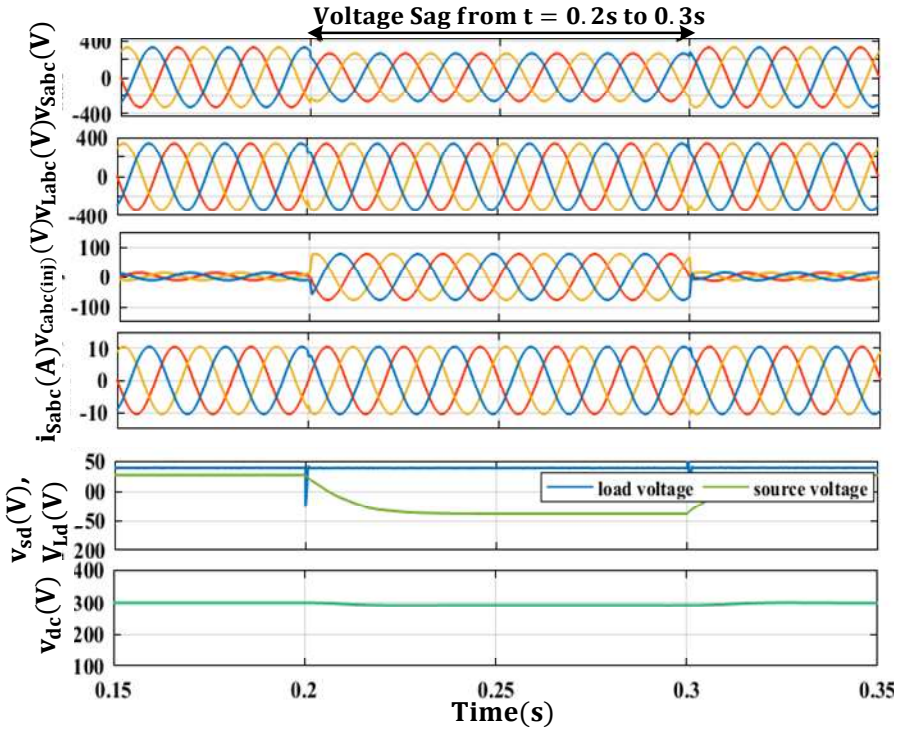

Fig. 5.5 Simulation result of proposed DVR system under Voltage Sag condition

II: Voltage Swell at the source side

Another most common disturbance at source voltages is voltage swell. At t=0.45 to 0.55s, voltage swell is developed at source voltages which is a 20% increase of source voltages for 5 cycles. Before t=0.45s the system is operating at steady-state. The voltage swell is cleared after 5 cycles. The battery DC voltage is slightly increased due to the transient effect but gets stable within 1 cycle. The direct component of source voltages is increased but load voltages are maintained to their rated value. The response of the proposed system under voltage swell conditions is depicted in Fig.5.6.

Case III: Voltage unbalance at the Source side

In this case study, voltage unbalancing is created at source voltages. A voltage unbalancing is provided in phase 'a'. Due to source voltages unbalancing, a slight regulation in Battery DC voltage is seen in Fig. 5.7. Despite voltage imbalance the load voltages are balanced and have constant magnitude. It is seen in Fig.5.7 the voltage

unbalancing occurs for 5 cycles (t=0.2s to t=0.3s). The battery DC voltage has slightly decreased. The source current is sinusoidal under linear load conditions.

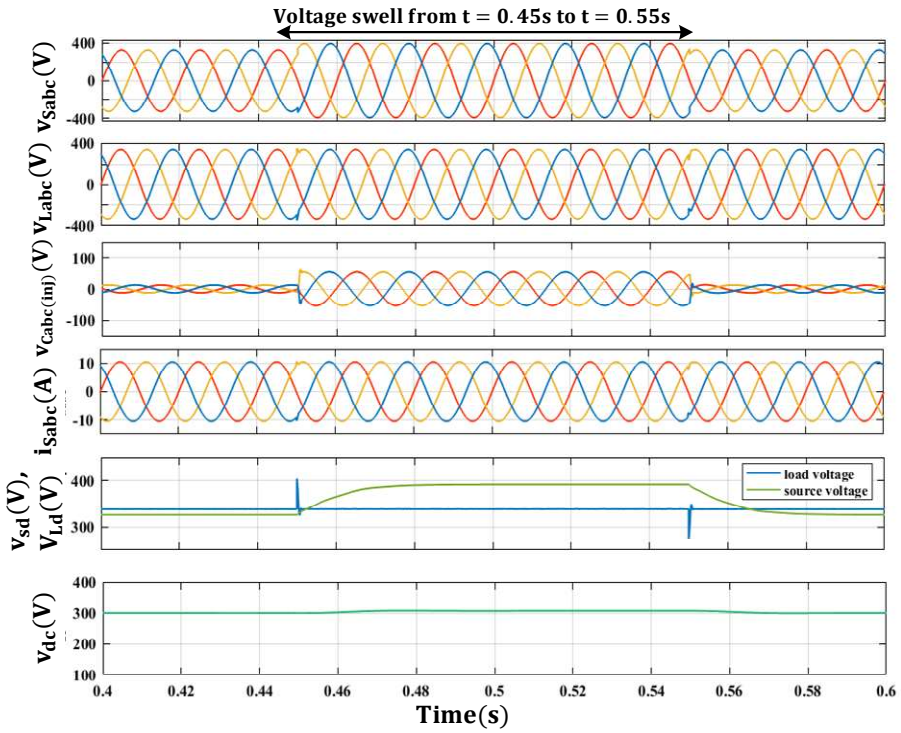

Fig. 5.6 Simulation result of proposed DVR system under Voltage Swell condition

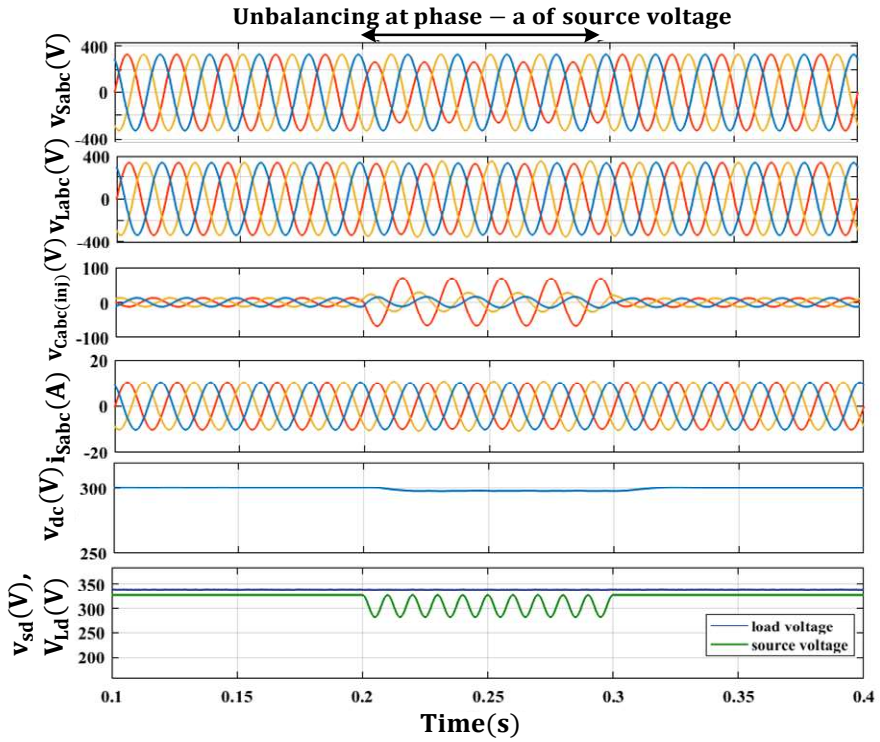

Fig. 5.7 Simulation result of proposed DVR system under Voltage Unbalancing condition

5.3.2 Performance analysis of MSTOGI-SRF based control of DVR

The performance of the proposed MSTOGI-SRF control scheme of a three-phase grid-connected DVR is investigated under various disturbances at grid supply or supply voltage. The various disturbances that are considered, are voltage sag, swell, imbalance, and harmonics. The transient response of DVR is shown in this section with the following cases:

Case I: Balanced Voltage Sag of 20% in source voltages

Case II: Balanced Voltage Swell of 20% in source voltages

Case III: Balanced Voltage harmonics (5^{th} and 7^{th} order harmonic)

Case IV: Voltage unbalanced with 20% sag in source voltages (Phase 'a')

Case V: Phase jump

Case VI: Frequency Variation

Case I: Voltage Sag in the source side

One of the most prominent voltage-related PQ issues is voltage sag. In this case scenario, a voltage sag of 20% is applied at the source voltages (v_{sabc}). At t=0.3s to 0.4s, a voltage sag is applied for 5 cycles in source voltages. The load voltages must be balanced and sinusoidal with the desired magnitude at voltage sag conditions. The PCC voltage (v_{sabc}), load voltages (v_{Labc}), series injecting compensating voltage (v_{Cinj}), grid current (i_{sabc}), a direct component of load and source voltages (V_{Ld} and V_{sd}), and battery DC voltage (V_{dc}) is shown in Fig. 5.8. During voltage sag condition at t=0.2 to 0.3s, the signal V_{sd} is decreased but load voltages have constant magnitude due to series compensating voltage. The required load voltages at voltage sag conditions is fed by a series injection transformer at PCC. The grid current is sinusoidal at voltage sag condition due to its control technique. The Battery DC voltage shows a very small variation of 2V.

Case II. Voltage Swell in the source side

Another most common disturbance at source voltages is voltage swell. At t=0.45 to 0.55s, voltage swell is developed at source voltages which is a 20% increase of source voltages for 5 cycles. Before t=0.45s the system is operating at steady-state. The voltage swell is cleared in 5 cycles. The battery DC voltage is slightly increased due to the transient effect but gets stable within 1 cycle. The direct component of source voltages is

increased but load voltages are maintained to their rated value. The response of the proposed system under voltage swell conditions is depicted in Fig. 5.9.

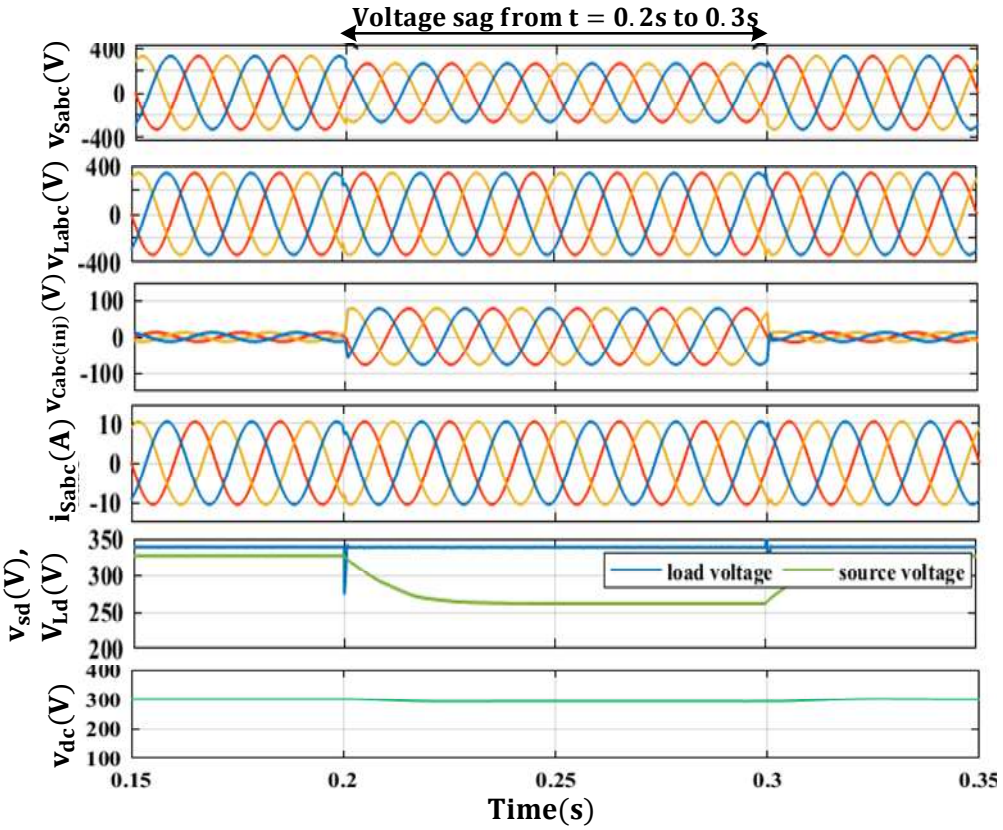

Fig. 5.8 Simulation result of proposed DVR system under Voltage Sag condition

Case III. Voltage Harmonics in the source side

To investigate the performance of DVR during voltage harmonics, 5th and 7th-order harmonics are incorporated into source voltages. The transient response of the system is noticed from t=0.5s to t=0.6s (5 cycles). It is depicted in Fig. 5.10, that load voltages are regulated at its rated value with constant magnitude. The effect of harmonics is cleared after 5 cycles. The required voltage for load voltage compensation is fed by a series injection transformer. The battery DC voltage is regulated at 300V with slight variation under transient conditions. The harmonic spectra of phase 'a' of load voltages and source voltages are shown in Fig.5.11. The source voltages are significantly polluted with 25% harmonics, while load voltages have THD of only 0.96% which is acceptable as per IEEE-519 standards due to DVR action.

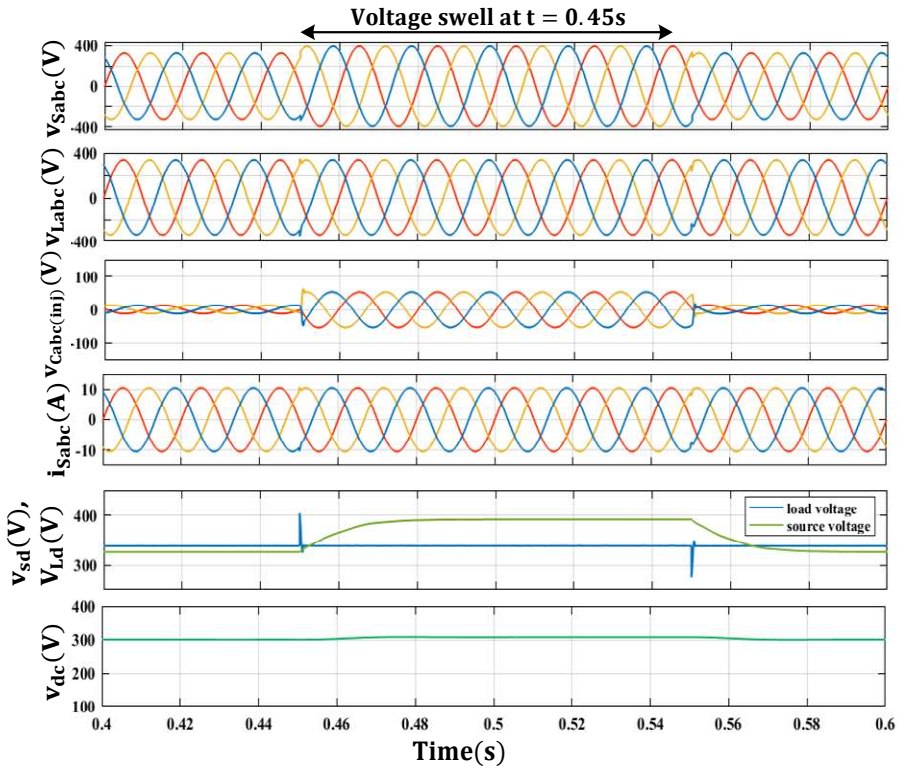

Fig. 5.9 Simulation result of proposed DVR system under Voltage Swell condition

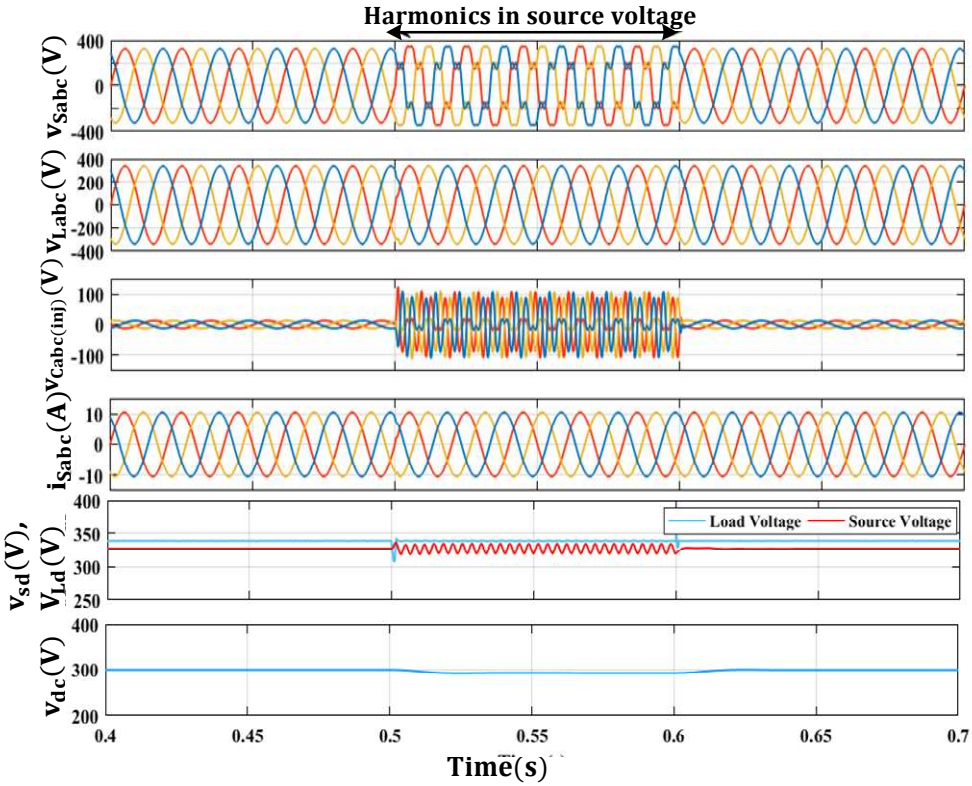

Fig. 5.10 Simulation result of proposed DVR system under Voltage Harmonics condition

Case IV. Voltage unbalance at the source side

In this case study, voltage unbalancing is created at source voltages. A voltage unbalancing is provided to phase 'a'. Due to source voltages unbalancing a slight regulation in Battery DC voltage is seen in Fig. 5.12 Despite voltage imbalance the load voltages are balanced and constant magnitude. It is seen in Fig. 5.12 that the voltage unbalancing occurs for 5 cycles (t=0.2s to t=0.3s). The battery DC voltage has slightly decreased. The d component of source voltages is decreased and shows some oscillations. However, the source current is sinusoidal under linear load conditions.

Case V. Performance under frequency change of +5 Hz and phase shift of 15 degrees

The performance of the proposed DVR is tested for frequency change and phase shift of +5Hz, and 15° respectively. The source voltages are experiencing the phase jump of 15° at t=0.3s to t=0.4s as shown in Fig. 5.13(a). The source voltages are experiencing the frequency change of +5Hz (i.e., 55Hz) at t=0.2s to t=0.3s as shown in Fig. 5.14(b) It is visible that even at frequency change, the load voltages are balanced and sinusoidal with the required magnitude in both phase jump and frequency shift. The series injection transformers inject the required voltage into the system.

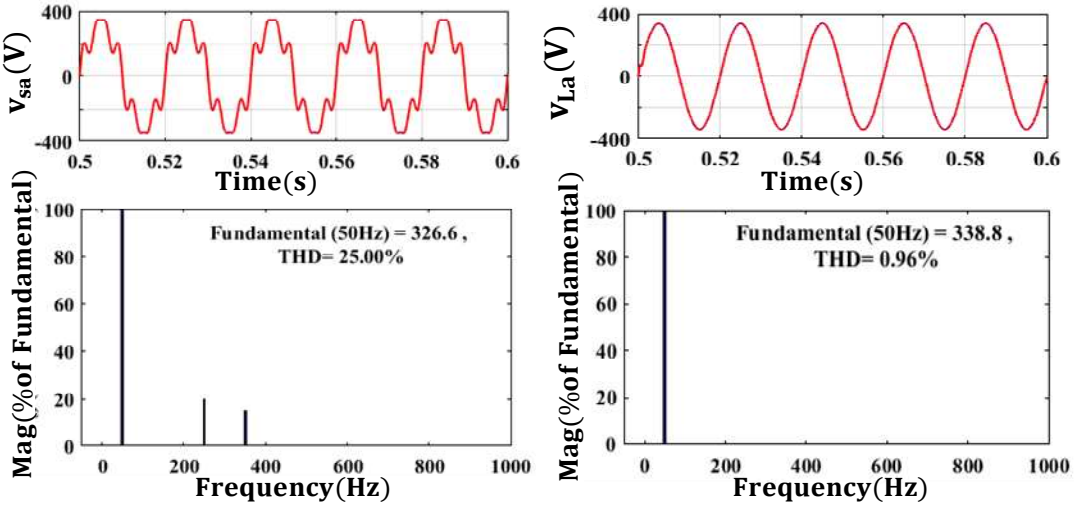

(a) (b)

Fig. 5.11 THD spectrum under source voltages harmonics (a) source voltages (b) load voltages

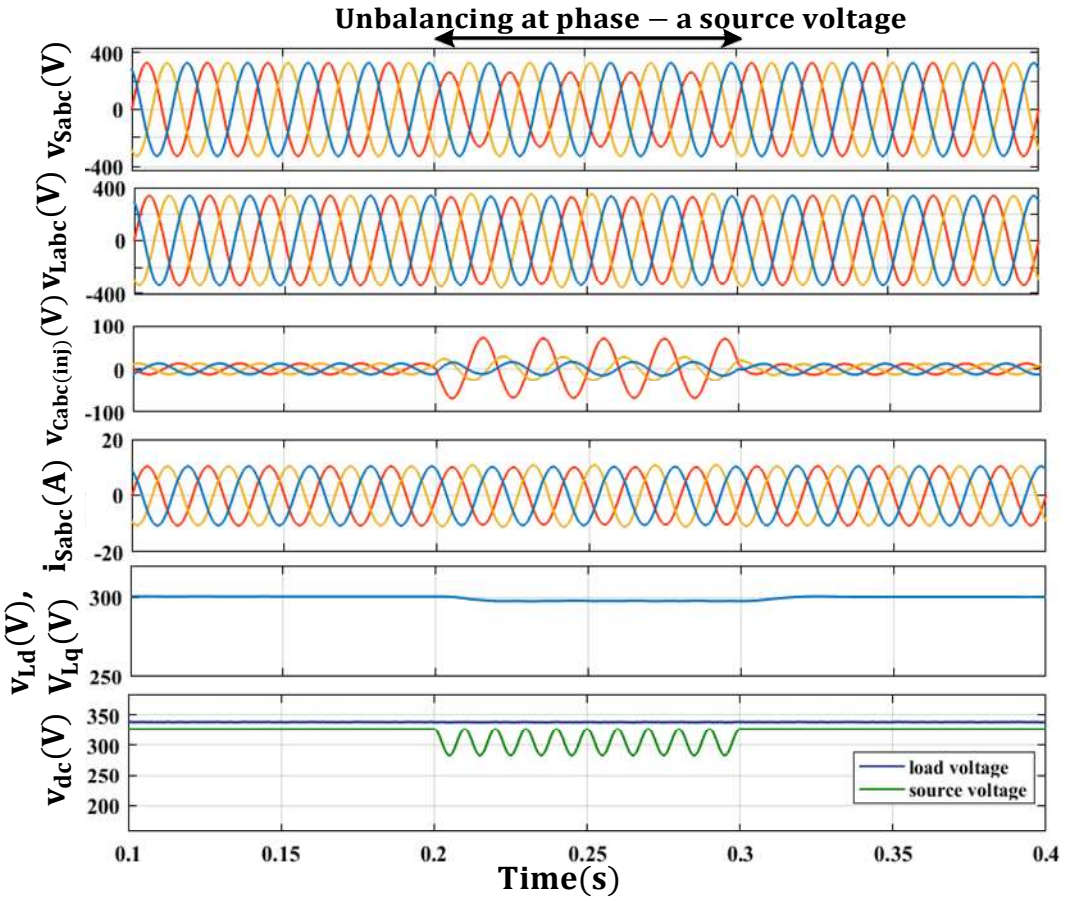

Fig. 5.12 Simulation result of proposed DVR system under Voltage Unbalancing condition

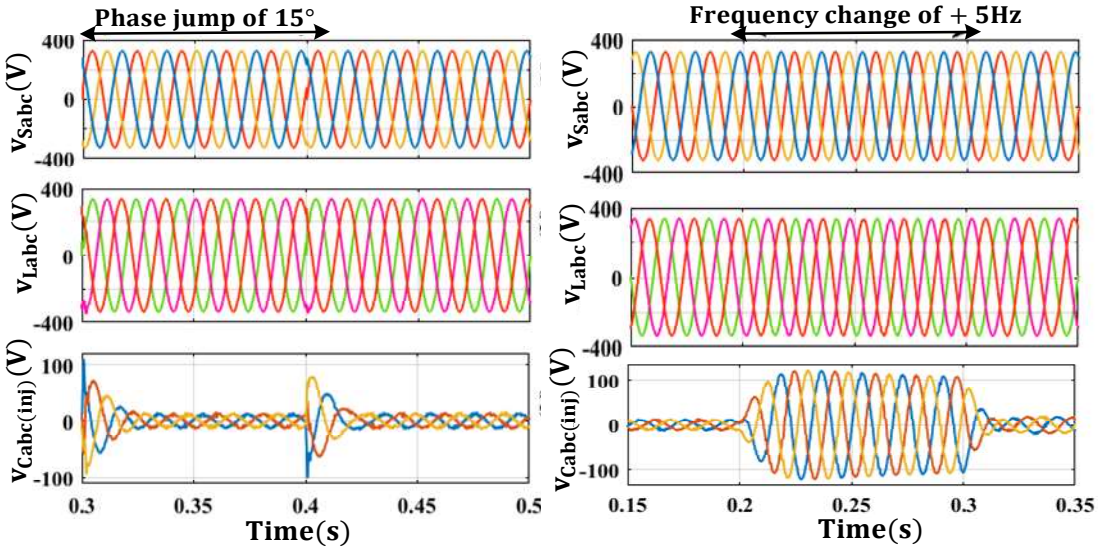

(a) (b)

Fig. 5.13 Simulation result of proposed DVR system under (a) Phase jump of 15° (b) frequency change +5Hz

5.3.3 Comparative Performance of three-phase DVR based on SRFT and MSTOGI SRFT control scheme

The performance of a three-phase grid-connected PV-based DVR is performed on the same system parameters as conventional SRFT and the proposed MSTOGI-SRF control scheme. The voltage-related PQ issues considered are voltage sag, voltage swell, voltage unbalancing, and voltage harmonics which are mitigated with the effect of designed control schemes. Table 5.2 shows the comparative performance of control schemes under all the mentioned PQ issues. It is seen from the Table that the proposed MSTOGI-SRF gives source current THD under voltage sag, swell, unbalancing, and voltage harmonics of 2.1%, 2.3%, 1.5%, and 0.96% respectively. Hence the proposed MSTOGI-SRF shows better performance than SRFT-based control scheme.

Table 5.2: Comparative performance analysis of SRFT and MSTOGI SRFT under various operating conditions

System Condition	**Phase**	**Conventional SRFT**		**Proposed MSTOGI-SRF**	
		Current	Voltage	Current	Voltage
Voltage Sag THD (%)	A	3.05%	4.63%	**2.1%**	4.63%
	B	3.4%	4.5%	**2.81%**	4.5%
	C	3.3%	5.41%	**2.6%**	5.41%
Voltage Swell THD (%)	A	3.8%	3.30%	**2.3%**	3.30%
	B	3.3%	5.29%	**2.14%**	5.29%
	C	3.5%	5.30%	**2.6%**	5.30%
Voltage Unbalancing THD (%)	A	3.15%	0.7%	**1.5%**	0.7%
	B	3.25%	0.6%	**1.6%**	0.6%
	C	3.12%	0.7%	1.32%	0.7%

Voltage Harmonics THD (%)	A	3.5%	25%	**0.96%**	25%
	B	3.1%	25%	1.02%	25%
	C	3.3%	25%	1.2%	25%

5.4 Experimental Results

A real-time hardware-in-the-loop (HIL) system is created to evaluate the viability of the proposed approach for DVR control. Figure 5.14 depicts a schematic of the designed laboratory experimental setup. The real-time HIL system is made up of an OPAL-RT real-time digital simulator with FPGA Xilinx Kintex-7 410T. The OPAL-RT is a real-time simulation platform powered by Intel Xeon Four-Core 3.7 GHz processors and operating in the RT-LAB software environment. The OPAL-RT features 32 digital inputs and 32 digital outputs. The proposed system is simulated in MATLAB Simulink and the results are verified using OPAL-RT.

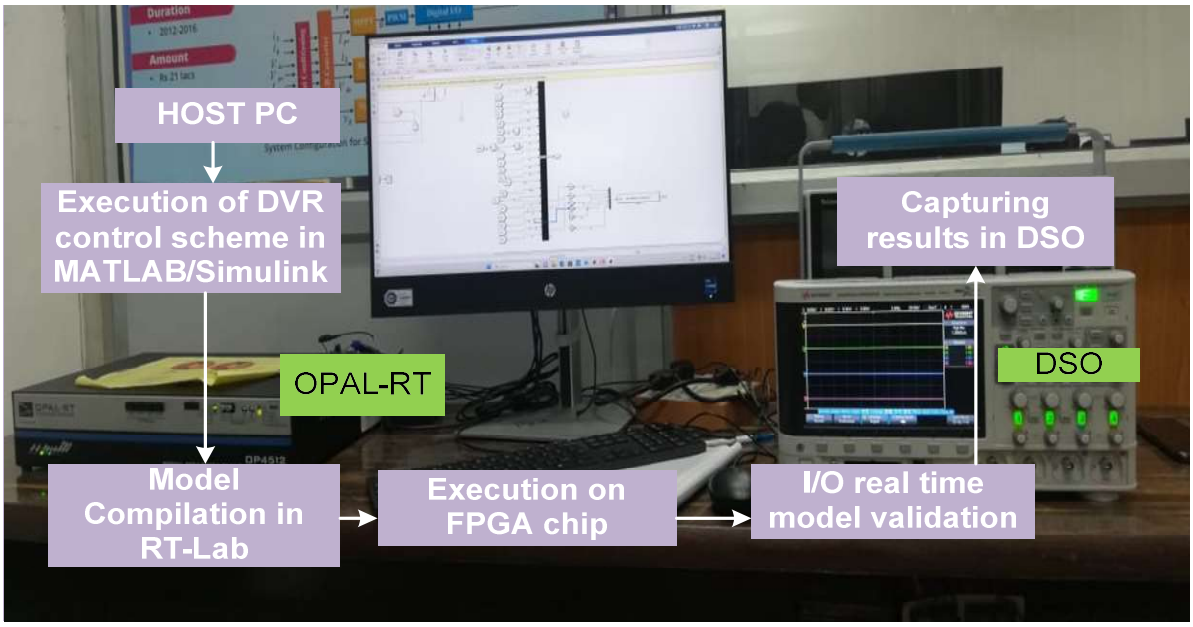

Fig. 5.14 Experimental Setup of proposed MSTOGI-SRF-based DVR implementation.

The experimental investigation of SRFT-based control of DVR under 20% voltage sag is shown in Fig. 5.15. The DVR injects the required voltage to regulate the load voltage magnitude constant using a series injection transformer with the control of SRFT. Fig. 5.15(a) shows the waveform of phase 'a' source voltage (v_{sa}), load voltage (v_{La}), series

injected voltage ($v_{Ca(inj)}$), and DC link voltage (V_{dc}). While Fig. 5.15(b) shows the three-phase source voltage (v_{sabc}) under voltage sag with constant magnitude load voltage.

5.4.1 Performance Analysis of SRFT control of DVR

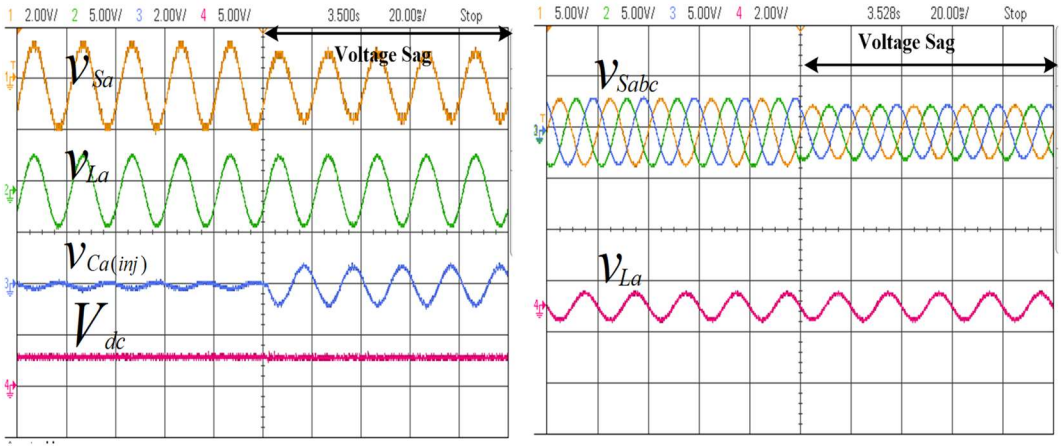

(a) (b)

Fig. 5.15 Experimental results of proposed DVR under voltage sag of 20% with signals (a) Phase 'a' source voltage (v_{sa}), phase 'a' load voltage (v_{La}), phase 'a' series injected voltage ($v_{ca(inj)}$), and DC voltage (V_{dc}) (b) three-phase source voltages (v_{sabc}), and phase 'a' load voltage (v_{La}).

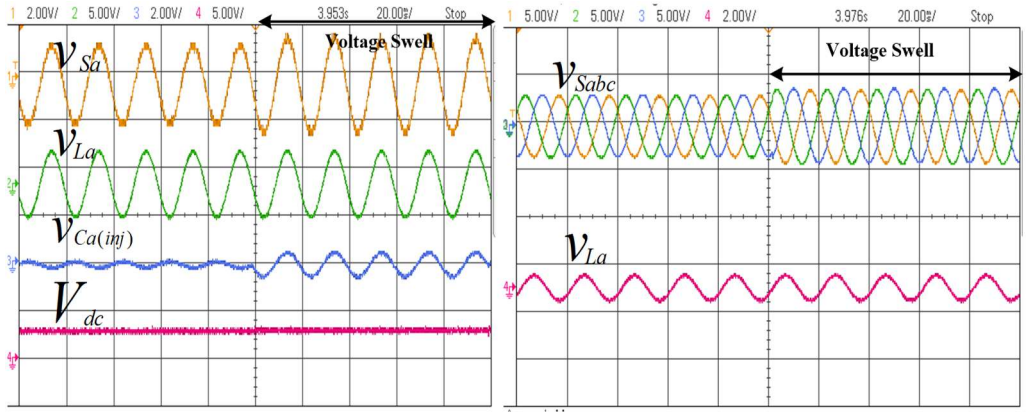

(a) (b)

Fig. 5.16 Experimental result of proposed DVR under voltage swell of 20% with signals (a) Phase 'a' source voltage (v_{sa}), phase 'a' load voltage (v_{La}), phase 'a' series injected voltage ($v_{ca(inj)}$), and DC voltage (V_{dc}) (b) three-phase source voltages (v_{sabc}), and phase 'a' load voltage (v_{La}).

Another most common power quality issues occur in power system is voltage swell. In the proposed system, 20% voltage swell is created at the source voltage as shown in Fig. 5.16. The load voltage of phase 'a' is regulated to constant magnitude under voltage swell as shown in Fig. 5.16(a-b). Thus, it is evident from the experimental results that SRFT-based DVR can mitigate voltage-related PQ issues.

5.4.2 Performance Analysis of *MSTOGI* DVR Technique

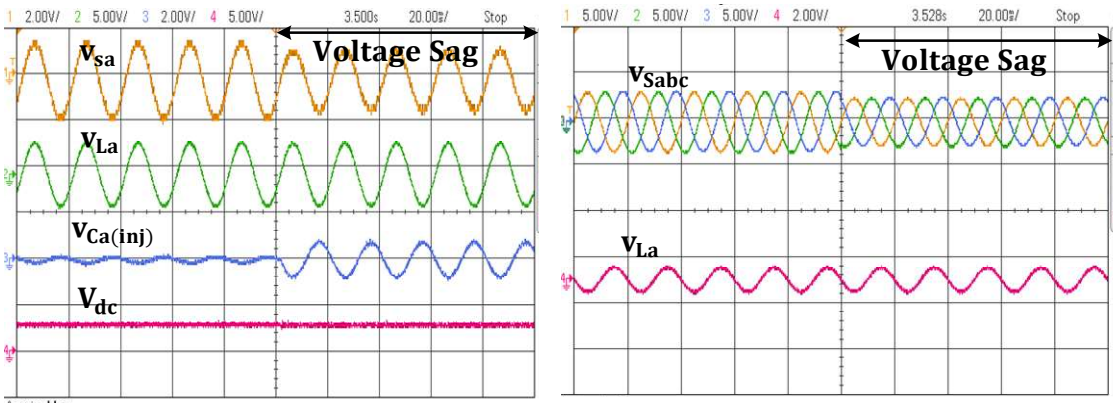

(a) (b)

Fig. 5.17 Experimental results of proposed DVR under voltage sag of 20% with signals (a) Phase 'a' source voltage (v_{sa}), phase 'a' load voltage (v_{La}), phase 'a' series injected voltage ($v_{ca(inj)}$), and DC voltage (V_{dc}) (b) three-phase source voltages (v_{sabc}), and phase 'a' load voltage (v_{La}).

A voltage sag of 20% is created in the grid voltages of phase 'a' as shown in Fig. 5.17(a). It is validated from Fig. 5.17(a) that the load voltages are always well regulated at pre-sag condition at constant magnitude.

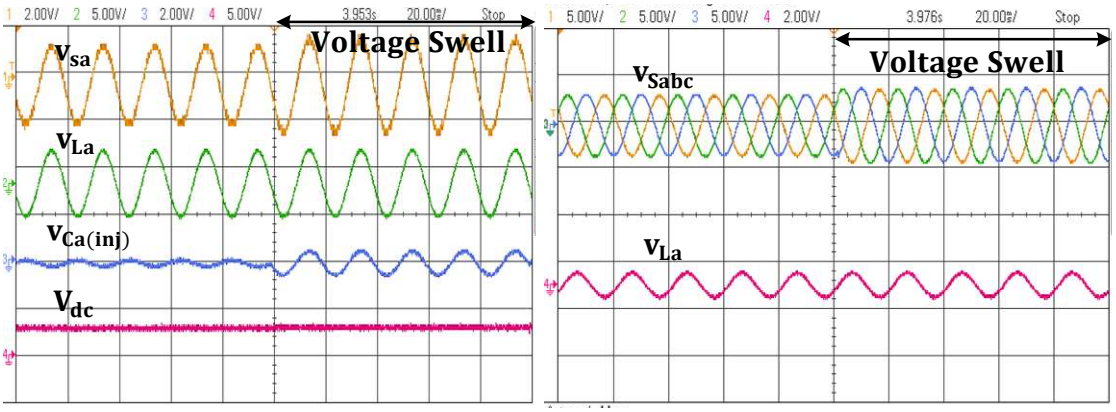

Fig. 5.18 Experimental results of proposed DVR under voltage swell of 20% with signals (a) Phase 'a' source voltage (v_{sa}), phase 'a' load voltage (v_{La}), phase 'a' series injected voltage ($v_{ca(inj)}$), and battery DC voltage (V_{dc}) (b) three-phase source voltages (v_{sabc}), and phase 'a' load voltage (v_{La}).

The required voltage to maintain the load voltages constant under voltage sag conditions is fed by a series injection transformer ($v_{ca(inj)}$). A small change in battery DC voltage is visible at the start of the voltage sag condition for less than 1 cycle. The series injection transformer injects very low voltage before the voltage sag condition.

Another important voltage-related PQ issue is Voltage swell. In Fig. 5.18(a), a voltage swell of 20% of grid voltages has been created at some instant of time to

investigate the performance of the proposed control scheme under voltage swell conditions. The load voltages of phase 'a' (v_{La}) is regulated to its required magnitude. A negligible change in battery DC voltage is seen. Fig. 5.18(b) shows the three-phase grid voltages under voltage swell conditions.

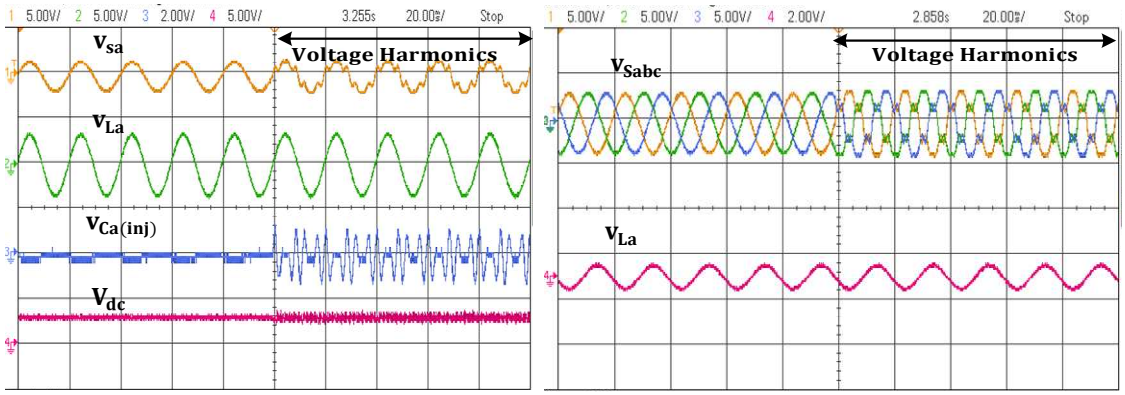

(a) (b)

Fig. 5.19 Experimental Results of proposed DVR under voltage harmonics having signals (a) Phase 'a' source voltage (v_{sa}), phase 'a' load voltage (v_{La}), phase 'a' series injected voltage ($v_{ca(inj)}$), and battery DC voltage (V_{dc}) (b) three-phase source voltages (v_{sabc}), and phase 'a' load voltage (v_{La}).

A voltage harmonic is created at three-phase grid voltages (v_{sabc}) with a THD of 25%. It is validated through the experimental results as shown in Fig. 5.19(a) that load voltages are pure sinusoidal with no harmonics component. The series injection transformer injects the required voltage to maintain the load voltages of phase 'a' constant. A small ripple is seen in the battery DC voltage across the battery. In Fig. 5.19(b), three-phase grid voltages with harmonics are shown, and the load voltages across phase 'a'. Voltage unbalancing is created at some instant of time at three-phase grid voltages (v_{sabc}). Phase 'a' grid voltage has sag in it. While there is no adverse effect on load voltages as shown in Fig. 5.20(a). In Fig. 5.20(b) series injection voltage ($v_{ca(inj)}$), and battery DC voltage (V_{dc}) is shown during unbalanced supply voltage condition.

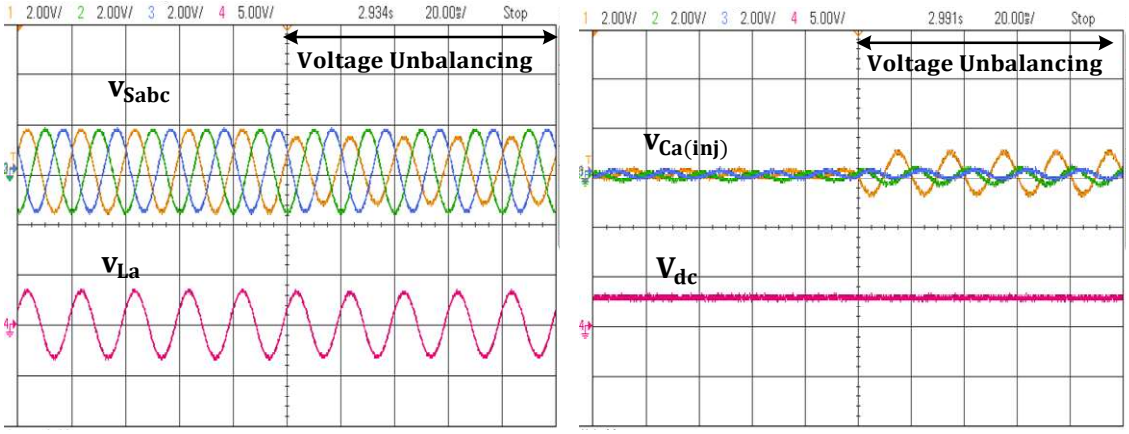

(a) (b)

Fig. 5.20 Experimental result of proposed DVR under voltage unbalancing with signals (a) Phase 'a' source voltage (v_{sa}), phase 'a' load voltage (v_{La}), phase 'a' series injected voltage ($v_{ca(inj)}$), and battery DC voltage (V_{dc}) (b) three-phase source voltages (v_{sabc}), and phase 'a' load voltage (v_{La}).

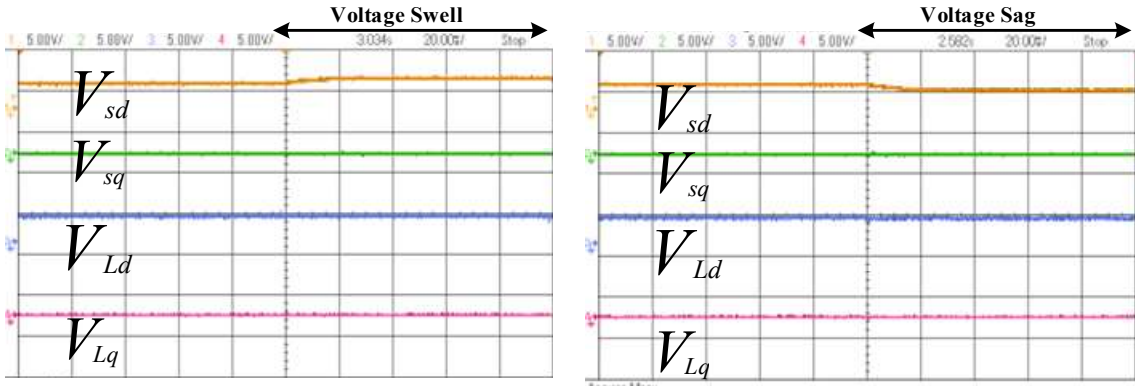

(a) (b)

Fig. 5. 21 Experimental results of proposed DVR intermediate signals of MSTOGI-SRF control scheme under voltage Swell (a) direct component of grid voltages (V_{sd}), quadrature component of grid voltages (V_{sq}), a direct component of load voltages (V_{Ld}), quadrature component of load voltages (V_{Lq}) (b) under voltage sag condition direct component of grid voltages(V_{sd}), quadrature component of grid voltages (V_{sq}), a direct component of load voltages (V_{Ld}), quadrature component of load voltages (V_{Lq}).

The intermediate signals of the proposed MSTOGI-SRF control scheme of BESS DVR are shown in Fig. 5.21 (a-b). In Fig. 5.21(a), the condition of voltage swell is chosen, and the direct component of grid voltages is increased in an appropriate ratio. While the quadrature component of grid voltages is always zero. The direct component of load voltages is constant under voltage swell conditions. The quadrature component has zero magnitude In Fig. 5.21(b) Voltage sag condition is chosen, and the direct component of grid voltages is decreased in an appropriate ratio. While the quadrature component of grid voltages is always zero. The direct component of load voltages is constant under voltage

sag conditions. The d and q component of load voltages are well regulated due to DVR action even during sag and swell conditions.

5.5 Conclusions

The design, mathematical modelling, and analysis of three-phase SRFT and proposed MSTOGI-SRFT algorithms for battery supported DVR control of three-phase grid-connected systems are covered in this chapter. Using MATLAB Simulink software, the results were obtained, and OPAL RT investigations were used to validate them. Tests were conducted on three-phase systems, under situations of voltage sag, swell, unbalancing, and Harmonics. This chapter presents a thorough control analysis of the developed systems. The system that performs best with MSTOGI-SRF is followed by conventional SRF. In both steady state and dynamic state settings, the SRF approach results demonstrate continuous persistent oscillations. The MSTOGI SRFT mitigates all the voltage related PQ issues. The Performance of MSTOGI-SRF is observed to be better under grid disturbance (DC offset, harmonics, sag, swell, and unbalancing). The load voltage is constant under all undesirable conditions which is necessary for connected sensitive loads.

CHAPTER 6

DESIGN AND CONTROL OF UNIFIED POWER QUALITY COMPENSATOR FOR GRID CONNECTED PV SYSTEM

6.1. Design of UPQC

A power electronics-based device called the Unified Power Quality Compensator (UPQC) is used in electrical distribution systems to enhance the quality of electric power. It is frequently used in three-phase grid-connected PV (Photovoltaic) systems to improve the system's overall performance while addressing power quality issues. In a grid-connected PV system, a UPQC's main function is to make sure that both the grid and the associated loads receive high-quality power. This involves addressing power factor problems, harmonic distortions, and voltage sags and swells. A UPQC consists of a series voltage compensator and shunt current compensator also known as DVR and DSTATCOM respectively. The main purpose of DVR is to mitigate source voltage-related issues such as sag, swell, unbalance, and harmonics. It can inject or absorb the reactive power to maintain the constant voltage level across the loads. While the DSTATCOM is used to mitigate the current related power quality issues such as current harmonics, and load unbalancing. Both the DVR and DSTATCOM are operated under the supervision of an advanced control system. The control system continuously checks the source voltage, current, and other variables and modifies the compensating actions as necessary. It makes sure that harmonic distortions are decreased, the source voltage stays within set parameters, and the power factor is enhanced.

A 3-leg VSC is connected in shunt with the load and another 3-leg VSC of DVR is connected in the series with the 3∅ grid using a series injection transformer. The DC link capacitor is connected to the shunt's VSC and is required to maintain a reference DC voltage by controlling the switching operation shunt's VSC. The VSC of DVR is also coupled with the common DC capacitor, as indicated in Fig.6.1. The VSC of DSTATCOM is coupled at PCC through an interfacing inductor (L_f) and the higher order frequency component of PWM voltage is filtered out through the ripple filter (R_f, C_f).

Similarly, the high order frequency component of PWM voltages of DVR's VSC is filtered out through (L_r, C_r).

6.1.1 Design of DSTATCOM

The supply voltage for simulation is considered as 400V (v_{L-L}) at 50Hz frequency, while for experimental validation (using OPAL-RT) the supply voltage is chosen 40V (v_{L-L}), 50Hz. The DC link voltage is calculated using Eq. (6.1),

$$V_{dc(ref)} > V_{dc(min)} = \frac{2\sqrt{2}}{\sqrt{3}} v_{L-L} = \frac{2\sqrt{2}}{\sqrt{3}} \times 400 = 653.19V \quad (6.1)$$

The reference DC link voltage $V_{dc(ref)}$ should be greater than the minimum DC link voltage $V_{dc(min)}$, and thus it is considered 800V for simulation. The experimental DC link voltage is calculated using Eq. (4.2),

$$V_{dc(ref)} > V_{dc(min)} = \frac{2\sqrt{2}}{\sqrt{3}} v_{L-L} = \frac{2\sqrt{2}}{\sqrt{3}} \times 40 = 65.31V \quad (6.2)$$

The reference DC link voltage $V_{dc(ref)}$ should be greater than the minimum DC link voltage $V_{dc(min)}$, and thus it is considered 80V for experimental setup. The designed value of the DC link capacitor is calculated using Eq. (6.3),

$$C_{dc} = \frac{6k_1 v_{ph} a i_{cc} \tau}{V_{dc(ref)}^2 - V_{dc(min)}^2} = \frac{6 \times 0.4 \times 230.94 \times 1.2 \times 25 \times 0.02}{(800^2 - 653.19^2)} = 1558.7\mu F \quad (6.3)$$

where,$V_{dc(ref)}$ is the DC link bus voltage, $V_{dc(min)}$ is the minimum DC link voltage, τ is the time constant, a is the overloading factor, k_1 is the gain constant and i_{cc} is the VSC's compensating current. Let $a = 1.2$, $i_{cc} = 25A$, $V_{dc(ref)} = 800V$, $V_{dc(min)} = 653.19\,V$, $\tau = 0.02s$, and $k_1 = 0.4$. The value of DC-link capacitance $C_{dc} = 1558.7\,\mu F$ and it is chosen as 1650 μF (simulation). The value of the interfacing inductor can be calculated using Eq. (6.4),

$$L_f = \frac{\sqrt{3} m V_{dc(ref)}}{12 a f_{sw} \Delta I_{cr}} \quad (6.4)$$

Here, 'L_f' is the interfacing inductor, 'm' is the modulation index, 'f_{sw}' is the switching frequency and ΔI_{cr} is the current ripple which is considered 5% of the maximum current. The value of L_f for simulation is calculated by Eq. (6.5) and for experimental setup, it is calculated by Eq. (6.6).

$$L_f = \frac{\sqrt{3} m V_{dc(ref)}}{12 a f_{sw} \Delta I_{cr}} = \frac{\sqrt{3} \times 1 \times 800}{12 \times 1.2 \times 10 \times 1000 \times 1.5} = 7.6mH \quad (6.5)$$

$$L_f = \frac{\sqrt{3}mV_{dc(ref)}}{12af_{sw}\Delta I_{cr}} = \frac{\sqrt{3}\times1\times80}{12\times1.2\times10\times1000\times1.5} = 0.76mH \quad (6.6)$$

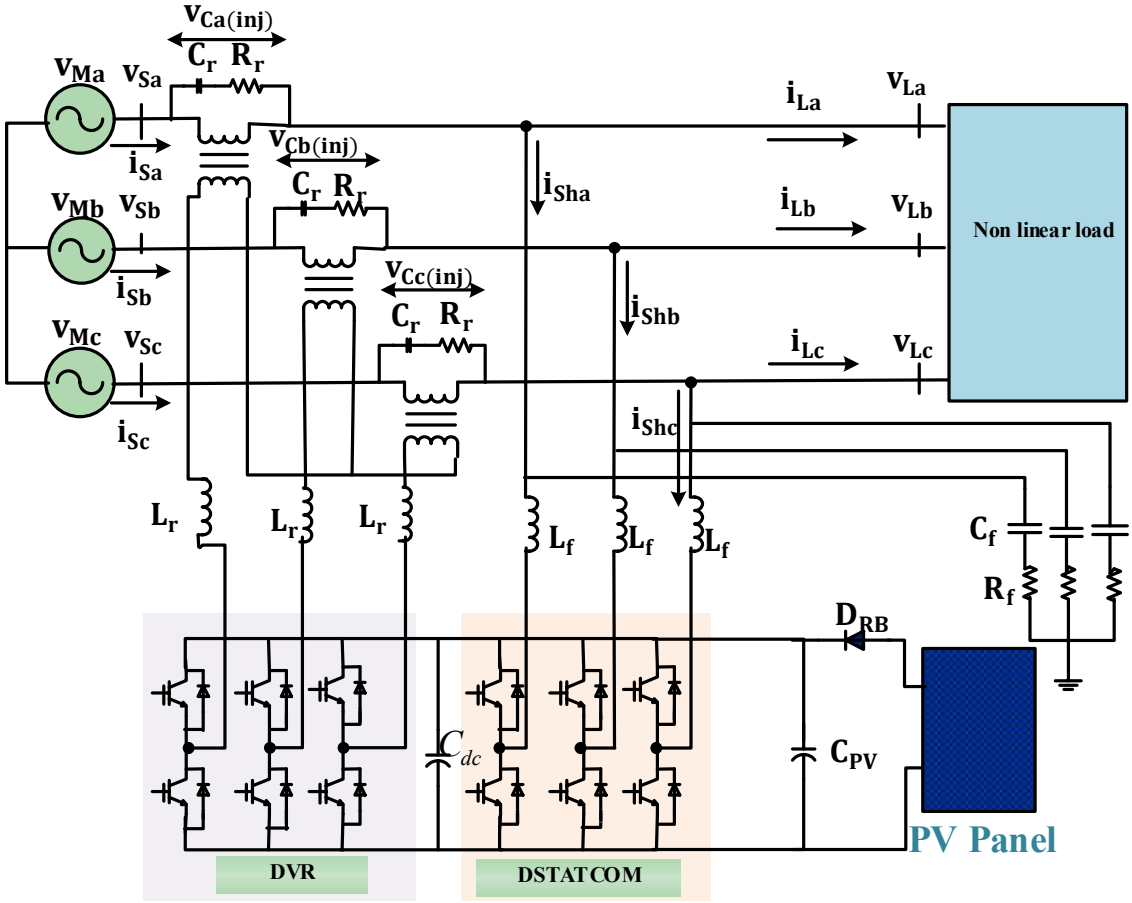

Fig. 6. 1 Schematic Diagram of three-phase grid-connected PV-UPQC

Design of PV array

There is no DC-DC boost converter in a single-stage PV system. The voltage of the PV array should be higher than the voltage of the voltage source converter (VSC)'s reference DC link. The highest voltage at MPP and reference DC voltage of the PV array must be produced by the MPPT method. Eq. (6.7) calculates the necessary minimum number of series-connected PV modules.

$$N_S = \frac{V_{dc(min)}}{V_{mp}} = \frac{653.19}{37.73} = 17.31 \quad (6.7)$$

Thus, the number of series connected PV modules selected to be 22. The parameters of PV string or array are given in Table 6.1.

Table 6.1: PV array Parameter at standard test condition (1Soltech 1STH-215-P)

Parameters	**Selected Value**
No. of series PV modules (N_S)	22
No. of parallel PV modules (N_P)	6
Maximum Power (P_{mp})	213.15 W
Open circuit voltage (V_{OC})	36.3 V
Short circuit current (I_{SC})	7.84 A
Voltage at MPP (V_{mp})	29 V
Current at MPP (I_{mp})	7.35 A

6.1.2 Design of DVR

To choose the rating of the series injection transformer, several parameters were taken into account, including DVR capacity, voltage sag assessment, needed DVR current, and DVR rating. The DVR's capacity is determined by the particular application and required level of voltage support. The 10kVA DVR capacity value is chosen. The maximum voltage sag on source voltage per phase that the DVR will mitigate is calculated as $230.9 \times 0.8 = 184.72\text{V}$. The required DVR's current rating is calculated as

$$\sqrt{3}v_{Sa}i_{Sa} = 10000 \tag{6.8}$$

$$i_{Sa} = 25\text{A}$$

The series injection voltage required to be injected per phase is given by Eq. (6.9)

$$V_{Ca(inj)} = \sqrt{v_{sa}^2 - v_{sag(max)}^2} = \sqrt{230.9^2 - 184.72^2} = 138.54\text{V} \tag{6.9}$$

$$\text{Transformer capacity (kVA)= } S = \frac{3 \times v_{Ca(inj)} i_{sa}}{1000} = 10.39\text{kVA} \tag{6.10}$$

The KVA rating of the series injection transformer will be the same as the KVA rating of VSC, i.e.,10.39 kVA. The interfacing inductor for DVR is expressed as

$$L_r = \frac{n \times (\sqrt{3/2} m V_{DC})}{6a_{\ sw} \Delta I_s} = 0.946\text{mH} \approx 1\text{mH} \tag{6.11}$$

where n is the transformation ratio of the series injection transformer, m is the modulation index, f_{sw} is the switching frequency and ΔI_s is the ripple current of DVR [69]. A ripple

filter is designed to filter the switching frequency ripples that occur due to a series injection transformer. The value of three-phase UPQC system parameters is shown in Table 6.2. The expression for ripple filter which consists of series resistance (R_r) and series capacitor (C_r) is given as

$$\frac{f_s}{2} = \frac{1}{2\pi\ {}_r C_r} \tag{6.12}$$

For, $R_r = 1\Omega, C_r = 31.8\mu F$

Table 6.2: Parameter Values of three-phase PV-UPQC

Element	**Parameters**	**Values**
Supply side	Source	415V(rms),50Hz
Unified Power Quality Compensator	DC link Capacitor	$C_{dc} = 6688\mu F$
	Interfacing filter inductor	L_r=2.5mH, L_f=2mH
	Ripple Filter	$R_r = 1\Omega$, $C_r = 100\mu F$
	Transformer Rating	10kVA
	Switching Frequency	f_s=5kHz
Loads	3-Ø diode rectifier	----
	R-L Load	R_L=30Ω and L_L=10mH

6.2 Control Technique of UPQC

Power quality problems including voltage sags, swells, harmonics, and changes in power factor, the UPQC must continuously monitor the source's voltage, current, and other data. The UPQC can process this data through control scheme and quickly modify its compensating components to address these problems. The issues with power quality in a distribution system are dynamic and subject to quick change. Control is designed to enable the UPQC to dynamically modify its corrective actions to take account of the shifting circumstances. For instance, to swiftly restore the voltage to its normal level after a voltage sag, the UPQC must inject reactive power. These real-time assessments benefit from the utilization of control algorithms. These control algorithms make the UPQC an

important tool for enhancing the quality and dependability of electrical power in distribution systems by ensuring that it can manage power quality concerns effectively and efficiently.

6.2.1 Conventional SRF-based Control Technique

DSTATCOM and DVR are vital components of grid-connected UPQC. DSTATCOM is used to address issues with harmonic current and reactive power demand in compensating load PQ. When grid-side PQ issues induce voltage concerns, the DVR is used. A DVR's function is to supply series voltage to the load if there are voltage anomalies, like sag and swell.

6.2.1.1 Control Scheme of Shunt Compensator

The control scheme implemented for shunt compensation is shown in Fig.6.2, the conventional SRFT is used for load compensation. The three-phase load current is transformed into a rotating frame d-q-0 component.

The expression for 'dq0' component of load current is given by Eq. (6.13)

$$\begin{bmatrix} i_{Ld} \\ i_{Lq} \\ i_{L0} \end{bmatrix} = \frac{2}{3}\begin{bmatrix} \sin\theta & \sin\left(\theta - \frac{2\pi}{3}\right) & \sin\left(\theta + \frac{2\pi}{3}\right) \\ \cos\theta & \cos\left(\theta - \frac{2\pi}{3}\right) & \cos\left(\theta + \frac{2\pi}{3}\right) \\ 1/2 & 1/2 & 1/2 \end{bmatrix}\begin{bmatrix} i_{La} \\ i_{Lb} \\ i_{Lc} \end{bmatrix} \tag{6.13}$$

To improve the grid current's performance due to grid voltage abnormalities, the PV array's feedforward current (I_{PVff}) is also included in the shunt compensation of UPQC

$$I_{PVff} = \frac{2}{3} \times \frac{P_{PV}}{V_t} \tag{6.14}$$

where, P_{PV} is the generated power by solar PV array, V_t indicates the amplitude of source voltage. The total fundamental current component is expressed as

$$i_d^* = i_{dDC} + i_{loss} - I_{PVff} \tag{6.15}$$

A 3Ø PLL has been utilized for frequency and phase information. The direct and quadrature component of load current is passed through LPF to reject the high-frequency component. The filtered direct component of load current which is also known as the fundamental frequency component is added to the DC link loss component. The DC link voltage error is regulated through the PI controller to minimize the active power losses. The resultant direct and quadrature components of load current are transformed into 'abc'

components. The reference source current (i_{sa}^{*}, i_{sb}^{*}, i_{sc}^{*}) is compared with the actual source's current (i_{sa}, i_{sb}, i_{sc}) in the Hysteresis current controller (HCC). The switching signals or PWM signals generated through this control scheme are given to IGBT switches.

6.2.1.2 Control Scheme of Series Compensator

Another important of UPQC is the active series compensator also known as DVR. To counteract the sag and swell at the grid side, DVR injects a sequence of three voltages of the required magnitude and frequency. Its objective is to protect sensitive loads from voltage-related PQ issues. The switches of DVR require switching signals or gating signals to fulfill their purpose. The control scheme used for DVR is conventional SRF. In this control scheme, three-phase source voltage is transformed into rotating components d-q-0. The direct and quadrature component of the source voltage is passed through LPF. The PCC voltage (v_{sa}, v_{sb}, v_{sc}) are transformed in 'dq0' frame using Clarke and Park transformation

$$\begin{bmatrix} v_{sd} \\ v_{sq} \\ v_{s0} \end{bmatrix} = \frac{2}{3}\begin{bmatrix} \sin\theta & \sin\left(\theta - \frac{2\pi}{3}\right) & \sin\left(\theta + \frac{2\pi}{3}\right) \\ \cos\theta & \cos\left(\theta - \frac{2\pi}{3}\right) & \cos\left(\theta + \frac{2\pi}{3}\right) \\ 1/2 & 1/2 & 1/2 \end{bmatrix}\begin{bmatrix} v_{sa} \\ v_{sb} \\ v_{sc} \end{bmatrix} \tag{6.16}$$

Both the fundamental (DC component) and harmonic components comprise the source voltage's direct and quadrature axis components. The v_{qr} is the reference voltage required by the load while the source voltage undergoes sag and swell condition

$$V_L = \left(2/3\right)^{1/2}\left(v_{La}^2 + v_{Lb}^2 + v_{Lc}^2\right)^{1/2} \tag{6.17}$$

The PI controller is used to regulate the magnitude of the load voltage V_L to a reference value

$$v_{qr}(n) = v_{qr}(n-1) + K_{pq}\{v_{te}(n) - v_{te}(n-1)\} + K_{iq}v_{te}(n) \tag{6.18}$$

where, $v_{te}(n) = v_L^{*}(n) - v_L(n)$ shows the error between sensed and actual terminal voltage magnitude. The reference quadrature load voltage is given by

$$v_q^{*} = v_{q\_dc} + v_{qr} \tag{6.19}$$

$$\begin{bmatrix} v_{La}^{*} \\ v_{Lb}^{*} \\ v_{Lc}^{*} \end{bmatrix} = \begin{bmatrix} \cos\theta & \sin\theta & 1 \\ \cos\left(\theta - \frac{2\pi}{3}\right) & \sin\left(\theta - \frac{2\pi}{3}\right) & 1 \\ \cos\left(\theta + \frac{2\pi}{3}\right) & \sin\left(\theta + \frac{2\pi}{3}\right) & 1 \end{bmatrix}\begin{bmatrix} v_{Ld}^{*} \\ v_{Lq}^{*} \\ v_{L0}^{*} \end{bmatrix} \tag{6.20}$$

The PWM controller receives the reference and real load voltages and generates duty cycles for DVR.

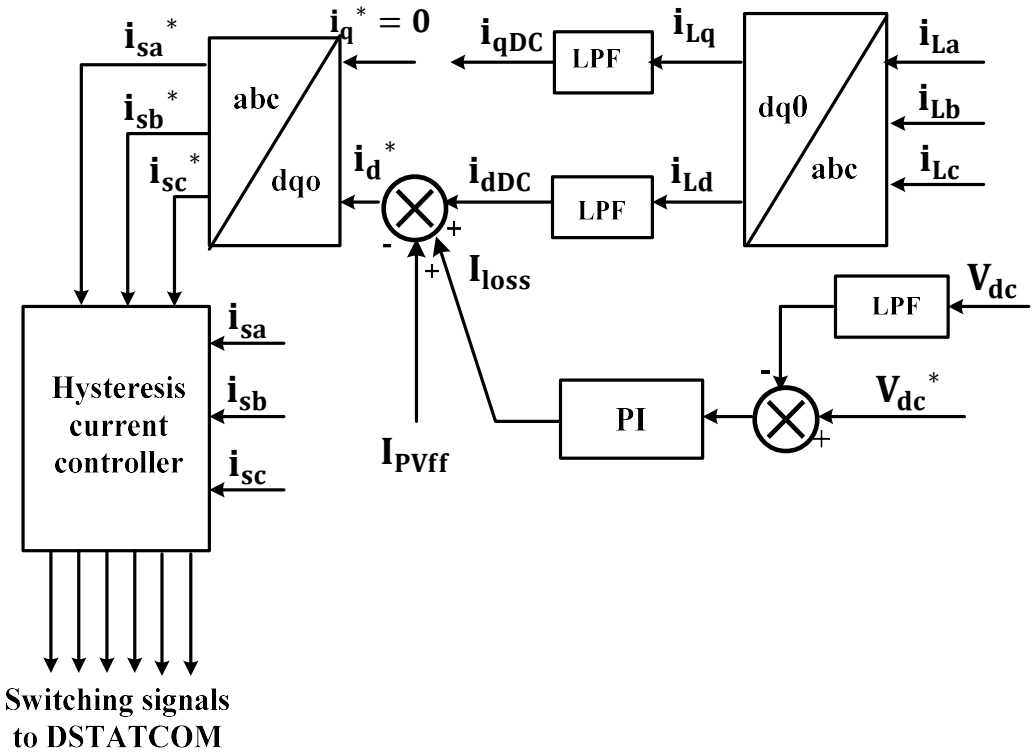

Fig. 6.2 Control Scheme of UPQC for Shunt Compensator (DSTATCOM) with SRFT control scheme

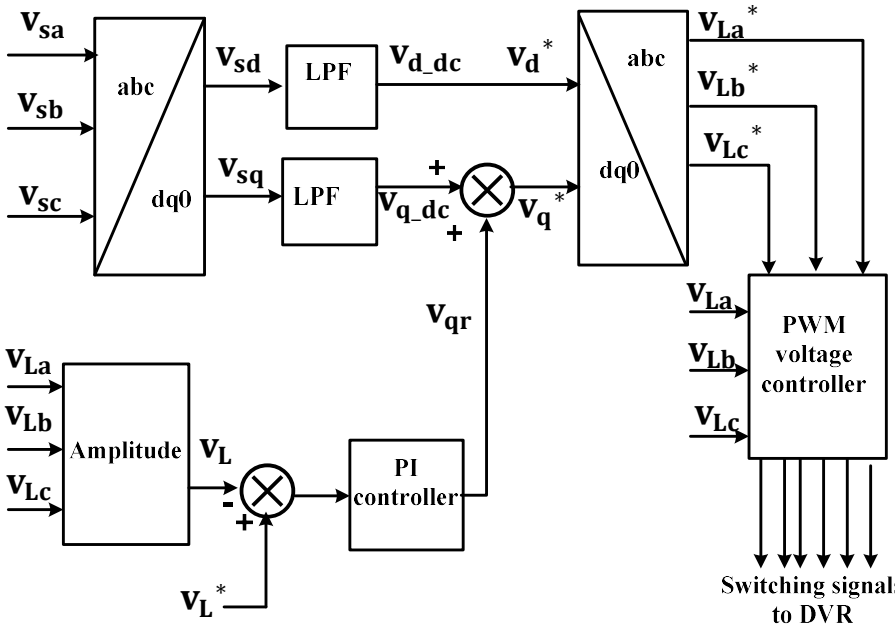

Fig. 6.3 Control Scheme of UPQC for series compensation (DVR) with SRFT control Scheme

6.2.2 Mittag Leffler Polynomial based control Technique (MiLeP)

Based on Synchronous Reference Frame Mittag Leffler Polynomial (SRF-MiLeP) NN and MiLeP NN for shunt and series and shunt compensation, respectively, a hybrid control method has been developed. SRF with MiLeP NN is used for series compensation whereas the MiLeP NN is intended for load compensation. The unique use of MiLeP NN for shunt compensation and series compensation is the important contribution. To derive the fundamental active load component from nonlinear load current, the MiLeP NN control technique is designed for shunt compensation. The shunt compensator reduces current-related PQ (load unbalance, reactive power correction, and harmonics mitigation). Voltage-related PQ challenges (Voltage Sag and Swell, Voltage Unbalancing) are mitigated by the SRF control with MiLeP NN acting as an adaptive filter for the series compensator. Under voltage sag, swell, load unbalancing, and changes in solar irradiation, UPQC's performance is evaluated.

In 1891, Mittag Leffler designed MiLeP. These polynomials can be used to approximate other functions and are mostly researched in complex system analysis. They were initially applied by Mittag-Leffler in a study of the integrals and invariants of the analytical form of a linear homogeneous differential equation. These polynomials have uses in solving differential equations, uniform approximation, and other areas. The MiLe polynomials are expressed by

$$\sum_{n=0}^{\infty} g_n(x)t^n = \frac{1}{2}\left(\frac{1+t}{1-t}\right)^x \quad \text{and} \tag{6.21}$$

$$\sum_{n=0}^{\infty} M_n(x)\frac{t^n}{n!} = \left(\frac{1+t}{1-t}\right)^x$$

$$M_n = (1+t)^x(1-t)^{-x} = \exp(2x\tanh t) \tag{6.22}$$

The polynomials are related by

$M_n = 2 \cdot n!\, g_n(x)$ and where $g_n(1) = 1$ for $n \geq 1$

Some of the first few dominant terms of MiLe polynomials are as follows

$M_0(x) = 1$, $M_1(x) = 2x$, $M_2(x) = 4x^2$,

$M_3(x) = 8x^3 + 4x$, and so on. (6.23)

By generalizing the pattern of polynomial, the recursion formula for MiLeP is given by

$$M_{n+1} = 2x\sum_{k=0}^{[n/2]} \frac{n!}{(n-2k)!} M_{n-2k}(x) \tag{6.24}$$

The MiLeP shows the orthogonality relation, and thus it can be used as a hidden layer in ANN. Also, this MiLeP consists of the tanh function which is the activation function in this MiLe ANN. The intermediate signals of phase 'a' load current are as follows:

$I_{La}\ (x) = 1 * W_{a0},\ I_{La1}(x) = 2i_{La} * W_{a1},\ \ I_{La2}(x) = 4{i_{La}}^2 * W_{a2},\ \ I_{La}\ (x) = (8{i_{La}}^3 + 4i_{La}) * W_{a3}$, and so on.

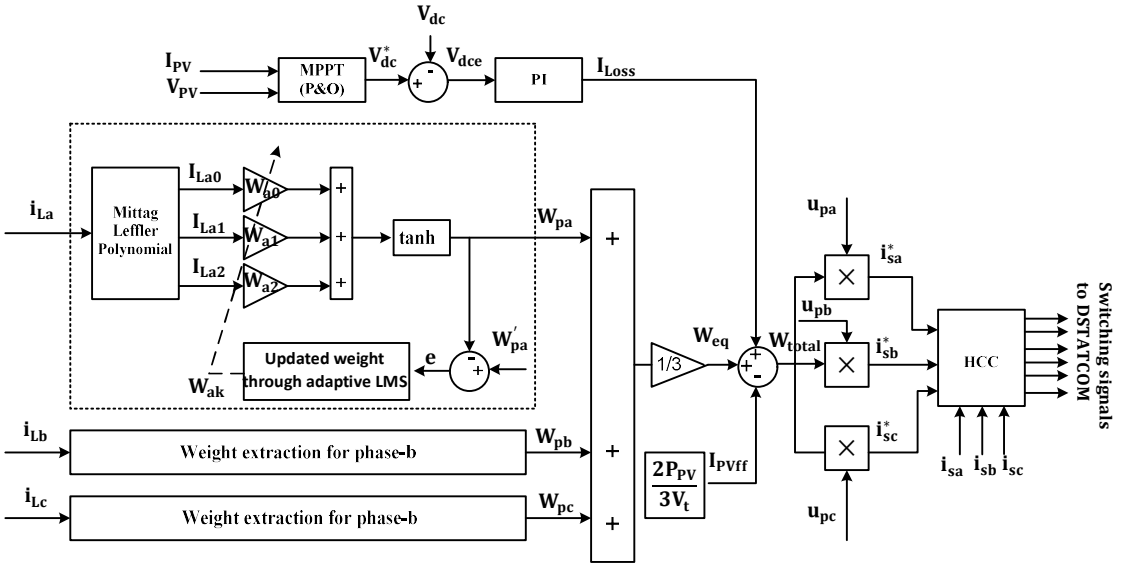

Fig. 6.4 Control Scheme of UPQC for Shunt Compensator (DSTATCOM) with Mittag-Leffler control scheme

6.2.2.1 Control Scheme of Shunt Compensator

Current-related PQ problems such as load unbalance, reactive power compensation, and current harmonics can be reduced via the shunt compensator. The essential load component is computed using a control method based on Mittag Leffler ANN. The load current is modeled using the MiLeP. Through the use of an adaptive LMS approach, the weight of the suggested control technique is trained. The generated reference current and the actual source current are compared to create the gating signals for the VSC of the shunt compensator. The approximation component of phase-a load current is obtained from the load current of phase-a flowing via MiLeP. The three approximated components of phase-a load current are I_{La0}, I_{La1}, I_{La2} and these components are multiplied by the Neural network weight.

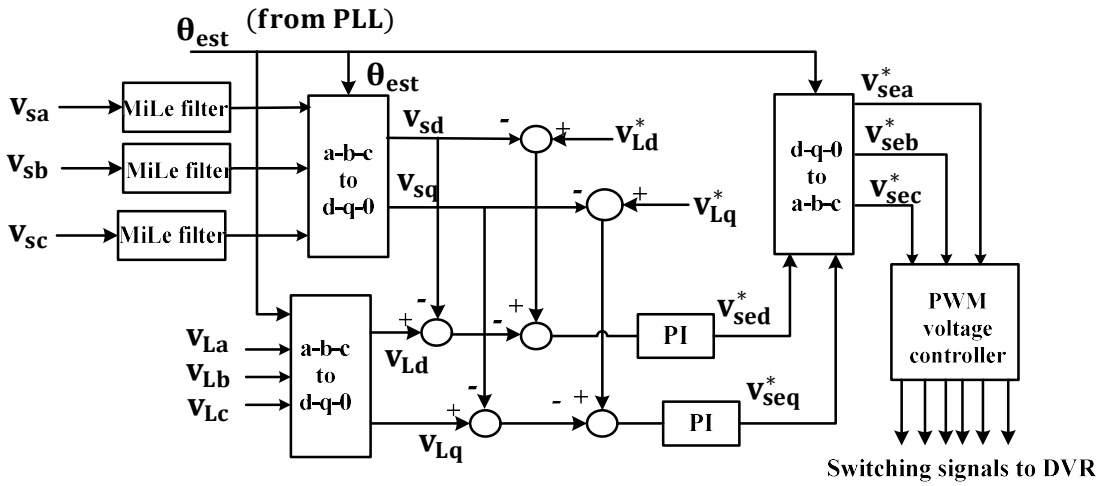

Fig. 6.5 Control Scheme of UPQC for Series Compensator (DVR) with MiLeP control scheme

Now, these components are added and passed through the activation function (tanh). Phase-a weight component (W_{pa}) will be provided by this. The shunt compensator control method is shown in Fig. 6.4. Similarly, the corresponding weight components for phases B and C are W_{pb}, W_{pc}. The equivalent weight component (W_{eq}) is created by averaging these three active weight components. The PV feed-forward current component (I_{PVff}) is deducted from the equivalent weight component's sum along with the switching loss component (I_{loss}). The updating weight equation for MiLeP ANN is obtained through LMS and expressed as

$$W_{ak}(n+1) = W_{ak}(n) + \mu e u_{pa} \tag{6.25}$$

The total equivalent active load component is expressed by

$$W_{eq} = \frac{1}{3}(W_{pa} + W_{pb} + W_{pc}) \tag{6.26}$$

The loss component of the proposed control scheme is expressed as

$$I_{loss}(n) = I_{loss}(n-1) + K_P\{V_{dce}(n) - V_{dce}(n-1)\} + K_i V_{dce}(n) \tag{6.27}$$

where K_P and K_i are the proportional and integral gain constants of the PI controller. Due to the integration of PV with the proposed system, its active contribution must be computed. The active power component of PV is shown by its feedforward component (I_{PVff}).

$$I_{PVff} = \frac{2P_{PV}}{3V_t} \tag{6.28}$$

The computed total current w_{total} is expressed as

$$W_{total} = W_{eq} + I_{loss} - I_{PVff} \tag{6.29}$$

The three-phase PCC voltage is sensed and its peak magnitude is calculated by

$$V_t = \sqrt{\frac{2}{3}(v_{sa}^2 + v_{sb}^2 + v_{sc}^2)} \tag{6.30}$$

The in-phase component is calculated by

$$u_{pa} = \frac{v_{sa}}{V_t}, u_{pb} = \frac{v_{sb}}{V_t}, u_{pc} = \frac{v_{sc}}{V_t} \tag{6.31}$$

The reference source currents are obtained by multiplying the in-phase component and total weight component.

$$i_{sa}^* = W_{total} * u_{pa}, i_{sb}^* = W_{total} * u_{pb}, \; i_{sc}^* = W_{total} * u_{pc} \tag{6.32}$$

6.2.2.2 Control Scheme of Series Compensator

The source side is connected in series with the series compensator. The major goal of the series compensator is to inject the voltage during the sag/swell situation that is in phase with the PCC voltage. To reduce the amount of injection voltage required by the DVR, the injected voltage must be in phase with the PCC voltage. The load voltage in the a-b-c frame is transformed into the d-q-0 domain via the Clarke and Park transformation. The PLL is used to estimate the phase angle data for the a-b-c to dq0 transformation. Fig.6.5 depicts the series compensator's control scheme. The d-axis and q-axis components of the load voltage are given by

$$\begin{bmatrix} v_{Ld} \\ v_{Lq} \\ v_{L0} \end{bmatrix} = \frac{2}{3}\begin{bmatrix} \cos\theta & \cos\left(\theta - \frac{2\pi}{3}\right) & \cos\left(\theta + \frac{2\pi}{3}\right) \\ \sin\theta & \sin\left(\theta - \frac{2\pi}{3}\right) & \sin\left(\theta + \frac{2\pi}{3}\right) \\ \frac{1}{2} & \frac{1}{2} & \frac{1}{2} \end{bmatrix}\begin{bmatrix} v_{La} \\ v_{Lb} \\ v_{Lc} \end{bmatrix} \tag{6.33}$$

Similarly, the PCC voltage is first passed through MiLe functional expansion which acts as a filter in series compensation and filters out higher-order harmonics from the PCC voltage, the transformation is given by

$$\begin{bmatrix} v_{sd} \\ v_{sq} \\ v_{s0} \end{bmatrix} = \frac{2}{3}\begin{bmatrix} \cos\theta & \cos\left(\theta - \frac{2\pi}{3}\right) & \cos\left(\theta + \frac{2\pi}{3}\right) \\ \sin\theta & \sin\left(\theta - \frac{2\pi}{3}\right) & \sin\left(\theta + \frac{2\pi}{3}\right) \\ \frac{1}{2} & \frac{1}{2} & \frac{1}{2} \end{bmatrix}\begin{bmatrix} v'_{sa} \\ v'_{sb} \\ v'_{sc} \end{bmatrix} \tag{6.34}$$

The difference between the actual and reference series voltage is fed to the PI controller.

$$v_{sed}^*(n) = v_{sed}^*(n-1) + K_{p1}\{v_{ted}(n) - v_{ted}(n-1)\} + K_{i1}v_{ted} \tag{6.35}$$

$$v_{seq}^*(n) = v_{seq}^*(n-1) + K_{p2}\{v_{teq}(n) - v_{teq}(n-1)\} + K_{i2}v_{teq} \tag{6.36}$$

where $v_{ted} = v_{Ld}^{*} - v_{Ld}$; $v_{teq} = v_{Lq}^{*} - v_{Lq}$ are the errors between the actual and reference load voltage. The peak value of the reference load voltage is the direct component of the reference load voltage, and the quadrature component is adjusted to zero to keep the reference load voltage in phase with the PCC voltage. The reference series component in direct (v_{sed}^{*}) and quadrature component (v_{seq}^{*}) is converted to 3Ø reference series injected voltage.

$$\begin{bmatrix} v_{sea}^{*} \\ v_{seb}^{*} \\ v_{sec}^{*} \end{bmatrix} = \begin{bmatrix} \sin(\theta) & \cos(\theta) & 1 \\ \sin\left(\theta - \frac{2\pi}{3}\right) & \cos\left(\theta - \frac{2\pi}{3}\right) & 1 \\ \sin\left(\theta + \frac{2\pi}{3}\right) & \cos\left(\theta + \frac{2\pi}{3}\right) & 1 \end{bmatrix} \begin{bmatrix} v_{sed}^{*} \\ v_{seq}^{*} \\ v_{se0}^{*} \end{bmatrix} \tag{6.37}$$

These three-phase reference series injection voltages ($v_{sea}^{*}, v_{seb}^{*}, v_{sec}^{*}$) is given to the three-phase pulse width modulation voltage controller and thus generates the switching signals to the DVR's switches.

6.3 Simulation Results

MATLAB Simulink is used to model the suggested system. Under voltage sag, swell, load unbalancing, and changing solar irradiation, the performance of the suggested control strategy based on MiLeP ANN has been examined. When observing the simulation results, a 400V (rms), 50 Hz, 3Ø supply is used. In a three-phase grid-connected system, the improved SRF control technique is used to regulate the shunt and series voltage source converter. The shunt inverter's current ($i_{sha}, i_{shb}, i_{shc}$) produced from the shunt compensator is introduced in the suggested control technique to suppress the harmonics in the supply current, improve the power factor, and satisfy the reactive power requirement of the nonlinear loads. The series compensator is utilized to inject the series voltage into the loads under voltage sag and swell conditions to maintain the load voltage constant, i.e., at pre-sag and pre-swell conditions. Under voltage sag and swell conditions, the series compensator is used to inject the series voltage into the loads to keep the load voltage constant, i.e., at pre-sag and pre-swell conditions.

6.3.1 Performance analysis of SRFT-based adaptive control of UPQC

The performance analysis of SRFT-based adaptive control of UPQC under different operating conditions is modeled in MATLAB Simulink. It is necessary to investigate the performance of SRFT for mitigating the current-related and voltage-related PQ issues such as voltage sag, swell, unbalancing, reactive power compensation,

and load unbalancing. A three-phase UPQC system consists of a three-phase AC supply, a three-leg shunt VSC, a three-leg series VSC via series injection transformer, a DC link capacitor, a three-phase uncontrolled diode bridge R-L load. The system parameter has a supply of 400V, 50Hz with non-linear R-L load. This UPQC system's goals are to maintain balanced supply currents at the AC mains with a unity power factor and to regulate load voltage to its rated value.

6.3.1.1 Performance under Voltage Sag and Swell

The dynamic performance of UPQC under connected load for both balanced and unbalanced conditions is shown in Fig.6.6. A voltage sag (0.2pu) in supply voltage us applied at t=0.3s for 3 cycles is created and it is found that load voltage is maintained to constant amplitude under voltage sag condition. The DVR will inject the required voltage during voltage sag to support the load voltage to the rated voltage. During voltage sag condition, the series injecting voltage is increased to maintain the power balance among load, PV array, and source. Fig. 6.6 shows the waveform of the source voltage (v_{sabc}), source current (i_{sabc}), series injecting voltage (v_{Cinj}), load voltage (v_{Labc}), load current (i_{Labc}), load voltage (v_{Labc}), compensating current ($i_{sh(abc)}$), PV current (I_{pv}), and DC-link voltage (V_{dc}) are investigated under normal and dynamic conditions.

Since the PV is part of the system, it provides the shunt compensator, which transfers the actual power to the grid when needed, with the power it needs. Because of the PI controller's action, the DC link voltage is kept constant at 700 V during voltage sag. Another voltage-related PQ problem is voltage swell. The suggested control method has been used to test this condition. The voltage swells of 20% at t=0.5s, which lessens the source current's magnitude, is depicted in Fig. 6.7. Fig. 6.7 shows that the source current is still sinusoidal and balanced. Additionally, even in the event of a voltage swell, the DVR will feed the load with a decreased magnitude voltage.

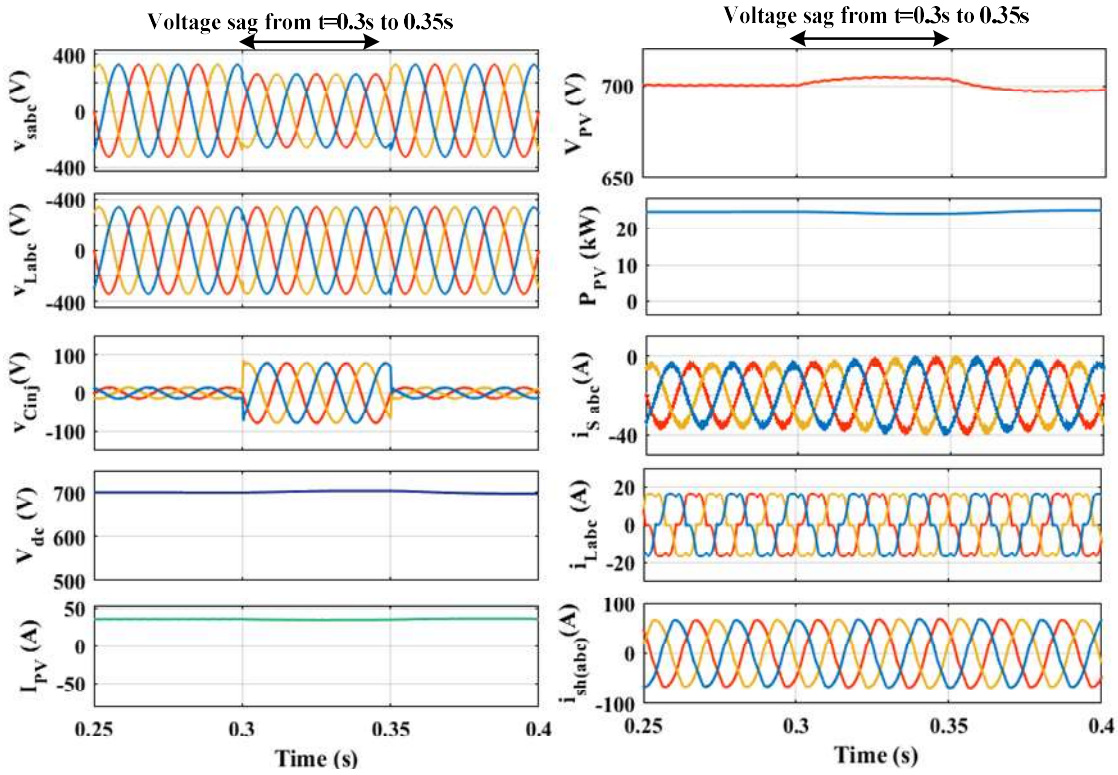

Fig. 6.6 Simulation results under voltage sag condition with SRFT control scheme

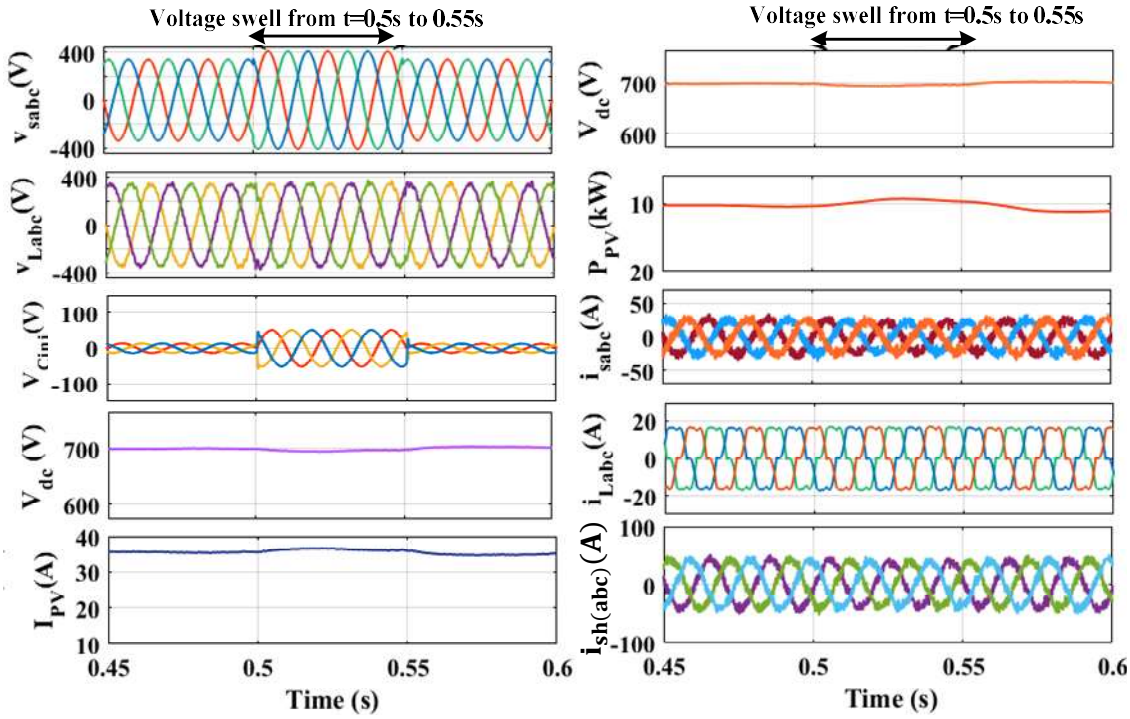

Fig. 6.7 Simulation results under voltage swell condition with SRFT control scheme

The load side creates the imbalanced load, and the shunt compensator's function is to maintain a sinusoidal and balanced source current. The load is disconnected at t=0.8 to 0.85 seconds, as seen in Fig. 6.8. Figure 6.8 shows both static and dynamic analysis of the waveforms of the source voltage (v_{sabc}), source current (i_{sabc}), series injecting voltage (v_{Cinj}), load voltage (V_{Labc}), load current (i_{Labc}), compensatory current ($i_{sh(abc)}$), PV current (I_{PV}) and dc-link voltage (V_{dc}). The DC link voltage increases to 730 V as a result of abrupt load changes, a decrease in PV current, and PV due to sudden load changes or disconnections.

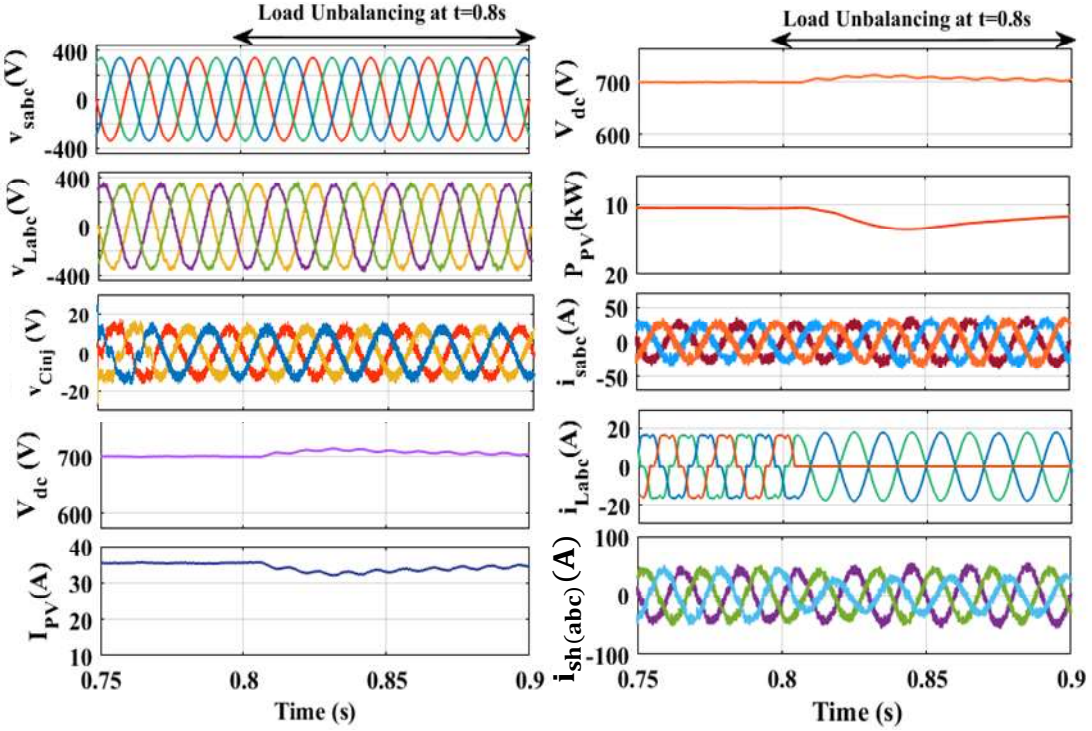

Fig. 6.8 Simulation results under load unbalancing condition with SRFT control scheme

6.3.1.2 Performance of three-phase grid-connected PV-UPQC under irradiance change and voltage harmonics

The suggested system's functionality is evaluated in a changing solar irradiance environment. At t=0.3s, the irradiance decreases from 1000 W/m^2 to 800 W/m^2. The PV can produce 25kW of real power at 1000 W/m^2, whereas the load's active power consumption is 14kW. The source is supplied with the remaining 14kW of active power. The shunt VSC provides the 7.2kVar reactive power demand of the load. Reactive power injection of 7.2kVar to the load is possible via the shunt compensator. The source current, on the other hand, continues to be sinusoidal and has a magnitude of 29A. The PV array's

irradiance drops to 800W/m^2 at t=0.3s. Only 21kW of PV power can be injected. The load's actual power consumption of 14 kW is still met by PV real power. The grid receives the remaining 6kW of active power. Changes in solar irradiation cause the source current to decrease, and Fig. 6.9(a) shows a slight variation in the DC link voltage. Fig. 6.9(b), shows the harmonics effect that occurred in source voltage at t=0.6s. It is seen that the source current is balanced and sinusoidal during voltage harmonics conditions. Thus, overall SRFT can mitigate both current and voltage-related PQ issues.

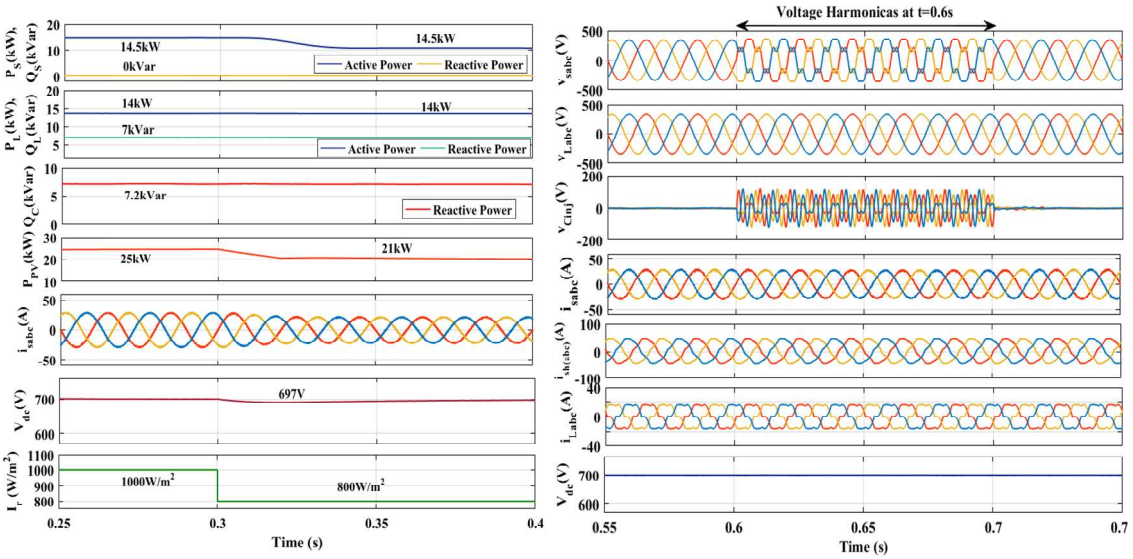

(a) (b)

Fig. 6.9 Simulation result of proposed UPQC system under (a) Solar irradiance change (b) Voltage Harmonics

6.3.2 Performance analysis of Mittag-Leffler based adaptive control of UPQC

6.3.2.1 Performance under Voltage Sag and Swell

Fig. 6.10, shows the waveform of the source voltage (v_{sabc}), source current (i_{sabc}), series injecting voltage (v_{Cinj}), load voltage (v_{Labc}), load current (i_{Labc}), load voltage (v_{Labc}), compensating current ($i_{sh(abc)}$), PV current (I_{pv}), and DC-link voltage (V_{dc}) are investigated under normal and dynamic conditions. At t = 0.3 s, voltage Sag of 20% is simulated, which requires increasing the source current to maintain the source power constant. To keep the load voltage constant, the VSC of the DVR provides the required voltage into the system. However, the grid current is balanced and sinusoidal with little distortion in dc-link voltage as shown in Fig. 6.10. The PV is connected to the system and thus supplies its real power to the shunt compensator, which will transfer it to the grid whenever that power is required.

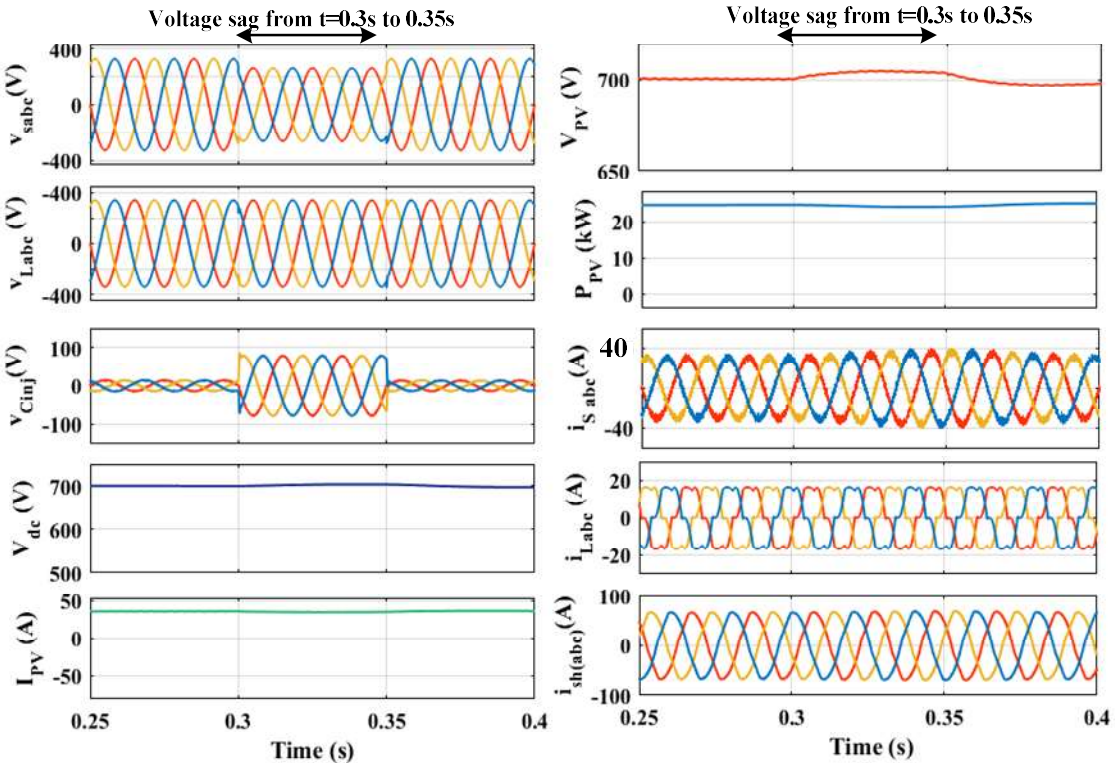

Fig. 6.10 Performance of proposed UPQC with MiLeP under Voltage Sag from t=0.3 to 0.35s.

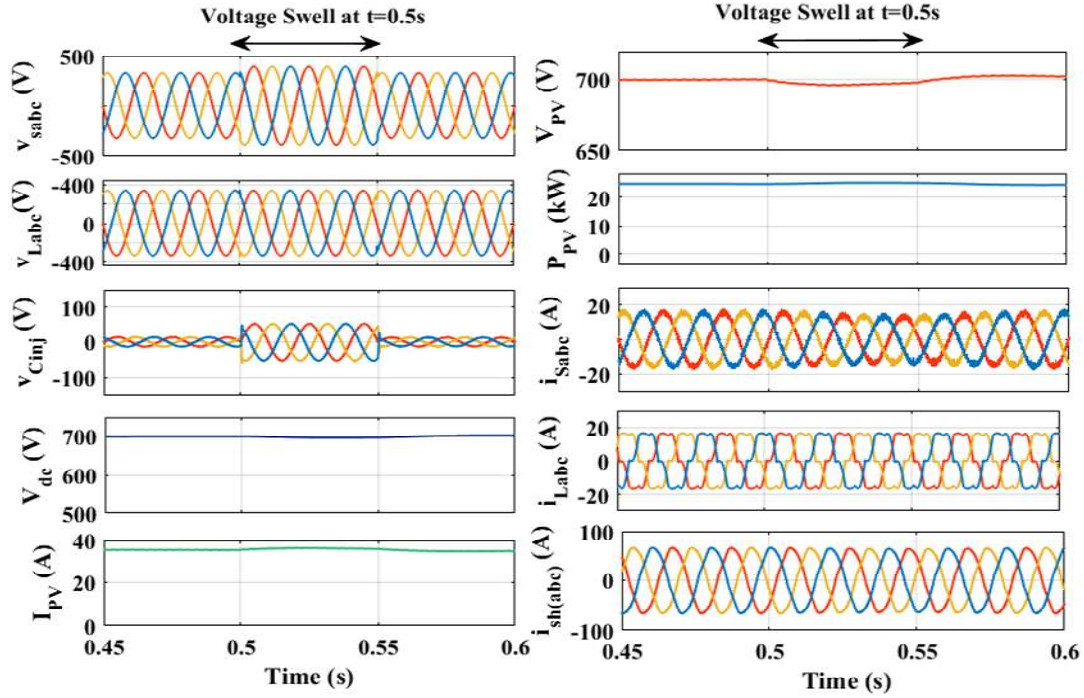

Fig. 6.11 Performance of proposed UPQC with MiLeP under Voltage Swell from t=0.5s to 0.55s.

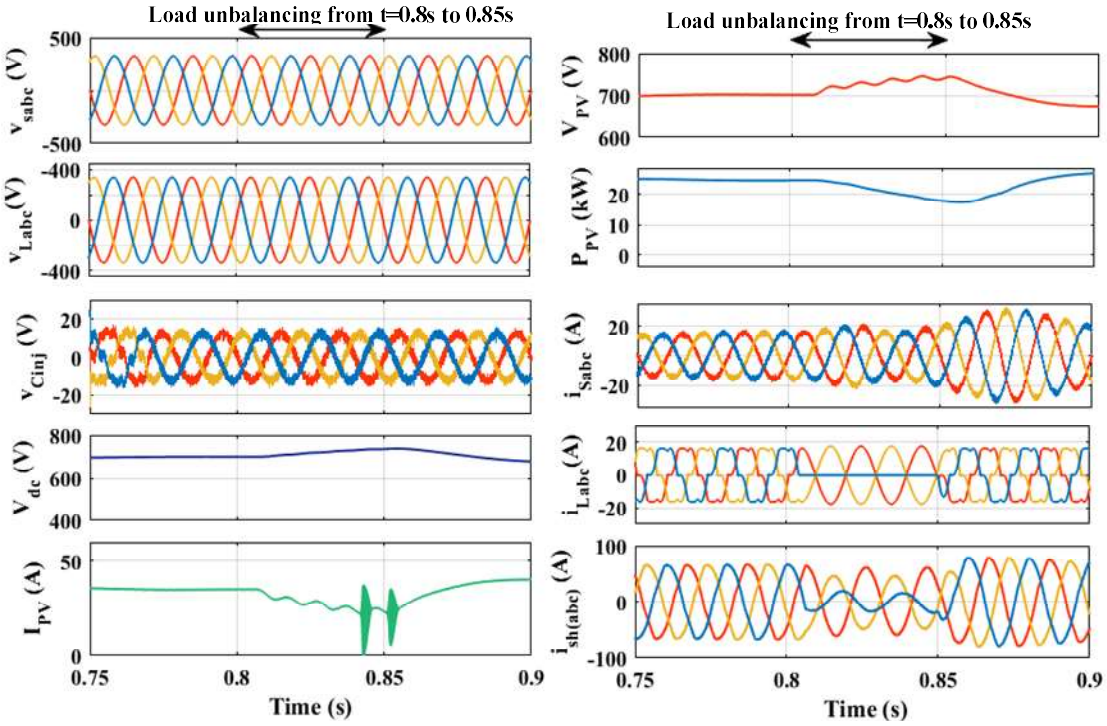

Fig. 6.12 Performance of proposed UPQC with MiLeP under load unbalancing from t=0.8 to 0.85s.

The DC link voltage is maintained constant at 700 V during voltage sag due to PI controller action. Voltage swell is another voltage-related PQ issue. This condition has been tested with the proposed control technique. Fig. 6.11 shows the voltage swell of 20 % at t=0.5s, which reduces the magnitude of the source current. It is seen from Fig. 6.11 that the source current remains balanced and sinusoidal. Also, the DVR will feed reduced magnitude voltage to the load so that the load voltage, even if there is the condition of voltage swell. The DC link voltage remains constant due to PI control.

6.3.2.2 Performance under load unbalancing

The unbalanced load is created on the load side, and the shunt compensator's purpose is to keep the source current balanced and sinusoidal. According to Fig. 6.11, the load is disconnected at t=0.8 to 0.85s. The waveforms of the source voltage (v_{sabc}), source current (i_{sabc}), series injecting voltage (v_{Cinj}), load voltage (v_{Labc}), load current (i_{Labc}), load voltage (v_{Labc}), compensatory current ($i_{sh(abc)}$), PV current (I_{PV}), and dc-link voltage (V_{dc}) are analyzed under both static and dynamic situations in Fig. 6.12. Due to sudden load changes, a fall in PV current, and PV due to sudden load changes or disconnections, the DC link voltage increases to 710 V.

6.3.2.3 Performance of three-phase grid-connected PV-UPQC under irradiance change and voltage harmonics

The performance of the proposed system is tested under solar irradiance change. The irradiance is changed from 1000 W/m^2 to 800 W/m^2 at t=0.3s. At 1000 W/m^2, the PV can provide 25kW real power and the active power demand of load is 14kW. The remaining 14kW active power is fed to the source. The reactive power demand of the load is 7.1kVar, and it is fulfilled the shunt VSC. The shunt compensator can inject 7.1kVar of reactive power to the load. In contrast, the source current remains sinusoidal with a magnitude of 29A. At t=0.3s, the irradiance of the PV array is reduced to 800W/m^2. The PV power is available to inject 20kW only. The real power demand of load remains the same, which is 14kW fulfilled by PV real power. The remaining 6 kW of real power is given to the grid. The source current reduces due to changes in solar irradiance, and a small variation in DC link voltage is seen in Fig. 6.13(a). Fig. 6.13(b), shows the harmonics effect occurred in source voltage at t=0.6s. It is seen that the source current is balanced and sinusoidal during voltage harmonics conditions. Thus, overall MiLeP can mitigate both current and voltage-related PQ issues. The THD of the source current is 0.79% under distorted source voltage.

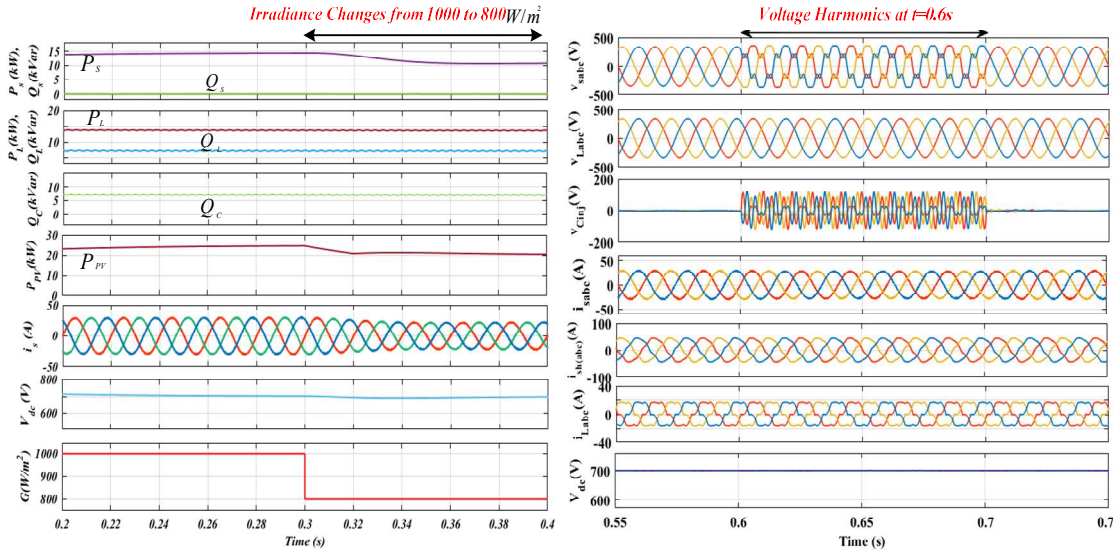

(a) (b)

Fig. 6.13 Performance of the proposed system under solar irradiance change at t=0.3s.

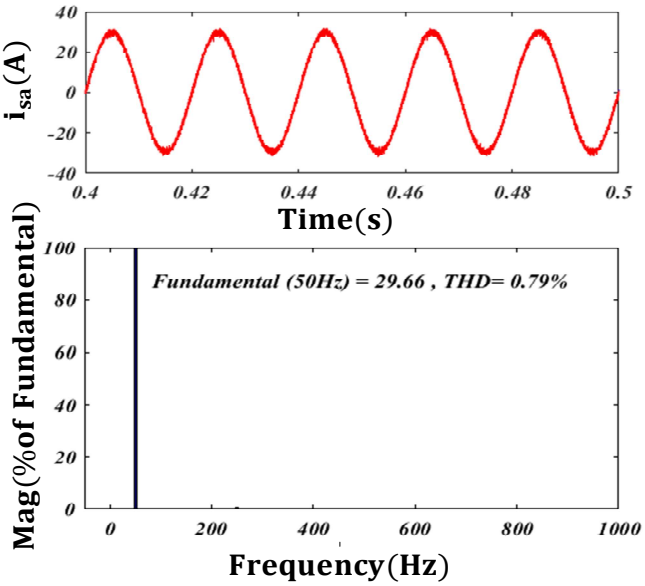

Fig. 6.14 THD of source current i_{sa}.

6.3.3 Comparative Performance of three-phase UPQC based on SRFT and MileP control scheme

The performance comparisons of both SRFT and MiLeP based control for UPQC under the condition of voltage sag, voltage swell, voltage harmonics, voltage unbalance and load unbalancing are given in Table 6.3. The THD of both source and load voltage is obtained through FFT analysis in MATLAB Simulink under all mentioned operating conditions. It is found that MiLeP performs better than SRFT under all operating conditions.

Table 6.3: Comparative performance analysis UPQC based on SRFT and MiLeP control schemes

System Condition	**Phase**	**Conventional SRFT**		**Proposed MiLeP**	
		Current	Voltage	Current	Voltage
Voltage Sag THD (%)	A	4.05%	4.63%	**3.78%**	4.63%
	B	5.09%	4.5%	**4.81%**	4.5%
	C	5.02%	5.41%	**4.5%**	5.41%
Voltage Swell	A	4.08%	3.30%	**3.96%**	3.30%

THD (%)	B	4.93%	5.29%	**4.19%**	5.29%
	C	4.91%	5.30%	**4%**	5.30%
Load Unbalancing THD (%)	A	4.06%	0.7%	**3.4%**	0.7%
	B	4.90%	0.6%	**3.2%**	0.6%
	C	4.89%	0.7%	**3.5%**	0.7%
Voltage Harmonics THD (%)	A	4.3%	25%	**3.1%**	25%
	B	4.9%	25%	**2.9%**	25%
	C	4.79%	25%	**3.2%**	25%
Irradiance Change THD (%)	A	5.58%	0%	**2.57%**	0%
	B	7.39%	0%	**3.26%**	0%
	C	6.77%	0%	**2.93%**	0%

6.4 Experimental Results

A hardware-in-the-loop (HIL) system is developed in real-time to assess the feasibility of the suggested method for DVR control. A schematic of the planned laboratory experiment setting is shown in Figure 6.15. The OPAL-RT real-time digital simulator with FPGA Xilinx Kintex-7 410T is the component of the real-time HIL system. Operating in the RT-LAB software environment, the OPAL-RT is a real-time simulation platform driven by Intel Xeon Four-Core 3.7 GHz processors. There are 32 digital inputs and 32 digital outputs on the OPAL-RT. OPAL-RT is used to verify the results of a MATLAB Simulink simulation of the suggested system.

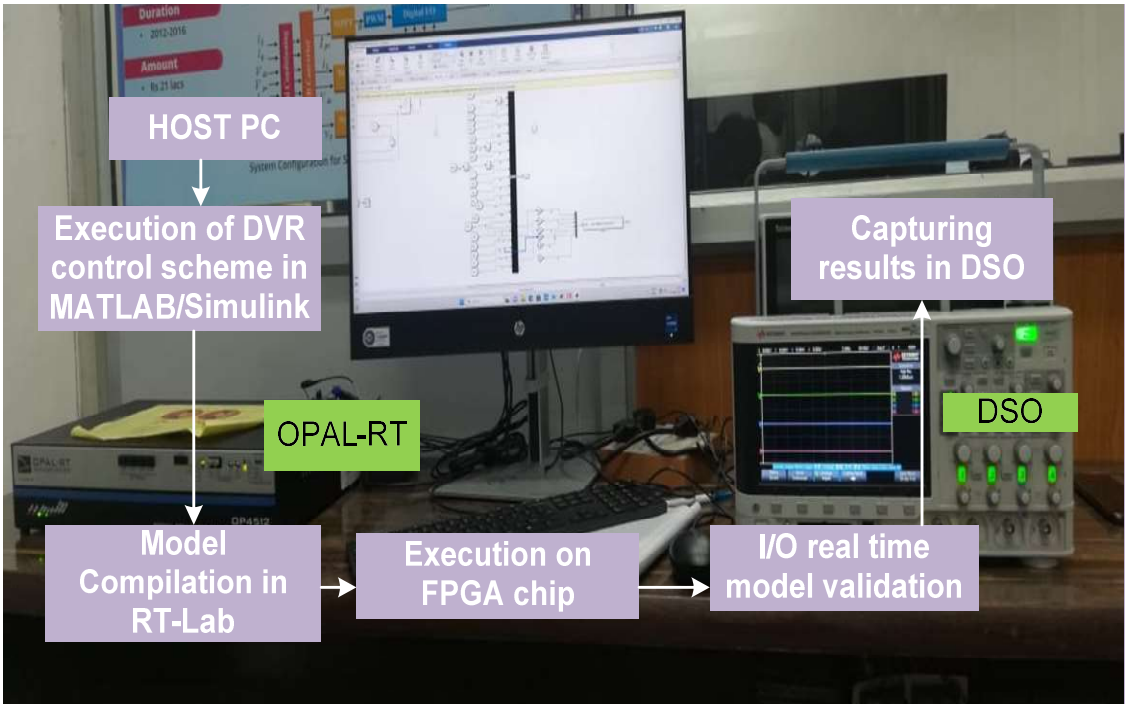

Fig. 6.15 Experimental Setup of UPQC implementation in OPAL-RT.

6.4.1 Performance analysis of SRFT-based adaptive control of PV-UPQC

The dynamic performance of PV-UPQC is shown in Fig. 6.16(a-c). The response of PV-UPQC under source voltage sag, swell, and load unbalance is shown in Fig. 6.16(a-c). The response of UPQC under 20% voltage sag is shown in Fig. 6.16(a-b). The recorded waveforms are source voltage (v_{sa}), load voltage (v_{La}), series compensator voltage ($v_{Ca(inj)}$), and terminal voltage (V_t). The response of UPQC under 20% voltage swell is shown in Fig. 6.16(b) with the captured waveform of the source voltage (v_{sa}), load voltage (v_{La}), series compensator voltage ($v_{Ca(inj)}$), and terminal voltage (V_t). The DVR will inject the voltage at PCC under the condition of voltage sag and swell to maintain load voltage. The intermediate signals of SRFT control of PV-UPQC are shown in Fig. 6.16(c). the direct component of source and load voltage under voltage sag condition is shown in Fig. 6.16(c). The direct component of the source voltage (v_{sd}^{*}) decreases under voltage sag, while the quadrature component oscillates (v_{sq}^{*}) to zero. The fundamental load component of load voltage (v_{Ld}^{*}) remains constant at its nominal value as desired.

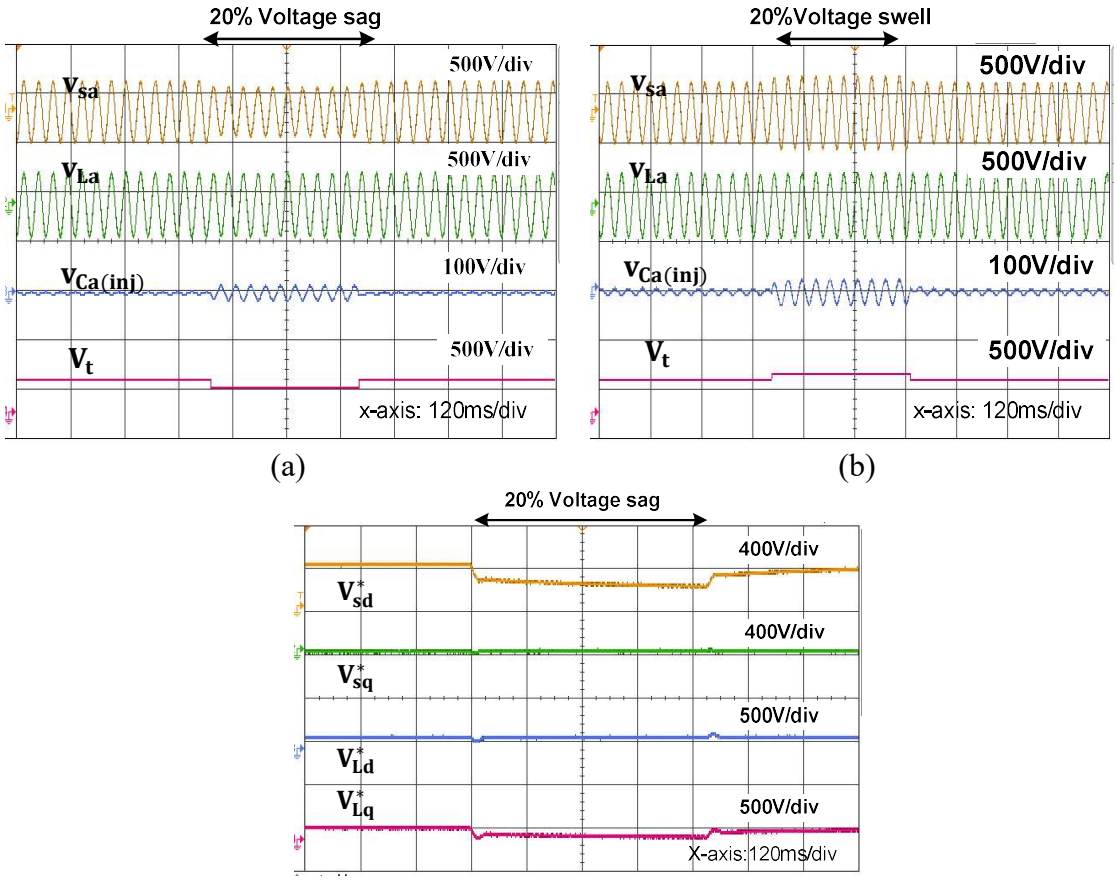

Fig. 6.16 Experimental results of proposed UPQC system under (a) Voltage Sag (b) Voltage swell (c) Intermediate Signals of series compensation with SRFT.

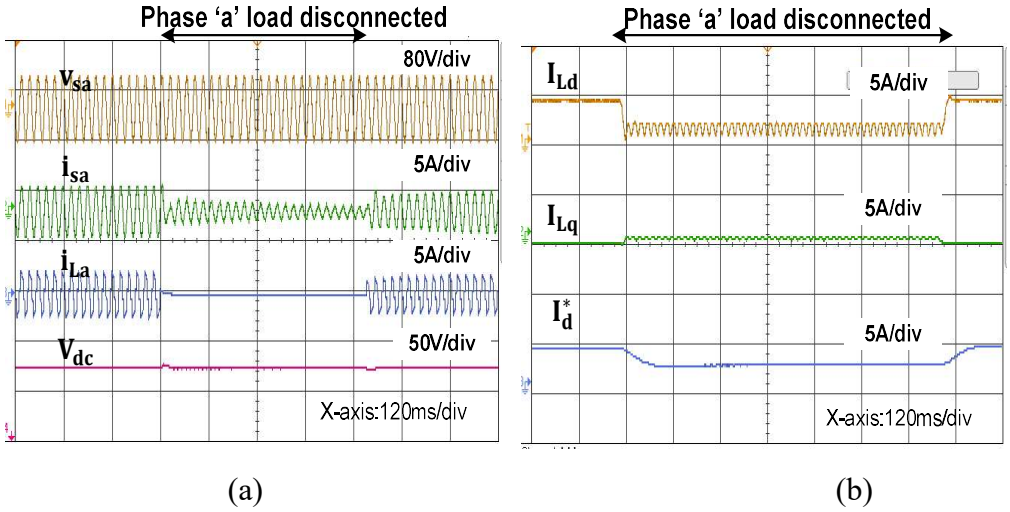

Fig. 6.17 Experimental results of proposed UPQC system under load unbalancing (a) source voltage, source current, load current, and DC link voltage (b) Intermediate signals of shunt compensation with SRFT.

The dynamic response of PV-UPQC under load unbalancing with SRFT control is shown in Fig. 6.17. The load of phase 'a' is disconnected from the system. The source current

decreases as the load is disconnected from the proposed three-phase grid-connected PV-UPQC to maintain the power balance among source, load, and PV. The captured waveforms are source voltage, source current, load current, and DC-link voltage as shown in Fig. 6.17(a). The intermediate signals of current controlled SRFT for load compensation is shown in Fig.6.17(b) under load unbalancing. The fundamental load component (i_{Ld}) decreases with disconnection of load. The total current (i_d^*) required for generating the reference source current is also decreased with load decrease.

6.4.2 Performance analysis of MiLeP based adaptive control of UPQC

The dynamic performance of PV-UPQC is shown in Fig. 6.18(a-c). The response of PV-UPQC under source voltage sag, swell, and load unbalance is shown in Fig. 6.16(a-c). The response of UPQC under 20% voltage sag is shown in Fig. 6.18(a-b). The recorded waveforms are source voltage (v_{sa}), load voltage (v_{La}), series compensator voltage ($v_{Ca(inj)}$), and terminal voltage (V_t). The response of UPQC under 20% voltage swell is shown in Fig. 6.18(b) with the captured waveform of the source voltage (v_{sa}), load voltage (v_{La}), series compensator voltage ($v_{Ca(inj)}$), and terminal voltage (V_t). The DVR will inject the voltage at PCC under the condition of voltage sag and swell to maintain load voltage. Fig. 6.18(c) shows the response of UPQC with MiLeP under the condition of voltage harmonics. It is evident from the dynamic response that the load voltage is balanced and sinusoidal due to series compensating voltage injection

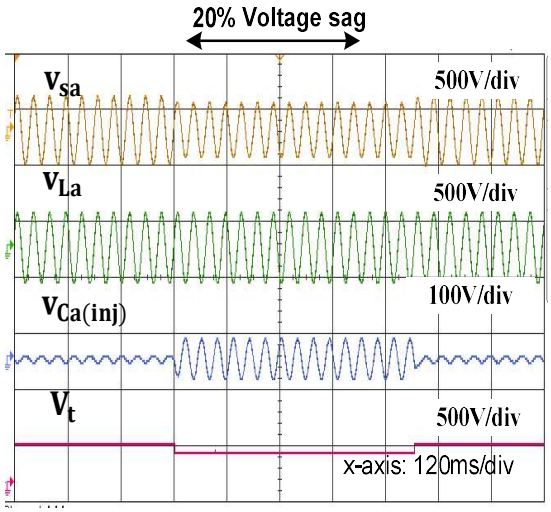

(a)

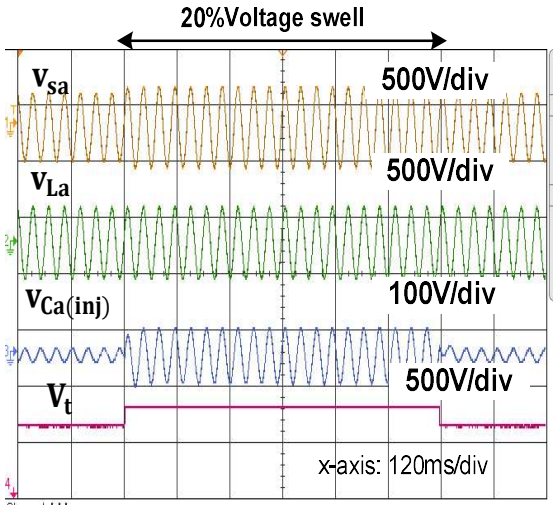

(b)

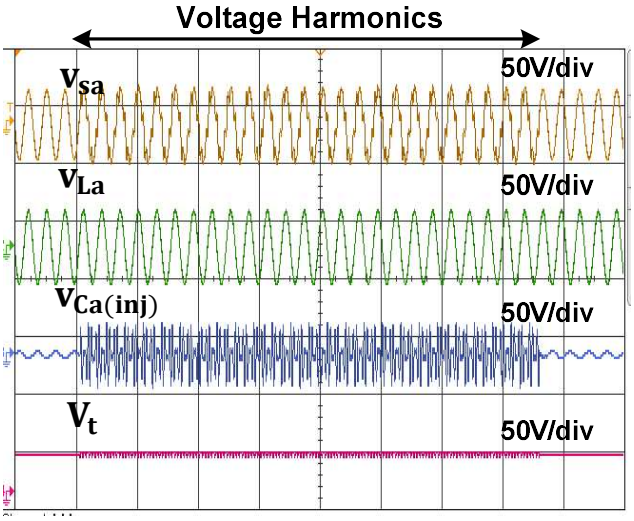

(c)

Fig. 6.18 Experimental results of proposed UPQC system under (a) Voltage Sag (b) Voltage swell (c) Voltage Harmonics with MiLeP

.

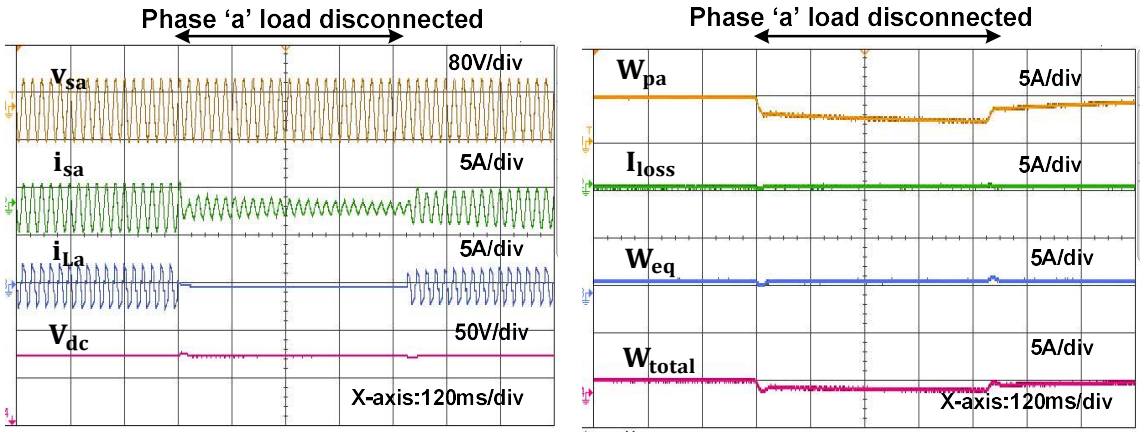

(a) (b)

Fig. 6.19 Experimental results of proposed UPQC system under load unbalancing (a) source voltage, source current, load current, and DC link voltage (b) Intermediate signals of shunt compensation with MiLeP

The dynamic response of PV-UPQC under load unbalancing with MiLeP control is shown in Fig. 6.19. The load of phase 'a' is disconnected from the system. The source current decreases as the load is disconnected from the proposed three-phase grid-connected PV-UPQC. To maintain the power balance among source, load, and PV. The captured waveforms are source voltage, source current, load current, and DC-link voltage as shown in Fig. 6.19(a). The intermediate signals of current controlled SRFT for load compensation are shown in Fig.6.19(b) under load unbalancing. The fundamental load

component (w_{pa}) decreases with disconnection of load. The total current (w_{total}) required for generating the reference source current is also decreased with load decrease.

6.5 Comparative Performance analysis of control schemes of three-phase UPQC

The performance of the MiLeP is contrasted with conventional SRFT control technique. Both methods are used for shunt and series compensation with UPQC under the same system parameters. From each algorithm, the fundamental active load component under load unbalance conditions is extracted and compared for weight convergence. Fig. 6.20 are displayed to provide a more accurate comparison of performance among the mentioned control schemes.

Both control schemes can mitigate current and voltage related PQ issues. The convergence of fundamental load components under load change is faster with MiLeP around 1 to 1.5 cycles as compared to SRFT.

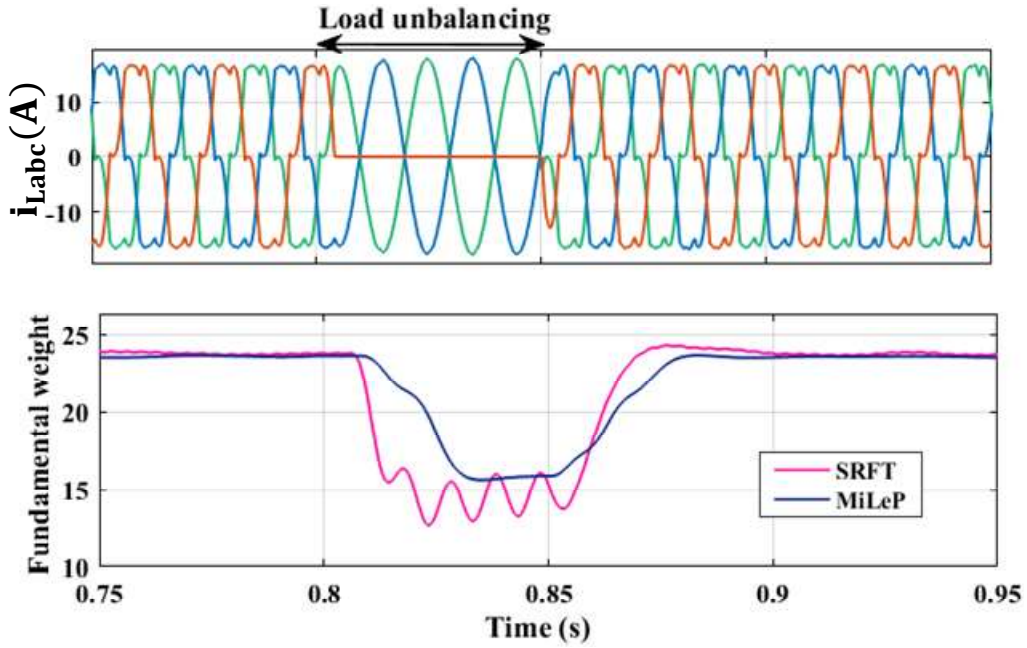

Fig. 6.20 Fundamental weight convergence under load unbalancing with conventional SRFT and MiLeP control schemes.

6.6 Conclusions

Design and control schemes of three-phase grid connected system with PV integration is discussed in this chapter. The UPQC is utilized to mitigate both current and voltage related PQ issues such as sag, swell, harmonics, DC offset, voltage unbalancing, load unbalancing, and reactive power compensation. Two control scheme one is conventional

SRFT and other is proposed MiLeP-SRFT control schemes are implemented in UPQC. The MiLeP-SRFT based control scheme is better than conventional SRFT in terms of weight convergence, and THD of source current as shown in Table 6.3.

CHAPTER 7

GRID SYNCHRONIZATION TECHNIQUES

7.1 Introduction

Integration of renewable energy resources into the existing utility system requires a seamless grid synchronization technique. As the demand for clean and sustainable energy continues to rise, PV systems have gained significant popularity for their ability to harness energy from the sun and convert it into electricity. However, to effectively contribute to the grid's stability and reliability, these PV systems must operate in perfect harmony with the grid. This is where the Phase-Locked Loop (PLL) comes into play, serving as a sophisticated control mechanism that enables PV systems to synchronize their output with the grid's voltage and frequency, facilitating efficient power injection while minimizing disruptions. Another important aspect of grid synchronization is synchronizing the VSCs with the source voltage helps in gaining improved power quality. A Phase-Locked Loop (PLL) is an essential control unit used to ensure that the output voltage from a grid-connected VSC is synchronized with the source's voltage. To transform DC power from a renewable energy source into AC power suitable for utility integration, VSCs are frequently employed in renewable energy systems.

Various PLL control scheme for the single-phase and three-phase systems is discussed in the literature review. The designing and control of PLL for a single-phase grid-connected VSC is more challenging then PLL for a three-phase system. Three-phase grid voltage has a natural phase shift of 120°. It is simple to use Park’s and Clark's transformation in the estimation of system frequency. While in a single-phase system, it is required to generate quadrature signals by using different methods. This chapter discusses some existing and novel synchronization methods for single-phase PLLs to estimate the phase, frequency, amplitude, and synchronizing signals under various sourced voltage scenarios.

7.2 Control Scheme

Some of the conventional and proposed control scheme is explained in this section. The conventional scheme such as SRF-PLL, SOGI PLL and proposed FAMAF-PLL and EPLL are discussed.

7.2.1 SRF-PLL based grid synchronization control scheme

The SRF PLL consists a transformation block, a trigonometric function, a P controller and an integrator. The source voltage (v_s) is transformed into its α and β components. The α component (v_α) is same as original source voltage (v_s) while the β component (v_β) has a phase shift of 90°. The phase shift obtained by delay the input signal by $T/4$, where T is the time period of source voltage. The α and β components are transformed into its d-q-0 component (V_d and V_q) using Park's transformation. The voltage V_d and V_q are fed into an 'arctangent' function to calculate the phase angle of the voltage component. The phase angle is passed through a PI controller and its output is known as frequency error ($\Delta\omega_0$). The frequency error is added with the actual standard frequency (ω_n) provides estimated frequency (ω_{est}). The estimated frequency is fed to integrator which gives phase angle (θ_{oc})

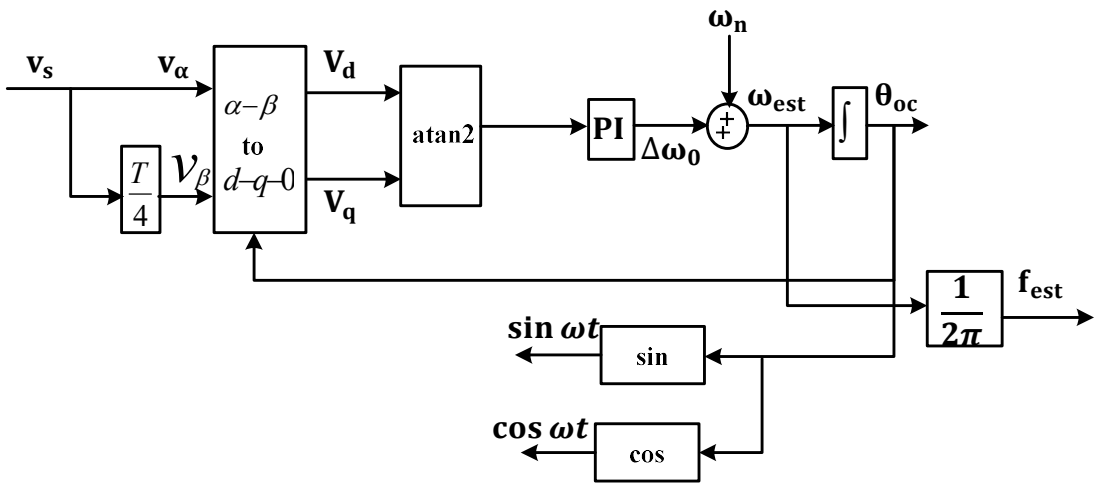

Fig. 7.1 Control Block of SRFT based PLL

The source voltage (v_s or v_α) is expressed as

$$v_s(t) = v_\alpha(t) = V_k \sin(\omega t + \varphi_k) \tag{7.1}$$

$$v_\beta(t) = v_\alpha\left(t - \frac{T}{4}\right) = V_k \sin\left(\omega t + \varphi_k - \frac{\omega T}{4}\right) \tag{7.2}$$

$$v_\beta(t) = V_k \sin\left(\theta_i - \frac{\omega T}{4}\right) = -V_k \cos\left(\theta_i - \Delta\omega_0 \frac{T}{4}\right) \quad (7.3)$$

The stationary frame components v_α and v_β are transformed into rotating frame components using Park's transformation,

$$\begin{bmatrix} V_d(t) \\ V_q(t) \end{bmatrix} = \begin{bmatrix} \sin\theta & -\cos\theta \\ \cos\theta & \sin\theta \end{bmatrix} \begin{bmatrix} v_\alpha(t) \\ v_\beta(t) \end{bmatrix} \quad (7.4)$$

$$V_d(t) = v_\alpha(t)\sin\theta - v_\beta(t)\cos\theta \quad (7.5)$$

$$V_q(t) = v_\alpha(t)\cos\theta + v_\beta(t)\sin\theta \quad (7.6)$$

$$V_q(t) = \frac{V_K}{2}[\sin(\theta_i + \theta) + \sin(\theta_i - \theta)] - \frac{V_k}{2}\left[\sin\left(\theta_i - \Delta\omega_0 \frac{T}{4} + \theta\right) - \sin\left(\theta_i - \Delta\omega_0 \frac{T}{4} - \theta\right)\right] \quad (7.7)$$

$$V_q(t) = \frac{V_K}{2}\left[\sin(\theta_i - \theta) + \sin\left(\theta_i - \Delta\omega_0 \frac{T}{4} - \theta\right)\right] + \frac{V_K}{2}\left[\underbrace{\sin(\theta_i + \theta) - \sin\left(\theta_i - \Delta\omega_0 \frac{T}{4} + \theta\right)}_{\text{double frequency term}}\right] \quad (7.8)$$

The resultant signal ω_{est} is passed through Voltage Controlled Oscillator (VCO) which gives phase angle (θ_{oC}) of the source voltage. The phase angle is expressed as

$$\theta = \tan^{-1}\frac{\bar{V}_q}{\bar{V}_d} \quad (7.9)$$

7.2.2 SOGI PLL based grid synchronization control scheme

The SOGI with a PI controller is used in Loop filter to provide a second-order transfer function, which allows for more efficient tracking and synchronization of the input signal's phase and frequency. The SOGI is used to produce stationary frame component of source voltage $v_{s\alpha}$ and $v_{s\beta}$. These in-phase and quadrature voltage component is transformed into d-q-0 component. The q-component V_q consists the phase and frequency information of source voltage.

The voltage V_q is compared with reference voltage and their error signal is fed to PI controller to regulate the obtained frequency $\Delta\omega_0$. The resultant frequency $\Delta\omega_0$ is added with the standard grid frequency ω_n which produces the estimated frequency ω_{est}.

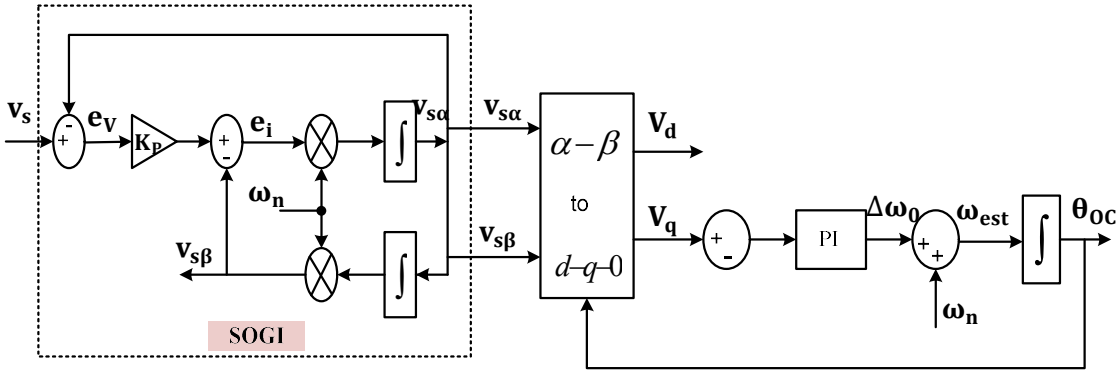

Fig. 7. 2 Block Diagram of SOGI PLL

The estimated frequency is integrated to obtain the phase angle (θ_{oc}).

$$v_s(t) = v_{s\alpha}(t) = V_k \sin(\omega t + \varphi_k) \tag{7.10}$$

$$v_{s\beta}(t) = v_{s\alpha}\left(t - \frac{T}{4}\right) = V_k \sin\left(\omega t + \varphi_k - \frac{\omega T}{4}\right) \tag{7.11}$$

$$v_{s\beta}(t) = V_k \sin\left(\theta_i - \frac{\omega T}{4}\right) = -V_k \cos\left(\theta_i - \Delta\omega_0 \frac{T}{4}\right) \tag{7.12}$$

The error signal e_v is expressed as

$$e_v(t) = v_s(t) - v_{s\alpha}(t) \tag{7.13}$$

$$v_{s\beta}(t) = \omega_n \int v_{s\alpha}(t)\, dt \tag{7.14}$$

The Laplace transform of Eq. (7.14) is expressed as

$$v_{s\beta}(s) = \frac{\omega_n v_{s\alpha}(s)}{s} \tag{7.15}$$

$$v_{s\alpha}(t) = \int e_i(t)\omega_n dt \tag{7.16}$$

$$e_i(t) = K_P e_v(t) - v_{s\beta}(t) \tag{7.17}$$

Put the value of '$e_i(t)$' from Eq. (7.17) in Eq. (7.18),

$$v_{s\alpha}(t) = \int \omega_n K_P e_v(t) dt - \int \omega_n v_{s\beta}(t)) dt \tag{7.18}$$

The Laplace transform of Eq. (7.18) is expressed as

$$v_{s\alpha}(s) = \omega_n K_P \left[\frac{v_s(s)}{s} - \frac{v_{s\alpha}(s)}{s}\right] - \omega_n \frac{v_{s\beta}(s)}{s} \tag{7.19}$$

$$v_{s\alpha}(s) = \omega_n K_P \left[\frac{v_s(s)}{s} - \frac{v_{s\alpha}(s)}{s}\right] - \omega_n^2 \frac{v_{s\alpha}(s)}{s^2} \quad (7.20)$$

By rearranging the above Eq. (7.20), the closed loop transfer of in-phase signal is expressed as

$$D(s) = \frac{v_{s\alpha}(s)}{v_s(s)} = \frac{K_P \omega_n s}{s^2 + K_P \omega_n s + \omega_n^2} \quad (7.21)$$

The quadrature signal is expressed as

$$Q(s) = \frac{v_{s\alpha}(s)}{v_s(s)} = \frac{K_P \omega_n^2}{s^2 + K_P \omega_n s + \omega_n^2} \quad (7.22)$$

Thus, the transfer function of SOGI is expressed as

$$G_{SOGI}(s) = \frac{v_{s\alpha}(s)}{K_P e_v(s)} = \frac{\omega_n s}{s^2 + \omega_n^2} \quad (7.23)$$

Transfer function of error signal $e_v(s)$ w.r.t source voltage $v_s(s)$ is expressed as

$$E(s) = \frac{e_v(s)}{v_s(s)} = \frac{s^2 + \omega_n^2}{s^2 + K_P \omega_n s + \omega_n^2} \quad (7.24)$$

7.2.3 FAMAF based grid synchronization control scheme

The fundamental component of grid voltage can be extracted using the moving average filter, a linear low pass filter. In-loop filter refers to a frequency adaptable MAF filter that is created and installed inside the PLL control loop. The dynamic response of the traditional MAF is slow. By including a correction component, the traditional MAF can be made frequency adaptive. With changes in grid frequency, the FAMAF's window size is constantly changed. The transfer function of conventional MAF is expressed as

$$G_{OL_{MAF}}(s) = \frac{1 - e^{-T_w s}}{T_w s} \quad (7.25)$$

where T_W denotes the FMAF window size. The MAF phase-delay is related to the MAF window length, hence the longer the MAF window length, the slower the dynamic reaction will be.

The open loop transfer function of FAMAF-PLL is expressed as

$$G_{OL\_FMAF}(s) = \left(\frac{(1 - e^{-T_W s})(1 + T_W s/2)}{T_W s(1 + \beta T_W s)}\right) \frac{(s + K_P)}{s} \quad (7.26)$$

where β is the attenuation factor and T_W is the FAMAF window length, whose value is equal to 1/2 of the fundamental time period. The FAMAF combines a standard MAF in series with a phase adjustment transfer function to increase the system's phase margin.

For hardware implementation of the proposed PLL, the transfer function in the 's' domain should be discretized in 'z' domain.

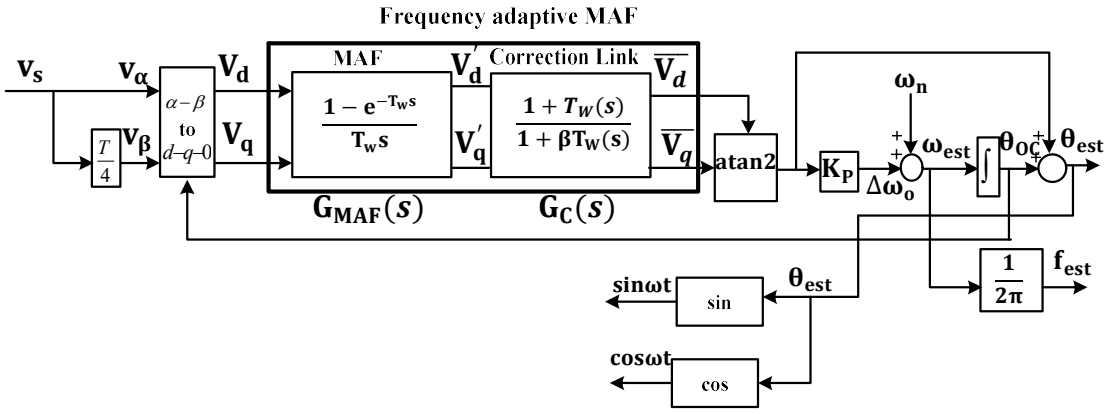

Fig. 7.3 Block diagram of FAMAF PLL

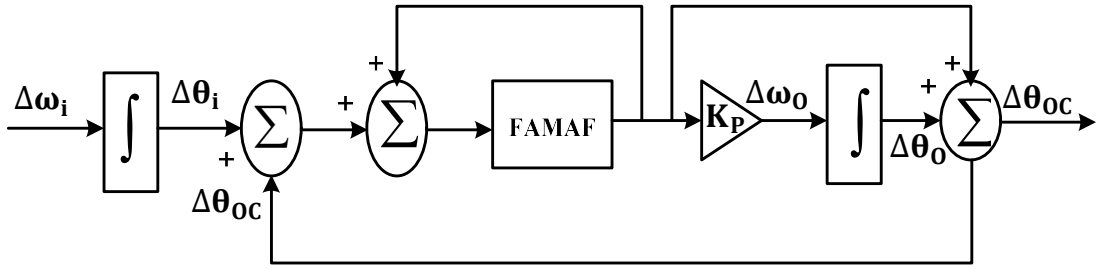

Fig. 7.4 Open loop model of FAMAF PLL

The transfer function of FAMAF in the 'z' domain is expressed in Eq. (7.27), where 'N' shows the no. of samples of the input signal and it is expressed as $\frac{T_w}{T_s}$; T_s is the sampling time of the proposed system

$$G_{OL\_FMAF}(z) = \left(\frac{(1-z^{-N})(2+N(1-z^{-1}))}{2N(1-z^{-1})(1+\beta N(1-z^{-1}))}\right)\frac{K_P}{z-1} \tag{7.27}$$

The transfer function of the modelled FAMAF PLL is represented as

$$G_{CL_{FAMAF}}(s) = \frac{G_{OL\_FAMAF}}{1+G_{OL\_FAMF}} \tag{7.28}$$

Using Fig. 7.4, the open loop transfer can be expressed as

$$G_{OL\_FAMAF} = \frac{\Delta\theta_{oc}}{\Delta\theta_i - \Delta\theta_{oc}} = \frac{FAMAF}{1-FAM}\left(\frac{s+K_P}{s}\right) \tag{7.29}$$

$$G_{OL\_FAMAF} = \frac{\left(\frac{1-e^{-T_w s}}{T_w s}\right)\left(\frac{1+T_w s/2}{1+\beta T_w s}\right)}{1-\left(\frac{1-e^{-T_w s}}{T_w s}\right)\left(\frac{1+T_w s/2}{1+\beta T_w s}\right)}\left(\frac{s+K_P}{s}\right) \tag{7.30}$$

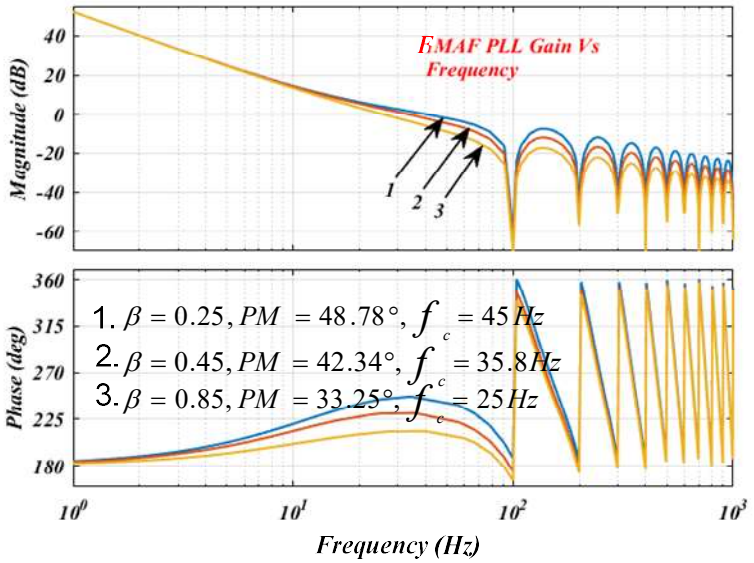

Fig. 7.5 Bode Plot of open loop FAMAF PLL at different values of attenuation factor 'β' and $T_W = 0.01s$

By using first-order Pade approximation, $e^{-T_w s}$ can be replaced by $\frac{1-T_w s/2}{1+T_w s/2}$.

$$\frac{\Delta\theta_{oc}}{\Delta\theta_i - \Delta\theta_{oc}} = \frac{\left(\frac{1}{1+T_w s/2}\right)\left(\frac{1+T_w s/2}{1+\beta T_w s}\right)}{1-\left(\frac{1}{1+T_w s/2}\right)\left(\frac{1+T_w s/2}{1+\beta T_w s}\right)} * \left(\frac{s+K_P}{s}\right) \tag{7.31}$$

After simplification in Eq. (7.31)

$$G_{OL_{FAMAF}}(s) = \left(\frac{1}{\beta T_w s(1+\beta T_w s)}\right)\left(\frac{s+K_P}{s}\right) \tag{7.32}$$

$$G_{OL_{FAMAF}}(s) = \left(\frac{1}{\beta T_w s^2}\right)\left(\frac{s+K_P}{1+\beta T_w s}\right) \tag{7.33}$$

Replace $T_w/2 = T_d$ in Eq. (7.33)

$$G_{OL_{FAMAF}}(s) = \frac{1}{2\beta\ _d s^2}\left(\frac{s+K_P}{1+2\beta T_d s}\right) \tag{7.34}$$

In the context of control having an additional control parameter "β" which is known as attenuation factor, Eq. (7.34) demonstrates that the suggested PLL is a type-2 PLL. As a result, the suggested PLL accomplishes the same function as a 'P' type LF without the use of a PI as a loop filter. Grid disturbance in the PLL control loop cannot be handled by type-2 PLL with PI controller as LF. A second filter, such as an MAF or Notch filter, is needed in the control loop to solve this issue. The proposed PLL operates as a Type-2 PLL but behaves as a quasi-Type-1 PLL (QT1 PLL) since the proposed FAMAF PLL's open loop transfer function has two poles at the origin, as indicated in Eq. (7.34). Instead of using traditional MAF, a frequency-adaptive MAF is employed to enhance the QT1 PLL's filtering capacity. The previous section has already covered the limitations of

conventional MAF. Applying the Symmetrical Optimum design method, the loop filter (LF) gain (K_p) of the proposed FAMAF can be chosen [125].

$$K_P = \frac{1}{(bT_d)} \tag{7.35}$$

For a phase margin of 48.78°, the value of 'b' is calculated by using Eq. (7.35),

$$PM = \tan^{-1}\left(\frac{b^2-1}{2b}\right) \tag{7.36}$$

7.3 Simulation Results

The performance of SRF-PLL, SOGI-PLL, and proposed FAMAF PLL are discussed in this section. The performance of various PLL is discussed under grid abnormalities. The mentioned PLL are simulated under following cases:

1. Voltage Swell
2. Voltage Sag
3. Source voltage harmonics
4. Frequency Change
5. DC offset

7.3.1 SRF PLL based grid synchronization

The performance of SRF-PLL is tested under steady-state and transient conditions is shown in Fig. 7.6. The source voltage is acquainted with voltage sag of 20% at t=0.4s. Prior t=0.4s, the source voltage is under normal grid condition. The estimated frequency error and calculated amplitude under voltage sag provides good results.

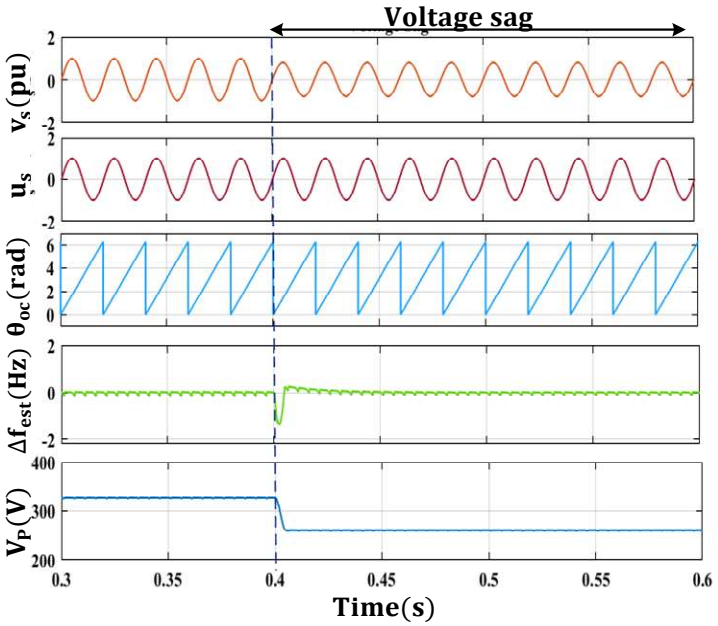

Fig. 7.6 Performance analysis of SRF PLL under voltage sag of 20% in source voltage

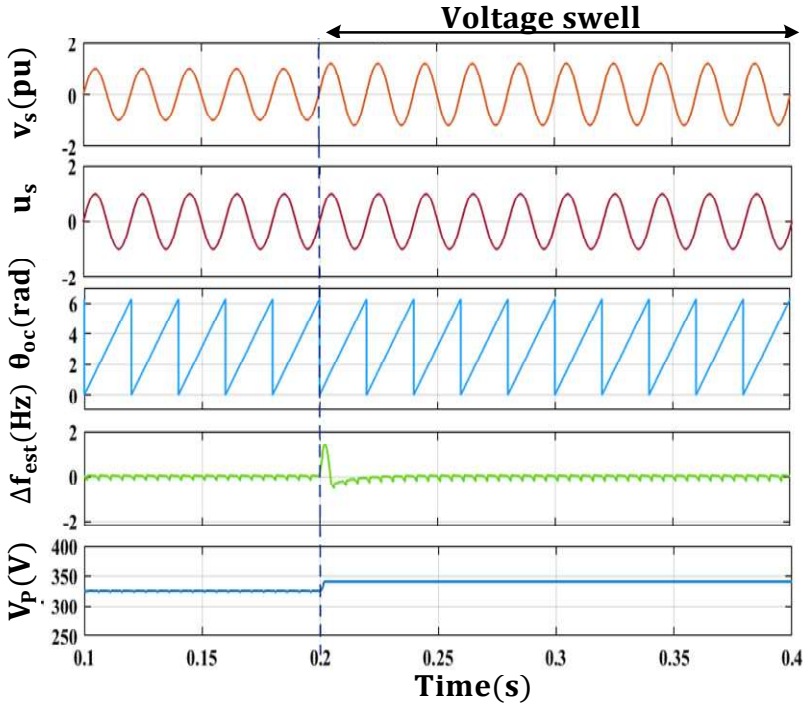

Fig. 7.7 Performance analysis of SRF PLL under voltage swell of 20% in source voltage

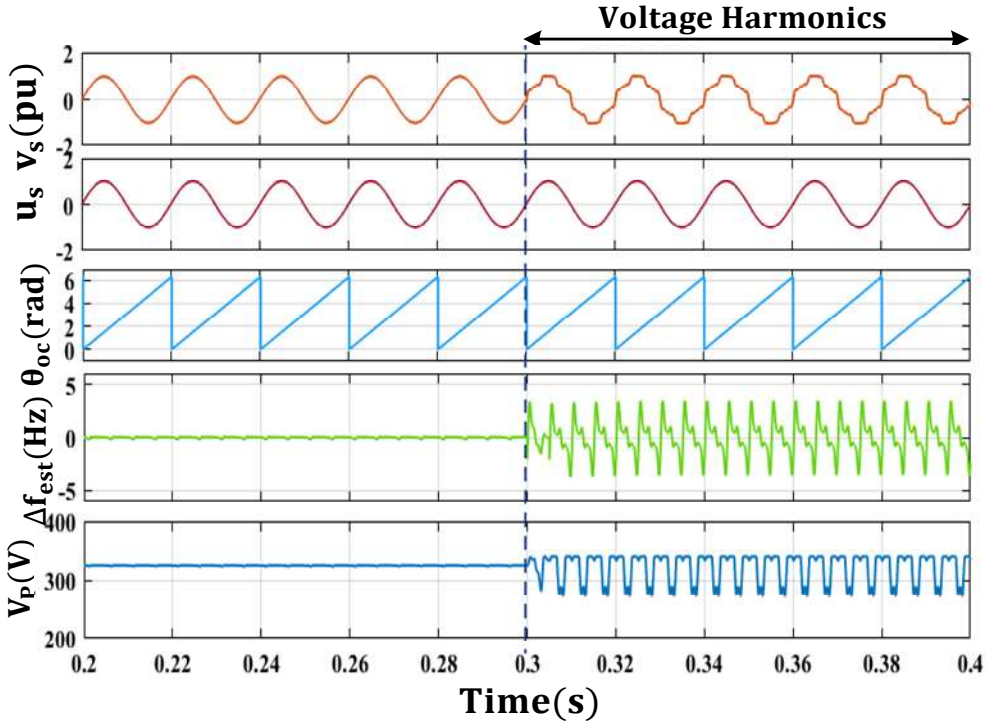

Fig. 7.8 Performance analysis of SRF PLL under source voltage harmonics

Another test case is a voltage swell of 20% in source voltage. The source voltage is acquainted by voltage swell at t=0.2s as shown in Fig. 7.7. Prior t=0.2s, the source voltage is under normal grid condition. The estimated frequency error and calculated amplitude

provide good results with very small ripples. The amplitude is increased when voltage swell occurs at the source voltage.

The performance of SRF-PLL is investigated under a polluted grid as shown in Fig.7.8. At t=0.3s, the source voltage is included with 5^{th}, 7^{th}, $11^{th,}$ and 13^{th} order harmonics. During harmonics, the ripples of 4.1Hz are seen while the calculated amplitude has ripples of 75V. The performance of SRF-PLL under voltage sag and swell is good but under polluted grid performance of SRF-PLL detoriates.

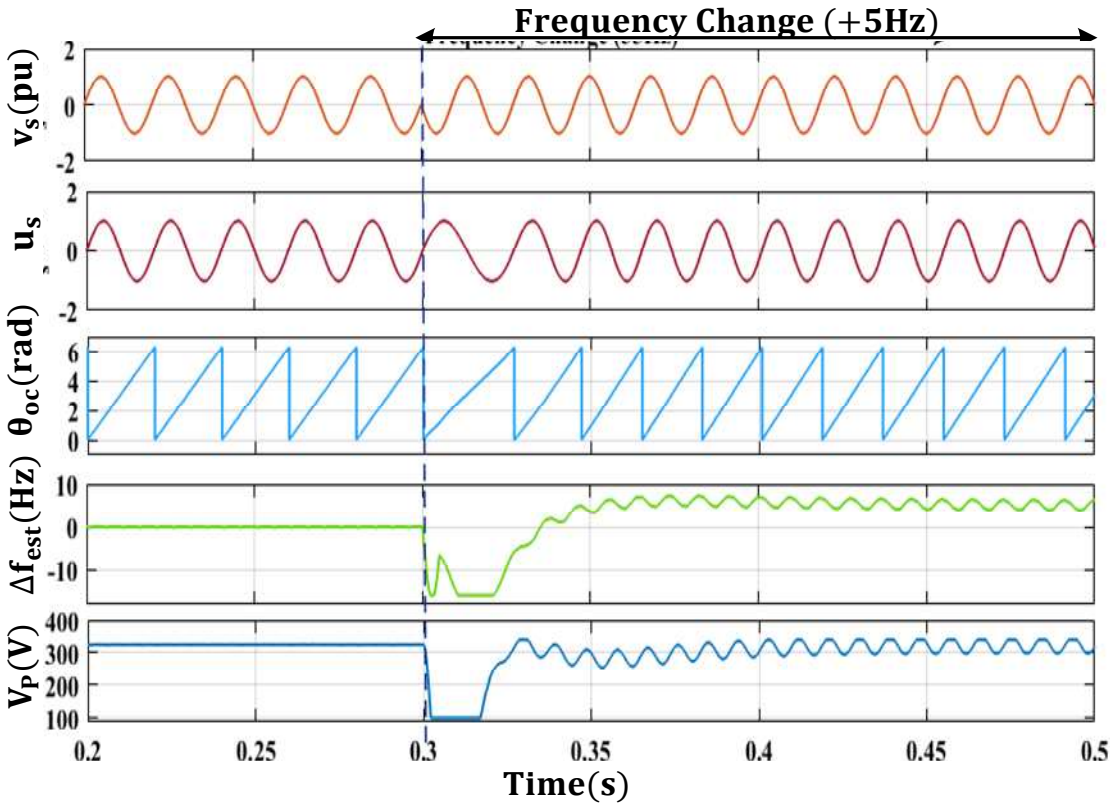

Fig. 7. 9 Performance analysis of SRF PLL under frequency change of +5Hz.

The SRF-PLL is tested under frequency change of source voltage as shown in Fig.7.9. The standard frequency of source voltage is 50Hz. While at t=0.3s source voltage will experience a frequency change of +5Hz. The estimate frequency error has a small oscillation with a ripple of 0.7Hz. The dynamic response of SRF-PLL under frequency change is slow as it takes around 3 cycles to reach its actual value.

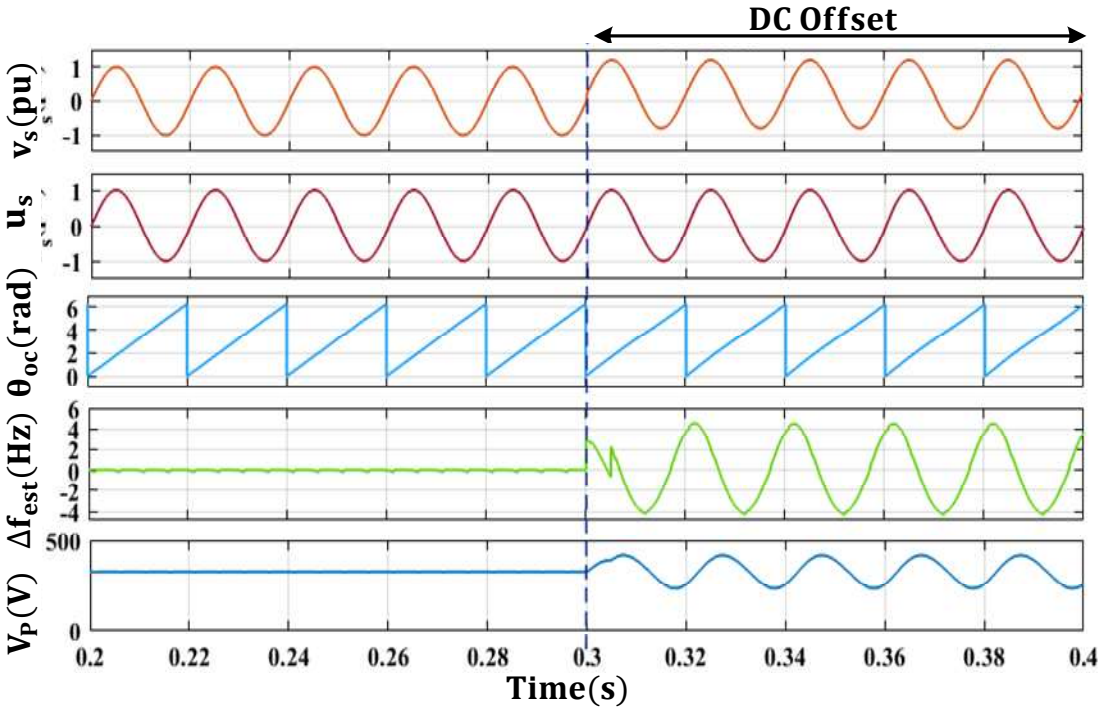

Fig. 7.10 Performance analysis of SRF PLL under source voltage DC offset

The Performance of SRF-PLL is now investigated under DC offset. A DC offset of 20% of the source voltage is initiated in the input source voltage. The estimated frequency error and calculated amplitude show large oscillations with slow dynamic response as shown in Fig. 7.10.

7.3.2 SOGI PLL-based grid synchronization

The Second-order generalized integrator (SOGI) PLL is used to track the frequency under normal and weak grid conditions. A better filtering is obtained when used at the input of source voltage (v_s). The weak grid conditions are considered here such as voltage sag, voltage swell, harmonics, frequency change, and DC offset. A 20% voltage sag is created at t=0.4s as shown in Fig. 7.11. The unit template (u_s) is sinusoidal and balanced under voltage sag conditions. The estimated error frequency (Δf_{est}) is deviates from zero approximately for 3 cycles. The estimated phase angle (θ_{oc}) is estimated correctly. While the source voltage (V_P) amplitude of the source is decreased due to voltage sag at the source voltage. Thus, SOGI PLL is performing satisfactorily under the condition of voltage sag.

The second undesirable condition might occur at the source voltage (v_s) side is 20% voltage swell at t=0.2s as shown in Fig. 7.12. The unit template (u_s) is sinusoidal

and balanced under voltage swell conditions. The estimated phase angle at voltage swell condition is tracked correctly through SOGI PLL. The estimated frequency error (Δf_{est}) is deviated for 2.5 cycles and after that it will oscillate to zero. The source voltage amplitude (V_P) is increased with an increase in source voltage. Thus, SOGI PLL is performing satisfactorily under the condition of voltage swell.

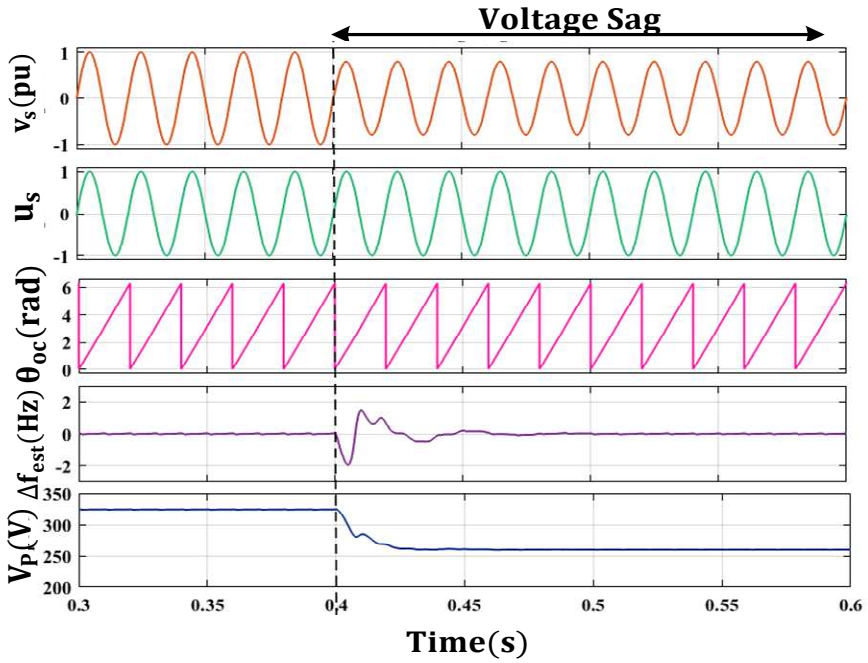

Fig. 7.11 Performance analysis of SOGI PLL under voltage sag

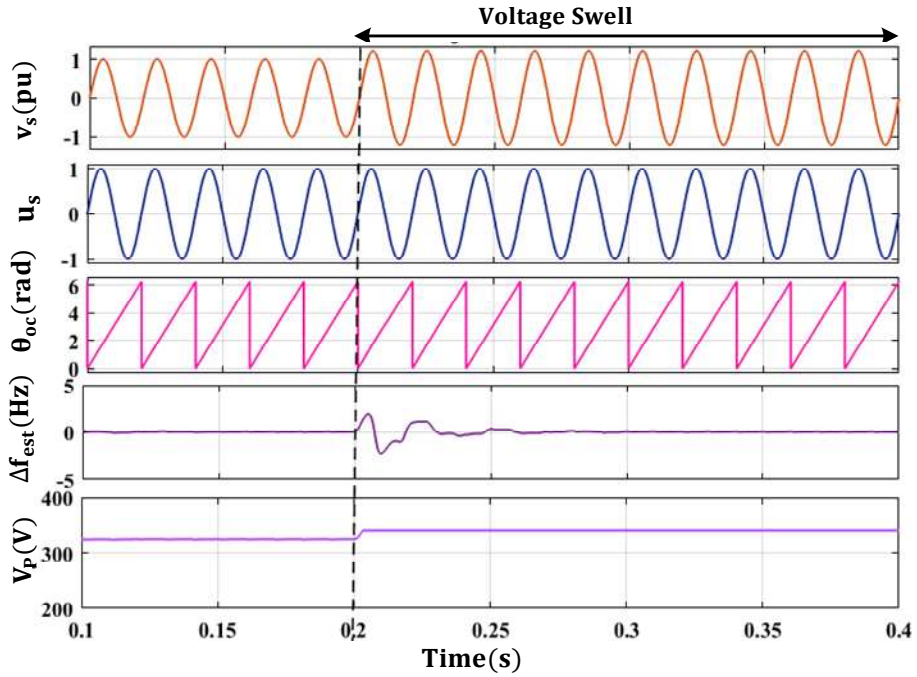

Fig. 7.12 Performance analysis of SOGI PLL under voltage swell

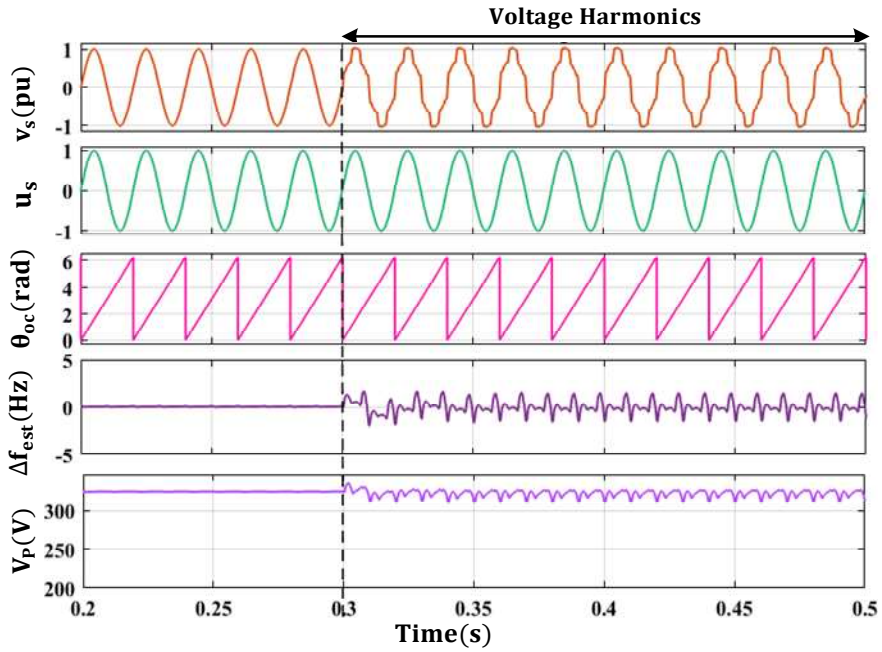

Fig. 7.13 Performance analysis of SOGI PLL under source voltage harmonics

The voltage harmonics can distort the shape of the voltage waveform, leading to increased Total Harmonic Distortion (THD) in the source voltage. This distortion can affect the performance of sensitive equipment. Harmonics at source voltage is created at t=0.3s as shown in Fig. 7.13. It is found that the obtained unit template is balanced and sinusoidal during source voltage harmonics. The estimated frequency error has sustained oscillations. Also, the source voltage peak amplitude has ripples.

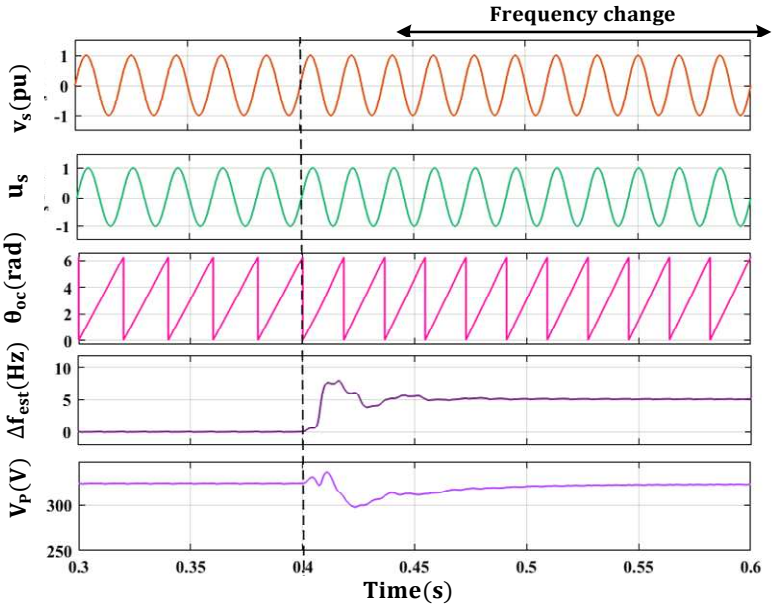

Fig. 7.14 Performance analysis of SOGI PLL under frequency change.

The performance of SOGI PLL under frequency change is shown in Fig. 7.14. The estimated frequency error is settled to 5Hz after 3 cycles. Also, the source voltage peak amplitude deviates from its nominal value. Thus, SOGI PLL does not work perfectly under frequency change.

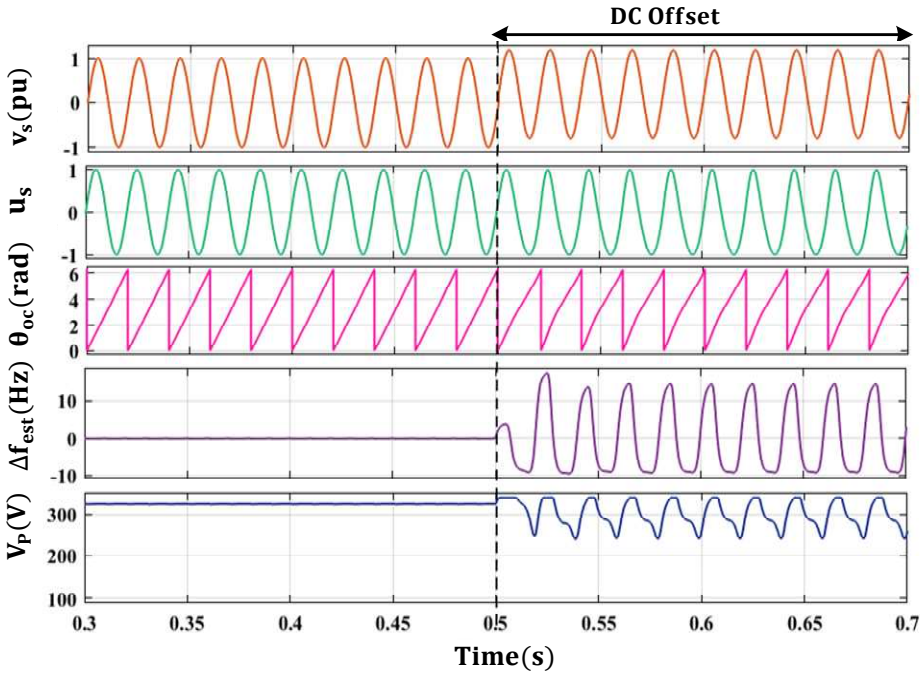

Fig. 7.15 Performance analysis of SOGI PLL under DC offset condition.

DC offset can result in an imbalance in the voltage waveform, leading to instability in the power system. This can affect the quality of the voltage supplied to connected loads. A DC offset is created in the single-phase system at t=0.5s. It is seen from Fig.7.15, that the obtained unit template as well as the phase angle is little deviated from its nominal value. The estimated frequency error under the DC offset condition has a large oscillation which justifies the inability of SOGI PLL to perform satisfactorily under the DC offset condition.

7.3.3 FMAF PLL-based grid synchronization

Fig.7.16 shows the synchronizing signals ($u_s, \theta_{oc}, \Delta f_{est}$) under the inclusion of voltage sag of 20% in grid voltage. At t = 0.4s, the grid voltage is reduced due to voltage sag and thus a small change in Δf_{est} is shown in Fig.10. The unit template (u_s) and source voltage (v_s) are in the same phase. The estimated frequency settles down to steady-state

within 30ms. The FAMAF-PLL shows the overshoot of 0.2 Hz in estimated frequency. Thus, ensuring precise tracking of frequency.

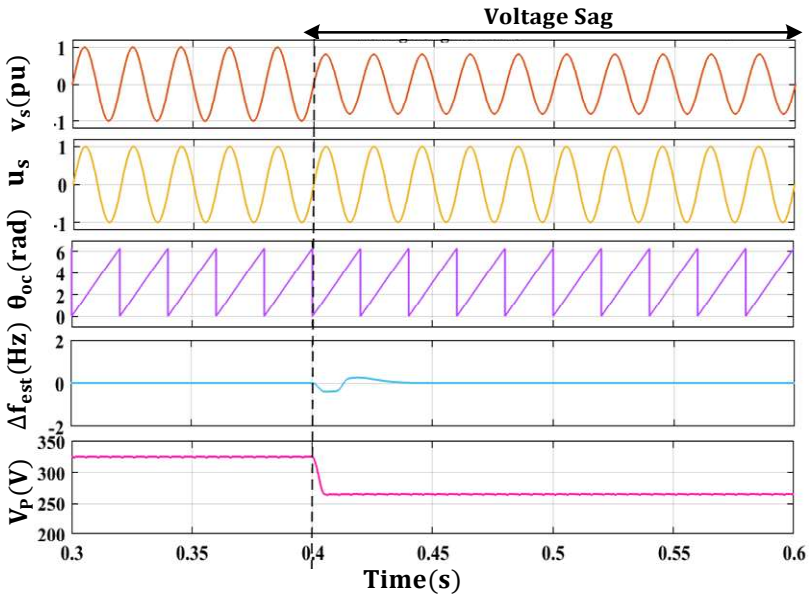

Fig. 7. 16 Simulation results of proposed FAMAF PLL under voltage sag of 20%.

In this test case, voltage swell is created in source voltage at t = 0.2s shown in Fig.7.17. The estimated frequency reaches steady-state within 2 cycles. The settling time for the estimated frequency to reach its steady state is 20ms. The synchronizing signal unit template (u_s)and estimated phase angle (θ_{oc}) are also shown in Fig.7.17. The sine signal comes in the same phase with the source voltage v_s. The signal Δf_{est} has a very small overshoot and subsequently it settles down to 5 Hz.

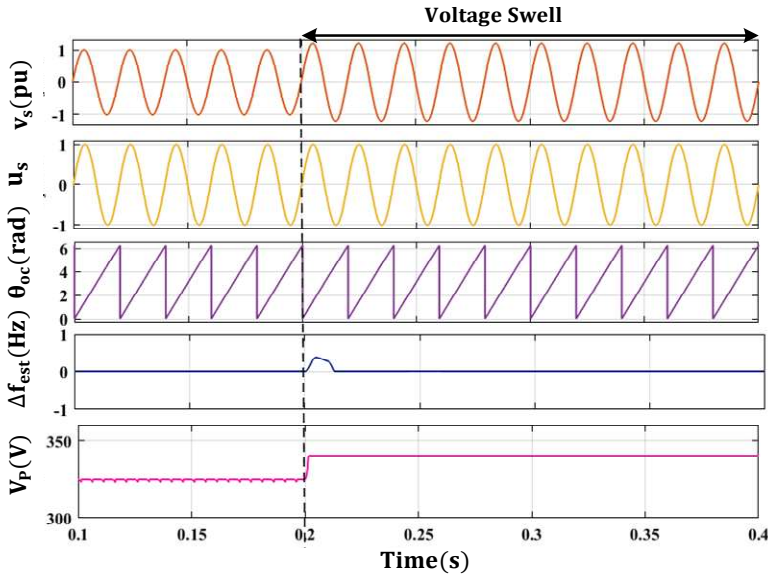

Fig. 7.17 Simulation results of proposed FAMAF PLL under voltage swell of 20%

Harmonics at source voltage is created at t=0.3s as shown in Fig. 7.18. It is found that the obtained unit template is balanced and sinusoidal during source voltage harmonics. The estimated frequency error has sustained oscillations. Also, the source voltage peak amplitude has ripples.

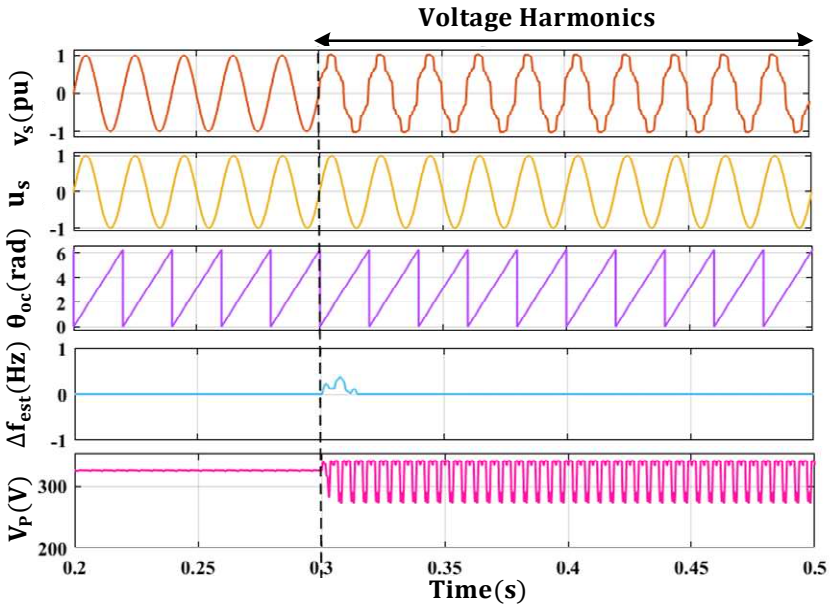

Fig. 7.18 Simulation Results of proposed FAMAF PLL under voltage harmonics

The FAMAF PLL performance under a frequency change of +5Hz from the nominal Frequency of 50Hz is shown in Fig. 7.19. The obtained synchronizing signal unit template in the same phase with the input source voltage. The estimated frequency error takes 4 cycles to settle to its nominal value.

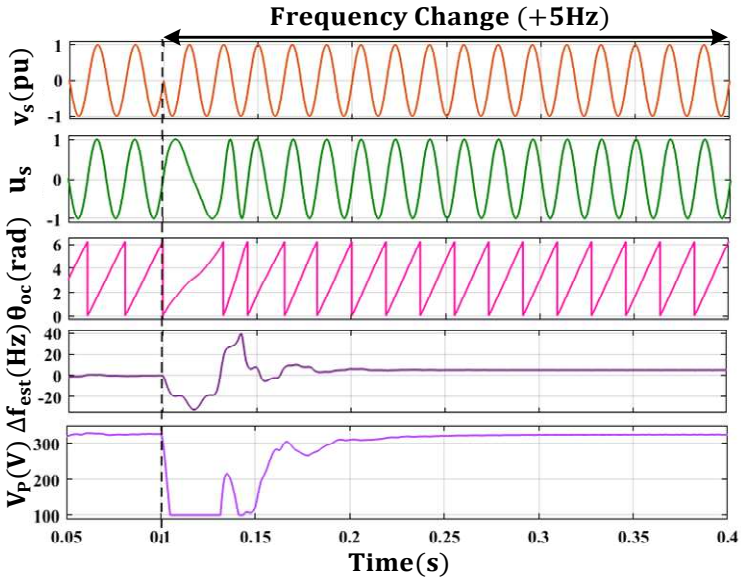

Fig. 7. 19 Simulation results of proposed FAMAF PLL under frequency change

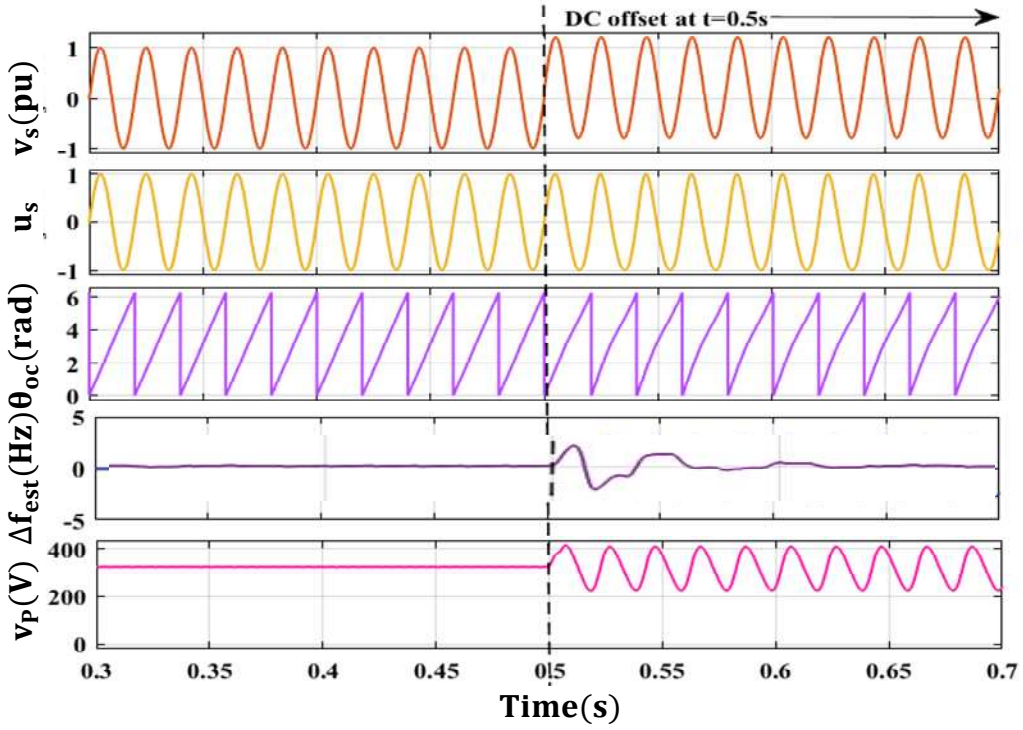

Fig. 7.20 Simulation results of proposed FAMAF PLL under DC offset at t=0.5s.

In Fig. 7.20, a 20% DC offset is added to the source voltage using a programmable AC source. It is noticed that the oscillation in estimated frequency is very small. The synchronization signals is unit template and correctly determined. The unit template is derived without any dc offset. Moreover, the frequency is correctly tracked and Δf_{est} is zero within 2.5 cycles.

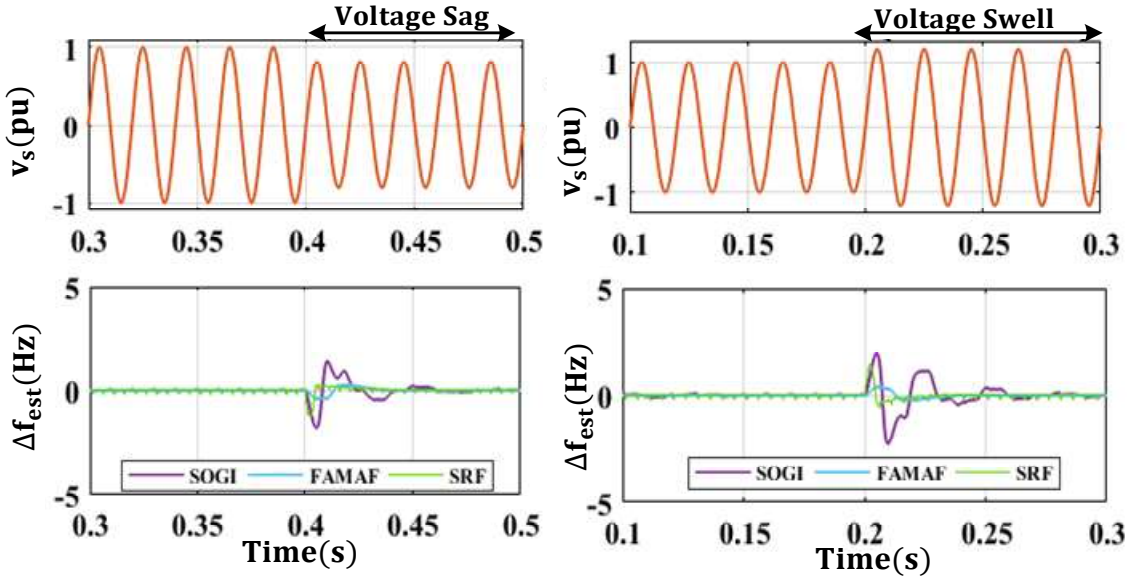

(a) (b)

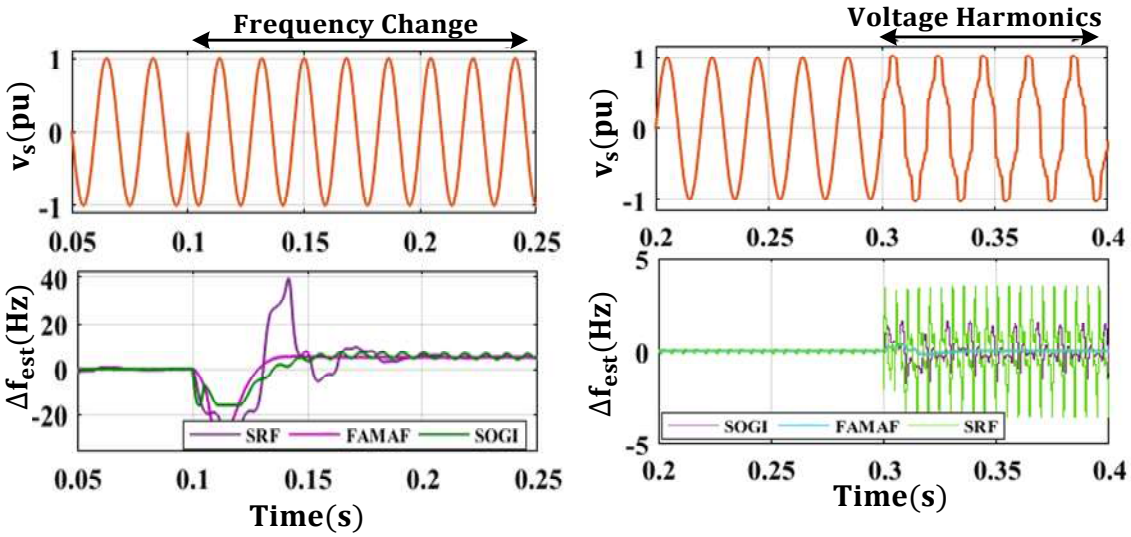

Fig. 7.21 Performance comparison among SRF, SOGI, and FAMAF PLL under (a) voltage sag (b) voltage swell (c) Frequency change (d) source voltage harmonics

The performance comparison based on simulation results under weak grid conditions is shown in Fig. 7.21. Fig. 7.22(a) shows the estimated frequency error waveform under voltage sag conditions with SRF, SOGI, and FAMAF PLL. FAMAF PLL gives a small deviation while estimating the frequency error as compared to SRF and SOGI PLL. It is also verified that FAMAF PLL shows lesser oscillation as compared to SRF and SOGI PLL as observed in Fig.7.21 (b).

Thus, FAMAF PLL performance under system frequency change and source voltage harmonics is better than SRF and SOGI PLL. SRF PLL shows larger oscillations in case of frequency shift as shown in Fig. 7.21(c). The sustained oscillations are seen in estimated frequency error with SRF PLL while very less oscillations are seen with FAMAF PLL under source voltage harmonics as shown in Fig.7.21(d).

7.4 Experimental Results

The proposed PLL has been tested experimentally. A programmable AC/DC single-phase AC supply GWInstek model (APS-1102A) has been utilized for creating disturbances in the source voltage supply. A LEMLV 25P voltage sensor has been utilized to measure grid voltage. The signals are processed by dSpace 1104. The experimental results of the proposed algorithm are studied and recorded by DSO Agilent DSO-X-2014A

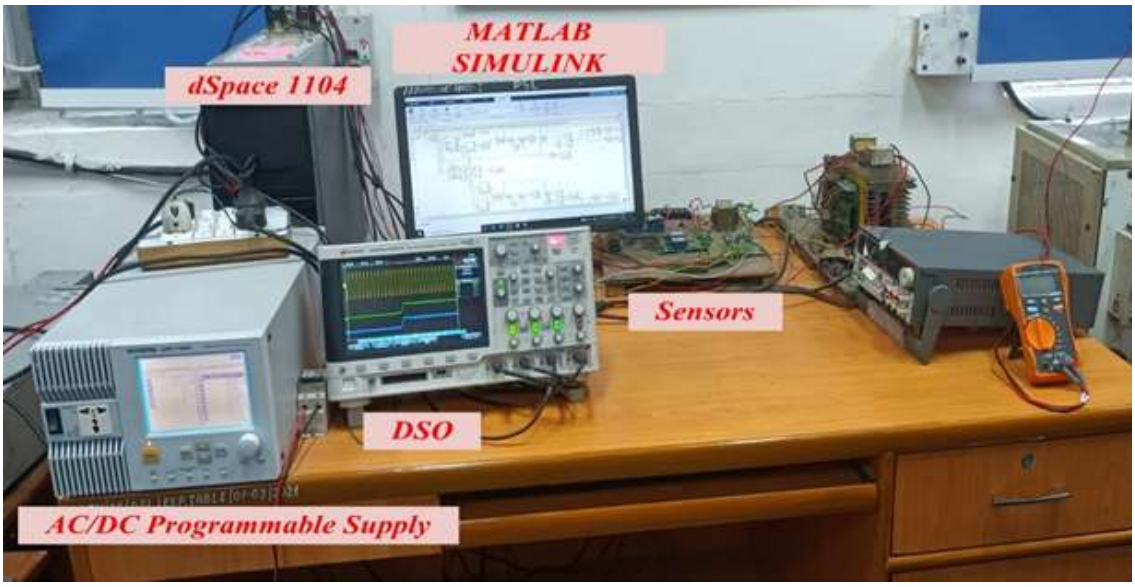

Fig. 7. 22 Photograph of the setup for testing of grid synchronization schemes

7.4.1 SRF PLL-based grid synchronization

The experimental investigation of SRF PLL under different weak grid conditions such as voltage sag, and voltage swell. Frequency change, DC offset, and voltage harmonics are shown in Fig. 7.23. In Fig. 7.23, synchronizing signal, phase angle of single-phase voltage, and frequency error have been shown for voltage sag and voltage swell condition. Under both conditions, the voltage parameters have been tracked instantly. The frequency error estimation under source voltage harmonics and frequency change conditions are depicted in Figures 7.23(c) and 7.23(d) respectively.

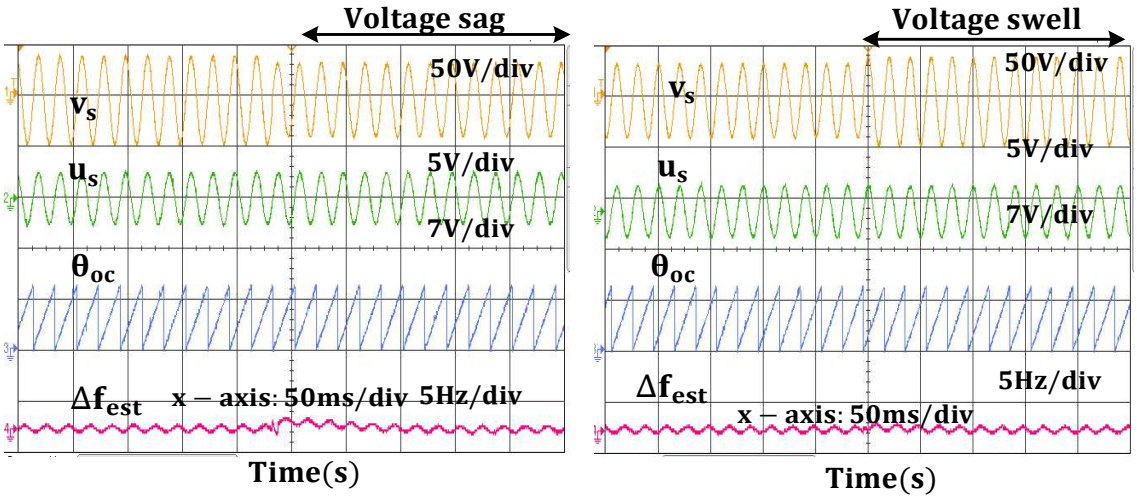

(a) (b)

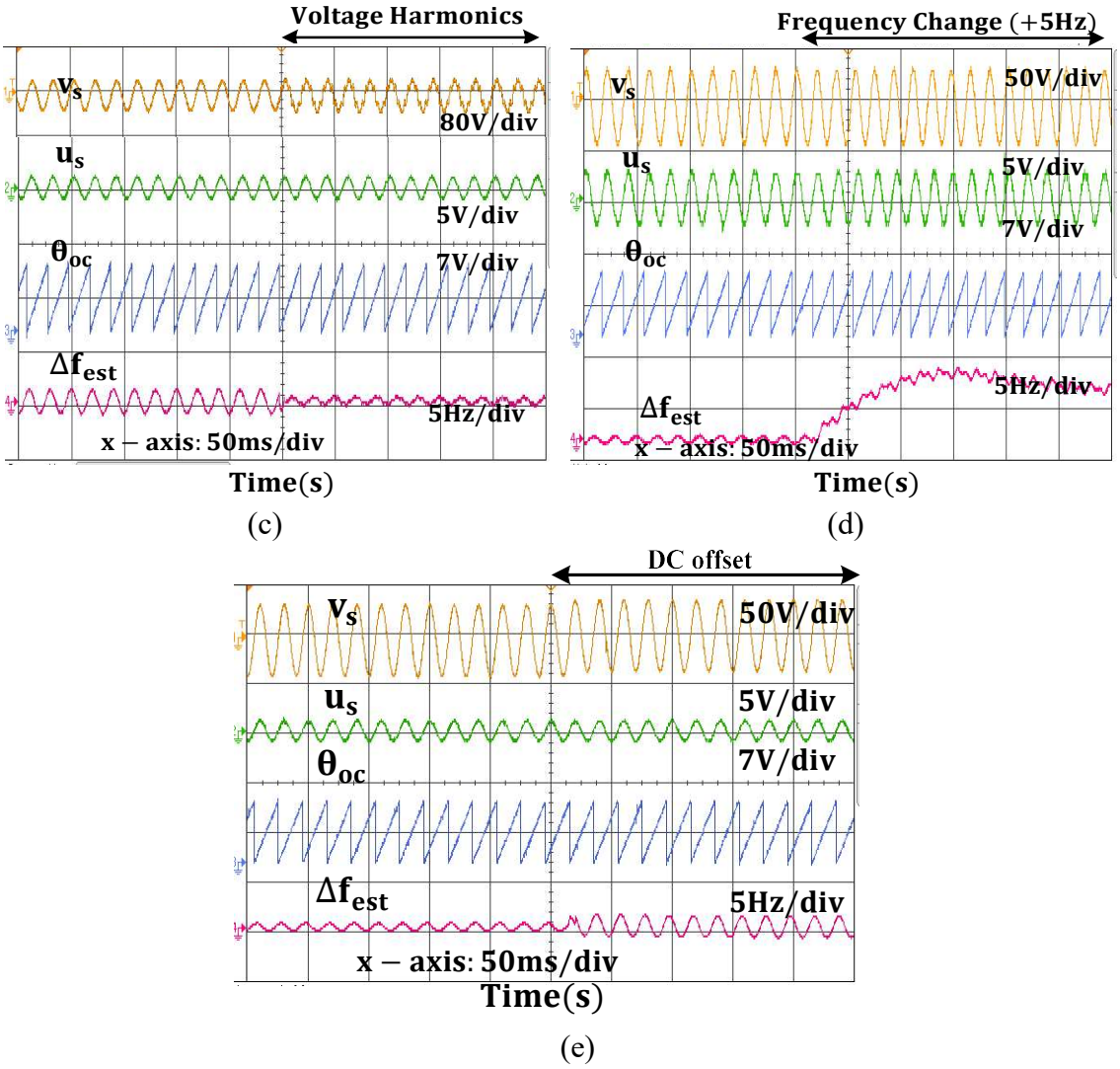

Fig. 7.23 Performance analysis of SRF PLL under (a) voltage sag (b) voltage swell (c) source voltage harmonics (d) frequency Change (e) DC offset in source voltage

The estimated frequency exhibits somewhat stronger oscillations under voltage harmonic conditions than it does under typical grid conditions. When there are grid voltage harmonics, the single-phase SRF-PLL performs better. The experimental performance of the SRF-PLL under frequency change is shown in Figure 7.23(d). For the frequency estimation, the dynamic response is nearly 2.5 cycles. The change in frequency error under the DC offset condition is shown in Fig. 7.23(e) which shows sustained oscillations.

7.4.2 SOGI PLL-based grid synchronization

The experimental study of SOGI PLL in various weak grid scenarios, including voltage swell and sag. Fig. 7.24 displays frequency variation, DC offset, and voltage harmonics. The synchronizing signal, the single-phase voltage's phase angle, and the

frequency error are displayed for both voltage swell and voltage sag conditions in Fig. 7.24. The voltage parameters were immediately tracked in both scenarios

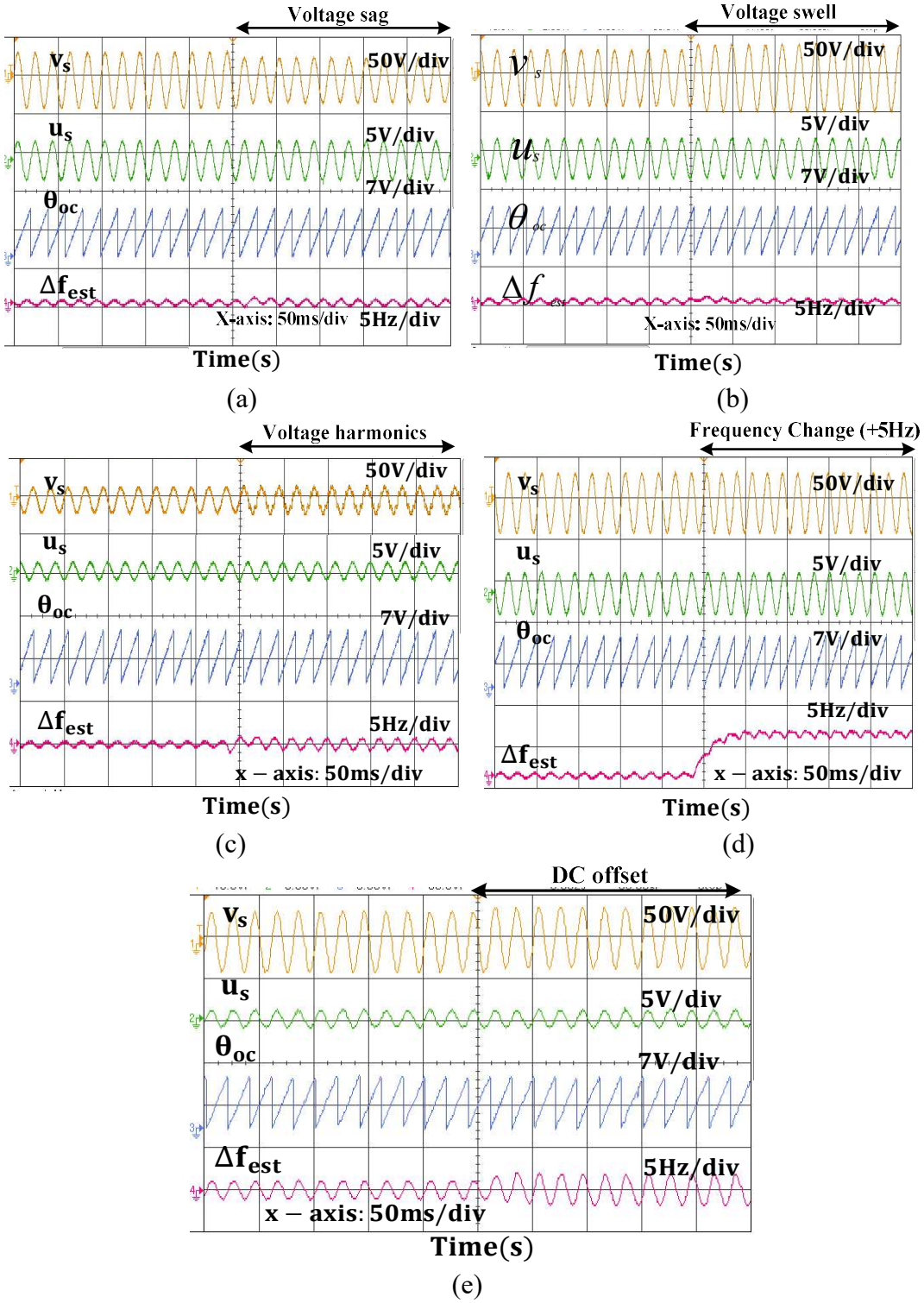

Fig. 7.24 Performance analysis of SOGI PLL under (a) voltage sag (b) voltage swell (c) source voltage harmonics (d) Frequency Change (e) source voltage DC offset

Figures 7.24(c) and 7.24(d) show the frequency error estimation under conditions of frequency change and source voltage harmonics, respectively. Under voltage harmonic conditions, the predicted frequency oscillates somewhat more than it does under usual grid conditions. The single-phase SOGI-PLL operates more efficiently when there are harmonics in the grid voltage. The SOGI-PLL's experimental performance at varying frequencies is displayed in Fig. 7.24(d). For the frequency estimation, the dynamic response is nearly 2 cycles. The change in frequency error under the DC offset condition is shown in Fig. 7.24(e) which shows sustained larger oscillations

7.4.3 FAMAF PLL-based grid synchronization

The synchronizing signal, the single-phase voltage's phase angle, and the frequency error are displayed for both voltage swell and voltage sag conditions in Figure 7.25(a-b). The voltage parameters were immediately tracked in both scenarios. Figures 7.25(c) and 7.25(d) show the frequency error estimation under conditions of frequency change and source voltage harmonics, respectively. Under voltage harmonic conditions, the predicted frequency oscillates somewhat more than it does under usual grid conditions. The single-phase FAMAF-PLL operates more efficiently when there are harmonics in the grid voltage. The FAMAF-PLL's experimental performance at varying frequencies is displayed in Fig. 7.25(d). For the frequency estimation, the dynamic response is nearly 1.5 cycles. The change in frequency error under the DC offset condition is shown in Fig. 7.25(e) which shows oscillations for 3 cycles only.

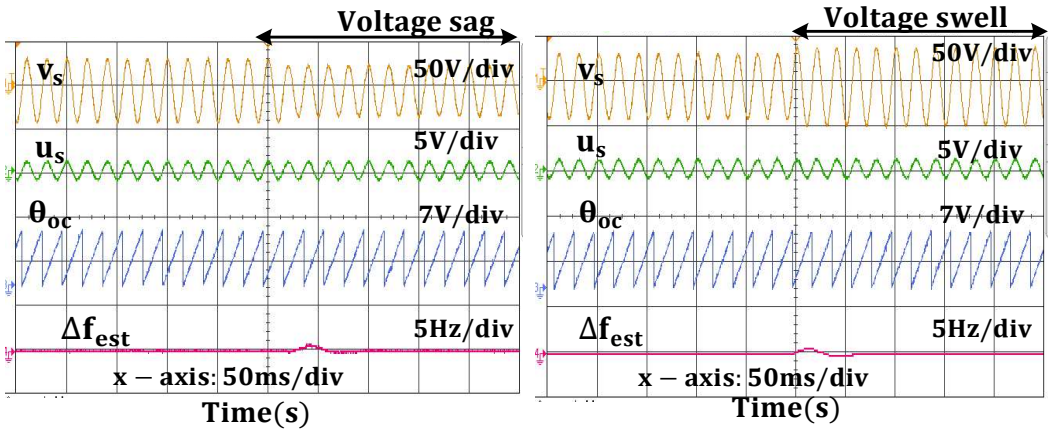

(a) (b)

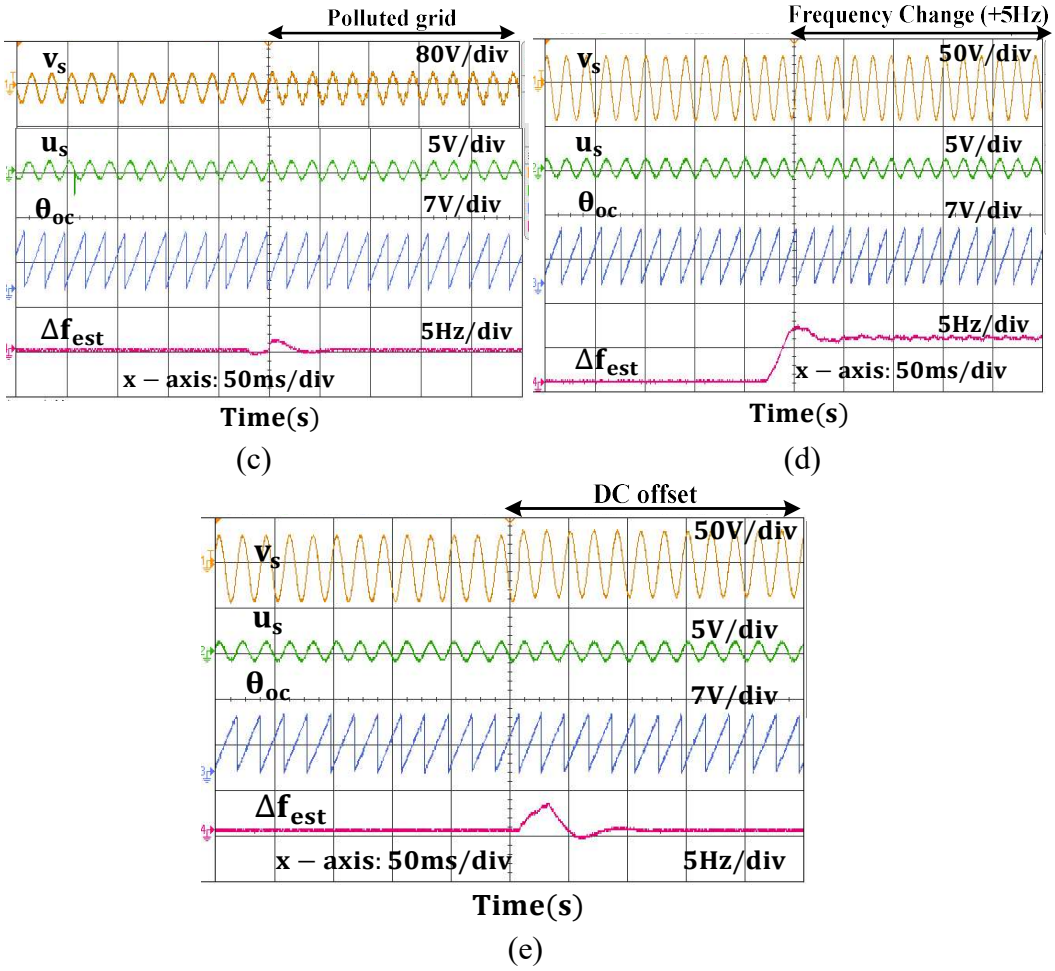

Fig. 7.25 Performance analysis of FAMAF PLL under (a) voltage sag (b) voltage swell (c) source voltage harmonics (d) frequency Change (e) DC offset in source voltage

7.5 Performance Comparison

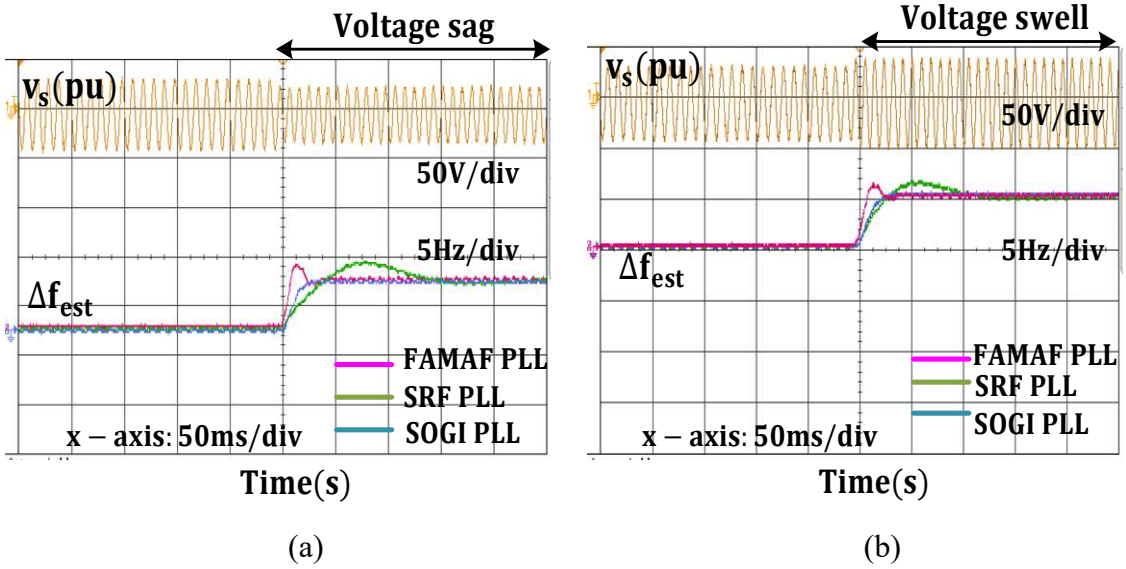

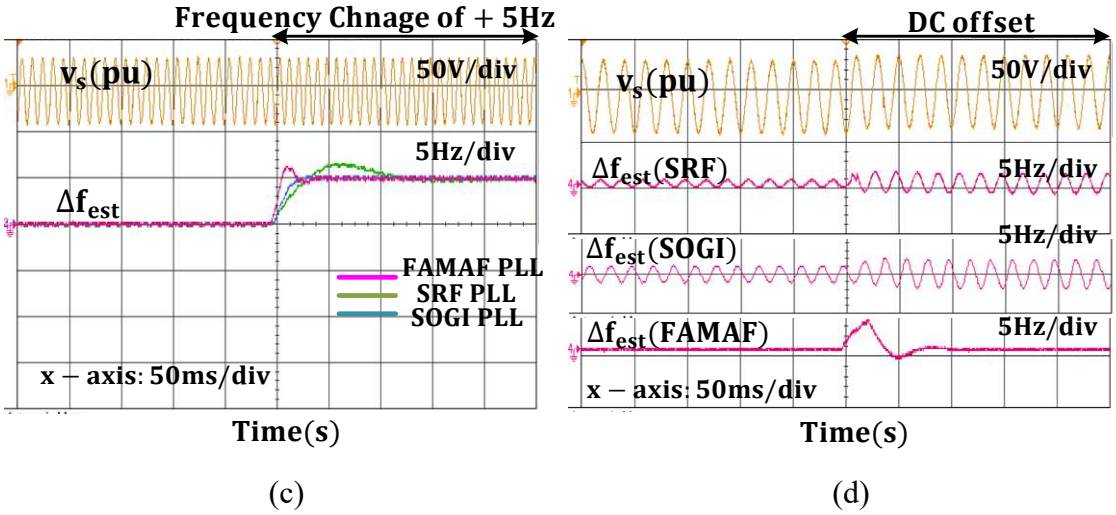

(c) (d)

Fig. 7. 26 Performance analysis among SRF PLL, SOGI PLL, and FAMAF PLL under (a) voltage sag (b) voltage swell (c) source voltage harmonics (d) frequency Change

Fig.7.26 (a) shows the frequency error tracking with SRF, SOGI, and proposed FAMAF PLL under 20% voltage sag in source voltage. It is noticed that the signal Δf_{est} shows oscillation with SRF with high convergence time and SOGI provides no oscillation as compared to SRF PLL. While FAMAF-based PLL has lesser oscillation with the fastest convergence (2 Cycles), SOGI PLL achieves convergence in 2.5 cycles. Both SOGI and the proposed FAMAF PLL show similar performance under voltage sag conditions. Fig. 7.26 (b) shows the case of voltage swell of 20% in grid voltage, SOGI-PLL shows better performance than SRF-PLL. SRF PLL shows oscillation in voltage swell conditions under both steady-state and dynamic conditions. In Fig. 7.26 (c) the condition of voltage harmonics is considered. The estimated frequency with FAMAF PLL has no oscillation with the fastest settling time response. The last case considered is a DC offset of 10% in source voltage. It is clearly shown in Fig.7.26(d) that SRF and SOGI are not able to reject the effect of DC offset in the estimated frequency error. FAMAF performs better in rejecting the effect of DC offset on the synchronization signal with the proposed PLL due to its filtering capability. Under DC offset conditions, FAMAF can estimate synchronizing signals and frequency accurately. The signal Δf_{est} calculated using SRF has undamped oscillations. Similarly, the SOGI PLL has the same performance as SRF-PLL but has slightly lesser oscillation. It is noticed that the signal $\Delta f_{est}$with FAMAF PLL for 2.5 cycles only and after that it gets stable. The results under all the test cases have been tabulated in Table 7.1

Table 7.1: Comparison among SRF-PLL, CCF-PLL, MAF PLL and FAMAF-

Type of PLL	**SRF-PLL**	**CCF-PLL**	**FAMAF-PLL**
Type	Non-adaptive	Adaptive	Adaptive
PI required	Yes	Yes	No only Proportional Filter is required
Oscillations 1. Voltage Sag 2. Voltage Swell 3. Voltage Harmonics 4. Frequency Change 5. DC offset	 2.6 Hz 0.4 Hz 2.2 Hz 3 Hz 2Hz (oscillatory)	 0.1 Hz 0.2 Hz 0.3 Hz 2.1 Hz 2 Hz (oscillatory)	 0.015 Hz 0.01 Hz 0.01 Hz 1.8 Hz 2.5 Hz (stable in 2.5 cycles)
Settling time (ms)	Does not settle under 2% error band	45 ms	40ms
Sampling time	$50\mu s$	$50\mu s$	$50\mu s$

7.6 Conclusions

The proposed control algorithm is developed for grid synchronization in single-phase distribution system. A prefiltering stage based PLL is proposed. The CCF and FAMAF filters are utilized to generate the orthogonal signals of input voltage. It is investigated from the discussion that typical SRF and CCF-PLL have higher oscillations under DC offset in the grid voltage. The proposed control algorithm consists of Frequency adaptive MAF (FAMAF), which acts as a filtering component to extract the fundamental frequency component of grid voltage, and SRF technique for frequency estimation. For the proposed PLL, the design consideration has been studied and its parameters are defined accordingly. The stability analysis has also been done for both CCF PLL and proposed FAMAF PLL. The performance of the proposed PLL is tested under various case scenarios, and the performance is analysed with both simulation and experimental results. The three PLLs (SRF-PLL, CCF-PLL, and FAMAF-PLL) are compared under various

grid disturbances such as frequency change, phase shift, voltage sag/swell, harmonics, and DC offset. It is observed that the proposed PLL has taken less settling time under all the disturbances. The estimated frequency with the proposed PLL has no oscillations in steady state and a small oscillation under grid disturbances. All the PLLs are compared for DC offset rejection capability and it is concluded that the proposed PLL performs satisfactorily as compared to the other two PLLs. Thus, the performance analysis indicates that the proposed FAMAF PLL can be an effective solution for single-phase grid synchronization under weak grid conditions. The design implementation of the proposed PLL is equivalent to CCF PLL, as both have additional parameters 'P' and 'β'. The application of PLL has also been executed in Active filtering for grid integrated PV system.

CHAPTER 8

CONCLUSION AND FUTURE SCOPE

8.1 Conclusion

Chapter 1 discusses the introduction to Power quality standards, power quality issues, classification of PQ problems, causes and effects, and mitigation techniques.

Chapter 2 discusses the literature survey on PQ issues, effects, and mitigations. Different control schemes for DSTATCOM, DVR, and UPQC are discussed. The research gaps and research objectives are discussed.

Chapter 3 discusses the design of a single-phase grid-connected inverter with PV integration. Designing parameters are calculated for the PV array, VSC, and distribution grid. After designing the grid-connected PV system, its control schemes are discussed to generate the switching signals for VSC and improve the PQ issues. A reference source current signal is generated which is compared with the actual source current in HCC. The effect of PV integration is discussed in this chapter. Both active and reactive power compensation of the grid is fulfilled effectively as per load requirement and PV power generation. The SRFT-based control scheme performs well under normal grid conditions but is not able to perform under polluted grid conditions. Two new control schemes have been developed based on orthogonal polynomials i.e., Hermite Polynomial and Bernuolli's Polynomial-based ANN. An LMS conventional algorithm is used in both HeANN and BePANN to make an adaptive nature. Both perform well under normal and polluted grids.

Chapter 4 discusses the design and control of a three-phase grid-connected VSC with PV integration. The performance of the system is tested under varying solar irradiance and load unbalancing. The SRFT, adaptive $\varepsilon-$NSRLMMN, and q-LMF control techniques are used for a three-phase grid-connected inverter which acts as a shunt active power filter. It is concluded from both experimental and simulation results the proposed q-LMF performs well among SRFT and $\varepsilon-$NSRLMMN under varying solar irradiance

and load unbalancing. The q-LMF shows lesser source current THD than obtained from the other two.

Chapter 5 discusses the design and control of a series active power filter. The DVR acts as a series active power filter which is used to mitigate voltage-related power quality issues such as voltage sag, swell, harmonics, DC offset, and voltage unbalancing. Design parameters of DVR are discussed in this chapter with proposer mathematical equations. Two control schemes conventional SRFT and proposed MSTOGI-SRF are utilized for a series of active power filters. A PWM voltage controller is used to generate the switching signals for DVR. The performance of MSTOGI-SRF is observed to be better under grid disturbance (DC offset, harmonics, sag, swell, and unbalancing). The MSTOGI acts as a filter and is used for grid synchronization. The load voltage is maintained constant under all undesirable conditions which is necessary for all the connected sensitive loads.

Chapter 6 discusses the design and control of a three-phase unified power quality compensator (UPQC). The UPQC is utilized to mitigate both current and voltage-related PQ issues. System configuration is shown and discussed in this chapter. The control scheme for both shunt and series compensation is discussed. The SRFT-based control scheme performs well under voltage sag, swell, and load unbalancing. But SRFT controller is not able to perform well under voltage harmonics and DC offset conditions. A Mittag Leffler polynomial (MiLeP) based ANN control scheme is used for both shunt and series compensation. The MiLeP is used for extracting fundamental load components to generate reference source current. The main objective of MiLeP in shunt compensation is to extract fundamental load component while it acts as a pre-filter in series compensation of UPQC. The pre-filter is utilized to filter out the unwanted components of source voltage under grid disturbances.

Chapter 7 discusses different single-phase grid synchronization techniques. The SRF, SOGI, and proposed FAMAF PLL techniques are developed and their performance is tested under grid disturbances such as sag, swell, frequency change, harmonics, and DC offset. The PLLs are discussed with their simulation and experimental results. It is investigated from both simulation and experimental results that proposed FAMF PLL shows almost no oscillation under all grid disturbances with lesser settling time than other PLL schemes.

8.2 Future Scope

- Custom power devices (CPDs) are demonstrated in this research work. New adaptive and polynomial-based control schemes are discussed for single and three-phase grid-connected PV systems.
- Some of the discussed control schemes are used under adverse grid conditions and while some have been tested under normal grid conditions.
- It is required to investigate new control schemes which will operate in adverse grid conditions.
- The orthogonal polynomials can be utilized for grid synchronization techniques.
- Very limited research has been done on controlling UPQC and DVR in the literature.
- Mathematical stability analysis can also be done for the stable operation of the synchronization techniques under various grid voltage conditions. These days PV is widely used for electricity generation.
- Hence, the impact of the larger number of PV integrations on the distribution grid should be analyzed. It may further enhance the reliability of the system.

Ph.D. Thesis Research Summary

Ph.D. Thesis Research Summary: Design and Control of Custom Power Devices for Power Quality Mitigation

Objective:

This research investigates the design and control strategies of custom power devices (CPDs) for mitigating power quality problems in modern power systems. The focus is on developing innovative solutions to address critical power quality issues faced by sensitive loads and ensure reliable power delivery.

Motivation:

The increasing proliferation of power electronics-based equipment and distributed generation has heightened the need for robust power quality. Power quality disturbances like voltage sags, swells, harmonics, and imbalances can lead to equipment malfunction, reduced efficiency, and economic losses. CPDs offer a dynamic and targeted approach to counteract these issues, improving power quality for critical applications.

Methodology:

The research will explore the design and control of various CPDs, including:

- **Distribution Static Compensator (D-STATCOM):** A shunt-connected device that regulates voltage and reactive power flow.
- **Dynamic Voltage Restorer (DVR):** A series-connected device that injects voltage to compensate for sags and swells.
- **Unified Power Quality Conditioner (UPQC):** A combination of D-STATCOM and DVR, offering comprehensive power quality correction.

Advanced control techniques, such as:

- SRF, IRPT, HeANN, q-LMF, SOGI, Bernoulli's Polynomial based ANN, $\in -$NSRLMMN, MSTOGI, and FAMAF.

Expected Outcomes:

- Development of novel CPD designs with improved efficiency, cost-effectiveness, and scalability.
- Design and implementation of advanced control algorithms for enhanced power quality mitigation.

- Comprehensive analysis of the effectiveness of CPDs in addressing various power quality problems.
- Contribution to improved power system reliability and increased resilience for critical loads.

Significance:

This research holds significant value for the advancement of power quality management in modern power systems. By developing innovative CPDs and control strategies, the research aims to contribute to a more reliable and efficient power grid, benefiting utilities, industries, and consumers alike.

Future Work:

Further research directions may include:

- Integration of renewable energy sources with CPDs for enhanced power quality management in distributed generation systems.
- Development of hybrid CPDs combining functionalities of different devices for broader power quality control.
- Investigation of communication protocols for seamless integration of CPDs into smart grid infrastructure.

This summary provides a concise overview of your Ph.D. thesis research on custom power devices. Remember to tailor the details to your specific research focus and expected contributions.

REFERENCES

[1] Sharma A, Rajpurohit BS, Singh SN. A review on economics of power quality: Impact, assessment and mitigation. Renew Sustain Energy Rev 2018; 88:363–72. https://doi.org/10.1016/j.rser.2018.02.011.

[2] Srivastava M, Goyal SK, Saraswat A, Shekhawat RS, Gangil G. A Review on Power Quality Problems, Causes and Mitigation Techniques. 2022 1st Int. Conf. Sustain. Technol. Power Energy Syst., IEEE; 2022, p. 1–6. https://doi.org/10.1109/STPES54845.2022.10006587.

[3] Gholami K, Azizivahed A, Arefi A, Rahman MM, Islam MR. Power Quality Enhancement of Smart Reconfigurable Grids by Integrating Renewable Energy Sources. 2022 IEEE Glob. Conf. Comput. Power Commun. Technol., IEEE; 2022, p. 1–6. https://doi.org/10.1109/GlobConPT57482.2022.9938282.

[4] Badoni M, Singh A, Singh B. Power Quality Enhancement Using Euclidean Direction Search Based Control Technique. IEEE Trans Ind Electron 2020; 67:2231–40. https://doi.org/10.1109/TIE.2019.2905835.

[5] Barker PP, Burke JJ, Mancao RT, Short TA, Warren CA, Burns CW, et al. Power quality monitoring of a distribution system. IEEE Trans Power Deliv 1994; 9:1136–42. https://doi.org/10.1109/61.296300.

[6] Kavitha V, Subramanian K. Investigation of power quality issues and its solution for distributed power system. 2017 Int. Conf. Circuit, Power Comput. Technol., IEEE; 2017, p. 1–6. https://doi.org/10.1109/ICCPCT.2017.8074372.

[7] M. H. Bollen, "Understanding power quality problems," in Voltage sags and Interruptions, IEEE press, 2000.

[8] Ignatova V, Villard D, Hypolite J-M. Simple indicators for an effective Power Quality monitoring and analysis. 2015 IEEE 15th Int. Conf. Environ. Electr. Eng., IEEE; 2015, p. 1104–8. https://doi.org/10.1109/EEEIC.2015.7165321.

[9] Broshi A. Monitoring power quality beyond EN 50160 and IEC 61000-4-30. 2007 9th Int. Conf. Electr. Power Qual. Util., IEEE; 2007, p. 1–6. https://doi.org/10.1109/EPQU.2007.4424114.

[10] Sakthivel KN, Das SK, Kini KR. Importance of quality AC power distribution and understanding of EMC standards IEC 61000-3-2, IEC 61000-3-3 and IEC 61000-3-11. 8th Int. Conf. Electromagn. Interf. Compat., IEEE; 2003, p. 423–30. https://doi.org/10.1109/ICEMIC.2003.238094.

[11] Adak S. Harmonics Mitigation of Stand-Alone Photovoltaic System Using LC Passive Filter. J Electr Eng Technol 2021; 16:2389–96. https://doi.org/10.1007/s42835-021-00777-7.

[12] Tali M, Obbadi A, Elfajri A, Errami Y. Passive filter for harmonics mitigation in standalone PV system for non linear load. 2014 Int. Renew. Sustain. Energy Conf., IEEE; 2014, p. 499–504. https://doi.org/10.1109/IRSEC.2014.7059834.

[13] Melo ID, Pereira JLR, Variz AM, Ribeiro PF. Allocation and sizing of single-tuned passive filters in three-phase distribution systems for power quality improvement.

Electr Power Syst Res 2020; 180:106128. https://doi.org/10.1016/j.epsr.2019.106128.
[14] Sanjay JS, Misra B. Power Quality Improvement for Non Linear Load Applications using Passive Filters. 2019 3rd Int. Conf. Recent Dev. Control. Autom. Power Eng., IEEE; 2019, p. 585–9. https://doi.org/10.1109/RDCAPE47089.2019.8979035.
[15] Kumar R, Bansal HO. Shunt active power filter: Current status of control techniques and its integration to renewable energy sources. Sustain Cities Soc 2018; 42:574–92. https://doi.org/10.1016/j.scs.2018.07.002.
[16] Khadem SK, Basu M, Conlon MF. Harmonic power compensation capacity of shunt active power filter and its relationship with design parameters. IET Power Electron 2014; 7:418–30. https://doi.org/10.1049/iet-pel.2013.0098.
[17] Tang Y, Loh PC, Wang P, Choo FH, Gao F, Blaabjerg F. Generalized Design of High Performance Shunt Active Power Filter With Output LCL Filter. IEEE Trans Ind Electron 2012; 59:1443–52. https://doi.org/10.1109/TIE.2011.2167117.
[18] Pal R, Gupta S. Topologies and Control Strategies Implicated in Dynamic Voltage Restorer (DVR) for Power Quality Improvement. Iran J Sci Technol Trans Electr Eng 2020; 44:581–603. https://doi.org/10.1007/s40998-019-00287-3.
[19] Moghassemi A, Padmanaban S. Dynamic Voltage Restorer (DVR): A Comprehensive Review of Topologies, Power Converters, Control Methods, and Modified Configurations. Energies 2020; 13:4152. https://doi.org/10.3390/en13164152.
[20] Khadkikar V. Enhancing Electric Power Quality Using UPQC: A Comprehensive Overview. IEEE Trans Power Electron 2012; 27:2284–97. https://doi.org/10.1109/TPEL.2011.2172001.
[21] Gu Jianjun, Xu Dianguo, Liu Hankui, Gong Maozhong. Unified power quality conditioner (UPQC): the principle, control and application. Proc. Power Convers. Conf. 2002 (Cat. No.02TH8579), vol. 1, IEEE; n.d., p. 80–5. https://doi.org/10.1109/PCC.2002.998518.
[22] Tang Y, Loh PC, Wang P, Choo FH, Gao F, Blaabjerg F. Generalized Design of High Performance Shunt Active Power Filter With Output LCL Filter. IEEE Trans Ind Electron 2012; 59:1443–52. https://doi.org/10.1109/TIE.2011.2167117.
[23] Chauhan SK, Shah MC, Tiwari RR, Tekwani PN. Analysis, design and digital implementation of a shunt active power filter with different schemes of reference current generation. IET Power Electron 2014; 7:627–39. https://doi.org/10.1049/iet-pel.2013.0113.
[24] Khadkikar V, Singh M, Chandra A, Singh B. Implementation of single-phase synchronous d-q reference frame controller for shunt active filter under distorted voltage condition. 2010 Jt. Int. Conf. Power Electron. Drives Energy Syst. 2010 Power India, IEEE; 2010, p. 1–6. https://doi.org/10.1109/PEDES.2010.5712526.
[25] Labeeb M, Lathika BS. Design and analysis of DSTATCOM using SRFT and ANN-fuzzy based control for power quality improvement. 2011 IEEE Recent Adv.

Intell. Comput. Syst., IEEE; 2011, p. 274–9. https://doi.org/10.1109/RAICS.2011.6069317.

[26] Badoni M, Singh A, Singh B. Adaptive Neurofuzzy Inference System Least-Mean-Square-Based Control Algorithm for DSTATCOM. IEEE Trans Ind Informatics 2016; 12:483–92. https://doi.org/10.1109/TII.2016.2516823.

[27] Chittora P, Singh A, Singh M. Simple and efficient control of DSTATCOM in three-phase four-wire polluted grid system using MCCF-SOGI based controller. IET Gener Transm Distrib 2018; 12:1213–22. https://doi.org/10.1049/iet-gtd.2017.0901.

[28] Ghamri A, Benchouia MT, Golea A. Sliding-mode Control Based Three-phase Shunt Active Power Filter: Simulation and Experimentation. Electr Power Components Syst 2012; 40:383–98. https://doi.org/10.1080/15325008.2011.639127.

[29] Das SR, Ray PK, Mohanty A. Improvement of Power Quality using Advanced Artificial Neural Network Algorithm. 2018 IEEE Int. Conf. Power Electron. Drives Energy Syst., IEEE; 2018, p. 1–6. https://doi.org/10.1109/PEDES.2018.8707591.

[30] Hua L, Yuguo W, Wei Z. Power Quality Disturbances Detection and Classification Using Complex Wavelet Transformation and Artificial Neural Network. 2007 Chinese Control Conf., IEEE; 2006, p. 208–12. https://doi.org/10.1109/CHICC.2006.4347508.

[31] Gupta N, Singh SP, Dubey SP. Neural network based shunt active filter for harmonic and reactive power compensation under non-ideal mains voltage. 2010 5th IEEE Conf. Ind. Electron. Appl., IEEE; 2010, p. 370–5. https://doi.org/10.1109/ICIEA.2010.5516896.

[32] Chittora P, Singh A, Singh M. Chebyshev Functional Expansion Based Artificial Neural Network Controller for Shunt Compensation. IEEE Trans Ind Informatics 2018; 14:3792–800. https://doi.org/10.1109/TII.2018.2793347.

[33] Chittora P, Singh A, Singh M. Harmonic current extraction and compensation in three phase three wire system using notch filter. 2015 IEEE Recent Adv. Intell. Comput. Syst., IEEE; 2015, p. 422–7. https://doi.org/10.1109/RAICS.2015.7488453.

[34] Singh B, Kant K, Arya SR. Notch filter-based fundamental frequency component extraction to control distribution static compensator for mitigating current-related power quality problems. IET Power Electron 2015; 8:1758–66. https://doi.org/10.1049/iet-pel.2014.0486.

[35] Jayasankar VN, Vinatha U. Backstepping Controller With Dual Self-Tuning Filter for Single-Phase Shunt Active Power Filters Under Distorted Grid Voltage Condition. IEEE Trans Ind Appl 2020; 56:7176–84. https://doi.org/10.1109/TIA.2020.3025520.

[36] S. Haykin and T. Kailath, “Adaptive Filter Theory”, Pearson education, New Delhi, India, 2003.

[37] T. Adalı and S. Haykin, Adaptive Signal Processing Next Generation Solutions, John Wiley & Sons, Hoboken, New Jersey, 2010.
[38] Modi G, Singh B. A Novel Multilayer N-LMS Adaptive-Filter-Based Control for Synchronization and Power Quality Improvement in Grid-Tied SPV System. IEEE Trans Ind Electron 2023; 70:9158–68. https://doi.org/10.1109/TIE.2022.3215826.
[39] Singh A, Badoni M, Singh B. Application of least means square algorithm to shunt compensator: An experimental investigation. 2014 IEEE Int. Conf. Power Electron. Drives Energy Syst., IEEE; 2014, p. 1–6. https://doi.org/10.1109/PEDES.2014.7042044.
[40] Arya SR, Singh B. Performance of DSTATCOM Using Leaky LMS Control Algorithm. IEEE J Emerg Sel Top Power Electron 2013; 1:104–13. https://doi.org/10.1109/JESTPE.2013.2266372.
[41] Ray PK. Power Quality Improvement Using VLLMS Based Adaptive Shunt Active Filter. CPSS Trans Power Electron Appl 2018; 3:154–62. https://doi.org/10.24295/CPSSTPEA.2018.00015.
[42] Hongbing Li, Ningning Tong, Nannan Liu, Jun Jiang. A new variable-step-size LMS adaptive filtering algorithm. 2008 9th Int. Conf. Signal Process., IEEE; 2008, p. 38–41. https://doi.org/10.1109/ICOSP.2008.4697063.
[43] Walach E, Widrow B. The least mean fourth (LMF) adaptive algorithm and its family. IEEE Trans Inf Theory 1984; 30:275–83. https://doi.org/10.1109/TIT.1984.1056886.
[44] Eweda E. Global Stabilization of the Least Mean Fourth Algorithm. IEEE Trans Signal Process 2012; 60:1473–7. https://doi.org/10.1109/TSP.2011.2177976.
[45] Agarwal RK, Hussain I, Singh B. Implementation of LLMF Control Algorithm for Three-Phase Grid-Tied SPV-DSTATCOM System. IEEE Trans Ind Electron 2017; 64:7414–24. https://doi.org/10.1109/TIE.2016.2630659.
[46] Mittal S, Singh A, Chittora P. Design and development of leaky least mean fourth control algorithm for single-phase grid-connected multilevel inverter. Int J Circuit Theory Appl 2023. https://doi.org/10.1002/cta.3746.
[47] Srinivas M, Hussain I, Singh B. Combined LMS–LMF-Based Control Algorithm of DSTATCOM for Power Quality Enhancement in Distribution System. IEEE Trans Ind Electron 2016; 63:4160–8. https://doi.org/10.1109/TIE.2016.2532278.
[48] Gui G, Adachi F. Adaptive sparse system identification using normalized least mean fourth algorithm. Int J Commun Syst 2015; 28:38–48. https://doi.org/10.1002/dac.2637.
[49] Patel N, Kumar A, Pota HR, Bansal RC, Gupta N. Adaptive q XE-LMF Filter for Improving Power Quality Using Grid-Supporting Photovoltaic System. IEEE Syst J 2023; 17:2709–20. https://doi.org/10.1109/JSYST.2023.3241346.
[50] Badoni M, Singh A, Singh B. Comparative Performance of Wiener Filter and Adaptive Least Mean Square-Based Control for Power Quality Improvement. IEEE Trans Ind Electron 2016; 63:3028–37. https://doi.org/10.1109/TIE.2016.2515558.

[51] Rai KB, Kumar N, Singh A. Design and analysis of Hermite function-based artificial neural network controller for performance enhancement of photovoltaic-integrated grid system. Int J Circuit Theory Appl 2023; 51:1440–59. https://doi.org/10.1002/cta.3486.
[52] Rai KB, Singh A, Kumar N. Bernoulli polynomial-based control technique for PV-integrated grid system under distorted supply. Int J Circuit Theory Appl 2023; 51:3204–25. https://doi.org/10.1002/cta.3578.
[53] Pandey A, Singh A. Laguerre polynomial function-based inverter control with low-voltage ride-through capabilities. Int J Circuit Theory Appl 2023; 51:764–86. https://doi.org/10.1002/cta.3463.
[54] J. Allmeling, A control structure for fast harmonics compensation in activefilters, IEEE T. Pow. Electr. 19 (2) (2004) 508–514.
[55] M. Popescu, A. Bitoleanu, V. Suru, A DSP-based implementation of the p–q the-ory in active power filtering under nonideal voltage conditions, IEEE T. Ind. Inf.9 (2) (2013) 880–889
.[56] B. Singh, S. Kumar, Control of DSTATCOM using I cos ˚ algorithm, in: 35thAnnual Conference of IEEE Industrial Electronics, 2009, pp. 322–327.
[57] L. Marconi, F. Ronchi, A. Tilli, Robust nonlinear control of shunt active filters forharmonic current compensation, J. Automat. 43 (2007) 252–263.
[58] A. Chaoui, J.P. Gaubert, F. Krim, Power quality improvement using DPC con-trolled three-phase shunt active filter, Electr. Pow. Syst. Res. 80 (2010) 657–666.
[59] S.A. Verne, M.I. Valla, Active power filter for medium voltage networks withpredictive current control, Electr. Pow. Syst. Res. 80 (2010) 1543–1551.
[60] P. Salmeron, R.S. Herrera, J.R. Vazquez, A new approach for three-phase loadscompensation based on the instantaneous reactive power theory, Electr. Pow.Syst. Res. 78 (2008) 605–617.
[61] S.R. Arya, B. Singh, CTF control algorithm of DSTATCOM for Power factor cor-rection and zero voltage regulation, in: IEEE Third International Conference onSustainable Energy Technologies, 2012, pp. 157–162.
[62] B. Singh, S.R. Arya, A. Chandra, K. Al-Haddad, Implementation ofadaptive filter based control algorithm for Distribution Static Com-pensator, in: IEEE Industry Applications Society Annual Meeting, 2012,pp. 1–8.
[63] B. Singh, S.R. Arya, Composite observer-based control algorithm for distributionstatic compensator in four-wire supply system, IET Pow. Electr. 6 (2) (2013)251–260.
[64] K. Vardar, E. Akpınar, T. Sürgevil, Evaluation of reference current extractionmethods for DSP implementation in active power filters, J. Electr. Pow. Syst.Res. 79 (2009) 1342–1352.
[65] W. Shireena, T. Li, A DSP-based active power filter for low voltage distributionsystems, J. Electr. Pow. Syst. Res. 78 (2008) 1561–1567.
[66] G. Bhuvaneswari, M.G. Nair, S. Kumar Reddy, Comparison of synchronousdetection and I cos ˚ shunt active filtering algorithms, in: IEEE

InternationalConference on Power Electronics, Drives and Energy Systems, 2006, pp. 1–5.

[67] C.E. Lin, C.L. Chen, C.L. Huang, Calculating approach and implementation foractive filters in unbalanced three-phase system using synchronous detectionmethod, in: Proceedings of International Conference on Industrial ElectronicsControl, Instrumentation and Automation, 1992, pp. 374–380.

[68] H.L. Jou, Performance comparison of the three-phase active-power-filter algorithms, IEE Proc. Gener. Transm. Distrib. 142 (6) (1995) 646–652.

[70] Singh B, Chandra A, Al-Haddad K, editors. Power Quality Problems and Mitigation Techniques. Wiley; 2015. https://doi.org/10.1002/9781118922064.

[72] Soomro AH, Larik AS, Mahar MA, Sahito AA, Soomro AM, Kaloi GS. Dynamic Voltage Restorer—A comprehensive review. Energy Reports 2021;7:6786–805. https://doi.org/10.1016/j.egyr.2021.09.004.

[73] Kassarwani N, Ohri J, Singh A. Design and performance of dynamic voltage restorer using genetic algorithm. Int J Electron 2018; 105:88–103. https://doi.org/10.1080/00207217.2017.1347828.

[74] Pradhan M, Mishra MK. Dual P-Q Theory Based Energy-Optimized Dynamic Voltage Restorer for Power Quality Improvement. IEEE Trans Ind Electron 2019; 66:2946–55. https://doi.org/10.1109/TIE.2018.2850009.

[75] Prasad D, Dhanamjayulu C. Solar PV integrated dynamic voltage restorer for enhancing the power quality under distorted grid conditions. Electr Power Syst Res 2022; 213:108746. https://doi.org/10.1016/j.epsr.2022.108746.

[76] Paramasivam SK, Ramu SK, Mani S, Muthusamy S, Sundararajan SCM, Panchal H, et al. Solar photovoltaic based dynamic voltage restorer with DC-DC boost converter for mitigating power quality issues in single phase grid. Energy Sources, Part A Recover Util Environ Eff 2022; 44:91–115. https://doi.org/10.1080/15567036.2021.1984614.

[77] Saeed AM, Abdel Aleem SHE, Ibrahim AM, Balci ME, El-Zahab EEA. Power conditioning using dynamic voltage restorers under different voltage sag types. J Adv Res 2016; 7:95–103. https://doi.org/10.1016/j.jare.2015.03.001.

[78] Sundarabalan CK, Selvi K. Real coded GA optimized fuzzy logic controlled PEMFC based Dynamic Voltage Restorer for reparation of voltage disturbances in distribution system. Int J Hydrogen Energy 2017; 42:603–13. https://doi.org/10.1016/j.ijhydene.2016.09.061.

[79] Kumar C, Mishra MK. Predictive Voltage Control of Transformerless Dynamic Voltage Restorer. IEEE Trans Ind Electron 2015; 62:2693–7. https://doi.org/10.1109/TIE.2014.2365753.

[80] Li P, Xie L, Han J, Pang S, Li P. New Decentralized Control Scheme for a Dynamic Voltage Restorer Based on the Elliptical Trajectory Compensation. IEEE Trans Ind Electron 2017; 64:6484–95. https://doi.org/10.1109/TIE.2017.2682785.

[81] Ajaei FB, Afsharnia S, Kahrobaeian A, Farhangi S. A Fast and Effective Control Scheme for the Dynamic Voltage Restorer. IEEE Trans Power Deliv 2011; 26:2398–406. https://doi.org/10.1109/TPWRD.2011.2132808.

[82] Khadem SK, Basu M, Conlon MF. Harmonic power compensation capacity of shunt active power filter and its relationship with design parameters. IET Power Electron 2014; 7:418–30. https://doi.org/10.1049/iet-pel.2013.0098.

[83] Hasan K, Othman MM, Meraj ST, Rahman NFA, Noor SZM, Musirin I, et al. Online harmonic extraction and synchronization algorithm-based control for unified power quality conditioner for microgrid systems. Energy Reports 2022; 8:962–71. https://doi.org/10.1016/j.egyr.2021.11.002.

[84] Devassy S, Singh B. Modified pq Theory-Based Control of Solar-PV-Integrated UPQC-S. IEEE Trans Ind Appl 2017;53:5031–40. https://doi.org/10.1109/TIA.2017.2714138.

[85] Heidari MA, Nafar M, Niknam T. A Novel Sliding Mode Based UPQC Controller for Power Quality Improvement in Micro-Grids. J Electr Eng Technol 2022; 17:167–77. https://doi.org/10.1007/s42835-021-00886-3.

[86] Jeraldine Viji A, Aruldoss Albert Victoire T. Enhanced PLL based SRF control method for UPQC with fault protection under unbalanced load conditions. Int J Electr Power Energy Syst 2014; 58:319–28. https://doi.org/10.1016/j.ijepes.2014.01.039.

[87] Chandrakala Devi S, Singh B, Devassy S. Modified generalised integrator-based control strategy for solar PV fed UPQC enabling power quality improvement. IET Gener Transm Distrib 2020; 14:3127–38. https://doi.org/10.1049/iet-gtd.2019.1939.

[88] Dheeban SS, Muthu Selvan NB. ANFIS-based Power Quality Improvement by Photovoltaic Integrated UPQC at Distribution System. IETE J Res 2023; 69:2353–71. https://doi.org/10.1080/03772063.2021.1888325.

[89] Devassy S, Singh B. Design and Performance Analysis of Three-Phase Solar PV Integrated UPQC. IEEE Trans Ind Appl 2018; 54:73–81. https://doi.org/10.1109/TIA.2017.2754983.

[90] Ghosh A, Ledwich G. Power Quality Enhancement Using Custom Power Devices. Boston, MA: Springer US; 2002. https://doi.org/10.1007/978-1-4615-1153-3.

[91] Rashid, M. H., Kumar, N., Kulkarni, A.: Power Electronics Devices. Circuits and Applications (4th Edition), England (2014).

[92] Kanjiya P, Khadkikar V, Moursi MS El. A Novel Type-1 Frequency-Locked Loop for Fast Detection of Frequency and Phase With Improved Stability Margins. IEEE Trans Power Electron 2016; 31:2550–61. https://doi.org/10.1109/TPEL.2015.2435706.

[93] R. K. Agarwal, I. Hussain, and B. Singh, "Application of LMS-based NN structure for power quality enhancement in a distribution network under abnormal conditions," *IEEE Trans. Neural Netw. Learn. Syst.*, vol. 29, no. 5, pp. 1598–1607, May 2018.

[94] S. Pradhan, I. Hussain, B. Singh, and B. K. Panigrahi, "Modified VSSLMS- based adaptive control for improving the performance of a singlestage PV-integrated grid system," *IET Sci., Meas. Technol.*, vol. 11, no. 4, pp. 388–399, 2017.

[95] S. R. Arya and B. Singh, "Performance of DSTATCOM using leaky LMS control algorithm," *IEEE J. Emerg. Sel. Topics Power Electron.*, vol. 1, no. 2, pp. 104–113, Jun. 2013.

[96] A. Bag, B. Subudhi, and P. K. Ray, "An adaptive variable leaky least mean square control scheme for grid integration of a PV system," *IEEE Trans. Sustain. Energy*, vol. 11, no. 3, pp. 1508–1515, Jul. 2020.

[97] B. Subudhi, P. K. Ray, and S. Ghosh, "Variable leaky least mean-square algorithm-based power system frequency estimation," *IET Sci., Meas. Technol.*, vol. 6, no. 4, pp. 288–297, Jul. 2012.

[98] Sahoo A, Mahmud K, and Ravishankar J. An Enhanced Frequency-Adaptive Single-Phase Grid Synchronization Technique. IEEE Trans Instrumentation and Measurement 2021; 70: 1-11. https://doi.org/10.1109/TIM.2021.3070882.

[99] Bangarraju J, Rajagopal V, Jayalaxmi A. Unit Template Synchronous Reference Frame Theory Based Control Algorithm for DSTATCOM. J Inst Eng Ser B 2014; 95:135–41. https://doi.org/10.1007/s40031-014-0087-y.

[100] Qian Q, Xie S, Xu J, Xu K, Bian S, Zhong N. Output Impedance Modeling of Single-Phase Grid-Tied Inverters With Capturing the Frequency-Coupling Effect of PLL. IEEE Trans Power Electron 2020; 35:5479–95. https://doi.org/10.1109/TPEL.2019.2946984.

[101] Hu Q, Fu L, Ma F, Ji F. Large Signal Synchronizing Instability of PLL-Based VSC Connected to Weak AC Grid. IEEE Trans Power Syst 2019; 34:3220–9. https://doi.org/10.1109/TPWRS.2019.2892224.

[102] Ciobotaru M, Teodorescu R, Blaabjerg F. A new single-phase PLL structure based on second order generalized integrator. 2006 37th IEEE Power Electron. Spec. Conf., IEEE; 2006, p. 1–6. https://doi.org/10.1109/pesc.2006.1711988.

[103] Yongheng Yang, Blaabjerg F. Synchronization in single-phase grid-connected photovoltaic systems under grid faults. 2012 3rd IEEE Int. Symp. Power Electron. Distrib. Gener. Syst., IEEE; 2012, p. 476–82. https://doi.org/10.1109/PEDG.2012.6254045.

[104] Kulkarni A, John V. Design of a fast response time single-phase PLL with DC offset rejection capability. 2016 IEEE Appl. Power Electron. Conf. Expo., IEEE; 2016, p. 2200–6. https://doi.org/10.1109/APEC.2016.7468172.

[105] Reza MS, Ciobotaru M, Agelidis VG. Estimation of single-phase grid voltage fundamental parameters using fixed frequency tuned second-order generalized integrator-based technique. 2013 4th IEEE Int. Symp. Power Electron. Distrib. Gener. Syst., IEEE; 2013, p. 1–8. https://doi.org/10.1109/PEDG.2013.6785589.

[106] Xiao F, Dong L, Li L, Liao X. A Frequency-Fixed SOGI-Based PLL for Single-Phase Grid-Connected Converters. IEEE Trans Power Electron 2017; 32:1713–9. https://doi.org/10.1109/TPEL.2016.2606623.

[107] Wu F, Li X. Multiple DSC Filter-Based Three-Phase EPLL for Nonideal Grid Synchronization. IEEE J Emerg Sel Top Power Electron 2017; 5:1396–403. https://doi.org/10.1109/JESTPE.2017.2701498.

[108] Roy S, Chishti F, Singh B, Panigrahi BK. GNLMP Control for Solar PV-Battery Based Microgrid With Ms-EPLL Synchronization. IEEE Trans Ind Appl 2022; 58:6599–611. https://doi.org/10.1109/TIA.2022.3178067.

[109] R H, Mishra MK. An Integrated Control of Enhanced-PLL and Synchronverter for Unbalanced Grid. 2020 IEEE Int. Conf. Power Electron. Drives Energy Syst., IEEE; 2020, p. 1–6. https://doi.org/10.1109/PEDES49360.2020.9379837.

[110] Prakash S, Singh JK, Behera RK, Mondal A. A Type-3 Modified SOGI-PLL With Grid Disturbance Rejection Capability for Single-Phase Grid-Tied Converters. IEEE Trans Ind Appl 2021; 57:4242–52. https://doi.org/10.1109/TIA.2021.3079122.

[111] Mansour AM, Arafa OM, Marei MI, Abdelsalam I, Aziz GAA, Sattar AA. Hardware-in-the-Loop Testing of Seamless Interactions of Multi-Purpose Grid-Tied PV Inverter Based on SFT-PLL Control Strategy. IEEE Access 2021; 9:123465–83. https://doi.org/10.1109/ACCESS.2021.3110013.

[112] Xu JHQSBYHSX. Comparative study of single-phase phase-locked loops for grid-connected inverters under non-ideal grid conditions. CSEE J Power Energy Syst 2020. https://doi.org/10.17775/CSEEJPES.2019.02390.

[113] Golestan S, Guerrero JM, Vasquez JC, Abusorrah AM, Al-Turki Y. Modeling, Tuning, and Performance Comparison of Second-Order-Generalized-Integrator-Based FLLs. IEEE Trans Power Electron 2018; 33:10229–39. https://doi.org/10.1109/TPEL.2018.2808246.

[114] Golestan S, Guerrero JM, Vasquez JC, Abusorrah AM, Al-Turki Y. Single-Phase FLLs Based on Linear Kalman Filter, Limit-Cycle Oscillator, and Complex Bandpass Filter: Analysis and Comparison With a Standard FLL in Grid Applications. IEEE Trans Power Electron 2019; 34:11774–90. https://doi.org/10.1109/TPEL.2019.2906031.

[115] Zhang C, Zhao X, Wang X, Chai X, Zhang Z, Guo X. A Grid Synchronization PLL Method Based on Mixed Second- and Third-Order Generalized Integrator for DC Offset Elimination and Frequency Adaptability. IEEE J Emerg Sel Top Power Electron 2018; 6:1517–26. https://doi.org/10.1109/JESTPE.2018.2810499.

[116] Roncero-Sanchez P, del Toro Garcia X, Torres AP, Feliu V. Fundamental Positive- and Negative-Sequence Estimator for Grid Synchronization Under Highly Disturbed Operating Conditions. IEEE Trans Power Electron 2013; 28:3733–46. https://doi.org/10.1109/TPEL.2012.2231944.

[117] Elsahwi ES, Amanci AZ, Dawson FP. A Digital Frequency Adaptive Synchronization Unit for On- and Off-Grid Systems. IEEE Trans Power Deliv 2017; 32:2070–80. https://doi.org/10.1109/TPWRD.2017.2650480.

[118] Wu F, Zhang L, Duan J. A New Two-Phase Stationary-Frame-Based Enhanced PLL for Three-Phase Grid Synchronization. IEEE Trans Circuits Syst II Express Briefs 2015; 62:251–5. https://doi.org/10.1109/TCSII.2014.2368257.
[119] Wu F, Li X. Multiple DSC Filter-Based Three-Phase EPLL for Nonideal Grid Synchronization. IEEE J Emerg Sel Top Power Electron 2017; 5:1396–403. https://doi.org/10.1109/JESTPE.2017.2701498.
[120] Ramezani M, Golestan S, Li S, Guerrero JM. A Simple Approach to Enhance the Performance of Complex-Coefficient Filter-Based PLL in Grid-Connected Applications. IEEE Trans Ind Electron 2018; 65:5081–5. https://doi.org/10.1109/TIE.2017.2772164.
[121] Singhal A, Suryawanshi HM, S KR, Nachankar PP, Govind D, Narayana CL. An Improved Dual Fixed Frequency SOGI-PLL For Three-phase Grid-Connected Converter Under Unbalanced Condition. 2022 IEEE IAS Glob. Conf. Emerg. Technol., IEEE; 2022, p. 687–91. https://doi.org/10.1109/GlobConET53749.2022.9872473.
[122] Hui N, Feng Y, Han X. Design of a High Performance Phase-Locked Loop With DC Offset Rejection Capability Under Adverse Grid Condition. IEEE Access 2020; 8:6827–38. https://doi.org/10.1109/ACCESS.2020.2963993.
[123] Li Y, Wang D, Han W, Tan S, Guo X. Performance Improvement of Quasi-Type-1 PLL by using a Complex Notch Filter. IEEE Access 2016; 4:6272–82. https://doi.org/10.1109/ACCESS.2016.2614008.
[124] Luo W, Wei D. A Frequency-Adaptive Improved Moving-Average-Filter-Based Quasi-Type-1 PLL for Adverse Grid Conditions. IEEE Access 2020; 8:54145–53. https://doi.org/10.1109/ACCESS.2020.2981426.
[125] Golestan S, Ramezani M, Guerrero JM, Monfared M. <italic>dq</italic>-Frame Cascaded Delayed Signal Cancellation- Based PLL: Analysis, Design, and Comparison With Moving Average Filter-Based PLL. IEEE Trans Power Electron 2015; 30:1618–32. https://doi.org/10.1109/TPEL.2014.2315872.
[126] Wang YF, Li YW. Three-Phase Cascaded Delayed Signal Cancellation PLL for Fast Selective Harmonic Detection. IEEE Trans Ind Electron 2013; 60:1452–63. https://doi.org/10.1109/TIE.2011.2162715.
[127] Neves FAS, de Souza HEP, Bradaschia F, Bueno EJ. Digital Filters for Fast Harmonic Sequence Component Separation of Unbalanced and Distorted Three-Phase Signals. IEEE Trans Ind Electron 2012; 59:3847–59. https://doi.org/10.1109/TIE.2011.2163284.
[128] Qasim M, Kanjiya P, Khadkikar V. Artificial-Neural-Network-Based Phase-Locking Scheme for Active Power Filters. IEEE Trans Ind Electron 2014; 61:3857–66. https://doi.org/10.1109/TIE.2013.2284132.
[129] B. Widrow and M. E. Hoff, “Adaptive switching circuits,” tech. rep., Stanford Univ Ca Stanford Electronics Labs, 1960.
[130] S. Golestan and J. M. Guerrero, "Conventional Synchronous Reference Frame Phase-Locked Loop is an Adaptive Complex Filter," in *IEEE Transactions on*

Industrial Electronics, vol. 62, no. 3, pp. 1679-1682, March 2015, doi: 10.1109/TIE.2014.2341594.

[131] M. Reyes, P. Rodriguez, S. Vazquez, A. Luna, R. Teodorescu and J. M. Carrasco, "Enhanced Decoupled Double Synchronous Reference Frame Current Controller for Unbalanced Grid-Voltage Conditions," in *IEEE Transactions on Power Electronics*, vol. 27, no. 9, pp. 3934-3943, Sept. 2012, doi: 10.1109/TPEL.2012.2190147.

[132] F. Xiao, L. Dong, L. Li and X. Liao, "A Frequency-Fixed SOGI-Based PLL for Single-Phase Grid-Connected Converters," in *IEEE Transactions on Power Electronics*, vol. 32, no. 3, pp. 1713-1719, March 2017, doi: 10.1109/TPEL.2016.2606623.

[1133] C. Zhang, X. Zhao, X. Wang, X. Chai, Z. Zhang and X. Guo, "A Grid Synchronization PLL Method Based on Mixed Second- and Third-Order Generalized Integrator for DC Offset Elimination and Frequency Adaptability," in IEEE Journal of Emerging and Selected Topics in Power Electronics, vol. 6, no. 3, pp. 1517-1526, Sept. 2018, doi: 10.1109/JESTPE.2018.2810499.

[134] A. Kulkarni and V. John, "Design of a fast response time single-phase PLL with DC offset rejection capability," *2016 IEEE Applied Power Electronics Conference and Exposition (APEC)*, 2016, pp. 2200-2206, doi: 10.1109/APEC.2016.7468172.

[135] Y. F. Wang and Y. W. Li, "Three-Phase Cascaded Delayed Signal Cancellation PLL for Fast Selective Harmonic Detection," in *IEEE Transactions on Industrial Electronics*, vol. 60, no. 4, pp. 1452-1463, April 2013, doi: 10.1109/TIE.2011.2162715.

[136] S. Golestan, M. Ramezani, J. M. Guerrero, F. D. Freijedo and M. Monfared, "Moving Average Filter Based Phase-Locked Loops: Performance Analysis and Design Guidelines," in *IEEE Transactions on Power Electronics*, vol. 29, no. 6, pp. 2750-2763, June 2014, doi: 10.1109/TPEL.2013.2273461.

[137] B. P. McGrath, D. G. Holmes and J. J. H. Galloway, "Power converter line synchronization using a discrete Fourier transform (DFT) based on a variable sample rate," in *IEEE Transactions on Power Electronics*, vol. 20, no. 4, pp. 877-884, July 2005, doi: 10.1109/TPEL.2005.850944.

[138] A. B. Shitole, H. M. Suryawanshi, S. Sathyan and M. M. Renge, "Adaptive notch filter-based synchronization technique for integration of distributed generation systems to utility grid," *IECON 2014 - 40th Annual Conference of the IEEE Industrial Electronics Society*, 2014, pp. 5457-5461, doi: 10.1109/IECON.2014.7049334.

[139] P. Shah and B. Singh, "Kalman Filtering Technique for Rooftop-PV System Under Abnormal Grid Conditions," in *IEEE Transactions on Sustainable Energy*, vol. 11, no. 1, pp. 282-293, Jan. 2020, doi: 10.1109/TSTE.2018.2890600. 27

[140] Saxena, H., Singh, A. & Rai, J.N., “Enhanced Third-Order Generalized Integrator-Based Grid Synchronization Technique for DC-Offset Rejection and Precise Frequency Estimation”. Arab J Sci Eng 46, 9753–9762 (2021).

https://doi.org/10.1007/s13369-021-05559-x
[141] Saxena, H., Singh, A., Rai, J. N., & Badoni, M, “PV integrated grid synchronization technique using modified SOGI-FLL and zero-crossing detector. Electrical Engineering”, Electr Eng 104, 1361–1372 (2022). https://doi.org/10.1007/s00202-021-01394-3
[142] Saxena, H., Singh, A. and Rai, J.N. (2020, Adaptive spline-based PLL for synchronisation and power quality improvement in distribution system. IET Gener. Transm. Distrib., 14: 1311-1319. https://doi.org/10.1049/iet-gtd.2019.0662
[143] Q. Zhang, X. Sun, Y. Zhong, M. Matsui and B. Ren, "Analysis and Design of a Digital Phase-Locked Loop for Single-Phase Grid-Connected Power Conversion Systems," in IEEE Transactions on Industrial Electronics, vol. 58, no. 8, pp. 3581-3592, Aug. 2011, doi: 10.1109/TIE.2010.2087295.
[144] N. Kumar, B. Singh and B. K. Panigrahi, "Framework of Gradient Descent Least Squares Regression-Based NN Structure for Power Quality Improvement in PV-Integrated Low-Voltage Weak Grid System," in *IEEE Transactions on Industrial Electronics*, vol. 66, no. 12, pp. 9724-9733, Dec. 2019, doi: 10.1109/TIE.2018.2886765.

Publications

List of publications in SCI/SCIE journals (Published)

1. Rai, KB, Kumar, N, Singh, A. Design and analysis of Hermite function-based artificial neural network controller for performance enhancement of photovoltaic-integrated grid system. Int J Circ Theor Appl. 2023; 51(3): 1440-1459. doi:10.1002/cta.3486
2. Rai, KB, Singh, A, Kumar, N. Bernoulli polynomial-based control technique for PV-integrated grid system under distorted supply. Int J Circ Theor Appl. 2023; 51(7): 3204-3225. doi:10.1002/cta.3578
3. Kanchan Bala Rai, Narendra Kumar & Alka Singh (2022) Design and Analysis of the Shunt Active Power Filter with the ε-NSRLMMN Adaptive Algorithm for Power Quality Improvement in the Distribution System, IETE Journal of Research, doi: 10.1080/03772063.2022.2152116.
4. K. B. Rai, N. Kumar and A. Singh, "Three-phase Grid Connected Shunt Active Power Filter based on Adaptive q-LMF Control Technique," in *IEEE Transactions on Power Electronics*, doi: 10.1109/TPEL.2024.3398369.

List of publications in SCI/SCIE journals (Communicated)

1. Rai, KB, Kumar, N, Singh, A, "Design and Analysis of Rook Polynomial based Neural Network for Shunt Compensation in PV integrated Grid system.", IEEE Transactions on Industrial Electronics **(Under Review).**
2. Rai, K. B., Kumar, N., & Singh, A, "Design and Analysis of Grid Synchronization Technique based on Frequency Adaptive Moving Average Filter (FAMAF) PLL" Electrical Engineering, Springer. (**Revision Submitted)**
3. Rai, KB, Kumar, N, Singh, A. Design and Control of DVR based on Adaptive Bateman Polynomial for Power Quality Improvement. Int J Circ Theor Appl. **(Revision Submitted)**

List of Publications in National and International Conferences

1. K. B. Rai, N. Kumar and A. Singh, "PV Integrated UPQC for Power Quality Improvement Based on MAF-SRF," *2022 IEEE Silchar Subsection Conference (SILCON)*, Silchar, India, 2022, pp. 1-7, doi: 10.1109/SILCON55242.2022.10028949.
2. K. B. Rai, N. Kumar and A. Singh, "Performance Analysis of UPQC using Mittag Leffler Polynomial based Neural Network Control," 2022 IEEE 2nd International Symposium on Sustainable Energy, Signal Processing and Cyber Security (iSSSC), Gunupur, Odisha, India, 2022, pp. 1-6, doi: 10.1109/iSSSC56467.2022.10051471

Similarity Report

PAPER NAME

Design and Control of Custom Power Devices for Mitigation of Power Quality Problems

AUTHOR

Kanchan Bala Rai

WORD COUNT

57573 Words

CHARACTER COUNT

317749 Characters

PAGE COUNT

235 Pages

FILE SIZE

19.4MB

SUBMISSION DATE

Jun 14, 2024 3:46 PM GMT+5:30

REPORT DATE

Jun 14, 2024 3:50 PM GMT+5:30

8% Overall Similarity

The combined total of all matches, including overlapping sources, for each database.

- 2% Internet database
- 7% Publications database
- Crossref database
- Crossref Posted Content database
- 1% Submitted Works database

Excluded from Similarity Report

- Bibliographic material
- Quoted material
- Cited material
- Small Matches (Less then 14 words)

Curriculum Vitae

DR. KANCHAN BALA RAI

(Researcher)

Highly motivated Electrical Engineer with a Ph.D. in design and control of custom power devices for mitigating power quality problems. Possesses research expertise in power electronics, control theory, and power system analysis. Eager to leverage research experience to develop innovative solutions for real world industry challenges.

Contact

PHONE: 9372016369

EMAIL: raikanchanbala@gmail.com

SCHOLASTIC ACHIEVEMENTS

- Prime Minister's Scholarship for Bachelor of Engineering
- University Topper in MTech.

KEY PROJECTS

- Single-phase and Three-phase grid integrated PV system with Power Quality improvements schemes
- Control techniques has been developed for Custom Power Devices.

SKILLS and knowledge

- MATLAB/Simulink, DSO, Power Analyser, AC/DC Programmable Supply
- Power Quality
- Power System
- Control System
- Power Electronics

EDUCATION

Ph.D. from Delhi Technological University

Jan 2020 – April 2024

SGPA: 9.56

Thesis Topic: "Design and Control of Custom Power Devices for Mitigation of Power Quality Problems".

Three SCI Journals and two IEEE international conferences.

M.Tech. from CSVTU, Bhilai

May 2014 – Aug 2016

Specialized in Electrical Devices and Power System

Percentage: 80.46%

B.E in EEE from CSVTU, Bhilai

May 2010-Aug 2014, 81.45%

Research experience

- The research area focuses on power quality (PQ) improvement in grid connected PV system with reactive power compensation, THD.
- Have knowledge of MATLAB/Simulink, dSPACE and hardware design.
- Knowledge of designing new controlling techniques for voltage source converter of Shunt and Series active power Filter.
- Key Findings: Mitigation of current and voltage related power quality (PQ) issues of grid connected distribution system.

Research Publications

- Rai, KB, Kumar, N, Singh, A. Design and analysis of Hermite function-based artificial neural network controller for performance enhancement of photovoltaic-integrated grid system. **Int J Circ Theor Appl. 2023**; 51(3): 1440-1459. doi:10.1002/cta.3486 2)
- Rai, KB, Singh, A, Kumar, N. Bernoulli polynomial-based control technique for PV-integrated grid system under distorted supply. **Int J Circ Theor Appl**. 2023; 51(7): 3204-3225. doi:10.1002/cta.3578 3)

- Kanchan Bala Rai, Narendra Kumar & Alka Singh (2022) Design and Analysis of the Shunt Active Power Filter with the ε-NSRLMMN Adaptive Algorithm for Power Quality Improvement in the Distribution System, **IETE Journal of Research**, DOI: 10.1080/03772063.2022.2152116
- K. B. Rai, N. Kumar and A. Singh, "PV Integrated UPQC for Power Quality Improvement Based on MAF-SRF," 2022 **IEEE** Silchar Subsection Conference (SILCON), Silchar, India, 2022, pp. 1-7, doi: 10.1109/SILCON55242.2022.10028949
- K. B. Rai, N. Kumar and A. Singh, "Performance Analysis of UPQC using Mittag Leffler Polynomial based Neural Network Control," 2022 **IEEE** 2nd International Symposium on Sustainable Energy, Signal Processing and Cyber Security (iSSSC), Gunupur, Odisha, India, 2022, pp. 1-6, doi: 10.1109/iSSSC56467.2022.10051471
- K.B Rai, N Kumar, A Singh," Three-phase Grid Connected Shunt Active Power Filter based on Adaptive q-LMF Control Technique.", **IEEE Transactions of Power Electronics**, 2024.